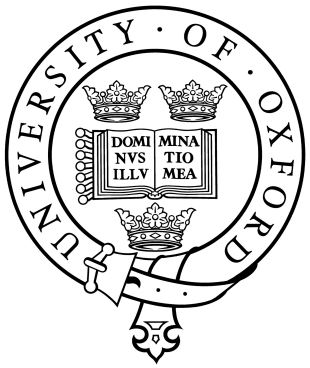
Signal Processing Methods for Characterisation of Ventricular Repolarisation Using the Surface Electrocardiogram



Thomas Brennan

Department of Engineering Science

University of Oxford

Hilary Term, 2009

Thomas Patrick Brennan
Keble College

Doctor of Philosophy
Hilary Term, 2009

Signal processing methods for characterisation of ventricular repolarisation using the surface electrocardiogram

Abstract

This thesis investigates the mechanisms underlying drug-induced arrhythmia and proposes a new approach for the automated analysis of the electrocardiogram (ECG). The current method of assessing the cardiac safety of new drugs in clinical trials is by the measurement and analysis of the QT interval. However, the sensitivity and specificity of the QT interval has been questioned and alternative biomarkers based on T-wave morphology have been proposed in the literature. The mechanisms underlying drug effects on T-wave morphology are not clearly understood. Therefore, a combined approach of forward cardiac modelling and inverse ECG analysis is adopted to investigate the effects of sotalol, a compound known to have pro-arrhythmic effects, on ventricular repolarisation.

A computational model of sotalol and I_{Kr}, an ion channel that plays a critical role in ventricular repolarisation, was developed. This model was incorporated into a model of the human ventricular myocyte, and subsequently arranged in a 1-D fibre model of 200 cells. The model was used to assess the effect of sotalol on I_{Kr}, action potential duration and biomarkers of ventricular repolarisation derived from the simulated ECG.

In parallel, an automated ECG analysis method based on machine learning, signal processing and time-frequency analysis is developed to identify a number of fiducial points in ECG waveforms so that timing intervals and a smooth T-wave segment can be extracted for morphology analysis. The approach is to train a hidden Markov model (HMM) using a data set of ECG waveforms and the corresponding expert annotations. The signal is first encoded using the undecimated wavelet transform (UWT). The UWT coefficients are used for R-peak detection, signal encoding for the HMM and a wavelet de-noising procedure. Using the Viterbi algorithm, the trained HMM is then applied to a subset of the ECG signal to infer the fiducial points for each heart beat. Furthermore, a method for deriving a *confidence measure* based on the trained HMM is implemented so that a level of confidence can be associated with the automated annotations. Finally, the T-wave segment is extracted from the de-noised ECG signal for morphology characterisation.

This thesis contributes to the literature on automated characterisation of drug effects on ventricular repolarisation in three different ways. Firstly, it investigates the mechanisms underlying the effects of drug inhibition of I_{Kr} on ventricular repolarisation as captured by the simulated ECG signal. Secondly, it shows how the combination of UWT encoding and HMM inference can be effectively used to segment 24-hour Holter ECG recordings. Evaluation of the segmentation algorithm on a clinical ECG data set demonstrates the ability of the algorithm to overcome problems associated with existing automated systems, and hence provide a more robust analysis of ECG signals. Finally, the thesis provides insight into the drug effects of sotalol on ventricular repolarisation as captured by biomarkers extracted from the surface ECG.

Acknowledgements

My greatest debt of thanks is to my supervisor, Lionel Tarassenko. Lionel has been an invaluable source of support, guidance and direction throughout the course of research. He gave me the freedom and encouragement to explore cardiac electrophysiological modelling, an new field to both of us at the time. I have benefited enormously from his wisdom during my time at Oxford. I would also like to thank my second supervisor, Blanca Rodriguez, who made me a welcome member of her research group and provided much needed support in entering a new field of research. I would also like to thank Nicholas Hughes for his support and useful input in the early stages of this work.

The research described in this thesis would not have been possible without the use of good ECG data. In this regards, I have been fortunate to benefit from collaborations with a number of ECG core labs and pharmaceutical companies. In particular, I am grateful to Covance, Pfizer and Eli-Lilly who have all provided valuable ECG data sets from clinical trials.

During the course of this research I have benefited from discussions with a number of people. I would like to thank Stephen Payne, Iead Rezek, David Clifton, Susannah Flemming, Gari Clifford, Oliver Gibson and Alex Rowley. In addition, Martin Fink, Esther Pueyo, Iain Strachan and Dave Stokeley deserve special thanks for their support at different stages of this work.

I am particularly grateful to the Rhodes Trust, the Cornhill Family Trust and the Keble Association for providing financial support during the course of my DPhil. I would also like to thank Keble College, the Royal Academy of Engineering and the Department of Engineering Science, who provided generous travel grants that enabled me to attend a number of key conferences during my research.

Last but not least, I would like to thank my family and friends who have always encouraged me and supported my academic pursuits. My parents, Paddy and Megan, and my sister, Brigid, have been a constant source of love and support. I am extremely grateful for everything they have done for me. Most of all, I would like to thank Karlee Silver and Salih Solomon, who have in different ways given me the love, support and happiness that has made this work possible.

Contents

1 Introduction **1**
- 1.1 The Electrocardiogram . . . 3
  - 1.1.1 The ECG waveform . . . 4
  - 1.1.2 ECG recording and analysis . . . 5
- 1.2 Limitations of the QT/QTc interval as a biomarker . . . 10
- 1.3 Alternative biomarkers of drug-induced arrhythmia . . . 11
- 1.4 Role of computational modelling . . . 12
- 1.5 Thesis outline . . . 13

2 Background **15**
- 2.1 Cardiac Electrophysiology . . . 16
  - 2.1.1 Heart anatomy and function . . . 16
  - 2.1.2 Ion channels and the action potential . . . 17
  - 2.1.3 Impulse generation and propagation . . . 21
- 2.2 Human *Ether-A-Go-Go* Related Gene . . . 22
  - 2.2.1 Molecular structure of HERG . . . 22
  - 2.2.2 Repolarising function of HERG . . . 24
  - 2.2.3 Structural basis for pharmacological properties . . . 25
  - 2.2.4 Drug inhibition of HERG . . . 25
- 2.3 Drug-induced arrhythmia . . . 26
  - 2.3.1 Mechanisms of drug-induced arrhythmia . . . 27
  - 2.3.2 Predicting drug-induced arrhythmia . . . 29
- 2.4 Discussion . . . 30

3 Modelling Cardiac Electrical Activity **31**
- 3.1 Electrical Propagation in Cardiac Tissue . . . 32
  - 3.1.1 Cable theory . . . 32
  - 3.1.2 Bidomain model . . . 34
- 3.2 Transmembrane ionic currents . . . 38
  - 3.2.1 Hodgkin-Huxley style models . . . 39
  - 3.2.2 Markov models of cardiac ion channels . . . 44
  - 3.2.3 Modelling K^+ channels . . . 46
- 3.3 Drug interactions with ion channels . . . 47
  - 3.3.1 Receptor theory applied to drug inhibition of ion channels . . . 47
  - 3.3.2 Molecular modulators of drug-ion channel interaction . . . 53
  - 3.3.3 Modelling drug effects on K^+ channels . . . 54
- 3.4 Discussion . . . 56

4 Modelling Effects of Sotalol on Ventricular Repolarisation 57
4.1 Modelling sotalol inhibition of I_{Kr} . . . 58
4.1.1 Pharmacology of Sotalol and HERG . . . 58
4.1.2 Modelling HERG and its interaction with sotalol . . . 59
4.2 Modelling the effect of sotalol on human ventricular myocyte electrophysiology . . . 65
4.2.1 Modelling the ventricular myocyte electrophysiology . . . 65
4.2.2 Effects of sotalol on action potential morphology . . . 68
4.2.3 Reverse-rate dependence of sotalol . . . 68
4.3 Modelling drug effects on the pseudo-ECG . . . 70
4.3.1 1-D model of cardiac tissue . . . 71
4.3.2 Effects of sotalol on 1-D model . . . 79
4.4 Discussion . . . 82

5 Automated Analysis of the Surface Electrocardiogram 84
5.1 Signal processing of the surface ECG . . . 85
5.1.1 Transform methods for ECG representation . . . 85
5.1.2 ECG de-noising . . . 93
5.2 Interval Analysis . . . 96
5.2.1 R-peak detection . . . 97
5.2.2 Waveform feature delineation . . . 100
5.2.3 Heart-rate correction . . . 109
5.3 Morphology analysis . . . 111
5.3.1 T-wave duration biomarkers . . . 111
5.3.2 Amplitude-based T-wave biomarkers . . . 112
5.3.3 Frequency-based T-wave biomarkers . . . 113
5.3.4 Biomarkers based on singular value decomposition of the T-wave . . . 114
5.3.5 T-wave loop morphology biomarkers . . . 115
5.4 Discussion . . . 117

6 Interval and Morphology Characterisation of Ventricular Repolarisation using the surface ECG 119
6.1 Automated ECG segmentation algorithm . . . 120
6.1.1 R-peak detection . . . 121
6.1.2 HMM feature delineation . . . 123
6.2 T-wave morphology characterisation . . . 131
6.2.1 De-noising ECG . . . 132
6.2.2 Morphology biomarkers . . . 132
6.3 Discussion . . . 134

7 The Effect of Sotalol on Ventricular Repolarisation 136
7.1 Analysis of 24-hour Holter ECG recordings . . . 137
7.1.1 Sotalol Holter ECG data set . . . 137
7.1.2 Overview of algorithm . . . 138
7.1.3 Heart-rate correction of biomarkers . . . 140
7.2 Effect of sotalol on biomarkers of ventricular repolarisation . . . 142
7.3 Discussion . . . 150

8 Discussion **152**
8.1 Summary . . . 152
8.2 Limitations and future work . . . 154
8.3 Conclusion . . . 158

A Wavelet Analysis **159**
A.1 Undecimated wavelet transform . . . 159
A.2 Inverse Undecimated Wavelet Transform . . . 164

B Algorithms for HMM Implementation **166**
B.1 Learning HMM parameters . . . 166
B.1.1 Baum-Welch algorithm . . . 167
B.1.2 EM for Gaussian mixture models . . . 169
B.2 HMM inference . . . 170
B.2.1 Viterbi Algorithm . . . 170
B.2.2 Forward-backward procedure . . . 172
B.2.3 Scaling for HMMs . . . 173

Bibliography **177**

Chapter 1

Introduction

In recent years, cardiac drug safety has been a growing concern for both regulatory agencies and pharmaceutical companies. This is partially due to an increase in adverse drug reactions. In the United States, a review of 39 prospective studies ranked adverse drug reactions as the sixth leading cause of death [1]. Of particular concern, is the number of non-cardiac drugs adversely affecting the heart. Non-cardiac drugs are those drugs, such as antihistamines, anti-depressants etc., that are not meant to have a specific effect on the rhythm or functionality of the heart. In spite of this, a growing number of non-cardiac drugs have shown to have adverse effects on the heart, resulting in the deterioration of the rhythmic contraction of the heart muscle into irregular patterns of excitation. This is known as *drug-induced arrhythmia* and can lead to sudden cardiac death if the heart is unable to supply sufficient blood to the body. A recent review showed that the incidence of sudden cardiac death due to drug-induced arrhythmia was one in every 1000 people treated [2]. This increase in adverse side effects of non-cardiac drugs on heart function prompted regulatory agencies to reassess cardiac safety assessment procedures and prescribe new guidelines for assessing the cardiac safety of non-cardiac drugs in clinical trials.

In May 2005, the International Conference on Harmonisation (ICH), the Food and Drug Administration (FDA) of the United States, the European Medicines Agency (EMA) and Japan's National Institute of Health Services finalised clinical trial guidelines for assessing cardiac safety of non-cardiac drugs [3]. The primary means by which the heart's functionality is assessed in clinical trials is through the analysis of the surface electrocardiogram (ECG[1]), a non-invasive signal that captures the electrical activity of the heart.

[1]The ECG is sometimes referred to as the EKG, which is derived from the Dutch word "elektrokardiogramm".

The ICH guidelines proposed that the prolongation of the QT interval, a time interval measured from each heartbeat in the ECG, be used to assess the risk of drug-induced arrhythmia in clinical trials. The QT interval is measured between the onset of the Q-wave and the end of the T-wave, two distinct waveform features of the ECG, and represents the total duration of the contraction and subsequent relaxation of the ventricles (the two lower chambers of the heart).

Drug-induced prolongation of the QT interval is widely accepted as an indicator of increased risk of *torsades de pointes*, a ventricular arrhythmia that can lead to syncope or sudden cardiac death [2]. Pharmaceutical companies are justifiably concerned about drug-induced QT prolongation because every drug associated with ventricular arrhythmia has been shown to prolong the QT interval [4]. Furthermore, QT prolongation is now the primary cause of delays in drug development, the non-approval of candidate drugs and the withdrawal of approved drugs from the market [5, 6].

Despite QT interval prolongation being the standard indicator (or biomarker) of cardiac safety in clinical trials, there are several limitations associated with the QT interval, including poor sensitivity and specificity in predicting drug-induced torsades de pointes. Section 1.2 discusses these limitations in more detail. These limitations impact the efficacy of the QT interval as a predictor of drug-induced arrhythmia and make it difficult to attain the measurement accuracy required by the regulatory agencies. As a result, there has been a growing interest in identifying alternative biomarkers of drug-induced arrhythmia. Studies of the electrophysiological mechanisms underlying drug-induced arrhythmia have identified the morphology of the T-wave as a potential indicator of proarrhythmic activity. The T-wave is a characteristic ECG waveform feature that corresponds to the relaxation (or repolarisation) of the ventricular muscle.

A number of studies have linked changes in T-wave morphology with proarrhythmic drug-related effects on ventricular repolarisation [7]. However, the cellular mechanisms underlying T-wave morphology are not well understood. In addition, T-wave morphology has been shown to vary significantly with heart rate, age and congenital disorders [8]. Therefore, identifying which changes in T-wave morphology are drug-related and can subsequently be used as biomarkers of arrhythmia remains an open question. Nevertheless, interest in morphology-based biomarkers continues to grow in an attempt to find a more sensitive and specific biomarker than the QT interval for predicting drug-induced

arrhythmia.

An objective of this thesis is to identify alternative biomarkers of drug effects on ventricular repolarisation using the surface ECG. The novelty of this thesis is that it combines forward cardiac modelling with inverse analysis of clinical ECG data. A detailed electrophysiologically-based model has been built to investigate mechanisms underlying drug effects on T-wave morphology. The aim is to exploit the understanding and insight gained through modelling drug-effects on ventricular repolarisation in developing an algorithm for extracting biomarkers from the surface ECG and analysing the effects of proarrhythmic drugs on these biomarkers. In this thesis, sotalol, an effective antiarrhythmic drug that is known to prolong QTc and induce torsades de pointes [9], will be used as the test compound for both the modelling and ECG analysis work.

This chapter describes the standard 12-lead ECG and its utility in assessing cardiac risk of drug-induced arrhythmia in clinical trials. Particular attention is given to the measurement, analysis and limitations of the QT interval. In addition, the possibility of using T-wave morphology as an alternative biomarker is discussed. Lastly, a motivation for the use of forward cardiac modelling as a means of investigating drug effects on T-wave morphology is presented.

1.1 The Electrocardiogram

Electrocardiography originated in the late 19th century through the pioneering work of Alexander Muirhead, John Burdon Sanderson and Augustus Waller [10]. However, it was the invention of the string galvanometer in 1901 by Willem Einthoven, a Dutch doctor and physiologist, that enabled the electrical activity of the heart to be measured on the surface of the body. Einthoven termed the resulting signal the "elektrokardiogramm". In 1924, he was awarded the Nobel Prize in Medicine for his work in electrocardiography and for describing the characteristic ECG features of a number of cardiovascular disorders.

Since the turn of the 20th century, the ECG has been used as a diagnostic tool to gather information about the heart's functionality and condition. Although the basic principles put forward by Einthoven are still used today, our increased understanding of cardiac electrophysiology has extended the diagnostic range of the ECG [11]. In addition, ECG monitors have evolved from cumbersome laboratory apparatus that would print the ECG signals onto specially calibrated graph paper, to compact, portable electronic

systems that save digital ECG recordings to flash memory. The following sections review the ECG waveform, how it is recorded and how informative measurements are derived from it.

1.1.1 The ECG waveform

In order to appreciate the different waveform features of the ECG, it is necessary to understand the basics of cardiac anatomy and electrophysiology. The heart is a four-chambered, electro-mechanical pump. The two upper chambers are referred to as the atria, whereas the two lower chambers are referred to as the ventricles, as previously mentioned. The right atrium pumps deoxygenated blood into the right ventricle, which then pumps the blood through to the lungs to be oxygenated. The left ventricle receives oxygenated blood from the left atrium and then pumps it around the body. The walls of the heart's chambers are made of muscle (referred to as the myocardium). The myocardium is specialised tissue that contracts when it is electrically stimulated, a process known as *depolarisation*. A detailed description of cardiac electrophysiology and the cellular mechanisms underlying cardiac function is provided in Chapter 2.

Figure 1.1 schematically illustrates the characteristic waveform features of a typical heart beat. Each heart beat consists of a sequence of distinctive features that correspond to the depolarisation or repolarisation of different regions of the myocardium. The characteristic waveform features of the ECG were assigned the letters P, Q, R, S, T and U by Einthoven. The ECG heartbeat cycle begins with the P-wave, which corresponds to the contraction of the atria. The Q, R and S waves follow the P-wave and are collectively referred to as the "QRS complex". The QRS complex is generally the most recognisable feature of the ECG and corresponds to the contraction of the left and right ventricles (ventricular depolarisation). The S-T segment follows the QRS complex and merges into the T-wave. A U-wave may follow the end of the T-wave; it is only visible in approximately 50% of ECG recordings [12]. The origin and clinical significance of the U wave is unresolved. This marks the end of the cardiac cycle. It is worth noting that atrial repolarisation activity is embedded within the QRS complex as its presence on the ECG is masked by the much stronger ventricular depolarisation.

The onset and offset points of different waveform features are often used in clinical practice to delineate the different ECG features so that important ECG timing intervals

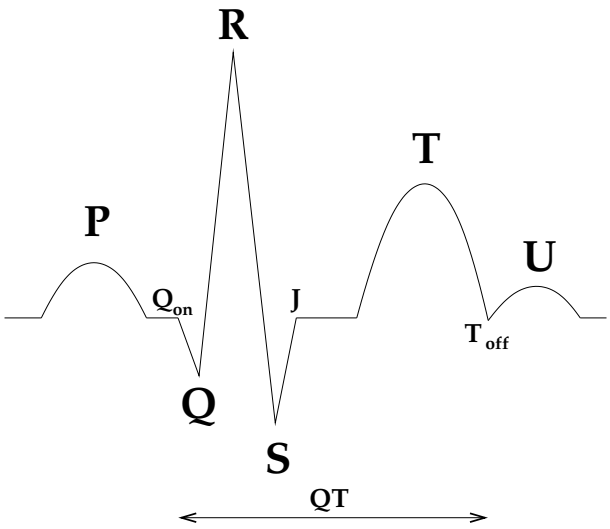


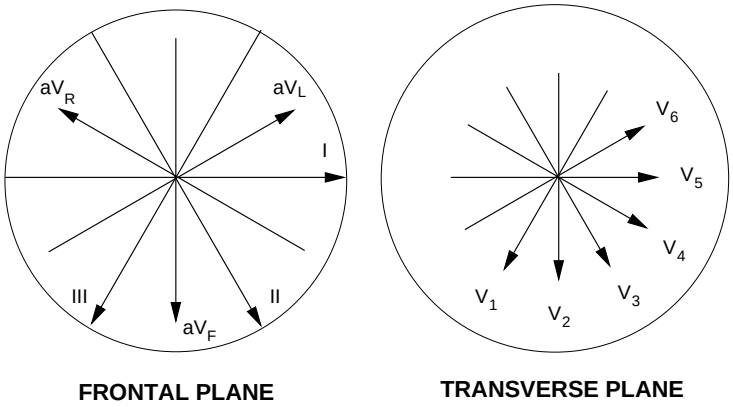
Figure 1.1: Schematic representation of a single cycle of the electrocardiogram signal corresponding to one heart beat. The characteristic features are labelled P, Q, R, S, T and U-waves. The QT interval is measured from the onset of the Q-wave (Q_{on}) to the end of the T-wave (T_{off}).

and segments can be identified. Figure 1.1 also illustrates the start and end points of the QRS complex, namely the onset of the Q-wave (Q_{on}) and the end of the S-wave (referred to as the J point). The end of the T-wave is referred to as T_{off}. The QT interval is defined as the time from the start of the QRS complex (Q_{on}) to the end of the T-wave (T_{off}), i.e. T_{off} - Q_{on}.

1.1.2 ECG recording and analysis

The basis of standard clinical electrocardiography is the 12-lead surface ECG system, jointly proposed by the American Heart Association and the British Cardiac Society in 1938 [11]. In electrocardiography, the term "lead" describes an electrical viewpoint and not the physical surface electrodes. Figure 1.2(a) shows the electrical viewpoints of the standard 12-lead system with respect to the frontal and transverse plane of the human body. The 12-lead system consists of six chest (or precordial) leads (V_1 - V_6) three limbs leads (I, II and III) and three augmented limb leads (aVR, aVL and aVF). The precordial leads view the heart's electrical activity in the transverse or cross-sectional plane, whereas the limb leads view the heart in the frontal or longitudinal plane.

The standard 12-lead ECG system is derived from 10 surface electrodes. Figure 1.2(b) shows the placement of four limb electrodes and six chest electrodes used in the standard 12-lead system [13]. Note that the limb electrodes do not necessarily have to be placed on the limbs as this does not affect the resulting signal. Each ECG lead is defined as the



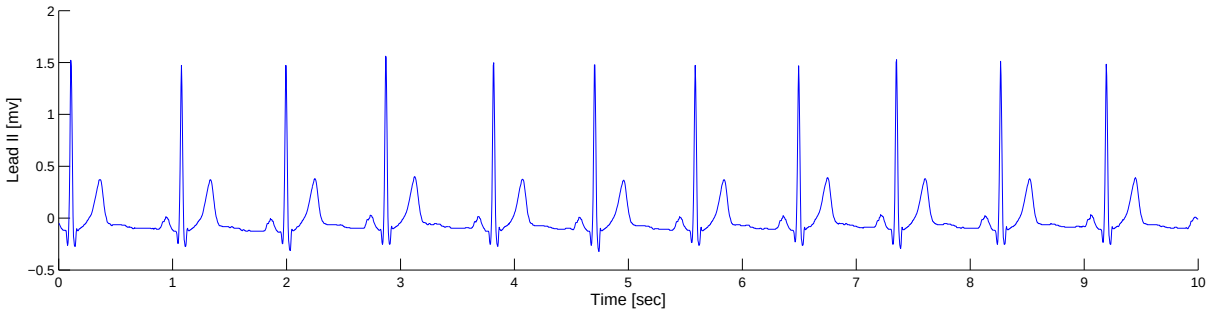
(a) Lead vectors (b) Electrode placement

Figure 1.2: (a) The ECG lead vectors in the frontal and transverse plane of the human body. (b) The placement of the ten surface electrodes from which the standard 12-lead ECG is derived. Reproduced from [13].

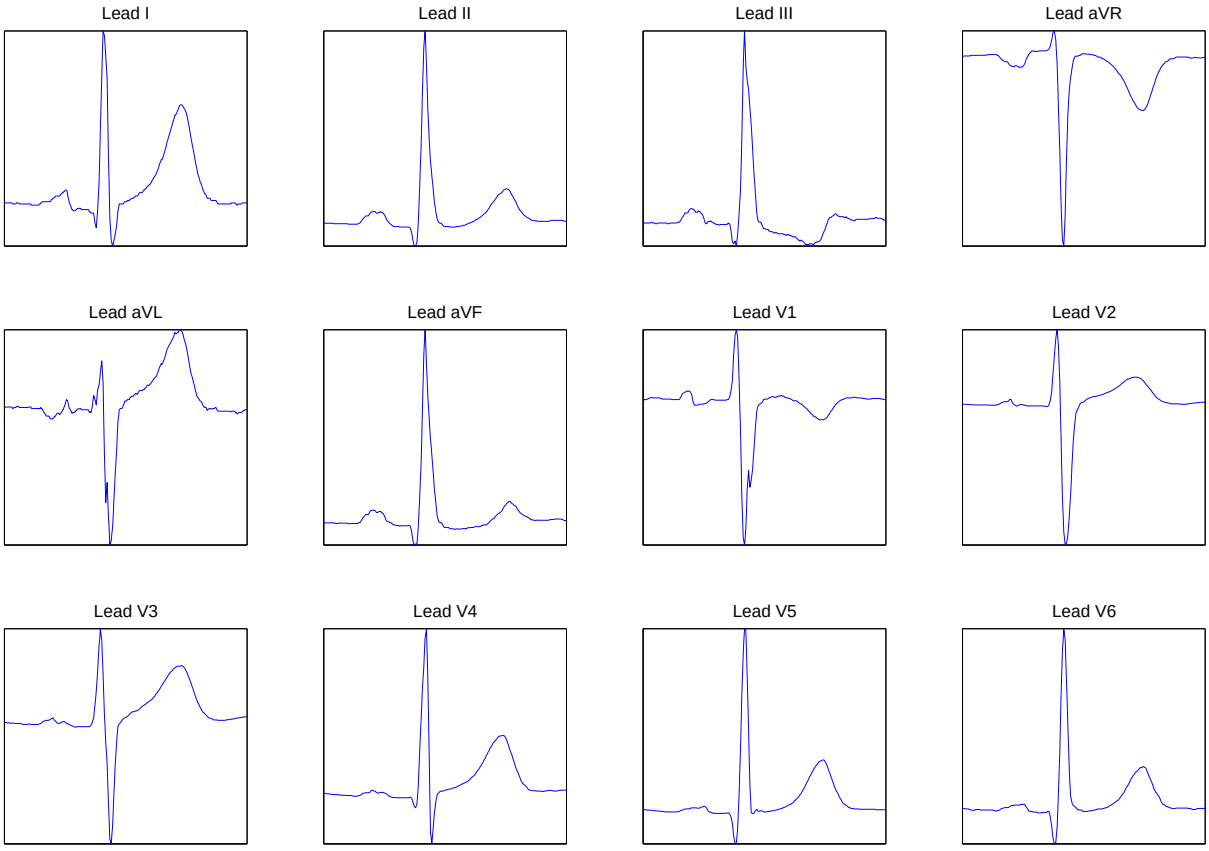
potential difference between two points, a positive and negative electrode. In the 12-lead ECG system, the limb electrodes are referred to as bipolar electrodes, i.e. they act as both a positive and negative electrode, whereas the chest electrodes are unipolar. The precordial leads are measured between the positive unipolar chest electrodes and what is referred to as *Wilson's central terminal*, a reference potential derived from the limb leads that approximates the potential of the body [14]. The augmented limb leads are similarly derived from the potential difference between each limb electrode and Wilson's central terminal.

Figure 1.3(a) shows an example of a standard 10-second ECG recording taken from lead II. The periodic nature of the ECG is clearly seen with each heartbeat waveform separated by a period of inactivity (referred to as the baseline or isoelectric line). As the electrical current flows through the heart muscle, it is measured as a positive deflection when it flows towards the positive electrode of any given lead and as a negative deflection when it flows away from the positive electrode. As a result, ECG waveform morphology will vary between leads because of their different electrical viewpoints. This is clearly seen in Figure 1.3(b), which shows the same heartbeat recorded with each of the 12 leads.

The standard ECG recording typically used in clinical trials is a 10-second recording of all 12 leads. Generally a 10-second recording is sufficient for clinical diagnosis and QT measurement. However, this is really only a snapshot of the heart's activity and



(a) 10-second ECG signal from Lead II



(b) ECG waveforms for one heart beat from all 12 leads

Figure 1.3: Examples of standard 12-lead ECG recordings

does not allow continuous monitoring of the heart's condition over a long period of time. Electrocardiographic ambulatory monitoring or *Holter* monitoring is an improved method of ECG recording that allows continuous ECG recording for 24 hours or more. The Holter monitor is a portable device that was invented by Dr Norman Holter in 1957. The Holter monitor is often worn on the belt and uses between 3 and 10 surface electrodes to record ECG data. Early Holter monitors saved ECG data to magnetic tape, whereas nowadays, with the improvement of solid-state memory devices, Holter monitors are able to record 12-lead ECG data to flash memory devices for up to 26 hours [15]. Holter sample rates vary between 100 to 1000 Hz, thus providing ECG recordings with a quality comparable to bedside ECG monitors [16].

Clinical ECG analysis is a combination of interval and morphology analysis that links changes of timing intervals and characteristic waveform morphologies with different cardiac pathologies and functional abnormalities. For example, S-T segment depression with respect to baseline is linked with ischaemia, electrolyte abnormalities, structural heart disease and congenital disorders [17, 18]. ECG interval analysis is based on timing intervals, such as the QT interval, that are defined between two fiducial points (e.g. the onset and offset points of particular waveform features) and provides insight into the functionality of different regions of the heart.

In most instances of ECG interval analysis *heart rate correction* is required to correct the measured interval for heart rate. The aim of the correction process is to produce measurements that are uncorrelated with heart rate, thus enabling ECG timing intervals measured at different heart rates to be compared. For example, the QT interval is inversely proportional to heart rate, i.e. the slower the heart rate, the longer the associated QT intervals. Heart rate correction of the QT interval results in a corrected QT (or QTc). By convention, the QTc interval is defined to be the estimate of the QT interval that would have been recorded at a heart rate of 60 beats per minute (bpm) [19].

QT dependence on heart rate was first recognised by Henry Cuthbert Bazett in 1920 [20]. Bazett published a heart rate correction formula that simply divided the measured QT interval by the square root of the preceding RR interval, the period between consecutive R peaks, i.e.

$$\mathrm{QTc} = \mathrm{QT}/\mathrm{RR}^{\alpha}, \tag{1.1}$$

where $\alpha = 0.5$. Because of its simplicity and ease of use, Bazett's correction formula

Category	QTc - Male	QTc - Female
Normal	350 - 430	370 - 450
Borderline	431 - 450	451 - 470
Prolonged	> 450	> 470

Table 1.1: Normal, borderline and prolonged QTc ranges for males and females between the age of 18 and 45 years [5].

became the standard correction formula for much of the 20th century. In addition to Bazett's correction factor, over 30 different values of α have been published, varying from 0.25 to 0.5. Fridericia's correction formula uses the cube root of the RR interval, i.e. $\alpha = 0.33\overline{3}$, to calculate QTc and is also widely used in clinical practice [21]. The difference between published values of α is primarily due to inter-subject variance and limited sample population groups [22].

The ICH guidelines described the design and implementation of a *Thorough Phase I QT/QTc Study* to assess the proarrhythmic effect of non-cardiac drugs by evaluating the extent of QTc prolongation in a study population. Phase I trials are *first-in-man* studies, the aim of which is to evaluate the drug's safety and identify potential side effects. The volunteer group usually consists of a small group of healthy, normal[2] volunteers between the ages of 18 and 45 years. The volunteers are given a placebo (a substance with no therapeutic effect), a drug known to have an effect on the heart (known as a "positive control") and various doses of the study drug. The ECG is recorded in each case. The QT interval is measured, either manually or using a supervised automated system, and corrected for heart rate. The QTc interval data is then compared with QTc intervals gathered at the beginning of the study under normal conditions (baseline), which act as a reference point for comparison. Once the effect of the drug on QTc is assessed for each volunteer, the *mean effect* of the drug is assessed for the entire study population. Quantifying how much QTc prolongation is proarrhythmic is not easy, as the QTc interval varies with age, heart condition and gender [5, 23]. Table 1.1 lists the QTc values which are generally considered normal, borderline or prolonged [5]. The threshold level for regulatory concern is approximately 5 ms prolongation, with respect to baseline, set by the lower bound of the 95% confidence interval around the mean effect of QTc prolongation in the study population [3].

[2]Normal volunteers produce ECG recordings that exhibit typical waveform features and timing intervals.

1.2 Limitations of the QT/QTc interval as a biomarker

There are a number of limitations associated with the QT/QTc interval as a biomarker of drug-induced arrhythmia. Firstly, T_{off} is difficult to identify because of the varying morphology of the T-wave, the presence of a U-wave and various types of noise and physiological artefacts [24]. A recent study showed that the state-of-the-art automated ECG analysis programme (12SL, GE Medical Systems, Milwaukee, WI) resulted in a ± 30 ms difference between manual and automated QT interval measurements [22]. Manual measurement, on the other hand, suffers from inter-analyst variability, with one study showing a maximum mean difference of 20 ms between four cardiologists measuring the QT interval from the same ECG waveforms [25].

Secondly, population-based QT heart rate correction formulae, such as Bazett's correction formula, tend to under-correct the QT interval at low heart rates (< 60 bpm) and over-correct at high heart rates (> 60 bpm) [26]. This results in shortened QTc values at high heart rates where risk of ventricular arrhythmia is generally increased [19]. However, despite this, a recent survey of Toxicology and Safety Pharmacology laboratories from 54 companies in Europe, Japan/Asia and the USA showed that 41% of the companies still used Bazett's heart rate correction [21]. In addition to heart rate dependence, it has been found that after a step change in heart rate, the QT interval can take up to three minutes to reach a new steady state [27]. This characteristic has been termed heart rate hysteresis and failure to take this phenomenon into account when measuring the QT interval could also lead towards a biased analysis.

Thirdly, the QT interval is known to vary between leads. This phenomenon is known as QT dispersion. At one stage, the difference between the longest and shortest QT interval measured across all 12 leads was proposed as an indicator of ventricular arrhythmia [28]. However, this dispersion of QT intervals was found to be caused by the different projections of cardiac repolarisation activity across the lead system [29] and not necessarily linked to proarrhythmic activity [30]. Nevertheless, this raises the question of lead selection in QT/QTc analysis. Some investigators have chosen to select the lead with the longest QT interval, or the lead that is deemed by the analyst to have the greatest measurable precision in identifying T_{off}, whilst others have adopted a single lead as a standard (usually lead II or V2) [31]. An alternative approach was proposed by Malik et al. to avoid lead selection issues by measuring the "global" QT interval [32]. This method

carefully superimposes all 12 leads and defines the global QT interval from the earliest Q_{on} to the latest T_{off}. However, this approach results in systematically longer QTc intervals, which could skew the analysis [33].

Last, but not least, an increase in the QT interval does not necessarily lead to ventricular arrhythmia. Experimental studies suggest that QT prolongation alone is not proarrhythmic [34]. Several drugs have been shown to prolong the QTc interval but do not necessarily induce arrhythmia. Amiodarone, for example, significantly prolongs the QT interval but has a very low incidence of inducing arrhythmia ($< 1\%$) compared with sotalol, another anti-arrhythmic, which has an incidence rate of $1-5\%$ of patients on treatment [35]. The difficulty, therefore, in accurately measuring, analysing and interpreting a 5 ms QTc prolongation, as required by regulatory agencies, a considerable challenge.

1.3 Alternative biomarkers of drug-induced arrhythmia

New insights into the mechanisms underlying drug-induced arrhythmia have identified T-wave morphology as a potential biomarker. In particular, the increase of spatial dispersion of repolarisation activity in the ventricular myocardium has been identified as proarrhythmic [36]. A detailed description of the mechanisms underlying drug-induced arrhythmia is presented in Chapter 2. A number of simulation studies of congenital disorders have attempted to link proarrhythmic changes in transmural dispersion of repolarisation with observed changes in T-wave morphology [37, 38]. However, the link between dispersion of ventricular repolarisation activity and the surface ECG is not clearly understood. This is due to the uncertainty of the precise mechanisms underlying T-wave morphology, in terms of the relative contributions of apex-basal versus transmural electrophysiological repolarisation gradients [39]. Similarly, the inverse problem of relating clinically observed changes in T-wave morphology with the underlying mechanisms remains a significant challenge.

A number of clinical studies have reported changes in T-wave morphology in patients with congenital disorders and cardiac pathologies that have an increase in risk of arrhythmia [40, 41]. However, the observed changes in T-wave morphology differed between the study populations and various pathophysiologies [41]. Limited work has been undertaken to describe drug effects on T-wave morphology [7, 42]. A recent study of the effects of sotalol on ventricular repolarisation showed a prolongation of the latter portion of the

T-wave from T-peak to T_{off} [7]. However, the link between changes in T-wave morphology and drug-induced arrhythmia has not been conclusively established by ECG analysis. Therefore, this thesis proposes a forward modelling approach to simulate the effect of drugs on T-wave morphology.

1.4 Role of computational modelling

Modelling cardiac electrophysiology is a well developed area of research with a variety of models of ventricular myocytes published for different species. More recently, a number of human ventricular cellular models have been published [43–45]. These models have been successful in replicating the cardiac dynamics of the human ventricular myocardium. A comprehensive review of modelling drug effects on human ventricular repolarisation is provided in Chapter 3.

There are advantages to using computational modelling in assessing the effects of drugs on ventricular repolarisation. Firstly, it bypasses the ethical limitations inherent to clinical and experimental investigation in human subjects [46]. For example, testing the effects of drug dosages outside the safe dosage range or testing drugs with high toxicity and high risk of adverse side effects. Secondly, modelling drug effects in multi-scale[3] models enables biomarkers to be monitored at each scale in the model. Thirdly, computational modelling provides a cost-effective platform for evaluating and assessing the effects of a candidate compound.

Multi-scale models of the ventricular myocardium have enabled studies of cardiac activity on different scales, namely the sub-cellular, cellular, tissue, organ and whole body level [45, 47, 48]. The most complex of these models uses electrophysiologically-based cellular models of the human ventricular myocyte in a three-dimensional model of the ventricles within a representative model of the human torso [47]. Although simulations using multi-scale, electrophysiologically-based models are computationally intensive, the associated simulation cost is generally far less than the costs of clinical trials. In addition, the relative ease by which different electrophysiological conditions and drug dosages can be simulated *in silico* enables a wide range of experimental conditions to be investigated, which might otherwise have been impossible due to logistical restrictions.

[3]Multi-scale models imply a model that incorporates multiple scales or levels of complexity, e.g. sub-cellular, cellular and tissue dynamics.

1.5 Thesis outline

The goal of this thesis is to identify alternative biomarkers of drug-induced effects on ventricular repolarisation using the surface ECG. The novel approach taken is to combine forward modelling with inverse clinical data analysis to investigate drug effects on T-wave morphology and identify potential biomarkers of drug-induced arrhythmia. The purpose of the forward modelling is to investigate the mechanisms underlying drug-induced changes of T-wave morphology. A multi-scale modelling approach is taken to enable drug effects to be investigated on a sub-cellular, cellular and tissue level. Simulations of a pseudo-ECG from multi-cellular preparations are used to evaluate the changes in T-wave morphology due to various drug concentrations and pacing rates. Observed changes in simulated T-wave morphology are then used to inform inverse analysis of drug-related, clinical ECG data with the aim of closing the loop, so to speak, between forward modelling and inverse analysis.

The approach is illustrated by focusing on the effects of sotalol, in both the forward modelling and inverse ECG analysis. Sotalol targets the delayed inward rectifying potassium ion current (I_{Kr}), which plays a significant role in cardiac repolarisation. The ECG data used in this thesis were recorded from healthy volunteers participating in an academic study in which the effects of sotalol on QTc interval prolongation were investigated [49].

The remaining chapters of this thesis are organised as follows:

- **Chapter 2** - provides a background of cardiac electrophysiology, describes the pharmacological structure of the human *ether-a-go-go* related gene (HERG), which encodes I_{Kr}, and describes the underlying mechanisms of drug-induced arrhythmia.

- **Chapter 3** - reviews the mathematical models of cardiac electrophysiology for ion channels, myocytes, impulse propagation and drug inhibition of ion channels.

- **Chapter 4** - describes the development, validation and simulation results of the computational models of cardiac activity implemented in this thesis.

- **Chapter 5** - reviews the state-of-the-art in ECG signal encoding and de-noising, as well as reviewing automated ECG interval and morphology analysis methods.

- **Chapter 6** - describes the development of the automated ECG analysis algorithm used in this thesis and compares the performance of the algorithm with existing

methods on non-drug clinical ECG data.

- **Chapter 7** - investigates the effects of sotalol on biomarkers of ventricular repolarisation 24-hour Holter ECG recordings from an academic drug study.

- **Chapter 8** - summarises the contributions of this thesis and identifies avenues of further research.

Chapter 2

Background

In this chapter we review the cardiac electrophysiology underlying the T-wave and how pharmaceutical compounds interact with the heart in such a way so as to induce arrhythmia. Section 2.1 provides a basic description of the anatomy and electrophysiology of the heart, paying particular attention to the makeup and dynamics of the ventricular myocardium. This is followed by a description of the human *ether-a-go-go* related gene (HERG), which encodes the delayed, rapidly inactivating potassium current (I_{Kr}). HERG plays a significant role in ventricular repolarisation and is particularly susceptible to binding with pharmaceutical compounds. As a result, the structure and function of HERG are of particular interest due to the role it plays in drug-induced arrhythmia. The final section in this chapter describes the mechanisms underlying drug-induced arrhythmia caused by the drug-inhibition of HERG.

Figure 2.1: Anterior view of the opened heart; arrows indicate normal blood flow. Reproduce from [50].

2.1 Cardiac Electrophysiology

The heart is, in essence, a highly specialised electrical pump that responds to circulatory demands and the sympathetic nervous system to pump blood efficiently around the body. Cardiac electrophysiology is the study of the mechanisms, function and performance of the electrical activity of the heart. This section aims to provide an overview of the basic physiology of the heart and the underlying cardiac electrophysiology.

2.1.1 Heart anatomy and function

Figure 2.1 illustrates the major regions and structures of the heart. There are four major chambers of the heart: the two upper, smaller chambers are the *atria*, while the lower and larger chambers are the *ventricles*. The lowest superficial part of the ventricles is known as the *apex* of the heart and is generally directed downward, forward and to the left of the body. The backward and upward facing portion of the heart is referred to as the *base* of the heart. The atria and ventricles are split into left and right halves by the septal wall or *septum*.

The heart pumps blood around the body using two major circulations systems, namely *systemic* and *pulmonary* circulation. The systemic circulation system supplies oxygenated blood to the body and involves the left atria and ventricle, whereas the pulmonary circulation pumps oxygen-depleted blood through the lungs to be reoxygented using the right atria and ventricle. The right atria collects deoxygenated blood from the body and pumps it to the right ventricle to be pumped into the lungs to enable gaseous exchange between carbon dioxide and oxygen. The left atria collects the reoxygenate blood from the lungs and pass it to the left ventricle which pumps it out to the body. As can be seen in Figure 2.1, the right ventricle wall is thinner than the left ventricle, as it only pumps blood through the lungs, whilst the left ventricle pumps blood throughout the body. Valves separate the left and right atria from their respective ventricle and ensure unidirectional flow of blood by opening on atrial contraction and closing on ventricular contraction.

The walls of the atria and ventricles are made up of muscle tissue known as the my-

ocardium. The outer layer of the heart muscle is referred to as the *epicardium*, whereas the *endocardium* refers to the innermost layer of the heart muscle that lines the chambers of the heart. The term *mid-myocardium* is used to describe the tissue between the epicardium and the endocardium. The structure of the myocardium is heterogeneous comprising of muscle fibres, blood vessels and non-conductive tissue. The muscle fibres are arranged in discrete layers of tissue separated that are roughly parallel to the heart surfaces (epicardium and endocardium). The orientation of the muscle fibres within the sheets of tissue continuously rotating from epicardium to endocardium [51].

Muscle fibres are comprised of interconnected cardiac muscle cells (or myocytes) lying end-to-end along the longitudinal fibre axis. Cardiac myocytes are different from skeletal muscle cells in that they have added ability of conducting electricity in a manner similar to nerve cells. Therefore, electrical stimulation of cardiac myocytes produces a contractive force along the direction of the fibre. The electrical activity associated with the contraction of a cardiac myocyte stimulates adjacent myocytes, preferentially along the axis of the fibre.

2.1.2 Ion channels and the action potential

??

The cardiac myocyte is an excitable system that responds to electrical stimulus, usually through contact with an adjacent cell. Each cell is encased by a membrane which separates the *extracellular* fluid from the *intracellular* fluid, which is composed of water, ions and organic molecules necessary for the cell to operate survive and perform its various functions [52]. As the intracellular and extracellular are separate solutions, a chemical concentration as well as a electric potential gradient exists across the cell membrane. The changes in the electrical *transmembrane potential* (V_m) cause the cell to contract or relax. Electrical sitmulus by an adjacent cell causes the transmembrane potential to depolarise to more positive potentials.

The cell membrane is a selectively permeable phospholipid bilayer that contains a wide variety of proteins and lipids which are used in ion transport across the cell membrane, inter-cellular coupling and cell signalling.

The three mechanisms of ion transport are ion channels, ion pumps and ion exchangers. These complex protein structures span the width of the cell membrane and enable ions to

Figure 2.2: Schematic of ion channel identifying the ion filter, inner pore and voltage-dependent gate. Reproduced from [55].

flow between the intracellular and extracellular fluid. Ion pumps and ion exchangers are examples of active transport mechanisms, i.e. they move ions across the membrane against the concentration gradient, whereas ion channels are passive transport mechanisms. In human cardiac electrophysiology, the ions that are of most interest are Na^+, Ca^{2+} and K^+.

Cardiac myocytes found in the human atria and ventricles have over 20 distinct ionic currents, each contributing to the net flow of electric charge across the cell membrane [53]. The ion channels and ion pumps can be categorised into those that allow ions to flow into the cell and those which flow outward. The inward currents (I_{Na}, I_{CaL} and I_{CaT}) allow Na^+ and Ca^{2+} to flow into the cell. The outward currents or repolarising currents (I_{to1}, I_{to2}, I_{Kr}, I_{Ks}, I_{K1}, I_{Kp}, I_{K-ATP}, I_{K-Ach} and I_{ur}) allow K^+ to flow into the cell [54]. The Na^+-Ca^{2+} ion exchanger allows ions to flow both into and out of the cell depending on the membrane potential at any given time.

Figure 2.2 illustrates the general structure of an ion channel. The selectivity of the channel is primarily determined by its shape, the diameter of its pore and the nature of the electrical charges along its interior surface. Although the protein structures of ion channels differ, the channel pore is usually just one or two atoms (1 Å) wide at its narrowest point [52]. The structure of the ion channel effects the susceptibility of the ion channel to blockage by foreign compounds and is crucial in understanding drug-inhibition of ion channels.

Access to the channel is generally restricted by a gating mechanism, as shown in Figure 2.2, which may be activated by chemical or electrical signals, mechanical force or temperature. The rate at which the channel activates varies between ion channels and depends on the type gating mechanism. Both sodium and potassium ion channels are voltage-gated, in other words the gates open and close in response to the membrane potential. In addition channel activation, certain ion channels have a secondary mechanism of restricting the flow of ions referred to channel *inactivation*.

At rest, the intracellular and extracellular concentrations of each ion are substantially different. This creates a chemical gradient that would force the ions to flow down their concentration gradient to establish an equilibrium. However, the different ionic concen-

Figure 2.3: Schematic representation of the ionic currents and their related transporters responsible for the different phases of the action potential. Red (depolarising) and blue (repolarising) shapes indicate the relative ionic current amplitude, duration and direction. The AP has four recognised phases: resting (0), depolarisation (1), plateau (2) and repolarisation phase (3). Reproduced from [56].

trations also imply a net difference in charge across the cell membrane, which is referred to as the membrane potential. Thus, an electrochemical gradient exists across the cell membrane. At rest the membrane potential is generally between -90 and -80 mV and is very close to the reversal potential for K^+, i.e. there is no substantial electrochemical gradient for K^+ to enter or exit cells [54].

The electrochemical equilibrium is broken under electrical excitation, which can be caused by impulse propagation or an experimentalist's stimulus current. This stimulus is sensed by the Na^+ channel protein, which alters its conformation to allow Na^+ ions to flow into the cell and thus altering the membrane potential. This results in the negative resting potential becoming more positive and it referred to as depolarisation of the membrane potential. This then triggers additional ion channels into action, changing the membrane potential even more. The rapid, non-linear response of the membrane potential to a sufficiently large electrical stimulus is known as the *action potential* (AP).

Figure 2.3 schematically illustrates the contributing ionic currents and the different phases of the action potential. The sharp upstroke (*phase 0*) after the supra-threshold stimulus, is due to a rapid influx of sodium ions (I_{Na}). The activation of I_{Na} occurs between -70 to -60 mV. The depolarisation of the membrane potential triggers the activation of Ca^{2+} and K^+ channels. The first repolarisation or notch (*phase 1*) is due to the rapid, transient outward flow of K^+ ions, for which the I_{to1} and I_{to2} channels are recognised. The notch is not present in all cell types and is most commonly seen in epicardial and sub-epicardial cells [54]. In *phase 2* the influx of calcium ions in the form of slower inward I_{Ca} currents and the Na^+-Ca^{2+} exchanger are able to compensate for the repolarising K^+ currents, creating a relatively flat plateau in the action potential. During repolarisation (*phase 3*) the flow of K^+ ions out of the cell through I_{Kr}, I_{Ks}, I_{K1}, I_{Kp}, I_{K-ATP}, I_{K-Ach} and I_{ur} channels and the simultaneous decrease in Ca^{2+} entry lowers the membrane potential back to its resting potential.

The action potential plays a fundamental role in the function of the myocyte as it allows Ca^{2+} to enter the cell. The change in membrane potential also excites adjacent

Figure 2.4: Schematic of gap junction showing hexagonal connexon subunits in each membrane, that lock to form the gap junctions connecting the two intracellular spaces. Reproduced from [57].

cells via gap junctions. Gap junctions are intercellular structures which consist of an array of cell-to-cell cylindrical elements as illustrated in Figure 2.4 [57]. The change in membrane potential therefore excites adjacent cells, thus enabling the electrical wave of stimulation to propagate from throughout the heart [53].

The action potential can varies in morphology and *action potential duration* (APD) across different regions of the heart. For example, atrial action potentials are significantly shorter than ventricular APs and the action potentials from the Purkinje fibre network are generally longer than those from the ventricular myocardium. These morphology changes are caused by different ion channel configurations and are optimised for the particular function of the associated tissue.

Differences in action potential duration and morphology are also observed within the ventricular myocardium *in vitro* wedge preparations [58]. Figure **??** illustrates the distribution of the three different regions found within the heart wall. These regions are referred to as the epicardium, mid-myocardium and endocardium. The human left ventricular myocardium is between 10-15 mm thick [**?**]. Mid-myocardial characteristics are observed within 1 mm and up to 4 to 5 mm from the epicardial surface in human left ventricular wedge preparation experiments [58]

Extensive research has been done to defined the unique characteristics of these regions [59]. Figure **??** illustrates the different AP morphologies recorded from the different regions in a human left ventricular wedge preparation experiment [58]. Relative to the epicardial and endocardial cells, the mid-myocardial cells have a longer AP than both the epicardial and endocardial regions due to a weaker repolarising I_{Ks} current and a more sustained I_{Na} [60]. In addition, I_{to1} and I_{to2} are largest in epicardial areas and decreases towards the endocardium, therefore endocardial cells do no exhibit a repolarisation notch. In addition, epicardial regions have a greater net repolarising current and thus tend to have a shorter APD than mid-myocardial or endocardial regions [61].

Figure 2.5: A illustration of the heart's electrical conduction system. The sinoatrial node (1) generates an electrical impulse which propagates across the atria to the atrioventricular node (2). The impulse is then transmitted along the Bundle of His (3), through the left and right bundle branches (4) to the Purkinje fibre network (5), which conduct the action potential to the endocardial region of the ventricles. Reproduced from [62].

2.1.3 Impulse generation and propagation

Figure 2.5 illustrates the heart's conduction system and broadly illustrates the sequence of electrical excitation throughout the heart and its relation to the ECG in the right hand panel. The rhythmic contractions of the myocardium are achieved through the generation and propagation of electrical impulses throughout the heart. This process is facilitated by a highly specialised conduction system that conducts the electrical impulses to the different regions of the heart. The sequence starts at the *sinoatrial (SA) node* located in the right atrial wall. The SA node consists of self-excitable or auto-rhythmic cells, which are able to periodically generate an electrical impulse. The SA node, therefore, acts as the pacemaker of the heart. From the SA node, the electrical impulse propagates throughout the left and right atria causing them to contract and pump it into their respective ventricular chamber. As can be seen in the right hand panel of Figure 2.5, the contraction of the atria corresponds to the positive P-wave in the ECG.

The *atrioventricular (AV) node* acts as the conductive bridge between the atria and ventricles in a normal heart. The conduction velocity through the AV node is considerably slower than the conduction velocity through the myocardium. This allows time for the atria to contract completely, thus filling the ventricles with as much blood as possible before they contract. This period of inactivity generally corresponds to a short period of baseline between the P-wave and the QRS complex (as seen in Figure 2.5). Electrical impulse propagate through the *bundle of His* to the apex of the heart through the *bundle branches*. The Bundle of His and the bundle branches are made up of specialised conductive tissue that conducts electrical impulses more quickly than typical cardiac muscle. The Bundle of His branches into three bundle branches: the right, left anterior and left posterior bundle branches that feed into the *Purkinje fibre* network. This intricate network of specialised nerve cells innervates the endocardium and ensures that electrical stimulation propagates to throughout the ventricles. The bundle branches and the Purkinje fibre network ensure that ventricular excitation is synchronised from the apex upwards

as rapidly as required to maximise *systolic* pressure. The contraction of the ventricles corresponds to the QRS complex, the sharpest and largest inflection in the ECG (as seen in Figure 2.5).

The final phase of the cardiac cycle is the repolarisation of the ventricles, which corresponds to the T-wave in the ECG as can be seen in the right hand panel of Figure 2.5. The plateau phase of the ventricular AP corresponds to the ST segment in the ECG. The outflow of K^+ triggers action potential repolarisation and the repolarisation of the myocardium, which corresponds to the T-wave. After ventricular repolarisation there is a diastolic (resting) interval when myocardium returns to its resting phase prior to the next heart beat initiated from the SA node.

The orientation of the muscle fibres effects the intercellular coupling. For instance, epicardial layers are orientated perpendicularly to mid-myocardial layers [63]. This results in relatively poor intercellular coupling between these two regions, which could possibly explain why the contrast of action potential duration between epicardial and mid-myocardial cells observed in wedge preparation experiments is relatively sharp [58]. In contrast, the transition of action potential duration between mid-myocardial cells and endocardial cells is more gradual as muscle fibre layers run parallel to each other.

2.2 Human *Ether-A-Go-Go* Related Gene

The human *ether a-go-go* related gene (HERG) encodes I_{Kr}. Due to its unique structural characteristics, HERG is particularly susceptible to binding with drug compounds. Drug inhibition of I_{Kr} decreases the net repolarising current and generally prolongs the duration of the action potential, which has been shown to have a proarrhythmic effect on the heart [64]. In addition, sotalol is known to bind with I_{Kr} [65]. This section describes the molecular structure and the unique pharmacological properties of HERG that make it particularly susceptible to binding with drug compounds. This is followed by a description of the functional characteristics of HERG during the action potential cycle and the role it plays in ventricular repolarisation.

2.2.1 Molecular structure of HERG

The function and the pharmacological properties of I_{Kr} are determined by HERG's molecular structure and the physical changes it undergoes during the action potential cycle.

Figure 2.6: Structural features of HERG channel, showing (a) the six transmembrane domains ($S1 - S6$), (b) two of the four α-subunits shown in the closed state (white spheres indicate K^+ ions) and (c) two of the four α-subunits shown in the open state. Reproduced from [71].

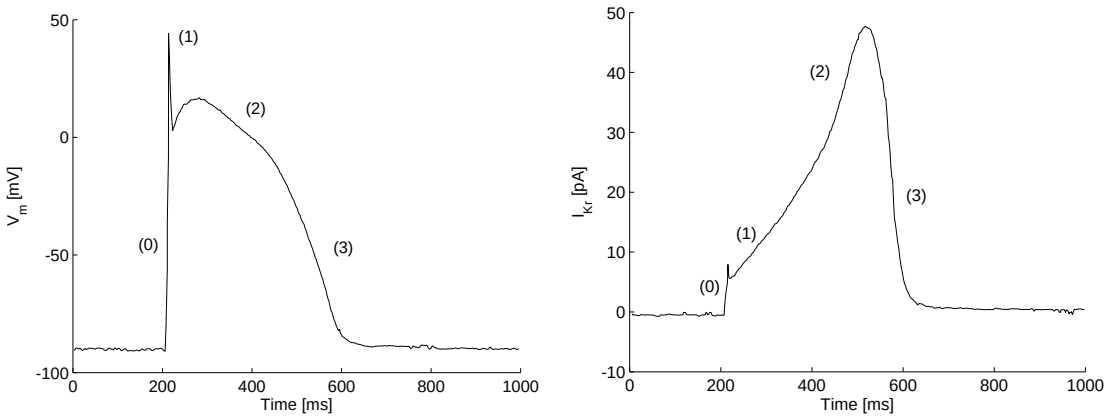
The crystal structure of HERG has not, as yet, been characterised as it is extremely difficult to crystallise ion channel proteins due to their dynamic characteristics. Therefore, most of HERG's known structural information is derived from several bacterial K^+ channels and a mammalian K^+ channel [66–68].

Figure 2.6(a) shows a schematic of HERG's transmembrane molecular structure. HERG is composed of four identical α-subunits, each containing six transmembrane domains[1] (S1-S6). The selectivity filter of HERG is found on the transmembrane pore helix (S5-S6) and ensures that the channel conducts dehydrated K^+ ions across the cell membrane [69]. The protein structure widens below the selectivity filter to form a water-filled region, referred to as the central cavity. The cavity is formed by the intracellular ends of the S6 transmembrane domains.

The activation of HERG is caused by the spatial arrangement (or conformation) of S5 and S6. The gating mechanism that controls this process is voltage-sensitive. The voltage-dependent activation is caused by the movement of positively charged S4 domain due to changes in membrane potential. Figure 2.6(b) shows two of the four α-subunits during the closed state. In the closed state, the opening to the pore is restricted by a criss-cross of the four S6 domains. The mechanical movement of S4 due to the depolarisation of the membrane potential, pulls on the S4-S5 linker, thus displacing S5 and S6 from the channel opening [70]. Figure 2.6(c) illustrates two of the four α-subunits in the open state. The voltage-sensitive S4 domains are not shown; however, the figure illustrates how the S6 domains have moved back to allow ions to flow through the channel.

HERG has an additional gating mechanism known as *inactivation*. The rapid inactivation of HERG is facilitated by what electrophysiologists refer to as *C-type inactivation*. The inactivation of the channel is caused by the conformation of the selectivity filter on the extracelullar ends of the S6 domains. This effectively pinches the pore shut [71].

[1] A domain in molecular biology describes a part of a protein that shares common biochemical properties or physical features, e.g. hydrophobic, polar or ATP binding.



(a) Action potential (b) I_{Kr}

Figure 2.7: I_{Kr} from HERG expressed in human embryonic kidney (HEK-293) cells [74]. The different stages of the action potential cycle are numbered: resting (phase 0), depolarisation (phase 1), plateau (phase 2) and repolarisation (phase 3).

2.2.2 Repolarising function of HERG

Potassium currents can be classified into four categories depending on the role they play in repolarising the membrane potential, namely transient outward, delayed rectifier, inward rectifier and leak currents [72]. I_{Kr} is defined as a rapidly inactivating, delayed rectifier current. The amplitude of I_{Kr} varies during the action potential due to conformational changes of the HERG structure described above and the transition rates associated with these changes. The activation and inactivation processes, as well as deactivation and recovery from inactivation, are voltage-dependent processes [73]. In other words, the gating mechanisms, as well as the time constants associated with these mechanisms, are dependent on the membrane potential.

Figure 2.7 illustrates the variation of I_{Kr} during a single action potential cycle recorded from HERG expressed in human embryonic kidney (HEK) cells [74]. HERG channels are closed at resting potentials. As the membrane potential depolarises to potentials greater than -60 mV, the voltage-sensitive gating mechanism activates allowing ions to flow through the channel pore. However, as the cell continues to depolarise to positive potentials, HERG channels rapidly enter the non-conducting inactivated state. The rate of inactivation of HERG channels is very much faster than that for activation (24 vs. 100 ms^{-1}) [75]. As a result, the balance between open and inactivated states during depolarisation favours the non-conducting inactivated state. This prevents a large I_{Kr} until late in the AP when the membrane potential repolarises, allowing HERG to recover from inactivation and conduct K^+ out of the cell.

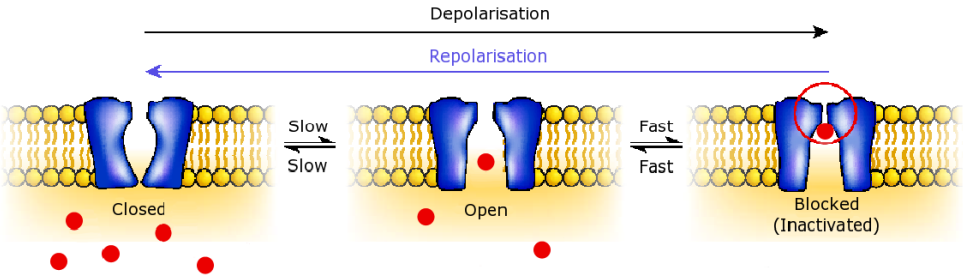


Figure 2.8: A schematic illustrating the drug-inhibition of HERG during the activated states and inactivated states. The drug molecules (represented by red dots) approach the channel protein from the intracellular side and gain access to the channel cavity during the open (activated) state, subsequent inactivation stabilises the block. Modified from [71].

2.2.3 Structural basis for pharmacological properties

Work by Sanguinetti and colleagues [76] have identified two distinct factors, which are unique to HERG, that increase its susceptibility to drug inhibition. Firstly, the volume of HERG's central cavity is larger than most K^+ channels due to the lack of proline residues[2] in the S6 helices, allowing larger drug molecules to gain access to the central cavity [77]. Secondly, HERG has several amino acids lining the channel cavity that have been shown to readily bind with drug compounds [71, 78, 79]. In these instances, drug-inhibition of HERG is dependent on whether the drug molecule has access to the central cavity. Figure 2.8 schematically illustrates the mechanisms of state-dependent drug-inhibition of HERG. The drug compound gains access to the central cavity through the intracellular opening created by the retracted S6 helices after channel activation.

The fast inactivation process of HERG means the drug-binding is able to stabilise once the channel has inactivated. In addition, due to the large dimensions of the central cavity the bound drug molecule is trapped inside the cavity once the membrane has repolarised and the S6 helices have closed [77]. The drug molecule is, therefore, effectively trapped inside the central cavity until the channel returns to the activated (open) state. This trapping mechanism is consistent with the very slow recovery from block observed between methanesulfonanilides compounds and HERG expressed in Xenopus oocytes [64].

2.2.4 Drug inhibition of HERG

Drug inhibition of HERG results in a significant decrease in I_{Kr} conductance. The magnitude of I_{Kr} drug inhibition is often rate-dependent. This was proven experimentally by observing the effects of sotalol on HERG expressed in human embryonic kidney (HEK-

[2] An amino acid that is found in most proteins.

293) cells [80]. The rate-dependencies of sotalol's effects on the ECG will be looked at in more detail in Chapter 7. An increase in temperature, which increases the rate of HERG activation, from room-temperature (22℃) to physiological temperatures (35℃) caused a 2.9 fold decrease in the IC_{50}[3]. In addition, a change in stimulus pulse protocol from a 2-second step-pulse to a 0.5-second step-pulse, resulted in an increase of IC_{50} from 278 to 320 μM. Therefore, the more the channel is in the activated conformation, the more chance the drug has of binding with the channel. The impact of drug-inhibition of I_{Kr} on cardiac repolarisation and the generation of ventricular arrhythmia is now discussed in more detail.

2.3 Drug-induced arrhythmia

Drug-induced arrhythmia is caused by the interaction of drug compounds with sub-cellular structures, such as ion channels. Drug-inhibition of HERG can result in ventricular *reentrant* arrhythmia [81]. Reentrant arrhythmias are those forms of arrhythmia for which the wavefront of excitation repeatedly re-circulates throughout the tissue, i.e. excitation does not originate from the SA node [82]. Due to these *reentrant waves* of excitation, reentrant arrhythmias are able to continue in a self-sustaining manner and are particularly dangerous as they render the heart unable to pump blood efficiently around the body. This section describes the mechanisms underlying drug-induced arrhythmia caused by the inhibition of I_{Kr}.

Torsades de pointes (or torsades) is a particularly life-threatening form of ventricular reentrant arrhythmia that has been linked with drug-inhibition of I_{Kr} [81]. More specifically, torsades is a polymorphic ventricular tachycardia[4]. It was first described by Dessertenne in 1966, who gave the arrhythmia its name, which translates literally from French into "twisting of points" [83]. Figure 2.9 schematically illustrates the characteristic twisting of points observed in the ECG during an episode of torsades. The rapid twisting of points observed in ECG recordings during an episode of torsades are caused by spiralling reentry waves in the ventricular myocardium [84]. Torsades renders the heart unable to pump blood efficiently to the body and can result in syncope (fainting) or sudden cardiac death if it is sustained.

[3]The IC_{50} is half maximal (50%) inhibitory concentration (IC) of a substance and, therefore, is often used as a measure of receptor affinity for a particular substance.

[4]Tachycardia is a form of arrhythmia characterised by a rapid heart action.

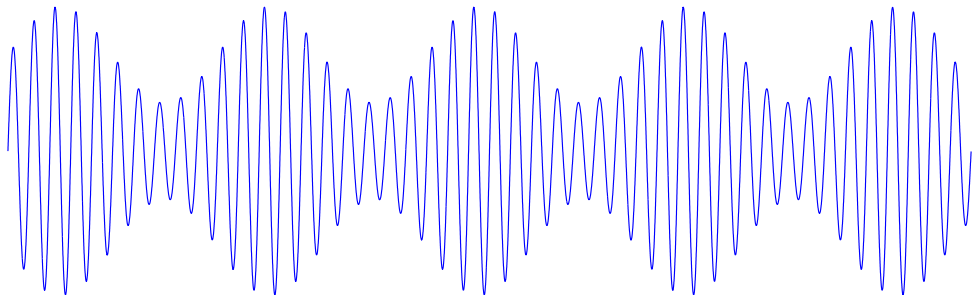


Figure 2.9: A simulated waveform illustrating the "twisting of pointes" characteristic of torsades de pointes as observed in the ECG.

Figure 2.10: A flow diagram of the electrophysiological mechanisms underlying torsades de pointes. Reproduced from [85].

2.3.1 Mechanisms of drug-induced arrhythmia

Figure 2.10 illustrates the mechanisms associated with the initiation of drug-induced torsades de pointes [85]. The decrease of I_{Kr} is caused by drugs binding with HERG resulting in a loss of function in HERG. The net effect of a reduction of I_{Kr} is a decrease in the overall repolarising current. This increases the time taken for the membrane potential to repolarise. The drug-induced prolongation of the action potential has two possible repercussions: firstly, an increase in APD increases the risk of early afterdepolarisations (EAD). An EAD is a secondary depolarisation that occurs during the plateau or repolarisation phase of the action potential. At a tissue level, EADs can initiate an ectopic beat[5] [12]. Given the right conditions (or substrate) an ectopic beat can trigger a wave of activation which can degenerate into torsades.

A decrease in I_{Kr} also results in a more prolonged APD in the mid-myocardial region compared with the epicardium or endocardium due to the heterogeneous nature of the myocardium, as discussed in Section 2.1. This results in what is referred to as increased *dispersion of repolarisation*. Dispersion of repolarisation implies that different regions of the ventricular myocardium are at different stages of repolarisation. This phenomenon is normal in the human ventricular myocardium due to the heterogeneous nature of the tissue. However, it is the increase in these electrophysiological heterogeneities within the myocardium that increases the risk of re-excitation, particularly in regions where repolarised tissue is found close to more depolarised regions. Experimental studies by Hondeghem and colleagues in rabbit hearts have highlighted the increase of heterogeneity

[5] An ectopic beat is an irregular beat of the heart originating somewhere other than the SA node.

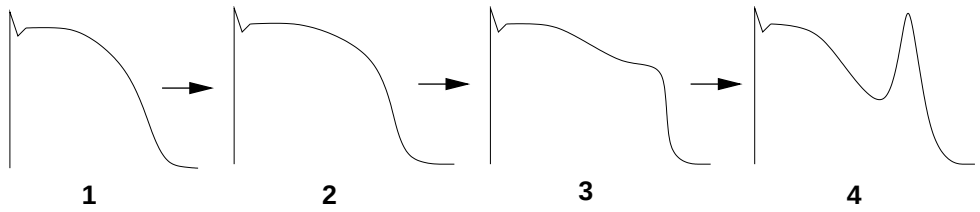


Figure 2.11: Prolongation of AP leading to early-afterdepolarisations (EAD), which can act as a trigger for ectopic beats and reentry waves that can lead to torsades de pointes: (1) normal AP, (2) AP prolongation, (3) EAD then (4) EAD induced ectopic beats.

of repolarisation activity in the ventricular myocardium as being one of the underlying substrates of arrhythmia [36]. In particular, Hondeghem proposes that an increase in duration of phase 3 of the action potential, referred to as AP *triangulation*, and the beat-to-beat variation of APD (termed APD *instability*) are both proarrhythmic factors in the initiation of torsades [86].

EADs play a critical role in the initiation of torsades. The EADs can trigger a wave of ectopic excitation that can degenerate in torsades. Figure 2.11 illustrates a sequence of prolonged action potentials resulting in an EAD. The prolonged action potential duration, caused by a decrease of I_{Kr}, increases the time taken for the cell to repolarise, thereby allowing more Ca^{2+} to enter the cell via I_{Ca-L} and I_{Ca-T}. As previously explained in Section **??**, intracellular Ca^{2+} concentration is closely linked with cardiac contraction, therefore an increase in intracellular Ca^{2+} significantly increases the risk of a secondary depolarisation (EAD) occurring [87]. EADs can initiate an action potential in neighbouring tissue, particularly in regions with significant dispersion of repolarisation.

The EAD-initiated activation wavefront will propagate outwards unless it is blocked by non-conductive tissue. This is referred to as *unidirectional block*. Non-conductive tissue could be due to anatomical, pathological or functional characteristics in that particular region of the myocardium. Anatomical obstructions are regions of non-conductive tissue, whereas pathological obstructions are most often caused by infarction as a result of cardiac ischaemia. Functional obstruction is most often caused by regions of the heart that have not yet repolarised and are therefore unable to initiate a secondary depolarisation. The result of unidirectional block is that the activation wavefront either breaks-up or alters direction and rotates around the obstacle, creating reentry circuits, spiral waves or vortexes, which can degenerate into reentrant arrhythmia.

In addition to a decrease in I_{Kr}, certain clinical factors have also been identified

that increase the risk of torsades. Firstly, hypokalaemia is a condition that occurs when there are abnormally low concentrations of potassium in the blood. This weakens the I_{Kr} current and therefore acts to prolong the action potential in a similar manner to drugs that inhibit I_{Kr} [88]. Secondly, women generally have longer APDs than men and therefore are at a higher risk of torsades occurring. A study showed that more than 70% of all reported cases of drug-induced torsades were found to have occurred in women [89]. Lastly, patients with Long QT Syndrome (LQTS)[6] are likely to be at higher risk from drug-induced arrhythmia due to the increased duration of repolarisation [56]. Furthermore, *low repolarisation reserve* has been proposed to describe those individuals at higher risk of drug-induced arrhythmia [90]. The concept of a repolarisation reserve describes the ability of the myocardium to resist prolongation of the action potential. It describes how I_{Ks} compensates for reductions in other repolarising currents, particularly I_{Kr}. This would imply that a low repolarisation reserve increases the risk drug-induced torsades. Camm et al. suggest that low repolarisation reserve is congenital, however symptoms are only exhibited under the influence of drugs [91].

2.3.2 Predicting drug-induced arrhythmia

It is clear from Figure 2.10 that both the prolongation of the action potential and the increase in dispersion of repolarisation play a role in drug-induced episodes of torsades de pointes. It would be reasonable to assume that, these mechanisms manifest themselves on the ECG waveform as an increase in QT interval and as changes in T-wave morphology, respectively. Hence QT interval prolongation alone does not necessarily lead to torsades, as is the case with amiodarone. Amiodarone significantly increases APD and the QT interval, however due to its complex pharmacological profile it does not significantly increase dispersion of repolarisation and therefore the incidence of drug-induced torsades is very low ($< 1\%$) [92]. Antzelevitch and Shimizu state that "the problem with the long QT syndrome is not long QT intervals but rather the dispersion of repolarisation that often accompanies prolongation of the QT interval" [93].

Dispersion of repolarisation in the myocardium is typical. In fact, it is due to the heterogeneities in the ventricular myocardium during repolarisation that the T-wave is observed on the surface ECG. However, it is the increase in these heterogeneities that

[6]LQTS is a congenital disorder. Patients exhibit abnormally prolonged QT intervals, due to electrophysiological defects that result in a prolonged APD

is deemed to be proarrhythmic. Changes in repolarisation heterogeneities due to drug action are therefore likely to affect the morphology of the T-wave. Indeed, *in vitro* wedge preparation experiments have shown that an increase in transmural dispersion of repolarisation prolongs the interval between T-peak and T_{off} [59]. However, the exact nature of drug-induced morphology changes to be expected in the intact human heart (as measured in the surface ECG) remains unknown. As a result, there is significant interest in not only quantifying changes in T-wave morphology that might provide an improved predictor of drug-induced arrhythmia, but also in investigating the molecular mechanisms underlying changes in T-wave morphology.

2.4 Discussion

The electrophysiology of the heart is a complex electro-mechanical process that enables the heart to effectively pump blood around the body. Ventricular repolarisation is a critical stage in the heart's cycle when the myocardium returns to it's resting state before the initiation of another heart beat from the SA node. The repolarising dynamics differ between the different cell types found in the myocardium, namely the endo-, mid- and epicardial cells. Nevertheless, I_{Kr} plays an important role in repolarising the membrane potential for all the cell types. However, the human ether-a-go-go related gene (HERG) that encodes I_{Kr} is particularly susceptible to binding with drug compounds and drug-inhibition of I_{Kr} has been shown to proarrhythmic.

The mechanisms underlying ventricular arrhythmia are two fold. Firstly, there is the prolongation of the APD, which can lead to an early after-depolarisation that can excited neighbouring cells. Secondly, the increase of repolarisation heterogeneities allows for the wave of activation, triggered by EAD-induced ectopic beat, to propagate and potential degenerate into re-entry waves of excitation and torsades de pointes. Therefore, in developing predictors of drug-induced arrhythmia it is important to characterise both the increase in repolarisation duration (currently capture by the QT interval) as well as the increase in repolarisation heterogeneities. Repolarisation heterogeneities are capture by the shape of the T-wave. The next chapter will investigate the use of cardiac modelling to investigate the effects of sotalol, a potent Class III anti-arrhythmic that is known to inhibit I_{Kr}, on repolarisation dynamics so that potential morphology-based biomarkers can be identified and investigated.

Chapter 3

Modelling Cardiac Electrical Activity

Over the past half century, mathematical modelling of cardiac electrophysiological behaviour has evolved into a mature field that has provided much insight into the mechanisms of cardiac arrhythmogenesis [94, 95]. Detailed single cell models of cardiac electrophysiology now exist for a variety of animal species and cardiac cell types, including human ventricular models [44, 96]. In addition, numerous models of atrial and ventricular cardiac electrophysiology have been developed [46]. These models have enabled the mechanisms underlying cardiac phenomena, such as arrhythmia, to be investigated from the ion channel to the whole organ level. In this chapter, the principles and techniques involved in modelling the dynamics of cardiac electrical activity and the effects of drugs on these dynamics are reviewed.

3.1 Electrical Propagation in Cardiac Tissue

As described in the previous chapter, the heart muscle is a heterogeneous tissue consisting of multi-cellular muscle fibres, connective tissue and interstitial fluid. Individual myocytes are electrically coupled to adjacent cells through gap junctions. In order to understand the principles of electrical propagation in cardiac tissue, it is first necessary to understand *cable theory* and how this is applied to the propagation of electrical impulses in cardiac muscle fibres.

3.1.1 Cable theory

The fundamental theory of electrical cables was first formulated in the 1850's by William Thomson, later to become Lord Kelvin, in describing the decay of current in the first transatlantic cable [97]. Thomson theorised that the current decay in a conductive cable is due to both the resistance and capacitance of the cable. Cable theory was first applied to nerve fibre conduction in the early 20th century and was later validated by experimental evidence [98]. The success of cable theory in describing impulse propagation in nerve fibres opened the way for its application to modelling electrical propagation in cardiac tissue.

Figure 3.1 illustrates a cylindrical conductor where the properties of resistance and capacitance are uniformly distributed over the volume of the conductor. The material properties of the cable determine its axial resistivity (R_a) and membrane capacitance (C_m). An axial current (I_i) flows down the length of the cable, whereas I_m represents the flow of charge through the walls of the cable, i.e. perpendicular to the longitudinal axis

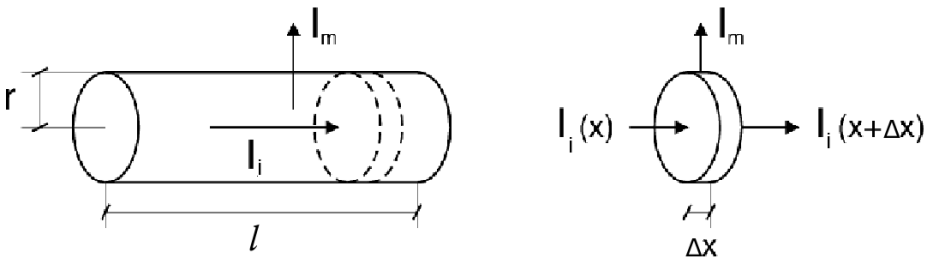


Figure 3.1: Schematic diagram of a cylindrical conductor used to study electrical propagation in excitable tissue. The conductor, with radius r and length l, has axial resistivity R_a. I_i is current flowing in the longitudinal direction and I_m is current flowing across the cell membrane.

of the cable. Thus, if the uniform conductor model represented a cardiac myocyte, I_m would represent the transmembrane ionic current.

In the simplest case, propagation of electrical activation in cardiac tissue is considered to be continuous, i.e. the cellular resistivity and membrane capacitance of the individual myocytes are incorporated into R_a and C_m of the cable conductor. This, in effect, amalgamates the electrical properties of individual cell and intracellular coupling (i.e. gap junctions) into one continuous problem. The axial resistivity, R_a, and the capacitance, C_m, of the conductor can then be averaged over the volume as follows:

$$c_m = C_m 2\pi r \tag{3.1}$$

$$r_a = \frac{R_a}{\pi r^2}, \tag{3.2}$$

where r is the radius of the myocyte.

The transmembrane current I_m can be split into two parts: the capacitive current (I_c) and the total ionic current (I_{ion}), i.e.

$$I_m = I_c + I_{ion}. \tag{3.3}$$

As discussed in Section **??**, the flow of ions across the cell membrane, through ion pumps, exchangers and ion channels, in response to a supra-threshold stimulus results in the cellular AP. Therefore, I_{ion} is a highly complex, non-linear term that is effectively the sum of all the transmembrane ionic currents observed in the cell. Mathematically, I_{ion} consists of a system of ordinary differential equations (ODEs), with the more complex cellular AP models including more than 60 ODEs [99]. Section 3.2 describes the mathematical modelling of I_{ion} in more detail.

In the cardiac myocyte, I_c arises from the separation of the extracellular and intracellular fluids by the lipid bilayer of the cellular membrane. As discussed in Section **??**, a difference of charge exists across the membrane due to the different ion concentrations in the extracellular and intracellular fluids. This gives the cell membrane capacitive qualities. The capacitive current is defined as

$$I_c = C_m \frac{\partial V_m}{\partial t}, \tag{3.4}$$

where V_m is the membrane potential and C_m is the cellular membrane capacitance. In contrast, the axial current is considered to be ohmic (i.e. solely dependent on resistivity

of the cell), such that

$$\frac{\partial V_m}{\partial x} = -R_a I_a. \tag{3.5}$$

Taking into account Kirchhoff's conservation of current law that the sum of all currents flowing towards a junction is equal to the sum of those currents leaving the junction, a loss of intracellular axial current I_a (per unit length) must equal the transmembrane current (per unit length), i.e.

$$I_m = -\frac{\partial I_a}{\partial x}. \tag{3.6}$$

Substituting Equation 3.6 into the derivative of Equation 3.5 yields

$$\frac{\partial^2 V_m}{\partial x^2} = R_a I_m. \tag{3.7}$$

The so-called *cable equation* can then be defined by substituting Equations 3.3 and 3.4 into Equation 3.7, such that

$$\frac{\partial^2 V_m}{\partial x^2} = R_a \left\{ C_m \frac{\partial V_m}{\partial t} + I_{ion} + I_{stim} \right\}, \tag{3.8}$$

where I_{stim} is the stimulus current. Experimental studies by Weidmann [100] and Clerc [101] on trabecular muscle from mammalian heart confirmed the theoretical predictions of classical cable theory in determining impulse propagation in cardiac fibres.

3.1.2 Bidomain model

The one-dimensional cable model does not take into consideration the heterogeneous structure of cardiac tissue, in particular, the extracellular space. Extending the uniform conductor framework into higher dimensions gives rise to the *bidomain model*. The bidomain model was developed in 1978 by Tung [102], Miller and Geselowitz [103]. The bidomain model was then used by Henriquez and Plonsey in 1990 to describe the propagation of electrical impulses in cardiac tissue [104, 105]. An extensive review of the development of the bidomain model is given by Henriquez [106].

The bidomain model considers two regions (or domains), namely the *intracellular* and the *extracellular* domain. The intracellular domain, in this context, includes the interior volumes of all the interconnected cardiac cells, whereas the extracellular domain describes the extracellular matrix, including interstitial fluid and connective tissues. The bidomain model represents these two separate regions coupled together by transmembrane currents and provides the most comprehensive description of electrical properties of cardiac tissue published to date.

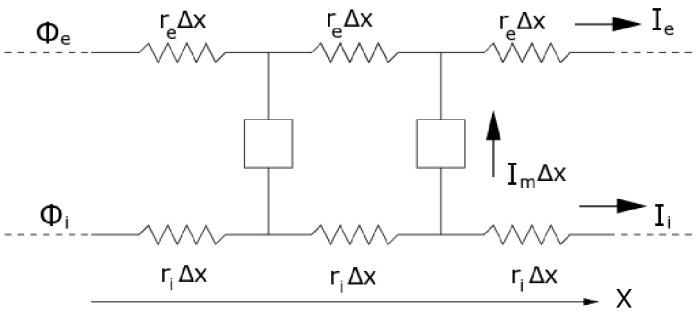


Figure 3.2: Equivalent circuit of the bidomain model for impulse propagation in a cardiac tissue. The transmembrane potential is given by $V_m = \phi_i - \phi_e$. The transmembrane current I_m flows between the intracellular and extracellular domains. Although the bidomain model is represented as a series of discrete resistors, the model is continuous, i.e. $\Delta x \to 0$.

Figure 3.2 is a schematic of the equivalent electrical circuit of the bidomain model. Although the circuit is graphically represented as a discrete repetition of resistors in the extracellular and intracellular domains for each segment (Δx), the bidomain is in fact continuous, i.e. $\Delta x \to 0$. In addition, the assumption that the electrical properties of resistance and capacitance are uniformly distributed over the volume of the conductor still holds. The transmembrane potential (V_m) is defined as the difference between the intracellular and extracellular potentials, i.e.

$$V_m = \phi_i - \phi_e, \tag{3.9}$$

where ϕ_i is the intracellular potential and ϕ_e is the extracellular potential. Similar to Equation 3.5, the intracellular and extracellular current densities are defined according to Ohm's law as

$$J_i = -\sigma_i \nabla \phi_i \tag{3.10}$$

$$J_e = -\sigma_e \nabla \phi_e, \tag{3.11}$$

where J_i and J_e are the intracellular and extracellular current densities, and σ_i and σ_e are the conductivities[1] (represented as tensors) associated with the two respective domains.

As previously mentioned, I_m flows between the intracellular and extracellular domains. Therefore, taking into account the conservation of current in a closed system, i.e. in the absence of any stimulus current, any transmembrane current flowing out of the intracellular domain must equal the inflow in the extracellular domain and vice versa, i.e.

$$I_m = -\nabla \cdot J_i = \nabla \cdot J_e. \tag{3.12}$$

[1]Conductivity is the inverse of the resistivity of a volume conductor.

The intracellular and extracellular current densities can then be related to the transmembrane currents as follows:

$$\nabla \cdot (\sigma_i \nabla \phi_i) = \beta_m I_m \tag{3.13}$$

$$\nabla \cdot (\sigma_e \nabla \phi_e) = -\beta_m I_m. \tag{3.14}$$

where β_m is the surface-to-volume ratio of the cellular membrane. In the simple case of a cylindrical cell, $\beta_m = 2(l + r)/lr$, where l is the length of the cable and r is its radius. Substituting Equations 3.13 and 3.14 into Equation 3.12 yields

$$\nabla \cdot (\sigma_i \nabla \phi_i) = -\nabla \cdot (\sigma_e \nabla \phi_e). \tag{3.15}$$

The first bidomain equation can then be defined by substituting $\phi_i = V_m + \phi_e$ from Equation 3.9 into Equation 3.15 and re-arranging such that

$$\nabla \cdot (\sigma_i \nabla V_m) = -\nabla \cdot \{(\sigma_i + \sigma_e) \nabla \phi_e\}. \tag{3.16}$$

Recall, from the previous section, that the transmembrane current comprises of a capacitive current and the total ionic current, i.e.

$$I_m = C_m \frac{\partial V_m}{\partial t} + I_{ion}. \tag{3.17}$$

Substituting Equation 3.17 into Equation 3.13 yields

$$\nabla \cdot (\sigma_i \nabla \phi_i) = \beta_m \left\{ C_m \frac{\partial V_m}{\partial t} + I_{ion} \right\}. \tag{3.18}$$

The second bidomain equation can then be defined by again substituting $\sigma_i = V_m + \sigma_e$ from Equation 3.9 into Equation 3.18, which yields

$$\nabla \cdot (\sigma_i \nabla V_m) + \nabla \cdot (\sigma_i \nabla \phi_e) = \beta_m \left\{ C_m \frac{\partial V_m}{\partial t} + I_{ion} \right\}. \tag{3.19}$$

Stimulation currents can be applied to both the intracellular and extracellular regions, represented as $I_{stim,i}$ and $I_{stim,e}$, respectively. Including the stimulus currents in the bidomain equations yields

$$\nabla \cdot (\sigma_i \nabla V_m) = -\nabla \cdot \{(\sigma_i + \sigma_e) \nabla \phi_e\} - I_{stim,ec} \tag{3.20}$$

$$\nabla \cdot (\sigma_i \nabla V_m) + \nabla \cdot (\sigma_i \nabla \phi_e) = \beta_m \left\{ C_m \frac{\partial V_m}{\partial t} + I_{ion} \right\} + I_{stim,tm} \tag{3.21}$$

where $I_{stim,ec} = I_{stim,e} - I_{stim,i}$, and $I_{stim,tm}$ is the transmembrane stimulus current density [107].

Boundary conditions

As previously mentioned, the bidomain model is a continuous, volume-averaged model of real tissue. However, boundary conditions on the surface separating the bidomain tissue model and the surrounding volume[2] must be considered [104]. Firstly, it is required that the intracellular current normal to the bidomain boundary vanishes, i.e. there is no current between the intracellular domain and the surrounding volume. This gives rise to the first boundary condition that is applied to the surface of the intracellular space

$$\mathbf{n} \cdot (\sigma_i \cdot \nabla \phi_i) = 0, \tag{3.22}$$

where $\mathbf{n}$ is the unit vector normal to the surface of the intracellular domain. Secondly, the extracellular current density and electric field must be continuous with the surrounding volume, i.e.

$$\mathbf{n} \cdot (\sigma_e \cdot \nabla \phi_e) = \mathbf{n} \cdot (\sigma_b \mathbf{I}) \cdot \nabla \phi_b \tag{3.23}$$

$$\phi_{e,\Gamma} = \phi_{b,\Gamma}, \tag{3.24}$$

where σ_b and ϕ_b are, respectively, the conductivity and potential of the surrounding volume, $\mathbf{I}$ is the identity tensor and Γ is the surface bounding the tissue from the surrounding volume.

Taking into account the boundary conditions, the first bidomain equation (Eq. 3.16) is used to solve for the extracellular potential ϕ_e for a given transmembrane potential V_m. The second bidomain equation (Eq. 3.19) is then used to update V_m. The conductivities σ_i and σ_e in Equations 3.16 and 3.19 are represented throughout the tissue volume by a 3-D orthogonal tensor of conductivity values corresponding to the electrical conductance in the fibre. The bidomain model takes into account that the intracellular and extracellular domains are each anisotropic[3] to a varying degree. This is represented by varying anisotropy ratios in the components of the respective conductivity tensors [107].

Monodomain representation

Although the bidomain model accurately represents both the extracellular and intracellular domains, it is computationally taxing, particularly in large multi-cellular geometries.

[2]This is sometimes referred to as the surrounding "bath" in reference to *in vitro* experiments wherein tissue preparations are placed in a bath of solution, such as Tyrode's solution.

[3]Possessing the power of both right- and left-handed polarisation.

For example, a 3-D bidomain model of the human ventricles using a finite difference mesh with 36 million nodes takes 39 hours on 32 processors to compute one heart beat (600 ms) [108]. To reduce the complexity of the bidomain model, a number of assumptions have been proposed: the extracellular domain is assumed to be highly conductive, or the domains are assumed to be equally anisotropic, or ϕ_e is assumed negligible [52]. In each of these instances, the two bidomain equations (Eq. 3.16 and 3.19) can be reduced to a single equation. This representation is referred to as the *monodomain framework* and is defined by the single equation

$$\nabla \cdot (\sigma_i \nabla V_m) = \beta_m \left\{ I_{ion} + C_m \frac{\partial V_m}{\partial t} \right\} + I_{stim}, \tag{3.25}$$

where σ is now the intracellular or bulk conductivity tensor. A *diffusion coefficient* (D) is often substituted into Equation 3.25, where D is defined by the equation

$$D = \frac{\sigma}{\beta_m C_m}, \tag{3.26}$$

where β_m is the surface-to-volume ratio of the cell, C_m is membrane capacitance and σ is the bulk conductivity tensor. The cable equation can then be rewritten as

$$\frac{\partial V_m}{\partial t} = \nabla \cdot (D \nabla V_m) - \frac{1}{\beta_m C_m} \left(\beta_m I_{ion} + I_{stim} \right), \tag{3.27}$$

assuming that β_M and C_m are spatially invariant.

Although the monodomain model is computationally more efficient than the bidomain model, it has a number of limitations. The most significant limitation is that the monodomain model is not able to simulate the response of the tissue to an extracellular stimulus due to the absence of the extracellular domain. This is of particular concern in modelling the response of a model to a defibrillatory shock. However, in the absence of applied extracellular currents, electrical activation and impulse propagation in multi-cellular models can be studied with a monodomain model [108].

3.2 Transmembrane ionic currents

As was discussed in Section **??** and illustrated in Figure 2.3 the transmembrane ionic currents regulate the action potential. In the bi- and monodomain models described above I_{ion} represents the total flow of ions across the cellular membrane. There are two major approaches to modelling I_{ion}, namely the electrophysiological approach, whereby

the dynamics of individual transmembrane currents that constitute I_{ion} are modelled, and the simplified representation, whereby the system of transmembrane currents is modelled collectively, such as the FitzHugh-Nagumo model [109, 110].

Simplified or phenomenological models of the human ventricular AP have been developed and can reproduce AP morphology and human ventricular restitution dynamics [45]. Bueno-Orovio, Fenton and Cherry's model of the human ventricular AP uses only four variables to model effectively three processes or "currents", namely a fast inward, a slow outward and a slow inward current [45]. However, because the model does not model individual ionic currents it is not possible to model the interaction between drug compounds and specific ion currents. Electrophysiologically-based models, on the other hand, capture the dynamics of the sub-cellular processes of the different ion transport mechanisms and are, therefore, better suited to modelling drug effects on cardiac electrophysiology. In this section the different approaches and techniques used to mathematically model the various ion channels are described. Particular attention is given to K^+ channels because of the role K^+ channels play in ventricular repolarisation and T-wave morphology.

3.2.1 Hodgkin-Huxley style models

The majority of cardiac cellular action potential models are based on the ion current formulation proposed by Hodgkin and Huxley in 1952 [111]. Hodgkin and Huxley were able to model the action potential of the squid giant axon[4]. The model was based on experimental data derived from *voltage clamp* experiments, which allow the transmembrane ionic currents to be measured while the membrane potential is held (clamped) at a set level by using two electrodes in a negative feedback circuit [112]. Despite the fact that the Hodgkin-Huxley formulation was based on nerve cells, the framework was readily applied to cardiac action potentials by Noble in 1962 [113] and continues to play a major role in modelling cardiac electrical activity.

Figure 3.3 shows the equivalent circuit proposed by Hodgkin and Huxley to model the AP in the giant squid axon. They proposed two voltage-dependent ion currents, I_{Na} and I_K, and a voltage-independent leakage current, I_L. The macroscopic current corresponding to a particular ion channel was formulated as follows:

$$I = \bar{g} \cdot \prod x_i \cdot (V_m - E_S), \tag{3.28}$$

[4] An *axon* is a type of nerve cell.

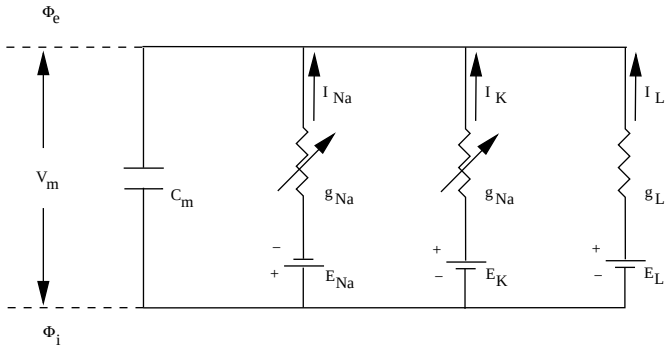


Figure 3.3: Equivalent circuit of the cell membrane proposed by Hodgkin and Huxley [111]. The membrane potential V_m is measured between the extracellular and intracellular electric potentials, $V_m = \Phi_e - \Phi_i$. The total transmembrane ionic current (I_{ion}) consists of three ion currents: two voltage-dependent ion currents, I_{Na} and I_K, and a voltage-independent leakage current, I_L. Each ionic current is modelled using the channel conductance $\bar{g}_s$ and E_S, the Nernst potential for the ionic species S, which reflects the concentration gradient across the cell membrane for S [52]. The variation of channel conductance is governed by time- and voltage-dependent gating variables.

where I is the transmembrane current (μA/cm^2), $\bar{g}$ is the maximum current conductance (mS/cm^2), x_i are the gating variables, V_m is the transmembrane potential, and E_S is the Nernst potential for the ionic species S. The Nernst potential reflects the electro-chemical gradient across the cell membrane for S and is defined by the Nernst equation:

$$E_S = \frac{RT}{zF} \log \frac{[S]_o}{[S]_i}, \tag{3.29}$$

where R is the gas constant, T is the temperature in Kevin, F is Faraday's constant, z is the charge of the ion species S, $[S]_i$ and $[S]_o$ are the intracellular and extracellular concentrations of S, respectively [52].

Hodgkin and Huxley modelled the dynamics of ion channel gating properties using gating variables. The processes of channel activation and inactivation are assumed to be independent and can therefore be modelled by the product of voltage and time-dependent gating variables. The time-dependent change in the probability that one particular gate is open is described by the following first-order differential equation:

$$\frac{dx}{dt} = \alpha \cdot (1 - x) - \beta \cdot x, \tag{3.30}$$

where α and β are the voltage dependent opening and closing transition rates (or *rate constants*) of the gate and x is the gating variable. The rate constants are defined as exponential functions dependent on V_m and are determined by fitting the function coefficients to experimental data [114, 115].

Hodgkin and Huxley proposed that Na^+ activation uses three identical gates, represented by gating variable m, that move from closed to open as V_m depolarises. A second gating parameter, h, was used to characterise Na^+ channel inactivation. For the K^+ channel, no inactivation was observed, so four identical, independent gates, represented by gating variable n, were used to model the level of channel activation. The conductance of the leakage current was assumed to be constant ($\bar{g}_L = 0.3$ mS.cm^{-2}) and invariant over time and V_m. The set of equations for the ionic currents of the Hodgkin-Huxley model can then be expressed as follows:

$$I_{Na} = \bar{g}_{Na} \cdot m^3 h \cdot (V_m - E_{Na}) \tag{3.31}$$

$$I_K = \bar{g}_K \cdot n^4 \cdot (V_m - E_K) \tag{3.32}$$

$$I_L = \bar{g}_L \cdot (V_m - E_L) \tag{3.33}$$

Incorporating the transmembrane ionic currents into Equation 3.17, the membrane potential for a single isolated cell can then be described as

$$\frac{dV_m}{dt} = \frac{I_{stim} - (I_{Na} + I_K + I_L)}{C_m}, \tag{3.34}$$

where the electrical conduction to adjacent cells is ignored. Therefore, I_m is solely dependent on the transmembrane ionic current I_{ion} and the stimulus current I_{stim}. Simulating the action potential therefore requires the solution to all of the coupled ODEs that make up the transmembrane ionic current I_{ion}, namely I_{Na}, I_K and I_L.

The first model of the cardiac AP was an adaption of the Hodgkin-Huxley formulation and published by Noble in 1962 [113]. Since then numerous models of cardiac AP for different cell types (e.g. atrial, ventricular and Purkinje cells) from a variety of species, including mouse, rat, guinea-pig, rabbit, dog, pig and, more recently, human, have been published with increasing complexity. For a comprehensive review of the development of cardiac modelling, please refer to [46]. A significant number of cardiac ionic models are also available for download from `www.cellml.org`.

The first model of the mammalian ventricular myocyte was the Beeler-Reuter (BR) model published in 1977 [116]. Luo and Rudy extended the BR model in the 1990s and developed a comprehensive model of the mammalian ventricular myocyte based on data from guinea-pig ventricular tissue [96,117,118]. The Luo-Rudy model introduced the changing dynamics of the intracellular ion concentrations (Na^+, K^+, Ca^{2+}) and so became

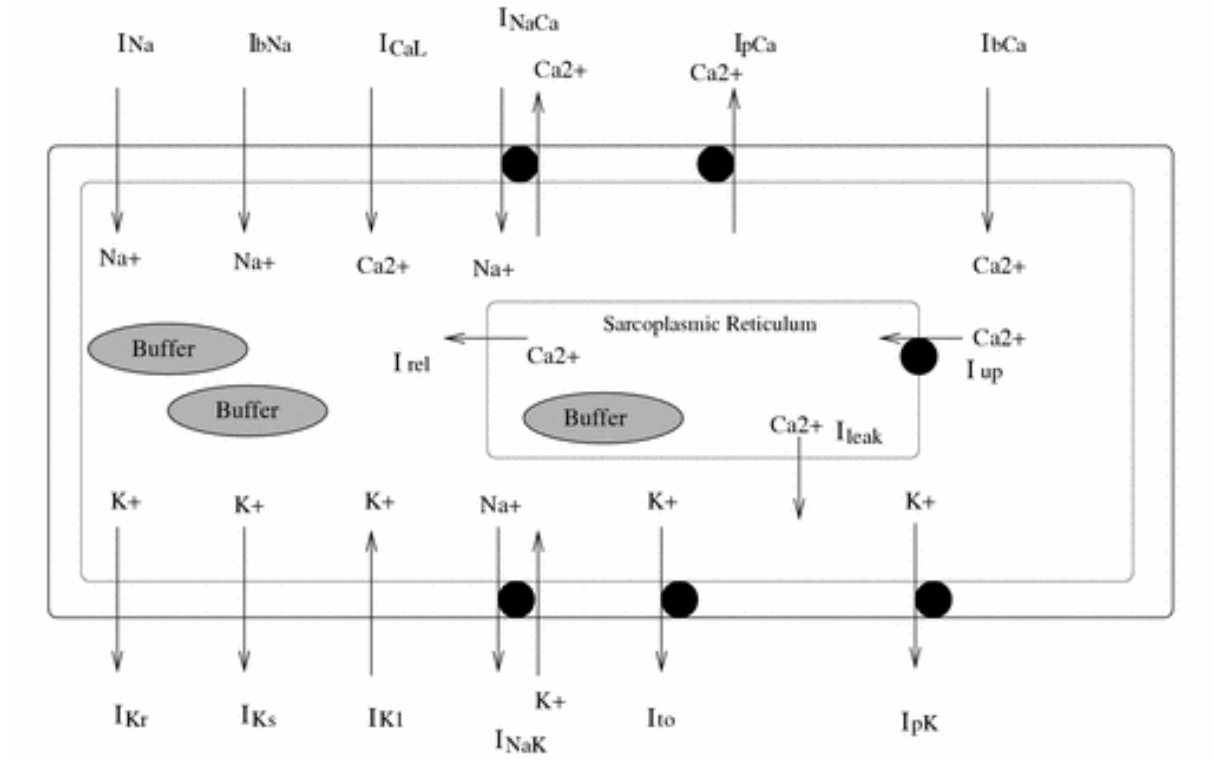
known as the *Luo-Rudy dynamic model* (LRd). In 1998, Priebe and Beuckelmann developed the first model of the human ventricular myocyte [119]. The Priebe-Beuckelmann (PB) model was largely based on the LRd guinea-pig ventricular model. The ten Tusscher et al. model, presented in 2004, used new human tissue data and updated the major ionic currents, namely I_{Na}, I_{Ca-L}, I_{To}, I_{Kr}, I_{Ks} and I_{K1} [43]. In addition, the ten Tusscher 2004 model included a representation of the three regions of the ventricular myocardium, namely the endocardium, epicardium and mid-myocardium, by varying g_{Ks} and g_{To}. In 2006, ten Tusscher and Panfilov updated their earlier model by including a more extensive description of intracellular calcium dynamics, updating the dynamics of I_{Ca-L} and I_{Ks}, and making minor changes to model parameters [44].

Figure 3.4(a) shows a schematic of the ten Tusscher 2006 model of the human ventricular myocyte. The total ion current is expressed as:

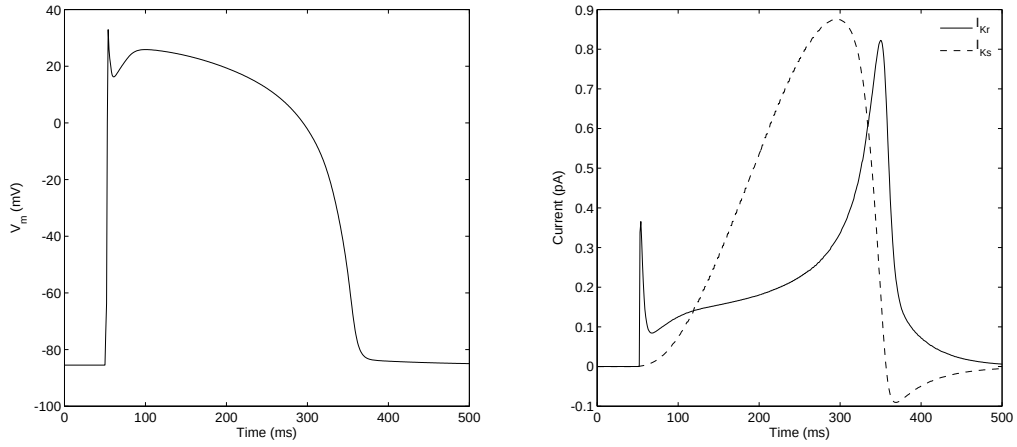
$$I_{ion} = I_{Na}+I_{K1}+I_{To}+I_{Kr}+I_{Ks}+I_{Ca-L}+I_{Na-Ca}+I_{Na-K}+I_{pCa}+I_{pK}+I_{bCa}+I_{bNa}, \quad (3.35)$$

where I_{Na-Ca} is the Na^+/Ca^{2+} exchanger current, I_{Na-K} is the Na^+/K^+ pump current, I_{pCa}, I_{pK}, I_{bCa} and I_{bK} are the plateau and background currents of Ca^{2+} and K^+, respectively. A full list of model parameters and model equations for the ten Tusscher and Panfilov 2006 model of the human ventricular myocyte is given in Appendix **??**. Figure 3.4(b) shows the AP generated by the ten Tusscher 2006 model of epicardial myocyte and the two major K^+ currents, I_{Kr} and I_{Ks}, during the AP cycle. The "notch-and-bump" morphology of the initial depolarisation (phase 1), characteristic of the human ventricular AP, is clearly captured. In addition, the APD of the model is within the normal range [120]. The APD is typically measured using the time it takes for AP to reach 90% of repolarisation from the point of maximum upstroke velocity and is termed APD_{90}. The APD_{90} values for the endo-, mid- and epicardial models are 308, 393 and 311 ms, respectively.

All the ionic currents in the ten Tusscher 2006 model are formulated using the Hodgkin-Huxley ion channel formulation (as per Equation 3.28). However, despite that fact that the Hodgkin-Huxley formulation is highly successful in replicating cardiac ion channel dynamics, gating current experiments by Benzanilla and Armstrong suggested that state transitions for the sodium channel are dependent on current state occupancy [121, 122]. For example, inactivation of the Na^+ channel has far greater probability of occurring when the channel is in the open state, and similarly for the closed to open state transition. In



(a)



(b)

Figure 3.4: (a) Schematic of the ten Tusscher 2006 human ventricular cell model showing ion channels, exchangers, pumps and intracellular Ca^{2+} buffers [43]. Reproduced with permission from `http://www.cellml.org/images/ten_tusscher_model_2004`. (b) The action potential (AP) from the ten Tusscher 2006 epicardial cell model [44] is shown on the left, I_{Kr} and I_{Ks} are shown on the right.

this instance, the Hodgkin-Huxley assumption of independent gating no longer holds and the ion channel formulation is insufficient. In this instance, a model that can represent the individual conformational states of the ion channel and the state transition dynamics is required. Continuous-time Markov models fit this profile as they are based on the Markov property that transitions between states depend on the current formation of the channel and not on previous behaviour.

3.2.2 Markov models of cardiac ion channels

A Markov model of ionic current includes a description of the specific molecular states of the protein and the transitions between them as identified experimentally. Markov models have been used successfully to model a number of cardiac ion channels, including I_{Na}, I_{Kr} and I_{Ks} [94]. However, the main drawback of Markovian formulations of ion channel behaviour is the increased complexity of the model, and the large number of parameters that need to be determined, often with limited experimental data. However, in the late 1970's, Neher and Sakmann developed the patch clamp experimental technique to record single ion channel currents through a glass micro-pipette clamped to the cell membrane [123]. This innovation enabled experimentalists to investigate the dynamics of single ion channels and provide experimental data that could support the increased complexity of the Markovian ion channel formulation. Furthermore, genetic transfection and mutagenesis techniques enabled ion channel proteins to be expressed in host cells (bacterium, yeasts, embryonic cells etc.), thus enabling individual ion channels (or their mutations) to be investigated in more detail.

Continuous-time Markov model of an ion channel process describes how a random variable $X(t)$ identifies the state of the process at time t. Given K kinetically distinguishable states and a matrix of transition rates (assumed not to be dependent on time), denoted $\mathbf{Q}$, we can define a matrix $\mathbf{P}$, with elements

$$P_{ij} = P\ (X(t) = j | X(0) = i) \tag{3.36}$$

where P_{ij} is the probability that the process is in some state j, given that it started in some state i. It is then a standard result [124] that

$$\frac{d\mathbf{P}(t)}{dt} = \mathbf{P}(t)\mathbf{Q}. \tag{3.37}$$

Initial conditions for transition probability matrix $\mathbf{P}$ are obtained by solving for the

steady-state equation

$$\frac{d\mathbf{P}(t)}{dt} = 0. \tag{3.38}$$

The state transition rates matrix $\mathbf{Q}$ must satisfy the following criteria:

- **conservative** - the i-th diagonal element of $\mathbf{Q}$ is given by

$$q_{ii} = q_i = \sum_{j \neq i}^{N} q_{ij}$$

- **stable** - for every state i all elements q_{ij} are finite and positive

An intuitive way of understanding continuous-time Markov models, as applied to ion channels, is to consider that upon entering any state i, a random timer $T_{ij} \sim e^{q_{ij}}$ is started for each possible transition from state i to another state j. The timers are independent of each other and when the first timer expires, the ion channel makes the corresponding transition. In the presence of a large number of identical channels the change in probability of occupying a particular state can be expressed in terms of state transition rates [124]. For a sufficiently small time change Δt, the probability of jumping from state i to state j can be expressed as:

$$P(s_{t+\Delta t} = j | s_t = i) = \frac{q_{ij}}{q_i}. \tag{3.39}$$

For cardiac ion channels, the state transition rates are dependent on the membrane potential V_m and are formulated based on thermodynamic principles as follows:

$$q_{ij} = \frac{k_B T}{h} \exp\left(\frac{\Delta S_\lambda}{R} - \frac{\Delta H_\lambda}{RT} + \frac{z_\lambda F V_m}{RT}\right), \tag{3.40}$$

where T is absolute temperature, ΔS_λ the change in entropy, ΔH_λ the change in enthalpy, z_λ the effective valence of moving charges and $k_B,\ h,\ F$ and R are the Boltzmann, Planck, Faraday and Gas constants, respectively [125].

The change in probability of occupying a particular state i for K discrete states is described by the first-order differential equation

$$\frac{dP_i}{dt} = \sum_{j=1}^{N} [q_{ji} \cdot P_j(t)] - \sum_{j=1}^{N} [q_{ij} \cdot P_i(t)], \qquad j \neq i \tag{3.41}$$

for $i = 1, 2, \ldots, K-1$ and $\sum_{j=1}^{K} P_i = 1$. The change of state probability $\Delta\mathbf{P}$ is then calculated at each time step Δt so that the state probability at time t_n can be defined as

$$\mathbf{P}(t_n) = \mathbf{P}(t_{n-1}) + \Delta\mathbf{P}. \tag{3.42}$$

The macroscopic ionic current can then be determined by considering the total probability of being in the open or conducting state(s), i.e.

$$I_S(t) = \bar{g}_S \cdot O(t) \cdot (V_m(t) - E_S(t)), \tag{3.43}$$

where $O(t)$ is the probability of being in the open state, or the sum of all the conducting state probabilities if there is more than one state that allows ions to flow through the channel, at time t.

3.2.3 Modelling K^+ channels

As discussed in Section 2.3, K^+ channels play an important role in the repolarisation phase of the AP and drug-induced torsades de pointes [126]. The first model of the K^+ channel was proposed by Hodgkin and Huxley in 1962, as previously mentioned. Based on new experimental results obtained by Hutter and Noble [127], Noble [113] split the I_K current into an (almost) instantaneous part (I_{K1}) and a delayed component (I_{K2}). The delayed component was responsible for the initialisation of the final repolarisation phase, and was later associated with either the outward transient K^+ current (I_{To}) or the delayed inwardly rectifying K^+ currents (I_{Kr} and I_{Ks}). The existence of two slowly activating, delayed rectifying potassium channels (representing I_{Kr} and I_{Ks}) was first discussed by Noble and Tsien, who proposed that I_{Kr} was dependent on extracellular K^+, whereas I_{Ks} was dependent on Ca^{2+} [128]. However, it was only in 1990 that Sanguinetti and Jurkiewicz [129] were able to separate I_{Kr} and I_{Ks} pharmacologically by using the I_{Kr}-specific blocker E4031. Zeng and Rudy were the first to introduce a separate formulation for I_{Kr} and I_{Ks} in an AP model [130].

Experimental studies of *Shaker* K^+ channels in *Drosophila* (fruit flies) and recent X-ray crystal structures of several bacterial K^+ channels have provided much insight into the molecular gating mechanisms of I_{Kr} [66, 70, 131], in particular, that the rapid C-type inactivation is not independent of activation. As a result, a number of Markov models of I_{Kr} have been developed based on experimental data from different species including guinea-pig [37] and rabbit [132], as well as HERG expressed in *human embryonic kidney* (HEK) cells [133–135], *Chinese hamster ovary* (CHO) cells [73] and *Xenopus oocytes* [136, 137]. Figure 3.5 illustrates the first Markov model state diagram of I_{Kr}, proposed by Kiehn, Lacerda and Brown in 1999 [136]. The channel is described using three closed states (C1, C2 and C3), one open state (O) and one inactivation state (I). The arrows

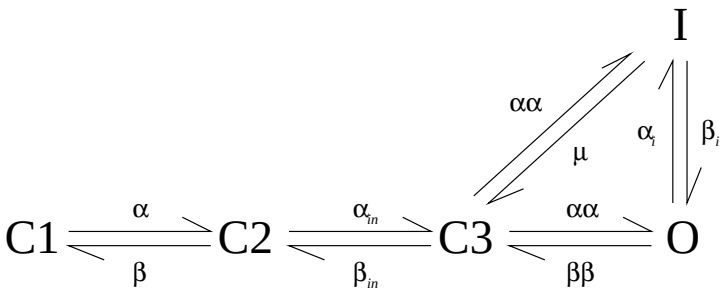


Figure 3.5: Schematic representation of a Markov model of K^+ channel I_{Kr} presented by Kiehn et al. [136]. The channel has three closed states (C1, C2 and C3), one open state (O) and one inactivation state (I). The state transition rates are identified by the characters associated with each arrow. Reproduced from [138].

and the associated values in Figure 3.5 represent state transition rates (i.e. $q_{ij} = \alpha$ where state i is C1 and j is C2). The state transition rate from C3 to I is small, therefore in some Markov models of I_{Kr} it has been deemed negligible [132, 133, 137]. The model developed by Fink et al. [133] is the only I_{Kr} model, so far, to consider original human data and with appropriate representation of the relationship between steady-state and inactivation curves (see [133]). A full list of model parameters and equations for the Fink, Noble and Giles I_{Kr} model is given in Appendix **??**.

3.3 Drug interactions with ion channels

Drug compounds bind with receptors on ion channel proteins and can theoretically affect both the functionality and conductivity of the ion channel. This section reviews receptor theory as it is applied to drug inhibition of ion channels and reviews several studies that have successfully used mathematical modelling to investigate the mechanisms of drug-induced changes in cardiac behaviour.

3.3.1 Receptor theory applied to drug inhibition of ion channels

Receptor theory in pharmacology and physical chemistry is used to explain the mechanisms of drug molecules binding with cellular receptors [139]. Clark was the first to apply the receptor model framework, previously used to describe enzyme kinetics, to describe the effects of drugs on ion channels [140]. Clark's aim was "to determine the extent to which the effects produced by drugs on cells can be interpreted as processes following known laws of physical chemistry" [141]. However, it was not until the development of the patch clamp experimental technique in the late 1970's that the interaction between

drug compounds and single ion channels could be investigated in detail. A number of early experimental studies of drug action on cardiac ion channels by Hille [142] paved the way for a mathematical representation of the interaction between drug molecule and ion channel receptor based on classical receptor theory and the laws of physical chemistry.

The interaction between drug molecules and ion channels can be loosely categorised into three sections. Firstly, there is simple pore block to be considered where the flow of ions is restricted by the drug binding with a continuously accessible receptor. Secondly, due to the dynamic nature of ion channels, there are state and voltage-dependent drug interactions, where access to the receptor is state and voltage dependent. Lastly, there are allosteric drug interactions where the drug binding results in allosteric effects on the channel protein. However, even though the mechanisms of drugs binding with ion channels are categorised into these three sections, in reality, a combination of all these processes is likely present in the interaction between a drug molecule and an ion channel. Therefore, it is important to identify and characterise the dominant effect in any given interaction.

Simple pore block

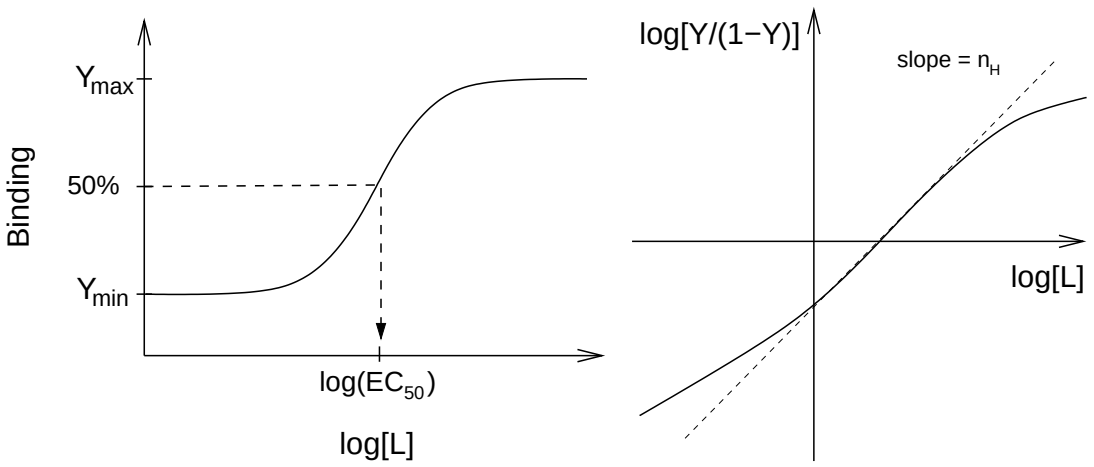
The simplest application of receptor theory to ion channel block is simple pore block, where the drug molecule is assumed to have continual access to the receptor site and the affinity of the drug molecule for the receptor is assumed to be time and voltage independent. There are two basic ways in which drug molecules binding with ion channel receptors can inhibit the flow of ions through the channel pore. The first occurs, if the receptor site is located in or near the channel pore, thus physically restricting the flow of ions through the channel pore. Alternatively, drug binding with an allosteric receptor can cause a conformational change which restricts the flow of ions.

The kinetics of the binding process between the drug ligand and ion channel receptors can be expressed as follows:

$$[L] + [R] \underset{k_2}{\overset{k_1}{\rightleftharpoons}} [LR], \tag{3.44}$$

where k_1 is the rate constant of association, k_2 is the rate constant of dissociation, $[L]$ is the drug concentration, $[R]$ is the concentration of receptors and $[LR]$ is the concentration of bound ligand-receptor complexes. Assuming the law of mass action[5] holds in

[5]The *Law of Mass Action* states that the rate of any chemical reaction is proportional to the product of the masses of the reacting substances, with each mass raised to a power equal to the coefficient that occurs in the chemical equation.



(a) EC_{50} (b) Hill Coefficient

Figure 3.6: (a) The dose-response curve measures the maximal total binding for varying concentrations of ligand concentrations. The EC_{50} value can be determined from the dose-response curve as the value which corresponds to half way between the baseline or binding response (Y_{min}) and the maximal response (Y_{max}). (b) The slope of the dose-response curve corresponds to the Hill coefficient. The Hill coefficient (n_H) is often calculated by determining the slope of the best straight-line fit to the dose response of the ratio of fraction of blocked sites (Y) and unblocked sites (1-Y).

Equation 3.44, the dissociation constant (K_d) is given by:

$$K_d = \frac{k_2}{k_1} \tag{3.45}$$

The dissociation constant is measured in moles (M) and is often used as a measure of affinity of a particular drug for a binding site. In addition to the dissociation constant, the drug concentration which inhibits 50% of the binding sites, referred to as the IC_{50} value, is also used to represent the inhibitory effect of drug compounds in competitive binding and functional antagonist assays. Similarly, the effective concentration that results in 50% of the maximal response, referred to as the EC_{50} value, is also used to characterise drug-receptor interactions. Figure 3.6(a) illustrates how the EC_{50} value is determined from a dose-response experiment. The EC_{50} value corresponds to half the binding response, i.e. half the difference between the maximal (Y_{max}) and minimum (Y_{min}) total binding of the drug. In the simplest case, when the effect of the drug binding with the protein directly inhibits the ionic current, $K_d = IC_{50} = EC_{50}$.

If the law of mass action applies, binding of a ligand to one binding site should not affect the affinity of another binding site. However, in many instances, cooperation between binding sites is observed, i.e. a ligand binding or dissociating from a binding site alters the affinity of other binding sites. The Hill equation is often used in cooperative

binding assays to assess the degree of cooperation between two or more ligands binding to the same receptor and was originally formulated by Archibald Hill in 1910 to describe O_2 binding with hæmoglobin [143]. The Hill equation is also used to describe the relationship between the binding ligand concentration and the fractional occupancy of binding sites[6] and is used in cardiac pharmacology to describe the nature of the affinity between a particular drug molecule and its binding sites on (voltage-dependent) ion channels [144]. The Hill equation is given as follows:

$$Y = \frac{[L]^{n_H}}{K_d + [L]^{n_H}}, \tag{3.46}$$

where Y is the fraction of blocked sites and n_H is the *Hill coefficient*. A Hill coefficient of one indicates independent ligand binding, where the binding affinity is not affected by whether or not other ligand molecules are already bound. A Hill coefficient greater or smaller than one means that a ligand binding to a receptor would increase or decrease the affinity of the unblocked receptors for remaining ligands, respectively. Equation 3.46 is often rewritten as follows:

$$\log\left(\frac{Y}{1-Y}\right) = n_H \log[L] - \log K_d, \tag{3.47}$$

such that the Hill coefficient n_H can be determined empirically from the slope of the straight line estimate of the dosage-response curve, as shown in Figure 3.6(b). The IC_{50} value and the Hill coefficient are used in physical chemistry to define the affinity of an enzyme for a particular binding site. These values are similarly used to represent the binding dynamics between drug molecules and ion channel binding sites for simple pore block. However, the drug action on ion channels is complicated by the voltage- and time-dependencies of the ion channel proteins, as described in the next section.

Voltage and state-dependent binding

As discussed in Section **??**, ion channels found in cardiac myocytes are dynamic protein structures that activate and deactivate in response to changes in cellular transmembrane potential. Not surprisingly, drug action on cardiac ion channels is often voltage- and time-dependent, as observed by Hondeghem and Katzung in investigating the effect of anti-arrhythmic drugs, lidocaine and quinidine, on the sodium channel I_{Na} [145]. Hondeghem and Katzung observed that the affinity of the anti-arrhythmic drug for the depolarised

[6]The Hill equation in this instance is equivalent to the *Langmuir equation*.

channel is greater than for the closed or repolarised channels. In addition, the rate of recovery from block is slower in depolarised channels than in resting or closed channels. The voltage- and time-dependency of drug inhibition of ion channels is often determined by the location of the drug binding sites in ion channel proteins and whether access to the binding sites is restricted due to the conformation of the channel protein during the AP cycle. Two main hypotheses have been proposed to describe state-dependent block, namely *modulated* and *guarded* receptor theory.

Modulated receptor theory

In 1977, Hille proposed the *modulated* receptor theory in his work on the effects of local anaesthetics on Na^+ channels in nerve cells [142]. The premise of the modulated receptor theory is that the affinity of the drug for the ion channel binding site is dependent on the state of the ion channel. Figure 3.7 illustrates the basic kinetic scheme of the modulated receptor theory proposed by Hille. In this case, the model of the ion channel includes three states, namely open (O), closed (C) and inactivated (I). The transition rates between states are represented by the variables, α_n and β_n. According to the modulated receptor theory, the drug can bind in all three states but the affinity of the drug for the ion channel binding sites is voltage- and time-dependent and is different for each state (characterised by the functions $f(v,t)$, $g(v,t)$ and $h(v,t)$ in Figure 3.7 that determine the affinity of that particular state for the drug compound). Drug binding with each state causes the channel to enter modified bound states (C^*, O^* and I^*), all three non-conducting states. From the bound states, the channel can either transition to an unbound state or to one of the other bound states until it recovers from binding.

Guarded receptor theory

In contrast to the modulated receptor theory, the guarded receptor theory proposes that the drug molecule binds with a single bindable conformation with fixed affinity and that access to the binding site is restricted due to the conformational changes of the protein. Thus, the inhibition of the ion channel is dependent on the conformation of the channel, which is voltage and time dependent. This scheme was originally utilised by Armstrong to describe TEA^+ binding to K^+ channels in giant squid axons [146]. However, in cardiac electrophysiology, the guarded receptor theory was pioneered by the work by Starmer and colleagues in the mid-1980's, investigating the effects of local anaesthetics on cardiac

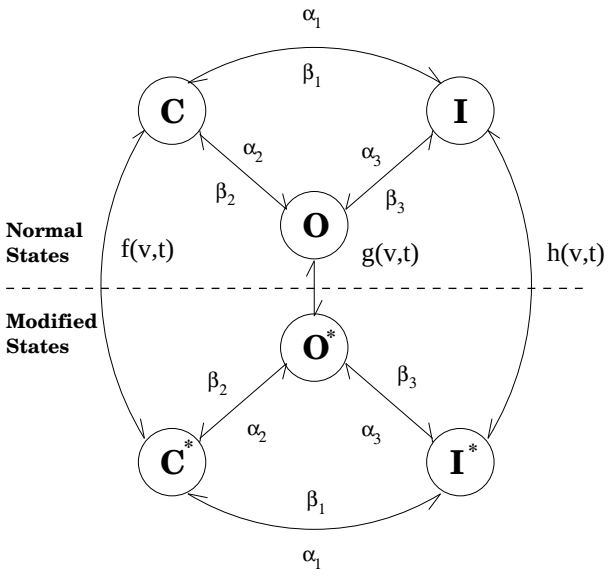


Figure 3.7: Schematic illustrating a drug binding with an ion channel. The channel is represented as having three states: closed (C), open (O) and inactivated (I). Modified or blocked states are marked with an asterisk (*).The state transition rates between channel states are represented by α_n and β_n values. The voltage and time-dependent affinity of the drug molecule for the channel states is represented by the functions $f(v,t)$, $g(v,t)$ and $h(v,t)$. Drug affinity is typically represented using the dissocidation constant (K_d) which is the ratio of the rate of dissociation over the rate of association.

Na^+ channels [147]. The major difference of the guarded receptor theory compared to the modulated receptor theory, is that the drug molecule binds to a particular state and access to the binding site is restricted for all other states. For example, for open (or activated) state binding in Figure 3.7, $f(v,t)$ and $h(v,t)$ would both be set to zero, such that binding only occurs during the open state. Furthermore, recovery from binding is often state-dependent. In the example of open-state block, this could be caused by the drug molecule being trapped by the closed or inactivated conformations of the channel and thus the channel is only able to recover from block when it returns to the activated state. This phenomenon was observed by Mitcheson et al. in the inhibition of HERG expressed in Xenopus oocytes by methanesulfonanilides compounds [77].

Allosteric Effector

Both the modulated and the guarded receptor theories focus on the voltage and time-dependent association and dissociation processes, but do not consider the drug effects on ion channel state transition dynamics. For example, lidocaine binding to Na^+ channels in rat skeletal muscle, for instance, slows the inactivation dynamics [148]. In this instance, the binding of lidocaine has an allosteric effect on the dynamics of I_{Na}. In an allosteric

effector model, there are no explicit drug bound states as the binding of the drug molecule is reflected as a change in the transition rates between states. However, the binding process of the drug compound to the allosteric receptor site can adhere to either simple receptor binding, or modulated or guarded receptor theory. Therefore, a complete model of drug-ion channel interaction including allosteric regulation, should consist of both unbound and bound states, with transitions between unbound states being different than those for bound states (e.g. $C^* \rightarrow O^* \neq C \rightarrow O$, as illustrated in Figure 3.7).

3.3.2 Molecular modulators of drug-ion channel interaction

Although the simple channel block, modulated and guarded receptor theories have been proposed to describe drug action on ion channels, there are a number of additional factors that affect drug action on cardiac activity on a molecular level, namely temperature, phosphorylation, pH and the presence of antagonists. On a cellular level, the animal species and ion channel expression systems must be taken into account as the drug action is likely to vary between different ion channel encoding genes and ion channel expression systems.

Temperature

The kinetics of ion channels are often dependent on temperature [149], therefore it seems likely that the dose-response of state-dependent ion channel blockers would also be affected by temperature. Yao et al. investigated the effects of voltage-stimulus and temperature on the affinity of several HERG channel blockers and found that an increase in temperature did not significantly affect the IC_{50} values of ketoconazole, terfenadine and E-4031, but significantly decreased the affinity of astemizole (IC_{50} = 0.5 at 22℃ vs. IC_{50} = 2.4 at 35℃) [150]. The mechanisms underlying the varied response of the affinity of ion channel blockers to changes in temperature are not clearly understood.

pH

Most anti-arrhythmic drugs, including the methanesulfonanilides, are weak bases that are found in either cationic or neutral form at physiologic pH in solution. Low pH, as it occurs in ischaemic tissue, promotes the cationic form of the drug molecule. This decreases the rate of dissociation and, hence, results in a greater amount of channel block in tissue with low pH [151]. Conversely, higher pH values promote the neutral drug form which

Ion Channel	Drug(s)	References
I_{Na}	lidocaine, quinidine	[142] [145] [153] [148] [154]
	mexiletine, lidocaine	[155]
I_{Kr}	dofetilide	[156]
	14-3-3ϵ	[157]
	quinidine	[158]
	dofetilide	[159]
	RPR260243	[160]
I_{K1}	Mg^{2+}, polyamine	[161]
I_{K-ATP}	pinacidil	[162]

Table 3.1: Examples of modelling studies of drug interactions with ion channels.

increases rate of dissociation and, hence, decreases channel block.

Antagonistic combinations

The combination of two or more drug compounds can result alter the drug-inhibition dynamics. For instance, the addition of a second drug compound with higher concentration or greater affinity for the receptor, coupled with a quicker rate of recovery than for the first compound can effectively result in the increase of ionic flow due to competitive displacement. The competing drug is able to bind to the receptor before the other drug is able to bind and due to the quicker rate of recovery, the channel is able to recover from block faster, thus effectively reducing the level of channel inhibition. This phenomenon has been shown by the displacement of lidocaine by bupivacine in guinea pig ventricular myocytes [152].

3.3.3 Modelling drug effects on K^+ channels

Mathematical modelling has been used in a variety of studies to investigate drug-induced effects on cardiac electrophysiology from the ion channel to the tissue level. Table 3.1 lists previous simulation studies of drug interactions with ion channels. The majority of early work focused on the effects of lidocaine and quinidine on I_{Na}. More recently, models of the drug-interactions with potassium channels, namely I_{Kr}, I_{K-ATP} and I_{K1}, have been published. Due to the prominent role that I_{Kr} plays in human ventricular repolarisation [71] and the number of non-cardiac drugs that have been shown to inhibit I_{Kr} [126], most of the research has focused on I_{Kr}.

Drug-induced inhibition of I_{Kr} has been simulated using both Hodgkin-Huxley formulations and Markov models. Snyders and Chaudhary proposed a Markov model to

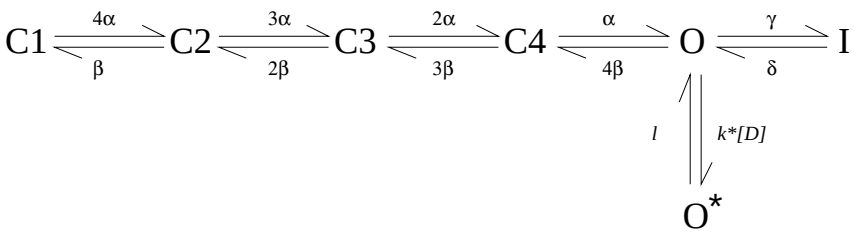


Figure 3.8: Schematic representation of a Markov model of HERG binding with dofetilide proposed by Snyders et al. [156]. The model consists of four closed states (C1 to C4), an open state (O) and an inactivated state (I). [D] is the drug concentration and blocked states are depicted with an asterisk (*).

investigate inhibition of HERG expressed in HEK cells by dofetilide [156]. The proposed model is illustrated in Figure 3.8. The state transition rates between the open and bound state were dependent on $K_d = l/k$ and drug concentration, where l is the rate of dissociation and k is the rate of association.

More recently, Tsujimae et al. used a Hodgkin-Huxley formulation to model the effects of various drugs, namely dofetilide, vesnarinone and quinidine, on I_{Kr} [159]. The drugs were classified into three categories: voltage- and time-independent block (dofetilide), fast voltage- and time-dependent block (quinidine) and slow voltage- and time-dependent block (vesnarinone). The voltage- and time-independent block by dofetilide was modelled by simply reducing the maximum channel conductance by a factor proportional to drug concentration. The binding kinetics of quinidine and vesnarinone were incorporated in the Hodgkin-Huxley formulation of I_{Kr} as follows:

$$I_{Kr} = \frac{\gamma_i \cdot \bar{g}_{Kr} \cdot x_r \cdot (V - E_K)}{1 + e^{\left(\frac{V+15}{22.4}\right)}}, \tag{3.48}$$

where γ_i is the fraction of I_{Kr} that is not blocked by the drug of type i. The fraction of unblocked channels is modelled using the first order differential equation

$$\frac{d\gamma_i}{dt} = \frac{\gamma_{\infty,i} - \gamma_i}{\tau_i} \tag{3.49}$$

$$\gamma_{\infty,i} = \frac{\alpha_i}{\alpha_i + \beta_i} \tag{3.50}$$

$$\tau_i = \frac{1}{\alpha_i + \beta_i}, \tag{3.51}$$

where α_i and β_i are the unbinding and binding rate constants of drug type i, respectively. It should be noted that this formulation assumes that the drug block is completely independent of the channel dynamics, i.e. the block is not state-dependent.

Tsujimae and colleagues incorporated their models of drug action on HERG in the Courtemanche human atrial cell model [163], in order to simulate drug-induced effects

on the atrial AP [159]. However, to obtain the expected effects of APD rate-dependence the I_{Ks} formulation was adapted to match the kinetics of guinea-pig ventricular myocyte. More specifically, I_{Ks} was modified to include an additional gating x_{s2} that was set to be six times the time constant of the x_s in the original model. The I_{Ks} was expressed as follows:

$$I_{Ks} = \bar{g}_{Ks} \cdot x_{s1} \cdot x_{s2} \cdot (V_m - E_K), \tag{3.52}$$

where x_{s1} and x_{s2} are the slow and fast activation gating variables, respectively. The model was then able to reproduce the reverse-rate dependence (i.e. larger drug-induced prolongation of the APD at slower heart rates) of dofetilide and quinidine on APD, as well as the rate-dependence of vesnarinone [159].

3.4 Discussion

In this chapter we have reviewed the theory underlying impulse propagation in cardiac tissue, different AP models and both Hodgkin-Huxley and Markov model formulations of ionic currents. In particular, the ten Tusscher and Panfilov model of human ventricular AP [44] and the Fink, Noble and Giles I_{Kr} model [133] have been identified as potential candidates for assessing the effects of sotalol on the human myocardium.

The application of classical receptor theory in describing the interactions between ion channels and drug compounds has also been reviewed. In most instances, the modelling studies have been able to replicate the effects of the drug compound observed experimentally, proving that mathematical modelling can indeed be used as a tool to investigate the effects of drugs on cardiac dynamics. However, none of the modelling studies reviewed in this chapter have investigated the effects of drugs on cardiac dynamics in human tissue. Some modelling studies have been conducted to investigate the effects of drugs in animal models. For instance, researchers at Novartis[7] developed a 1-D fibre model, using a canine Purkinje fibre AP model [164], to investigate the effect of a number of drug compounds on cardiac tissue dynamics [165]. The next chapter will describe the model implemented in this thesis for investigating the effects of sotalol on human tissue.

[7] A large pharmaceutical company based in the United States

Chapter 4

Modelling Effects of Sotalol on Ventricular Repolarisation

In previous chapters, the limitations of current methods of assessing the cardiac toxicity of drugs during clinical trials and the electrophysiology underlying drug-induced arrhythmia have been discussed. In addition, mathematical modelling of cardiac activity has been identified as a viable tool for providing insight into drug effects on ventricular repolarisation dynamics. As discussed in Section 1.5, the anti-arrhythmic *sotalol* is proposed as the test compound for assessing the effects of I_{Kr} inhibition on ventricular repolarisation dynamics and T-wave morphology. Therefore, in this chapter we develop a model of the interaction of sotalol and I_{Kr}. The I_{Kr}-sotalol model is next incorporated into a human ventricular cellular model that is then used to assess the effects of sotalol on cellular and multi-cellular dynamics. The goal of this modelling study is to provide insight into the electrophysiological mechanisms underlying drug effects on ventricular repolarisation as captured by the ECG.

The chapter comprises of three main sections. The first section presents the Markov model developed for characterising sotalol's interactions with HERG and compares the model with experimental data. In the second section, the I_{Kr}-sotalol model is incorporated into the model of human ventricular myocyte developed by ten Tusscher et al. in 2006 [44] and the effects of sotalol on action potential duration are investigated. In the final section, the cell model is incorporated into a multi-cellular 1D fibre geometry that is used to investigate the effects of sotalol on electrical impulse propagation and the resulting pseudo-ECG simulations.

4.1 Modelling sotalol inhibition of I_{Kr}

A number of models of I_{Kr} have been published, including both Markov models and Hodgkin-Huxley based formulations. In choosing between a Markov model and a Hodgkin-Huxley based formulation of I_{Kr}, there are a number of considerations and trade-offs that need to be taken into account. Firstly, and arguably most importantly, it is necessary to define the goal of the modelling study. In this instance, the goal of the modelling study is to understand the effects of sotalol concentration on I_{Kr} over time, and how this affects cellular and multi-cellular repolarisation dynamics. Secondly, a choice must be made as to which model should be implemented to best characterise the electrophysiological and pharmacological properties of I_{Kr} and its interaction with sotalol. And lastly, the trade-offs between model complexity and model predictivity need to be assessed. In order to assess what type of model would best characterise sotalol's interaction with I_{Kr}, it is first necessary to understand the pharmacology of sotalol binding with HERG.

4.1.1 Pharmacology of Sotalol and HERG

Drugs interact with the heart at a molecular level once they have been introduced into the body, either intravenously or orally. Sotalol is a combination of two drugs, namely *l*-sotalol and *d*-sotalol [166], which differ in their pharmacology. Firstly, *l*-sotalol is a β-adrenergic blocker that suppresses the function of the SA node and slows AV nodal conduction, which effectively slows the heart rate. *d*-Sotalol, on the other hand, prolongs the action potential by blocking I_{Kr}. For the purposes of this modelling study we will only consider the effects of *d*-sotalol as I_{Kr} inhibition has been shown to play a major role in drug-induced arrhythmia (as discussed in Section 2.3.1).

Sotalol's inhibition of I_{Kr} is voltage and state-dependent [167]. This is likely due to the fact that sotalol binds with receptors in the internal channel cavity, as is the case with other methanesulfonanilides [78]. The sotalol molecule gains access to the binding site when the channel is in activated (open) state. This was supported by a study by Numaguchi et al. that showed that increasing the rate of channel inactivation (by hyper-depolarisation) reduced the affinity of HERG for *d*-sotalol, suggesting that *d*-sotalol binds with the open state and that inactivation plays a role in stabilising the binding [168].

Recovery from block is also subject to channel state. It has been shown for several methanesulfonanilides, including MK-499, almokalant, dofetilide and E-4031, that

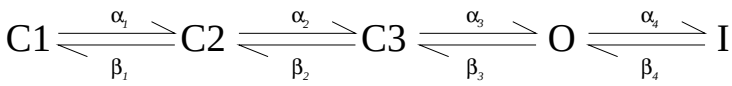


Figure 4.1: Schematic of the Markov model of HERG proposed by Fink et al. [133]. The channel has three closed states (C1, C2 and C3), one open state (O) and one inactivated state (I). The arrows and associated variables represent the state transition rates. See Appendix **??** for full list of model parameters and equations.

recovery from binding with I_{Kr} is restricted to the open state, due to "trapping" of the drug-compound by the activation gate [77]. With respect to sotalol, there is little data to confirm whether sotalol is also trapped inside the internal cavity by the activation gate. However, considering that the sotalol molecule is comparable in size to that of dofetilide (approx. 15 Å in diameter) [169] and that sotalol binds with receptors in the internal cavity [71], it would be reasonable to assume that sotalol is similarly trapped inside the internal cavity by the activation gate. Furthermore, there is little experimental data due to an absence of experimental studies to suggest that sotalol binding with HERG has an allosteric effect on protein dynamics [168,170]. Therefore, our basic assumption would be that the dynamics of the activation and inactivation gating mechanisms are not affected by the bound drug molecule.

4.1.2 Modelling HERG and its interaction with sotalol

The interaction between sotalol and HERG would best be characterised by the guarded receptor theory, whereby sotalol binds to receptors during the open state and recovery from binding is only possible when the activation gate is open. Both Markov models and Hodgkin-Huxley based formulations of I_{Kr} can accommodate implementations of the guarded receptor theory, as discussed in Section 3.3. However, as reviewed in Section 2.2, the activation and inactivation processes of HERG are not independent. Therefore, the Hodgkin-Huxley formulation, which assumes independent gating, does not accurately represent the molecular dynamics of the HERG channel and a Markov model should be used. It should be noted that although Markov models are stochastic the simulation results are deterministic due to the fact that the transition rates are constant (for a particular V_m) and consequently the change in state occupancy probabilities are deterministic.

The focus of this modelling study is on the effects of sotalol on ventricular repolarisation in humans. Therefore, every effort is made to incorporate experimental data and associated cardiac models that are based on data from human tissue at physiological tem-

peratures (approx. 37℃). The Markov model of I_{Kr} developed by Fink, Noble and Giles (FNG08) [133], illustrated in Figure 4.1, is derived from recently published experimental data of HERG expressed in *human embryonic kidney* (HEK) cells at physiological temperatures [74]. The model discounts the state transition between the inactivated state and the closed state (C3), because the state transition rate from the inactivated to the closed state is an order of magnitude smaller than the transition rate from the inactivated to the open state. Hence, the impact of the additional state transition on HERG's inactivation is deemed negligible [133]. The full list of the model parameters are given in Appendix **??**.

Figure 4.2 shows the time constants, activation and steady state I-V curve FNG08 I_{Kr} model [133]. The model includes dependencies on temperature and extracellular K^+ concentration, such that the I_{Kr} is calculated as follows:

$$I_{Kr} = \bar{g}_{Kr} \cdot \left(\frac{T}{35} - \frac{55}{7}\right) \cdot \sqrt{\frac{[K^+]_e}{5.4}} \cdot O(t) \cdot (V_m - E_K), \tag{4.1}$$

where V_m is the membrane potential, E_K is the Nernst potential for potassium, $O(t)$ is the probability of the model occupying the open state, $\bar{g}_{Kr}$ is the maximum channel conductance of 0.024 μS/nF, T is the base temperature in Kelvin and $[K^+]_e$ is the extracellular concentration (mM).

Figure 4.3 illustrates the Markov model structure for representing the interaction between sotalol and I_{Kr}. The basic I_{Kr} model structure, as proposed by Fink, Noble and Giles [133], remains unchanged. Five modified (blocked) channel states are included and depicted with an asterisk (*). As no evidence is available to suggest that the sotalol binding with HERG alters the activation and inactivation dynamics the transition rates between the modified states are set to be the same as the transition rates between the normal, unblocked states. The model structure ensures that sotalol can only bind and recover from binding when the channel is in the open state. The transition rates between the open (O) and blocked open state (O^*) can be defined as follows:

$$\mathbf{O} \rightarrow \mathbf{O}^* = k_1 \cdot [D]$$

$$\mathbf{O}^* \rightarrow \mathbf{O} = k_2,$$

where k_1 and k_2 are, respectively, the association and dissociation rate constants of the drug and $[D]$ is the intracellular sotalol concentration. Therefore, according to Equation 3.41 the change in open state probability is defined as

$$\frac{dO(t)}{dt} = -(\alpha_4 + \beta_3 + k_1[D]) \cdot O(t) + \alpha_3 \cdot C3(t) + \beta_4 \cdot I(t) + k_2 \cdot O^*(t), \tag{4.2}$$

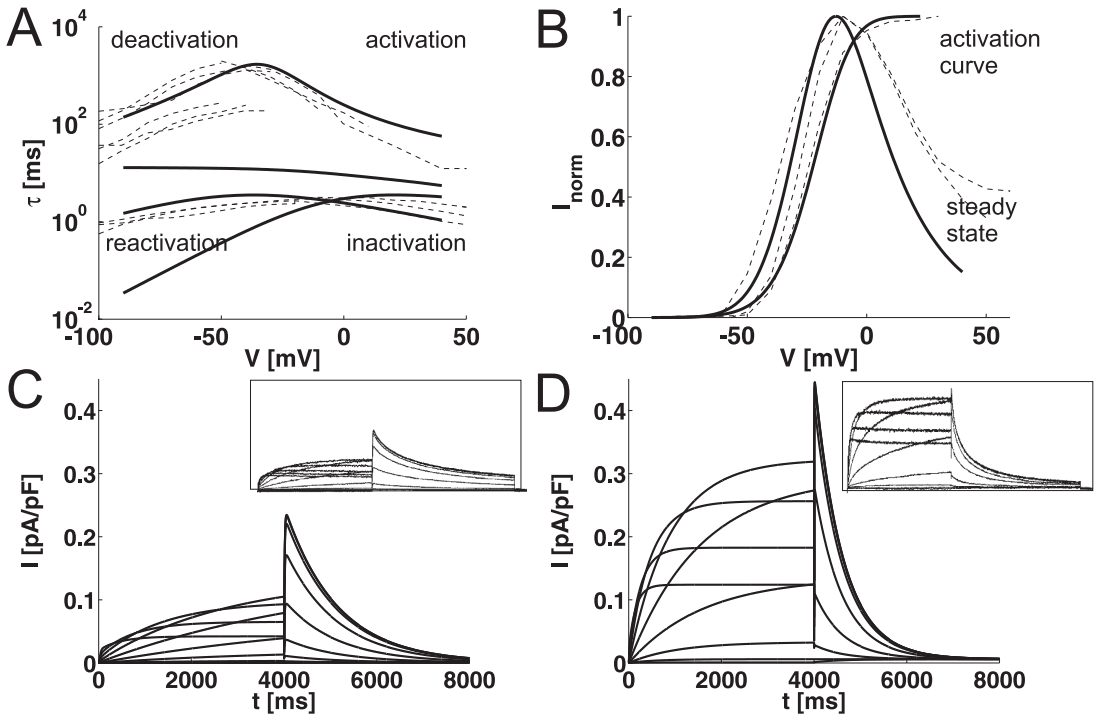


Figure 4.2: A comparison of the I_{Kr} model proposed by Fink, Noble and Giles [133] with experimental data from HERG expressed in HEK cells at 36℃ [74]. (A) Activation, deactivation, inactivation and reactivation time constants on a logarithmic scale. (B) Steady-state $I - V$ curve and the activation curve. Dotted lines denote experimental data. (C) Superimposed I_{Kr} simulations at room temperature (23℃) using a voltage step protocol. (D) Identical to Plot C, except that I_{Kr} is simulated at 36℃. Experimental data from Berecki et al. [74] shown in insets. Figures reproduced with permission from [133].

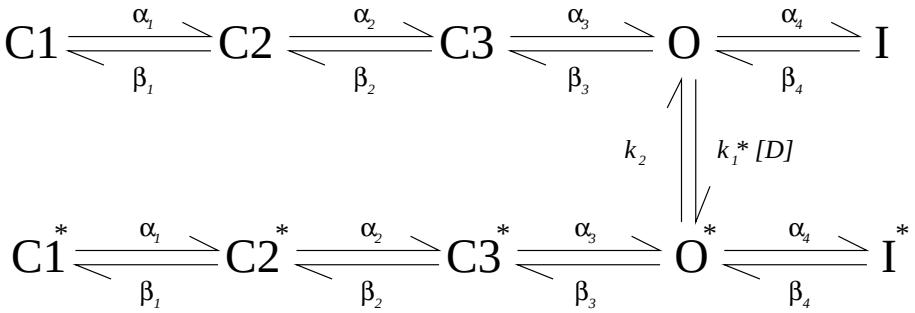
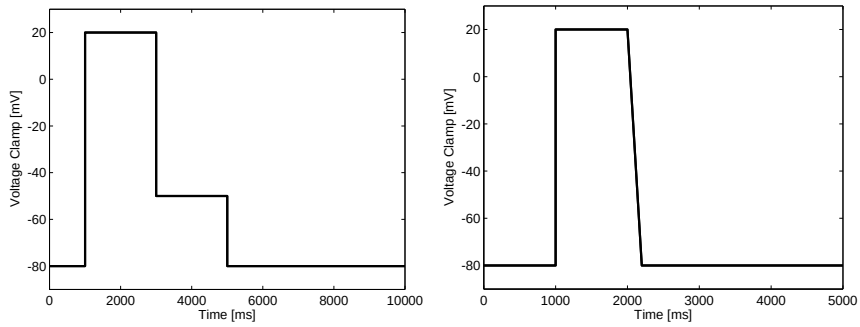


Figure 4.3: A novel Markov model of sotalol's interaction with HERG. The HERG model has three closed states (C1, C2 and C3), one open state (O) and one inactivated state (I), as proposed by Fink, Noble and Giles [133]. Drug-bound states are depicted with an asterisk (*). The transition rates are depicted as the values associated with the arrows between states.



(a) Step Protocol (b) Ramp Protocol

Figure 4.4: Experimental voltage clamp protocols used to stimulate model for comparison with experimental data from Kirsch et al. 2004 [80].

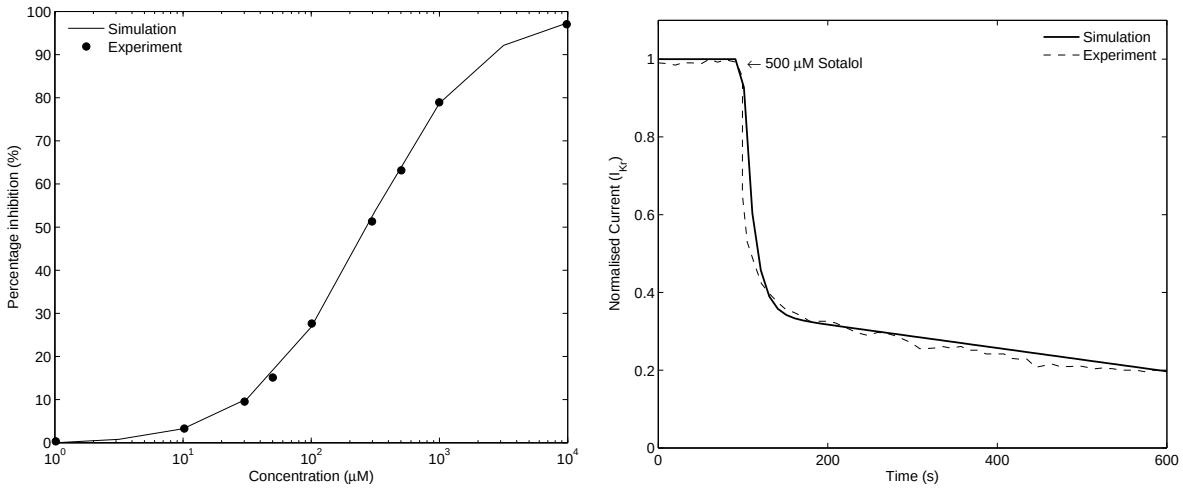
where $O(t)$ is the open state probability, $[D]$ is the intracellular concentration of sotalol and α_i and β_i are the state transition rates as shown in Figure 4.3.

The association and dissociation binding rate constants, k_1 and k_2, could not be found in literature. Therefore, the sotalol binding dynamics were obtained from experimental data obtained from HERG expressed in HEK cells at near-physiological temperatures (35℃) [80]. To facilitate comparison with experimental data, two voltage clamp protocols (illustrated in Figure 4.4) were implemented as follows:

- **Step-ramp:** a conditioning step (+20 mV amplitude, 1 s duration) followed by a repolarising test ramp (+20 to -80 mV at -0.5 V/s) repeated at 5 s intervals from a holding potential of -80 mV

- **Step-pulse**: a pre-pulse to +20 mV for 2 s followed by a test pulse to -50 mV for 2 s repeated every 10 s intervals from a holding potential of -80 mV

Recall from Section 3.3.1 that the dissociation constant (K_d) is the ratio given by



(a) (b)

Figure 4.5: (a) Concentration-response curve of sotalol and HERG showing the percentage HERG inhibition as a function of sotalol concentration. Experimental data from HERG expressed in HEK cells at 35℃ is shown as black dots. The step-ramp protocol was used to stimulate the model at varying concentrations for 10 min to ensure steady state block. The model simulation is shown as the solid line. (b) Time course of drug-induced HERG inhibition. Experimental data of normalised I_{Kr} from HERG expressed in HEK cells is shown as a dotted line [80]. The step-pulse protocol was used to simulate the model. The concentration of sotalol was increased to 500 μM after 100 seconds.

the dissociation rate over the association rate. The affinity with which sotalol binds with I_{Kr} has only been established *in vitro* animal models, using guinea-pig, neonatal mouse ventricular cells and HERG expressed in Chinese Hamster Ovary (CHO) cells [171]. Therefore, the value of K_d was determined from the concentration inhibition curve in Figure 4.5(a) from HERG expressed in HEK cells at physiological temperatures. A sigmoidal function was fit to the experimental data using MATLAB's *fit* function[1] resulting in $K_d = 269$ μM with unity Hill coefficient. The model simulations were then compared with the experimental data. The step-ramp protocol was used to stimulate the model at varying concentrations for 10 min to ensure steady state block. Initial intracellular and extracellular potassium concentrations, $[K^+]_i$ and $[K^+]_e$, were set to 130 mM and 4 mM in line with experimental data.

Given the dissociation constant of $K_d = 269$ μM, the association rate constant could be derived from the dynamics shown in Figure 4.5(b). The rate of association k_1 was set to 2 $mM^{-1}.ms^{-1}$ by fitting the model to the experimental data shown in Figure 4.5(b) using the MATLAB *fminsolve* function[2]. The constant decline in HERG inhibition after 200

[1]MATLAB's *fit* function implements a non-linear, least-squares curve fitting method
[2]MATLAB's *fminsolve* implements the Nelder-Meade algorithm to minimise a predefined cost function

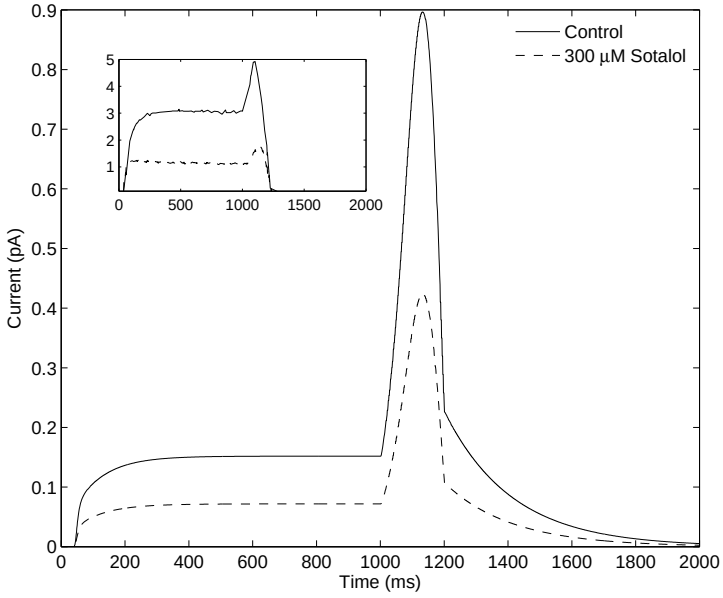


Figure 4.6: Comparison of I_{Kr} in the presence of 300 μM sotalol between experimental data of I_{Kr} from HERG expressed in HEK cells at 35℃ from [80], shown in inset, and the I_{Kr}-Sotalol‘ model stimulated using the step-ramp protocol. The model was simulated for 10 minutes to ensure that steady state inhibition had been reached.

seconds is attributed to a constant decline in the Nernst potential of K^+ (E_K). This effect could be caused by a reduction in intracellular K^+ concentration due to the prolonged depolarisation protocol. This dynamic was incorporated for in this simulation by linearly decreasing the K^+ Nernst potential by 0.1% per second for the duration of the simulation.

The I_{Kr}-sotalol model was validated by comparing it to experimental data of I_{Kr} from HERG expressed in HEK cells at 35℃ obtained from [80]. The model was stimulated using the step-ramp protocol for 10 minutes to ensure steady state block was reached. Figure 4.6 compares experimental data of I_{Kr} with the model simulation. The resulting decrease in I_{Kr} caused by 300 μM of sotalol is clearly shown. In both experiment and simulation, the increase in sotalol concentration resulted in a reduction of both plateau and peak I_{Kr} current. The 300 μM sotalol resulted in a 53% reduction in the peak current in simulation, compared with a 64% reduction observed experimentally. Differences in I_{Kr} activation levels between the experimental data and the model might be due to differences in phosphorylation of the channel and ion concentrations in the intra- and extracellular medium.

4.2 Modelling the effect of sotalol on human ventricular myocyte electrophysiology

In order to model the effects of sotalol on human ventricular myocyte electrophysiology it was necessary to select the cellular model most appropriate for the modelling study. Aspects to consider are model complexity, accurate representation of human ventricular AP morphology and restitutive dynamics. Of the action potential models described in Section 3.2, the model proposed by ten Tusscher and Panfilov in 2006 (TP06) meets the necessary criteria [44]. It is the latest AP model of the human ventricular myocyte electrophysiology based predominantly on human experimental data. This section describes how the I_{Kr}-sotalol model is incorporated into the TP06 model and investigates the effects of sotalol on AP morphology and restitution dynamics.

4.2.1 Modelling the ventricular myocyte electrophysiology

The I_{Kr}-sotalol model, described in the previous section, was included in the TP06 model by replacing the model's Hodgkin-Huxley I_{Kr} formulation with Equation 4.1. However, to ensure that the I_{Kr} for zero sotalol concentration did not alter the APD and restitution dynamics, the maximum conductance $\bar{g}_{Kr}$ of the I_{Kr}-sotalol was rescaled to 0.043 mS/nF from 0.153 mS/nF so that the peak amplitudes for I_{Kr}-sotalol with zero sotalol concentration and the original TP06 I_{Kr} were identical. This is necessary to ensure that the repolarisation dynamics (for zero sotalol concentration) of the TP06 model are not significantly altered by the inclusion of the I_{Kr}-sotalol Markov model.

Figure 4.7 compares the AP morphology from endocardium, mid-myocardium and epicardium of the TP06 model with that of the modified TP06 model (including the I_{Kr}-sotalol model for zero sotalol concentration). The model simulations are compared with experimental AP recordings from epicardium, endocardium [172] and mid-myocardium [58]. The cell models are simulated for 5 minutes with a basic cycle length (BCL) of 1000 ms, in line with the experimental protocols [58, 172]. The inclusion of the I_{Kr}-sotalol model does not significantly alter AP morphology of the TP06 model, despite the fact that the TP06 I_{Kr} exhibits a large spike during depolarisation whereas the I_{Kr}-sotalol does not. Referring back to Figure 2.7, it is clear that I_{Kr} in epicardial cells does not exhibit a large spike, therefore the FNG08 Markov model better captures the morphology of I_{Kr}.

Figure 4.8 compares the restitution of the TP06 human ventricular myocyte model

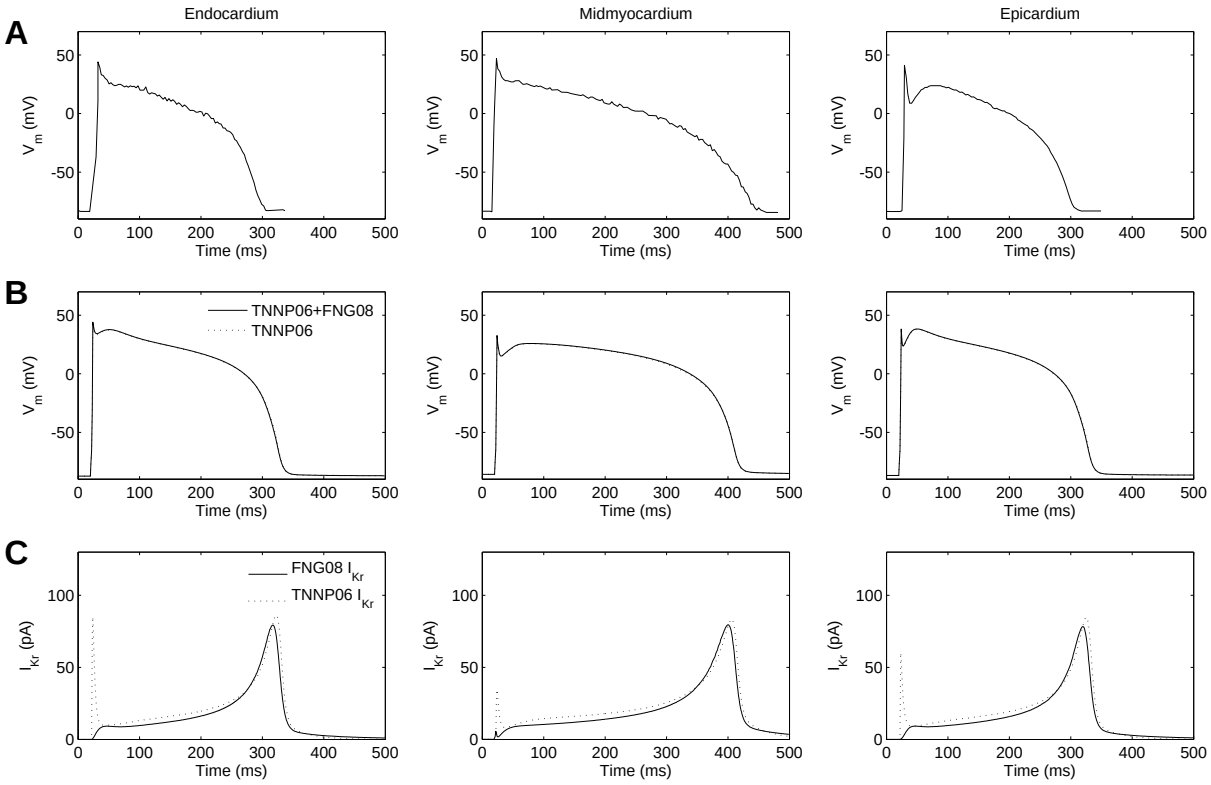


Figure 4.7: Experimental and simulated human ventricular AP from endocardium, mid-myocardium and epicardium. Panel A shows experimental AP recordings for sub-epicardial and sub-endocardial myocytes from [172] and mid-myocardial AP recordings from [58]. The models are simulated for 5 minutes with a basic cycle length (BCL) of 1000 ms, in line with the experimental protocols [58, 172]. In Panel B, the ten Tusscher 2006 model (TP06) is compared with the modified TP06 model, including the I_{Kr}-sotalol model with rescaled $\bar{g}_{Kr}$ of 0.043 mS/nF and zero sotalol concentration. Panel C compares the TP06 I_{Kr} model with the I_{Kr}-sotalol model with zero sotalol concentration.

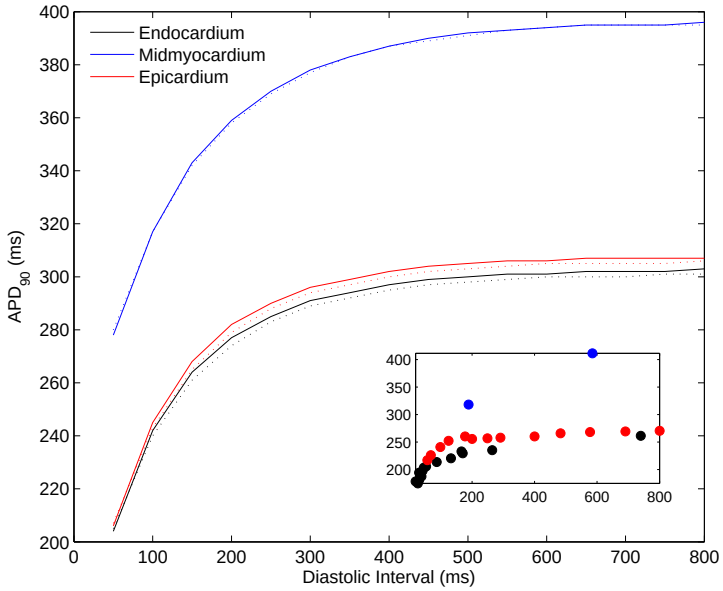


Figure 4.8: Simulated APD restitution curves from the endocardium, mid-myocardium and epicardium using the modified TP06 model with I_{Kr}-sotalol model. The dotted lines are simulations from the original TP06 model. The models are stimulated using the S1-S2 protocol with a BCL of 600 ms. Inset: Experimental data from endocardial [58, 173, 174], epicardial [175] and mid-myocardial cells [58, 174].

with the modified TP06 model. The APD restitution curves are compared with experimental restitution data from the endocardium [58, 173, 174], the epicardium [175] and the mid-myocardium [58, 174]. The restitution curve was simulated using the S1-S2 protocol with a driving BCL of 600 ms (S1). This is followed by an extra stimulus (S2) after a set diastolic interval. The models broadly capture the restitution dynamics, i.e. increased APD_{90} (90% of repolarisation duration) with increased diastolic interval. However, there is limited human experimental restitution data, particularly from the mid-myocardial region. The slopes of the restitution curves in the simulations are within the normal range of restitution curves observed by Nash et al. [176], where the slope of the restitution curve above 400 ms diastolic interval varies significantly between different regions of the heart, with flatter restitution curves observed towards the posterior, base portion of right ventricles and the anterior, base region of the left ventricle. The important aspect to consider is the slope of the restitution curve between 30 and 100 ms because steep APD restitution has been shown to lead to electrical instability resulting in re-entrant waves and ventricular fibrillation [177]. In this respect, the gradient of the APD_{90} restitution curve between 30 - 100 ms for the epicardial cell model is similar to experimental data (0.82 vs. 0.91) [178].

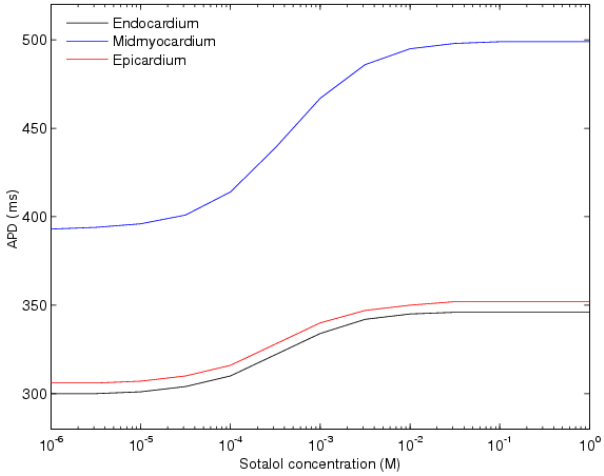
4.2.2 Effects of sotalol on action potential morphology

As discussed in Section **??**, there are different AP morphologies observed in the epi-, mid- and endocardial regions of the human myocardium [58]. These heterogeneities are due to the varying channel densities and have been included in the TP06 model by varying the conductances of I_{to} and I_{Ks}. Therefore, the increase of sotalol concentration will likely affect the epi-, mid- and endocardial cell models differently. Figure 4.9 illustrates the effects of varying sotalol concentration on the different cell models. Figure 4.9(a) illustrates the APD_{90} from the endo-, mid- and epicardial models with varying concentration of sotalol. It is clear that the mid-myocardial model is most sensitive to an increase in sotalol concentration. This is clearly seen in Figure 4.9(b), which illustrates the effect of 100 μM, 1 mM and 10 mM sotalol on epi-, mid- and endocardial AP. To ensure steady state inhibition of I_{Kr}, the models are simulated for 10 minutes using a BCL of 1000 ms. For the three cell types, an increase in sotalol concentration results in a prolongation of the APD. This prolongation is more pronounced in mid-myocardial cells than in the endo- and epicardial cells (11.6% vs. 7.31% and 7.28% for 100 μM, respectively) This is due to the fact that I_{Ks} density is lower in the mid-myocardium than in endo- and epicardium. Therefore, sotalol inhibition of I_{Kr} reduces the net repolarising current and thus slows repolarisation more in the mid-myocardial cells than in the other two cell types. Similarly, prolongation in the endocardium is marginally greater than APD_{90} prolongation in epicardial cells due to a decrease of I_{to} density in endocardial cells.

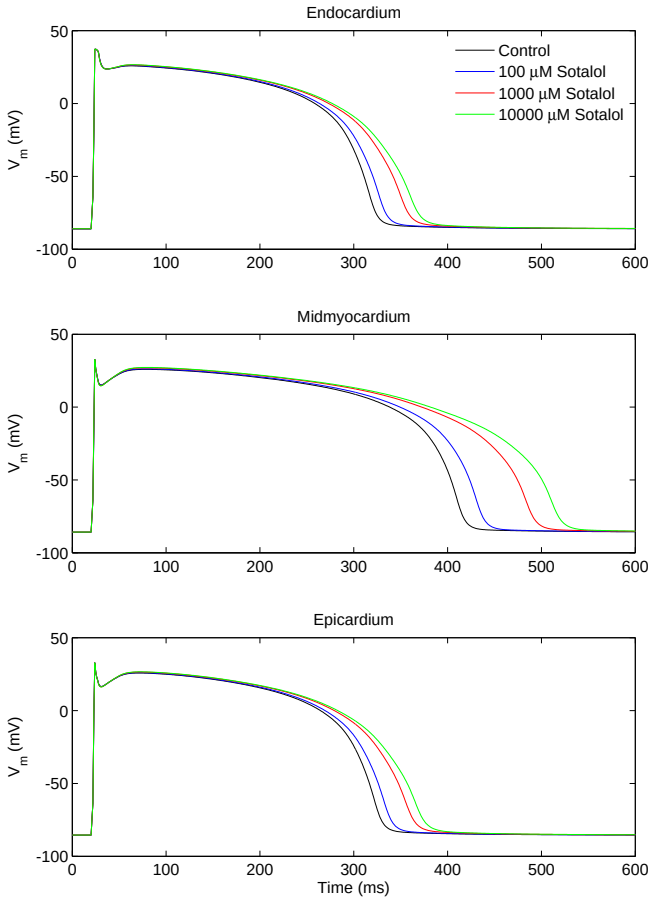
4.2.3 Reverse-rate dependence of sotalol

A number of clinical studies, both *in vivo* and *in vitro*, have shown that the prolonging effects of sotalol are rate dependent in that prolongation is smaller at high heart rates [179–181]. This phenomenon is known as *reverse-rate dependence* and is often ascribed to Class III anti-arrhythmics [5]. The term is derived from the fact that Class III anti-arrhythmics are often prescribed for treatment of ventricular tachycardia (fast heart rates), however it is at slower heart rates that the effect of the drug is more pronounced.

Figure 4.10 shows the rate dependent prolongation of APD_{90} of the modified TP06 model. Figure 4.10(a) illustrates the percentage of steady state APD_{90} prolongation by 300 μM sotalol at varying BCLs. The simulation results are compared with *in vivo* experimental data from monophasic AP recordings from six patients given 2.0 mg/kg

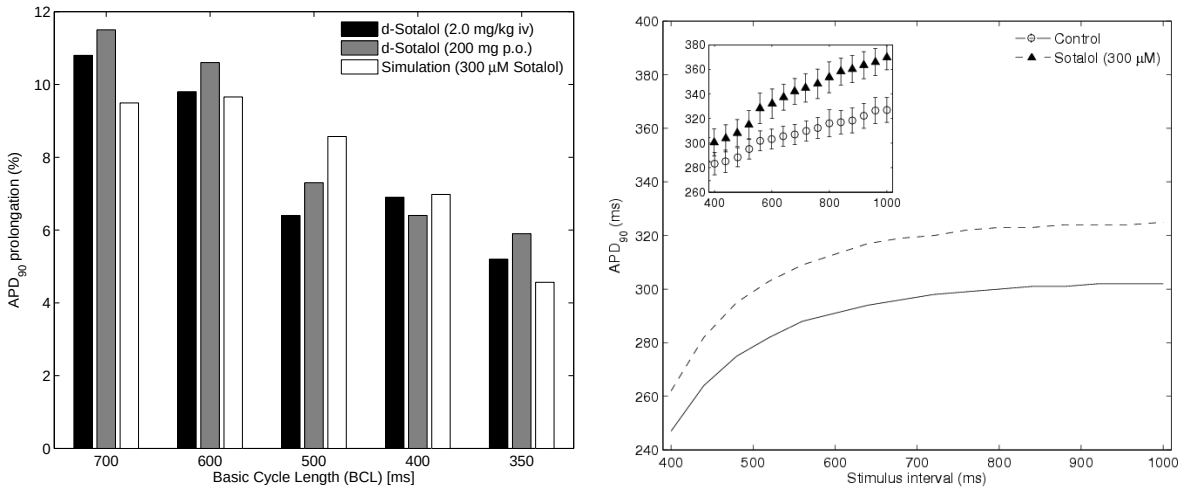


(a)



(b)

Figure 4.9: Simulation results of varying sotalol concentration on endo-, mid- and epicardial modified TP06 models. (a) APD_{90} with varying sotalol concentrations (b) AP of endocardial (top), mid-myocardial (middle) and epicardial (bottom) in the presence of 100 μM, 1 mM and 10 mM sotalol. Steady state I_{Kr} inhibition was reached by simulating the models for 10 minutes using a BCL of 1000 ms.



(a) (b)

Figure 4.10: Reverse-rate dependent block of I_{Kr} by sotalol compared with experimental data from Huikuri et al. [179]. (a) Mean steady state APD_{90} prolongation for 2.0 mg/kg intravenous *d*-sotalol intravenously and 200 mg *d*-sotalol given orally. The model was simulated using 300 μM sotalol. (b) Restitution dynamics with the effect of 300 μM sotalol. Model simulated using S1-S2 protocol by stimulating the model for 8 beats with a BCL of 600 ms followed by an extra stimulus (S2) after a particular stimulus interval.

d-sotalol intravenously and four patients given 200 mg of *d*-sotalol orally. The prolonging effect of sotalol is clearly more exaggerated at longer cycle lengths, i.e. at slower heart rates. Figure 4.10(b) shows the effects of 300 μM sotalol on APD_{90} restitution. The inset shows the effect of 2.0 mg/kg of *d*-sotalol, administered intravenously to six patients, on APD_{90} restitution [179]. The restitution curve was simulated using the S1-S2 protocol with eight driven beats with a BCL of 600 ms (S1). This is followed by an extra stimulus (S2) after a set stimulus interval. The APD_{90} resulting from S2 is plotted against the stimulus interval. The simulated restitution curves show a greater APD_{90} prolongation at larger stimulus intervals. Thus, the reverse-rate dependence observed experimentally is captured by the model.

4.3 Modelling drug effects on the pseudo-ECG

Computational models of activation and impulse propagation in multi-cellular geometries are established research methods for investigating the mechanisms underlying normal and abnormal cardiac dynamics [182]. In selecting the most appropriate multi-cellular geometry, it is necessary to consider the objective of the modelling study and the computational restrictions associated with each geometry. As previously mentioned, the goal of the modelling study is to investigate the effects of sotalol on repolarisation dynam-

ics. At a multi-cellular level this would involve investigating how sotalol affects impulse propagation and repolarisation gradients. These effects can be investigated by measuring and examining the pseudo-ECG. The pseudo-ECG is an aggregate potential of all the electrical activity in the model.

Both 1-D fibre, 2-D tissue and 3-D volume models have been used to calculate pseudo-ECGs and investigate impulse propagation. However, an increase in model dimensionality significantly increases computational complexity. For example, a 3-D monodomain model of the human ventricles using a finite-difference mesh with 26 million nodes takes more than 1200 CPU-hours to simulate one heart beat (600 ms) [108]. This model would not allow the dynamic effects of sotalol to be thoroughly investigated. Therefore, a simplified 1-D fibre geometry that would enable the model to be stimulated repeatedly is preferred. This would allow the dynamic effects of sotalol on repolarisation dynamics to be investigated. 1-D fibre models have been extensively used to investigate sub-cellular and cellular mechanisms of the pseudo-ECG [45, 183]. In addition, a simple 1-D fibre modelling study would provide proof of concept that modelling of drug effects on cardiac dynamics can provide insight into drug mechanisms on the heart so that more extensive computing resources can be allocated for modelling the drug effects in higher dimensions.

4.3.1 1-D model of cardiac tissue

A 1-D model was developed to investigate the effects of sotalol on impulse propagation and repolarisation dynamics. Cellular ionic currents were computed with the modified TP06 model, as described in Section 4.2.1. The 1-D model parameters were determined, where possible, to be consistent with human ventricular tissue. For instance, the diffusion coefficient (D) in Equation 3.26 was set to reflect the surface-to-volume ratio, cellular capacitance and cytoplasm resistivity of the human ventricular myocyte. Therefore, D was determined according to have a value of 1.162 cm^2/s, given that the human myocyte is found to be 18.5 ± 1.2 μm ($n = 15$, range 12-25 μm) in diameter, 148.3 ± 8.8 μm (range 112-185 μm) in length, with membrane capacitance of 179 ± 10 pF [184] and cytoplasm resistivity of 180 ± 34 Ωcm [185]. For comparison, ten Tusscher and Panfilov used a diffusion coefficient of 1.54 cm^2/s [44], whereas Bueno-Orovio et al. used $D =$ 1.171 cm^2/s [45] in their published 1-D models.

The length of a human myocardial fibre varies from 2 to 6 cm [53]. Therefore, given

that the length of the human myocyte is 148 μm and myocytes are connected orientated along the longitudinal axis of the fibre, a fibre 3 cm in length corresponds to a 1-D model comprising of 200 cells connected end-to-end. In addition, transmural heterogeneities can be included in the fibre to roughly reflect the distribution of heterogeneities observed in human ventricular tissue, i.e. 50% endocardial, 30% mid-myocardial and 20% epicardial cells [58]. This distribution of heterogeneities has been included in previously 1-D fibre models [45] and 3-D models of human ventricular tissue [47].

Numerical methods

Recall from Section 3.1.1, assuming a monodomain framework that the propagation of the action potential in a 1-D fibre of cells can be determined using the monodomain cable equation (Eq. 3.25). The solution to Equation 3.25 can be approximated by a finite difference scheme and solved using the Crank-Nicolson implicit method [186], such that for each cell the change in membrane potential can be expressed as

$$\frac{\partial V_m(x,t)}{\partial t} = D \cdot \left\{ \frac{V_m(x-1,t) - 2V_m(x,t) + V_m(x+1,t)}{\Delta x^2} \right\} - \sum I_j - I_{stim}. \qquad (4.3)$$

Extracellular resistance is neglected as the fibre is assumed be in an extensive medium, i.e. the surrounding volume has a high conductivity. Boundary conditions of zero flux are applied to the fibre by setting $\partial V_m(x,t)/\partial x = 0$ at the beginning and end of the fibre [187]. In keeping with previously published 1-D models of cardiac activity, the diffusion coefficient ($D = 1.162$ cm^2/s) is constant through the fibre, except for a 5-fold decrease for two cells either side of the mid-to-epicardium transition region [183, 188].

Direct explicit solutions to Equation 4.3 necessitate a very small time increment (Δt) for numeric convergence. Therefore, for all simulations Δt was set to 1 μs. For a continuous, monodomain fibre, i.e. where there are no gap junctional discontinuities, the numerical accuracy and successful convergence of the solution to Equation 4.3 requires that the spatial discretisation (Δx) is no longer than one tenth of the space constant[3] (λ) [189]. Therefore, given that the space constant for human myocytes is several myocyte cell lengths (approx. 1 mm) [190], the cell length (148 μm) was used as the spatial discretisation. Solutions for all cellular transmembrane currents were obtained using the algorithm for solving dynamic membrane equations proposed by Rush and Larsen, which implements a first-order Euler method [189].

[3]The space constant of an AP in a myocyte is given by $\lambda = \sqrt{r_m/r_i}$ where r_m is the resistance across the membrane and r_i is the intracellular axial resistance.

Calculation of pseudo-ECG

It is possible to calculate an extracellular potential or *pseudo-ECG* at any point in surrounding the model of cardiac tissue. For a 1-D model that sits in a volume conductor with uniform conductivity (σ_e), the extracellular unipolar potential (Φ_e) generated by the propagation of electrical impulses throughout the model can be defined as the following:

$$\Phi_e(x', y', z') = \frac{r^2 \sigma_i}{4\sigma_e} \int (-\Delta V_m) \cdot \left[\Delta \frac{1}{d}\right] dx \tag{4.4}$$

$$d = \sqrt{(x - x')^2 + (y - y')^2 + (z - z')^2}, \tag{4.5}$$

where ΔV_m is the spatial gradient of V_m, σ_i is the intracellular conductivity, r is the radius of the cell and d is the distance from a source point (x, y, z) to the "electrode" point (x', y', z') [52]. Given that boundary effects of the monodomain model are limited to one space constant [191], 10 cells on both the endocardial and epicardial boundaries were excluded from the pseudo-ECG calculation to reduce the boundary effects on pseudo-ECG morphology.

Simulation of normal conditions

Figure 4.11 illustrates the APD_{90} profile (APD_{90} for each cell in the fibre), the different AP morphologies from the epi-, endo- and mid-myocardium and the pseudo-ECG resulting from the simulations. The virtual electrode for the pseudo-ECG is set to 0.5 cm from the epicardial surface. The model was simulated with zero drug concentration. The 1-D model is stimulated from the endocardium side for 20 beats at 1000 ms BCL. The panel on the left shows the APD_{90} profile. The transmural dispersion of repolarisation (TDR) is measured as the difference between the longest and shortest APD_{90} in the fibre and is measured as 50.0 ms for this simulation. The conduction velocity in the fibre for 1000 ms BCL was found to be 64.5 cm/s, which is within the normal range (50 to 68 cm/s) [192].

Preclinical and clinical biomarkers

In both preclinical and clinical studies, biomarkers are used to assess the proarrythmic effects of drugs on cardiac activity. In preclinical studies, APD prolongation and reverse-rate dependence are most often used as proarrythmic biomarkers. In addition, increased TDR is linked with drug-induced torsades de pointes (as discussed in Section 2.3.2). In clinical studies the QT interval is typically used to assess the effects of drugs on the

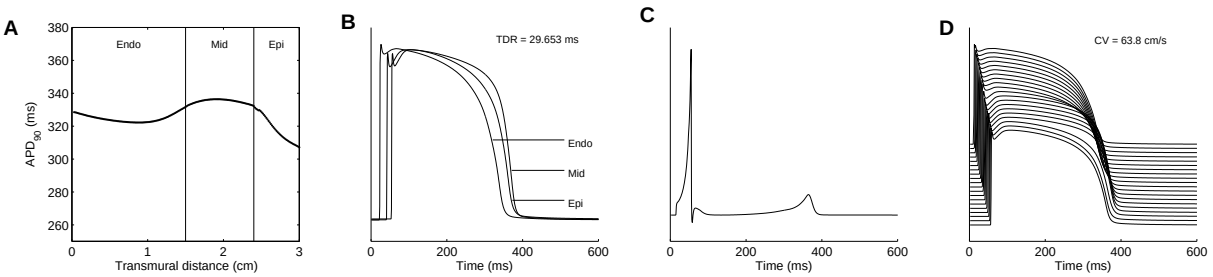
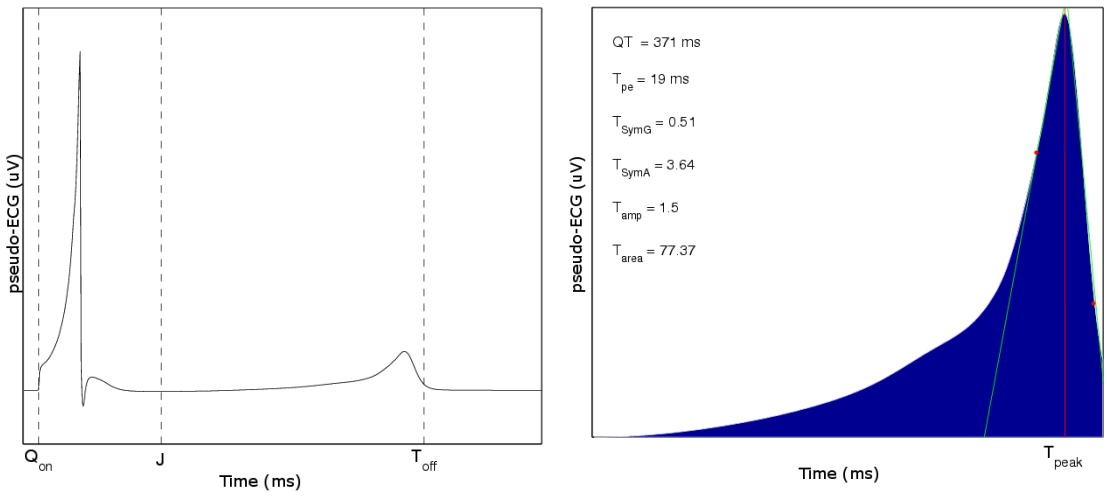


Figure 4.11: Simulation results from 1-D fibre model of 200 modified TP06 models for 1000 ms BCL. The distribution of epi-, endo- and mid-myocardial cells in the fibre is 50:30:20. (A) APD_{90} profile (B) Action potentials from the cells in the middle of the endo-, mid- and epicardial regions. (C) Pseudo-ECG calculated from a virtual electrode placed 0.5 cm from the epicardial boundary. (D) Action potentials from fibre highlighting the impulse propagation in the fibre. In D, the action potentials are vertically displaced for visualisation.

heart. However, as discussed in Chapter 1, T-wave morphology-based biomarkers have been proposed as alternative biomarkers of drug-induced arrhythmia. Results presented in Chapter 7 will show that T-wave morphology-based biomarkers are also sensitive to drug effect. Therefore, in investigating the effect of sotalol on cardiac activity using the pseudo-ECG, both timing and morphology-based biomarkers are implemented. The most relevant timing intervals are the QT interval and the T-wave peak to T_{off} (T_{pe}) interval. Based on a review of T-wave morphology biomarkers in Section 5.3, four morphology-based biomarkers have been selected for characterising the effects of sotalol on ventricular repolarisation in this thesis. These are the T-wave peak amplitude (T_{amp}), T-wave area (T_{area}) and two symmetry biomarkers, one based on the ratio of up-slope gradient to the down-slope gradient (T_{symG}) and the other based on the ratio of area under the up-slope of the T-wave to the area under the down-slope (T_{symA}). T-wave width was not included as a biomarker due to the lack of a clinical definition of the T-wave onset point.

The physiological interpretation of biomarkers, in the context of the modelling study, can be described as follows: firstly, the QT interval captures the entire duration of the depolarisation and repolarisation process and therefore is largely dependent on the duration of APs in the model. T_{pe} is a measure of transmural dispersion of repolarisation [193]. T_{amp} is seen as a measure of the magnitude of the repolarisation gradients, whereas T_{area} captures not only the magnitude but the duration of the repolarisation gradients. The symmetry biomarkers, T_{SymA} and T_{SymG}, are seen as a measure of AP triangulation, i.e. capturing the changes in repolarisation dynamics towards the latter phases of AP repolarisation.



(a) (b)

Figure 4.12: Timing and morphology analysis of pseudo-ECG: (a) identification of fiducial points Q_{on}, J and T_{off} in the pseudo-ECG, (b) morphology biomarkers are derived from the JT segment (J - T_{off}) extracted from the pseudo-ECG shown in (a). The T-peak and the best-fit lines for determining the portions of the T-wave to calculate the symmetry biomarkers are shown.

In order to derive the biomarkers mentioned above, it is necessary to identify the waveform feature limits and fiducial points in the pseudo-ECG, namely Q_{on}, R-peak, J, T-peak and T_{off} points. The automated ECG segmentation algorithm implemented in this thesis is presented in Section 6.1. However, that algorithm has not been applied to the pseudo-ECG due to the absence of noise and different waveform morphologies. Instead, the fiducial points are identified in the follow ways

- **Q_{on}** - the first non-zero value initiating a new beat. Recall that the BCL and number of beats is known
- **R-peak** - the maximum value for each beat.
- **J** - the first local minimum following the S-wave.
- **T-peak** - the maximum value in the scanning window defined from 200 ms from R-peak and the following Q_{on}.
- **T_{off}** - the point of intersection between the steepest tangent after T-peak and the isoelectric line. This method is referred to as the tangent method [194] and is discussed in more detail in Section 5.2.2.

Figure 4.12(a) illustrates the waveform limits and fiducial points in the pseudo-ECG.

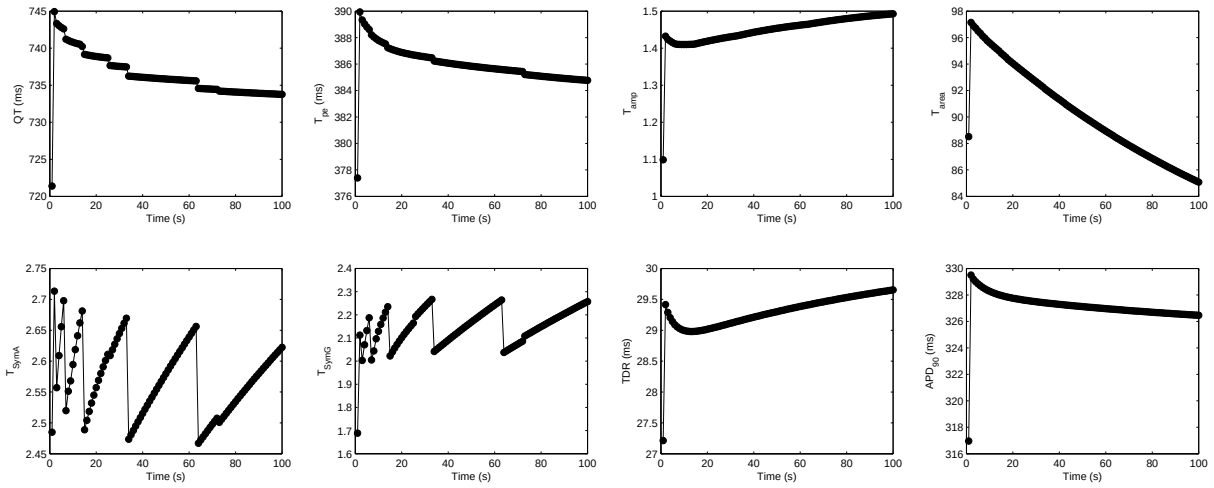


Figure 4.13: Pseudo-ECG biomarkers extracted from each beat. The 1-D model is simulated for 100 beats using 100 ms BCL with zero sotalol concentration.

Once the waveform limits and fiducial points for each heart beat in the pseudo-ECG have been identified, the timing and morphology biomarkers can be determined. The morphology biomarkers derived from the pseudo-ECG are determined in much the same way as implemented for automated clinical ECG analysis (described in Section 6.2.2). Figure 4.12(b) illustrates how the morphology biomarkers are derived from the JT segment. The timing intervals are calculated as follows: QT = T_{off} - Q_{on}, T_{pe} = T_{off} - T_{peak}. The T-wave area is determined as the area under the T-wave from J to T_{off}. T_{amp} is the maximum value of the pseudo-ECG between J and T_{off}. T_{symG} is the ratio of the ascending gradient over the descending gradient of the T-wave and T_{symA} is the ratio of the area under the ascending slope of the T-wave over the area under the descending slope of the T-wave. The portions of the T-wave used for the symmetry biomarkers are T-peak $\pm 0.75 \times T_{pe}$ on either side of T-peak. Figure 4.13 illustrates the pseudo-ECG biomarkers over time with constant pacing. The discrete jumps observed in QT and T_{pe} are due to measurement rounding to milliseconds. Due to the lack of interpolation the measurement rounding is mirrored in the T-wave symmetry biomarkers, as seen in Figure 4.13. Nevertheless, it is clear to see that with continued stimulation the biomarkers tend towards a steady state.

Effects of pacing rate on biomarkers

Figure 4.14 illustrates the variation of the timing and morphology biomarkers derived from the pseudo-ECG for different BCLs. It is clear that the QT interval, T_{pe}, T_{amp} and T_{symA} increase with increasing BCL. T_{amp} and T_{pe} are the most sensitive to change in

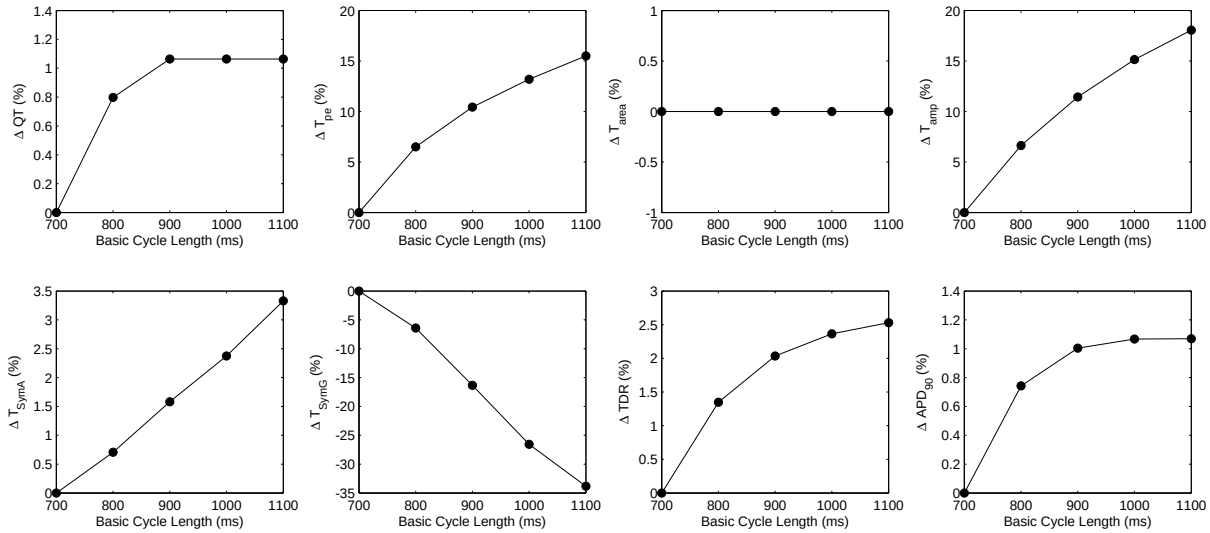


Figure 4.14: Simulation results of pseudo-ECG biomarkers for varying basic cycle lengths (BCL), namely QT interval, T-wave peak to T_{off} (T_{pe}), T-wave area (T_{area}), T-peak amplitude (T_{amp}), T-wave area-based symmetry (T_{symA}), T-wave gradient-based symmetry (T_{symG}), TDR and mean APD_{90}.

BCL, with over 15% increase from 700 to 1100 ms BCL, compared with only 1.05% for the QT interval. The percentage increase in TDR and mean APD_{90} from 700 to 1100 ms BCL is of the same order of magnitude as the increase in QT interval ($\sim$ 1 to 2%). The effect of RR interval on QT interval in clinical studies is generally more pronounced (eg. 5.5 - 25% QT prolongation from 600 to 1200 ms) [195]. Clinical studies have also shown that T_{pe} increases with RR interval, with a 11.4% increase in T_{pe} with an increase in RR interval from 550 to 1150 ms [196]. The gradient-based T-wave symmetry biomarker, on the other hand, shows a significant decrease with increasing BCL (-35% from 700 to 1100 ms). Section 7.1.3 investigates the dependency of the biomarkers in clinical Holter ECG recordings on heart rate.

The mechanisms underlying the effects of pacing rate on pseudo-ECG biomarkers are most likely due to the change in APD_{90} profile. Figure 4.15 illustrates the effects varying BCLs on the 1-D model. As can be seen in the figure, the increase in BCL results in an increase of TDR and mean APD_{90}. However, the increase in TDR and mean APD_{90} seems to have a varied effect on T-wave morphology. T_{amp} is seen to increase with BCL, whereas T_{area} remains constant with increasing BCL. In contrast, T_{SymG} shows a decrease with increasing BCL. This might be due to the fact that sotalol effects the latter phase of AP repolarisation, i.e. increased AP triangulation.

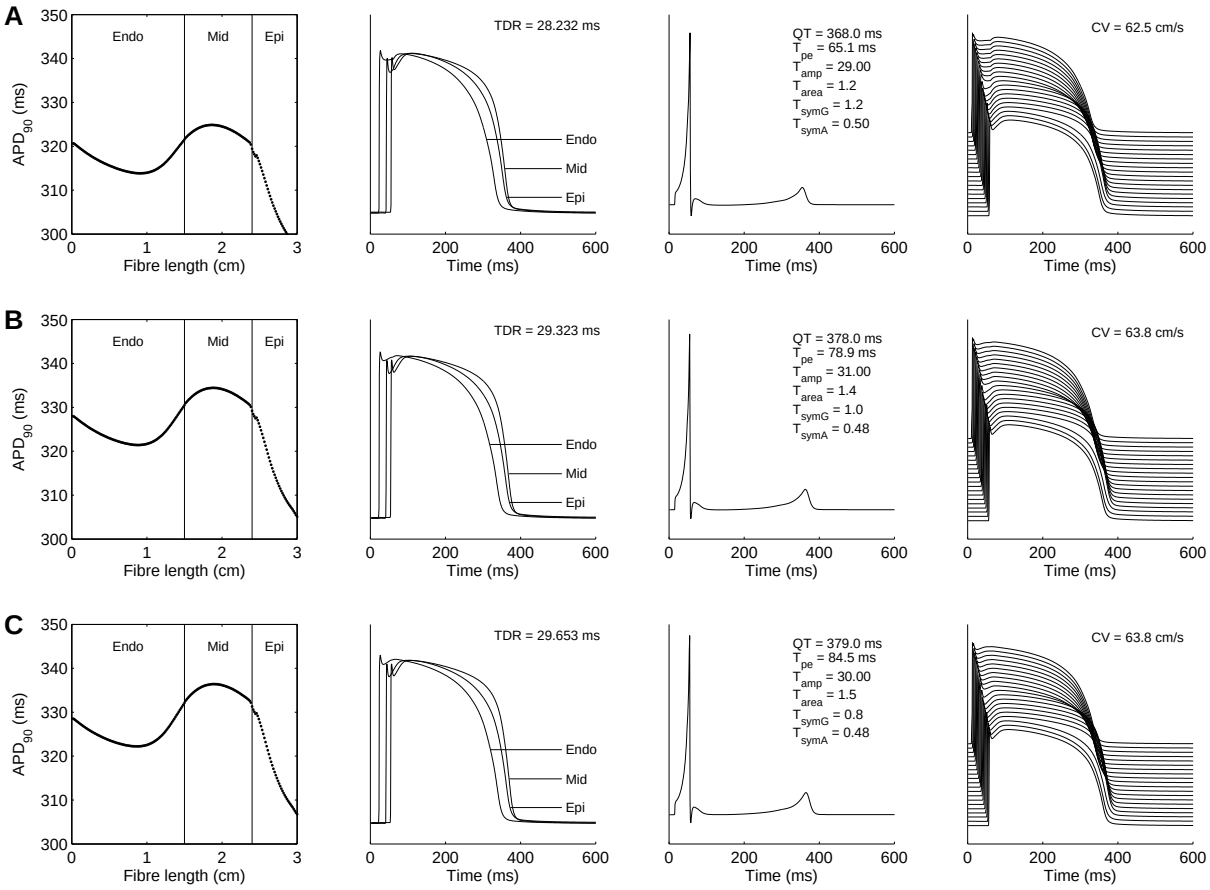


Figure 4.15: Simulation results from 1-D fibre model of 200 modified TP06 models for (A) 600, (B) 800 and (C) 1000 ms BCL. From left to right: APD_{90} profile, AP tracings from epi-, mid- and endocardial cells from the middle of each respective region, pseudo-ECG and AP propagation in the fibre. In column on the right, the APs are vertically displaced for visualisation.

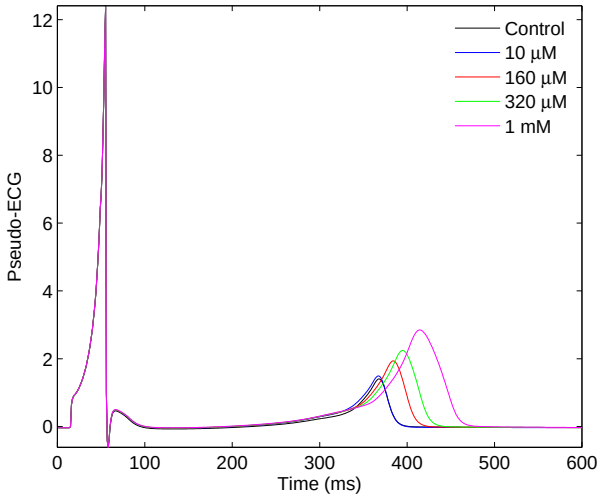


Figure 4.16: Pseudo-ECG simulations from 1-D fibre model with varying sotalol concentrations. The fibre is composed of 200 modified TP06 cellular models with a 50:30:20 distribution of epi-, endo- and mid-myocardial cells in the fibre.

4.3.2 Effects of sotalol on 1-D model

The effects of sotalol on AP morphology, as discussed in Section 4.2.1, showed that an increase in sotalol concentration resulted in an increase in APD_{90}. This prolongation was most pronounced in the mid-myocardial AP. Furthermore, the prolongation effects were rate dependent, in that a decrease in pacing rate resulted in an increased prolongation of APD_{90}. To assess the effects of sotalol on AP propagation and pseudo-ECG biomarkers, the 1-D model was stimulated for 60 beats with 1000 ms BCL at varying sotalol concentrations. Figure 4.16 illustrates the effects of varying sotalol concentration on the pseudo-ECG. As can be seen in the figure, an increase in sotalol concentration results in an increased prolongation of the QT interval and an increase in T-wave peak amplitude.

Figure 4.17 illustrates the percentage change of the pseudo-ECG biomarkers, with respect to baseline, at varying sotalol concentrations. The largest drug effect is observed in T_{pe}, where 1 mM sotalol results in over 350% increase in T_{pe}. All of the biomarkers, except T_{symG}, show an increase with increasing sotalol concentration. T_{symG} shows a decrease with sotalol concentrations greater than 500 μM. Of all the clinical biomarkers that show an increase with increasing drug concentration, the QT interval is the relatively least sensitive biomarker to change in sotalol concentration. However, it should be noted that the sensitivity of the biomarkers should be weighed against the volatility and variance of the measurements, particularly in the clinical setting.

To understand the mechanisms underlying the effects of sotalol concentration on the

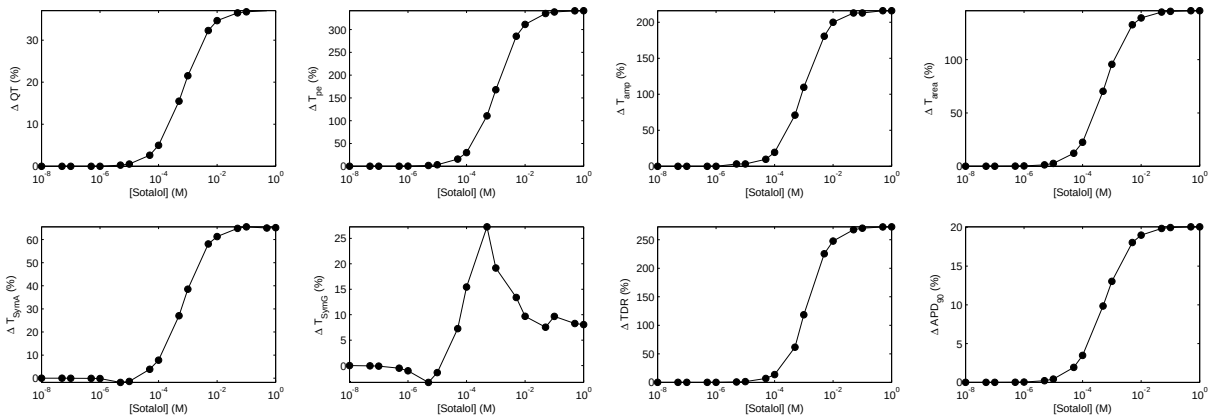


Figure 4.17: Simulated effects of drug concentration on pseudo-ECG biomarkers with respect to baseline (zero sotalol concentration). The biomarkers include namely QT interval, T-wave peak to T_{off} (T_{pe}), T-wave area (T_{area}), T-peak amplitude (T_{amp}), T-wave area-based symmetry (T_{symA}), T-wave gradient-based symmetry (T_{symG}), TDR and mean APD_{90}.

timing and morphology biomarkers, the APD_{90} profile, AP tracings from epi-, mid- and endocardial cells from the middle of each respective region, the pseudo-ECG and AP propagation in the fibre for control, 500 μM and 5 mM sotalol are shown in Figure 4.18. It is clear from the left-most column in Figure 4.18 that the increase in sotalol concentration increases TDR by prolonging the APD_{90} in the mid-myocardial region. The effect of sotalol on T-wave amplitude is likely due to the increased TDR, which results in larger repolarisation gradients throughout the fibre, particularly towards the latter phases of repolarisation. This can be clearly seen in the column second from the left, where the dispersion during phase 3 of the AP in the epi-, mid- and endocardial cells increases with sotalol concentration. The differences between the APD_{90} of the endo- and epicardial AP with respect to the mid-myocardial AP for 1 mM are 74 and 68 ms, respectively; compared with values of 24 and 38 ms in the control simulation.

Effects of pacing rate on drug action in 1-D model

In single cell simulations, the prolongation effects of sotalol on APD_{90} were reverse-rate dependent. To assess whether the effects of sotalol concentration on pseudo-ECG biomarkers are also rate dependent, the 1-D model was stimulated for 60 beats at BCL values from 600 to 1200 ms. Figure 4.19 illustrates the impact of varying BCL on the drug effect of 10 μM, 160 μm, 320 μM and 1 mM, with respect to baseline, on the timing and morphology biomarkers. The increase in BCL results in an increase in the drug effect on QT, T_{pe}, T_{area}, T_{symA} and mean fibre APD_{90}, whereas the drug effect on T_{amp} seems to

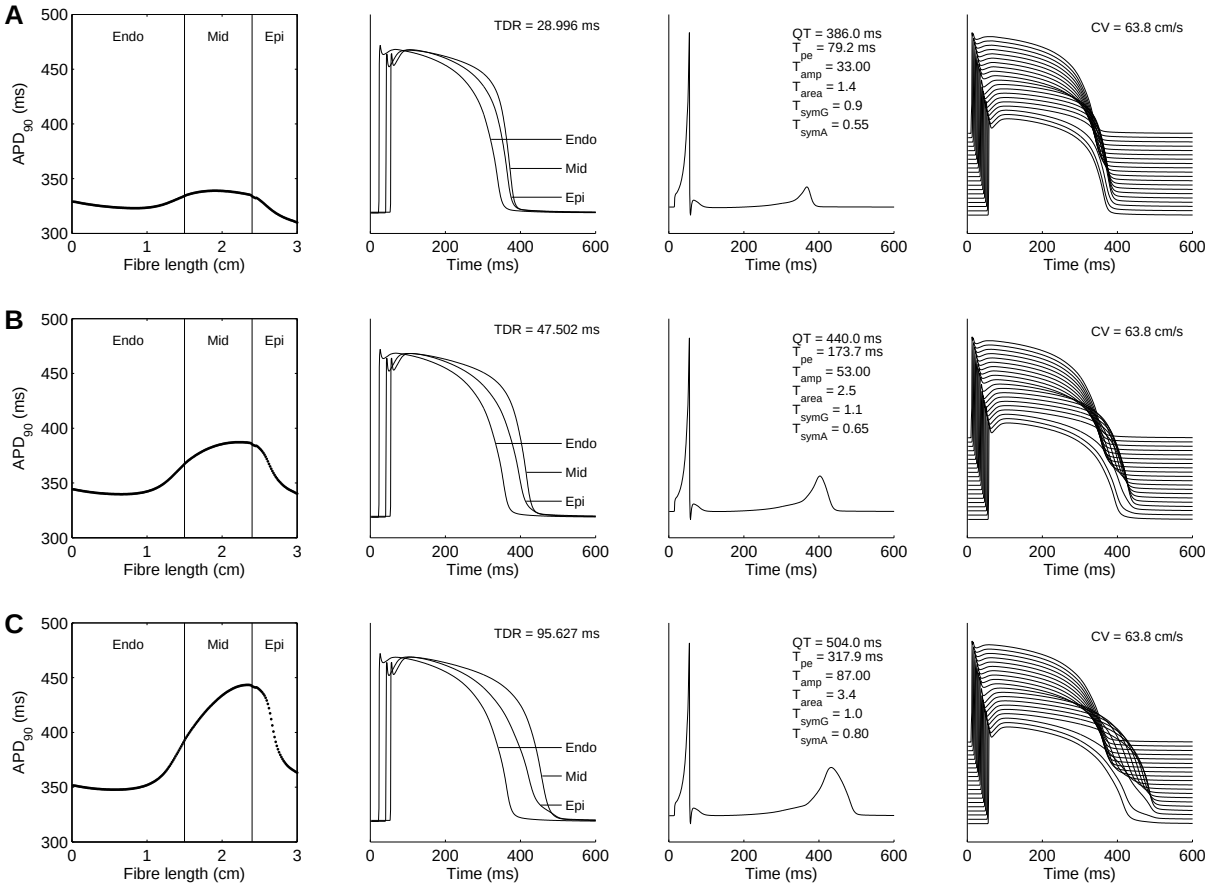


Figure 4.18: Simulation results from 1-D fibre model with varying drug concentrations: (A) control, (B) 500 μM and (C) 5 mM sotalol. From left to right: APD_{90} profile, AP tracings from epi-, mid- and endocardial cells from the middle of each respective region, pseudo-ECG and AP propagation in the fibre. In column on the right, the APs are vertically displaced for visualisation.

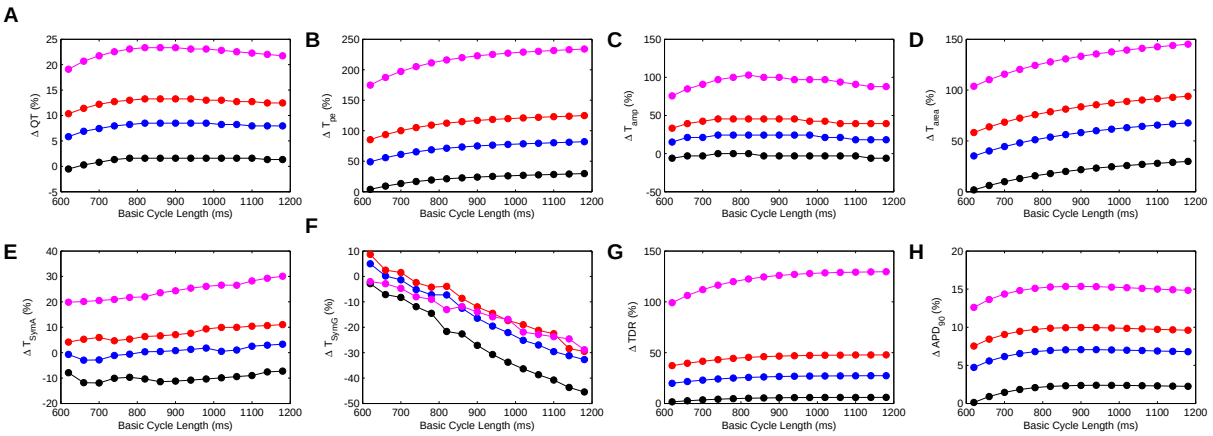


Figure 4.19: Percentage change of simulated drug effects on biomarkers, with respect to baseline, for varying BCLs. The biomarkers shown include (A) QT interval, (B) T_{pe}, (C) T_{area}, (D) T_{amp}, (E) T-wave area-based symmetry (T_{symA}), (F) T-wave gradient-based symmetry (T_{symG}), (G) TDR and (H) mean fibre APD_{90}. The 1-D fibre was stimulated for 60 beats to reach steady state inhibition at 10 μM, 160 μm, 320 μM and 1 mM sotalol

remain relatively independent of BCL for low concentrations of sotalol. In contrast, the increasing BCL results in a decrease‘ ‘ in the drug effect on T_{symG}. This could be linked with the increase in drug effect on TDR observed in Figure 4.19(g). The mechanisms underlying this effect are unclear, but is most likely due to the dual effects of sotalol, i.e. increasing TDR and increasing repolarisation duration (APD_{90}), as previously discussed.

4.4 Discussion

In this chapter, the development of a novel Markov model of sotalol's interactions with HERG has been described . The model has been shown to adequately represent the interactions between HERG and sotalol by comparing the simulation results with experimental data from HERG expressed in human embryonic kidney cells at physiological temperatures. An increase in sotalol concentration resulted in a decrease in I_{Kr}, with steady state inhibition reached after approximately 10 minutes of simulation. The I_{Kr}-sotalol model was incorporated into the ten Tusscher 2006 model of the human ventricular AP. The simulations of the modified cellular model were compared with experimental data of human restitutive dynamics and AP morphology for endo-, mid- and epicardial cells. The model was then used to investigate the effects of sotalol on APD. An increase in sotalol concentration resulted in an increase in APD_{90}, particularly in the mid-myocardial AP. The prolongation effects of sotalol were also shown to be reverse-rate dependent.

The modified cellular model was then incorporated into a 1-D model. The 1-D model

included transmural heterogeneities and was able to simulate a positive T-wave. Duration of repolarisation biomarkers (QT and T_{pe}) and T-wave morphology biomarkers (T_{area}, T_{amp}, T_{symA} and T_{symG}) were extracted from the pseudo-ECG. The effects of increased sotalol concentration resulted in a prolongation of the QT and T_{pe} intervals, as well as an increase in T-wave area and peak amplitude. The area-based symmetry biomarker also increased with sotalol concentration. However, the same increase in sotalol concentration resulted in a decrease in the gradient-based symmetry biomarker because sotalol was shown to affect the latter stages of the T-wave. The T-wave-based biomarkers, particularly T_{pe}, T_{area} and T_{amp}, were more sensitive to sotalol concentration than the QT interval. The effects of sotalol were shown to be reverse-rate dependent.

There are a number of limitations of the model that should be mentioned. Firstly, a 1-D fibre model is an over-simplification of cardiac tissue and electrophysiological dynamics. In cardiac tissue, there is AP propagation in both the axial and transversal directions. This effect would diminish the impact of the mid-myocardial cells and act to reduce TDR. Secondly, the pseudo-ECG is not an accurate representation of the surface ECG in that it only measures the aggregated electrical activity in a single 1D-fibre source - a gross simplification of the heart. Nevertheless, the model has shown that T-wave morphology is sensitive to sotalol concentration and that these effects are reverse-rate dependent.

Chapter 5

Automated Analysis of the Surface Electrocardiogram

The ECG is a periodic signal with a combination of high frequency variations (QRS complex) and low frequency features (P and T-wave). The varying spectral dynamics of the ECG and the wide range of noise and artefacts makes automated analysis of the ECG a non-trivial problem. Automated analysis of the ECG can be categorised into two main areas, namely interval and morphology analysis. This chapter reviews of the automated signal processing techniques, including signal encoding and de-noising methods, followed by a review of automated interval and morphology analysis methods.

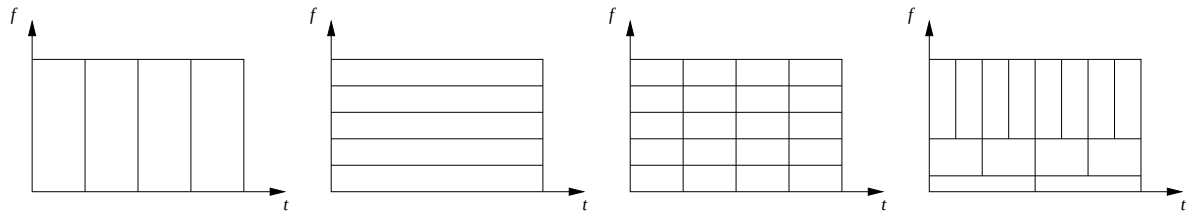
5.1 Signal processing of the surface ECG

The ECG, like any electrical signal, can be distorted by various electrical noise, ranging from electrode noise to mains interference [24]. In addition, the ECG is also sensitive to physiological artefacts, such as muscle contractions. Therefore, in order to identify the onset and offset points of ECG waveform features, it is necessary to extract key information from the ECG to allow fiducial points in the signal to be identified. From a signal processing perspective, this entails transforming the signal into a domain in which the effects of noise are easier to identify and remove. The subsequent feature delineation is often implemented in the transform domain. Similarly, in order to characterise the morphology of the T-wave, it is necessary to remove noise interference from the signal so that the underlying T-wave shape can be captured in a robust and reproducible manner. This section discusses transform methods for ECG encoding and de-noising techniques.

5.1.1 Transform methods for ECG representation

The ECG can be characterised by its temporal and spectral characteristics. The most common transform for analysing the spectral characteristics of a signal is the well-known Fourier transform. However, considering that the basis functions for the Fourier transform are sine and cosine functions, which have infinite support in the time domain, the Fourier transform effectively averages the signal frequency components over the length of the analysis window. This has the effect of obscuring the temporal information, such as the timing of the QRS complex. This limitation can partly be overcome by using the short time Fourier transform (STFT), which uses a short, sliding window to analyse the signal thereby retaining some of the temporal information in the resulting encoding. Wavelet analysis is an improved signal encoding that can represent the signal in both the time and frequency domains by using a sliding analysis window of variable width [197]. The wavelet basis functions are, therefore, localised in both the time and frequency domain and thus able to capture the changing spectral characteristics of the ECG.

Figure 5.1 illustrates the different time-frequency analysis paradigms by representing the time and frequency domains as a two-dimensional plane. Analysis in the time domain implies characterising the temporal characteristics of the raw signal, such as the gradient or amplitude of the signal. This provides perfect localisation in time but no localisation in frequency. In contrast, Fourier analysis provides perfect localisation in frequency but



(a) Time domain (b) Fourier analysis (c) STFT (d) Wavelet analysis

Figure 5.1: Time-frequency analysis of different signal analysis paradigms.

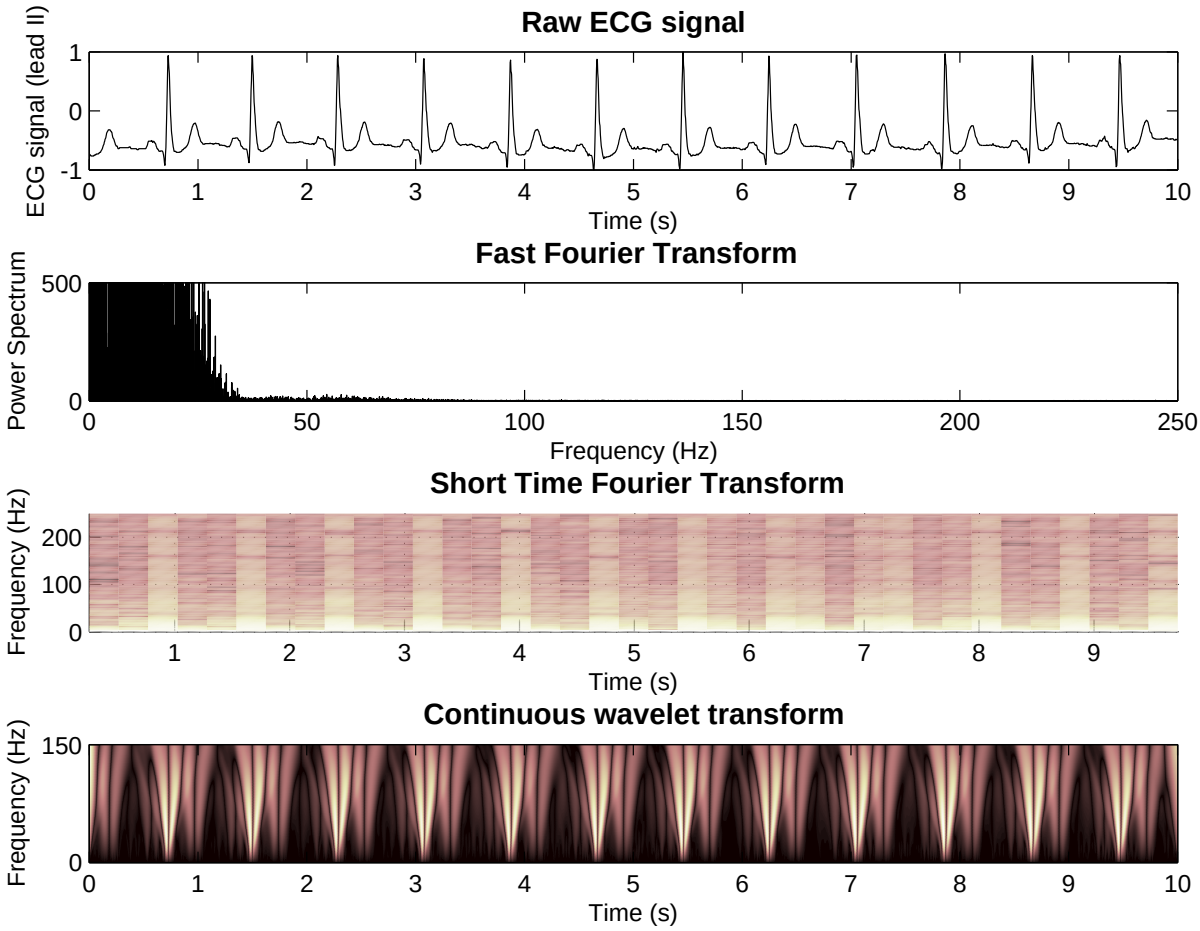


Figure 5.2: Different spectral encodings of a 10-second ECG recording from lead II, namely the Fourier transform, the short time Fourier transform and the continuous wavelet transform.

no localisation in time. The short-time Fourier transform provides a time-frequency description of the signal by tiling the time-frequency plane with analysis blocks of fixed size, as shown in Figure 5.1. Wavelet analysis, on the other hand, tailors the size of the analysis blocks to the time-frequency characteristics, i.e. low frequency components are analysed using longer analysis blocks, whereas high frequency components are captured using shorter analysis blocks. Figure 5.2 highlights the difference between the Fourier transform, the STFT and a continuous wavelet transform of a 10 second segment of ECG signal from lead II sampled at 500 Hz. The STFT spectrogram is produced using a Hanning window 256 samples in length with an overlap of 128 samples. It is clear from the plot that the resulting STFT representation loses temporal definition, such as the timing of QRS complexes, whereas such temporal information is retained in the wavelet coefficients.

Wavelet analysis

The basis functions of the wavelet transform are known as *wavelets* and are generated by scaling and translating a single *mother* wavelet function. To scale (or dilate) a wavelet means to stretch or shrink the function in the time domain, whereas translating a wavelet means to shift the wavelet along the time axis. By scaling the wavelet function to a number of different scales and translating the set of scaled wavelets, the wavelet transform is able to capture the different frequency components of the signal at varying time points. More specifically, the set of analysing wavelets or time-frequency atoms can be generated by scaling and translating the *mother* wavelet, i.e.

$$\psi_{s,\tau}(t) = \frac{1}{\sqrt{s}}\psi\left(\frac{t-\tau}{s}\right), \tag{5.1}$$

where $\psi_{s,\tau}(t)$ is the mother wavelet scaled by a factor s and translated by an amount τ. The $1/\sqrt{s}$ term normalises the wavelet atom to conserve its unit energy when the wavelet is scaled by s. The mother wavelet is a specialised function that satisfies the following conditions:

- $\psi(t) \in \mathbb{L}^2(R)$, where $\mathbb{L}^2$ represents the space of finite energy functions
- It has zero average

$$\int_{-\infty}^{+\infty} \psi(t)dt = 0 \tag{5.2}$$

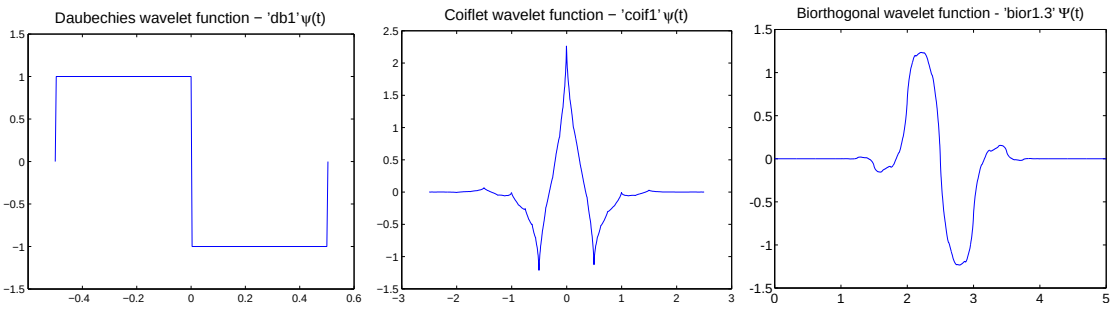


Figure 5.3: The first wavelet function from three wavelet families: Daubechies, coiflets and bio-orthogonal.

- It has unit energy

$$\int_{-\infty}^{+\infty} |\psi(t)|^2 dt = 1 \tag{5.3}$$

- It satisfies an *admissibility condition* that can be formulated as:

$$C_\psi = \int_0^{+\infty} \frac{|\Psi(\omega)|^2}{\omega} d\omega \tag{5.4}$$

  where $\Psi(\omega)$ as the Fourier transform of $\psi(t)$ and $0 < C_\psi < \infty$.

The admissibility condition is satisfied if the wavelet has no zero-frequency component, i.e. $\Psi(0) = 0$ and $\Psi(\omega)$ is continuously differentiable [198]. The zero average and unit energy constraints ensure that the wavelet is localised in time to some extent. This characteristic is commonly referred to as *compact* support [199]. The admissibility condition ensures that the set of wavelet atoms is complete; in other words, that any function f in $\mathbb{L}^2(R)$ can be perfectly reconstructed by a linear combination of a set of translated and scaled wavelet atoms.

Wavelet functions are clustered into *families* that share similar characteristics. For example, Ingrid Daubechies presented a family of orthogonal wavelets in 1992 that were characterised by a maximal number of vanishing moments for a given temporal support [200]. Figure 5.3 shows three examples of wavelet functions from different wavelet families including Daubechies, coiflets and biorthogonal wavelets. The large number of wavelet families is an additional advantage of wavelet analysis in that the "optimal" wavelet function, for any particular signal and associated application, can be selected. For example in ECG segmentation, the wavelet function that minimises the segmentation error compared with expert manual measurements could be selected as the optimal wavelet function.

An additional characteristic of wavelet functions is that the spectral components of the wavelet atom are inversely proportional to the dilation of the wavelet, i.e. $f \propto 1/s$ [198]. A trade-off exists between the temporal and spectral resolution, as illustrated in Figure 5.1(d), in that as temporal resolution increases, the spectral resolution decreases. The specific frequency associated with any particular scale s is given by

$$f_s = \frac{f_c}{s}, \tag{5.5}$$

where the characteristic or centre frequency (f_c) is defined as the frequency at which the magnitude of the Fourier transform of the mother wavelet at $s = 1$ and $\tau = 0$ is maximised [201]. The scale, therefore, governs the degree of frequency *localisation* whereas the translation parameter determines the position of the analysing wavelet on the time axis.

Overview of wavelet transform

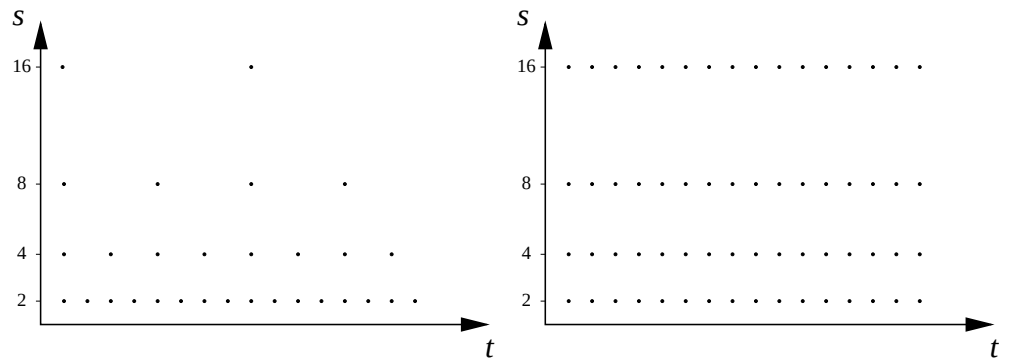
The wavelet transform (WT) is essentially a measure of the degree of similarity between the signal and the set of scaled and translated wavelet atoms. This similarity is quantified in what is known as the *wavelet coefficient* and is computed as the inner product (or convolution) between the analysing wavelet and the signal. The wavelet coefficient at scale s and position τ, computed with respect to the wavelet $\psi_{s,\tau}(t)$, is defined as:

$$W_s(\tau) = x * \psi_{s,\tau} = \frac{1}{\sqrt{s}} \int_{-\infty}^{\infty} x(t)\psi^* \left(\frac{t-\tau}{s} \right) dt, \qquad s, \tau \in \mathbb{R} \tag{5.6}$$

where $\psi^*(t)$ is the complex conjugate of the analysing wavelet function. Intuitively, the WT calculates the wavelet coefficient for the smallest scale at the earliest possible time point ($\tau = t_0$). The wavelet is then shifted along the time axis by τ and the wavelet coefficient is re-calculated. This is repeated until the whole signal has been covered. The wavelet is then scaled (dilated) and the whole process is repeated for all scales. This process can be reversed in what is known as the *inverse* WT, i.e. the original signal $x(t)$ can be reconstructed from the wavelet coefficients. The admissibility condition of the wavelet function ensures that the signal can be perfectly reconstructed, i.e. there is no loss of information in the transform process. The inverse WT is defined as follows:

$$x(t) = \frac{1}{C_\psi} \int_{-\infty}^{\infty} \int_{0}^{\infty} W_{s,\tau} \psi_{s,\tau}(t) \frac{ds d\tau}{s^2} \tag{5.7}$$

In order to implement the WT, it is necessary to define the range of possible scales and translation. Different types of WTs are characterised by the range of the scales



(a) DWT (b) UWT

Figure 5.4: Sampling points of the discrete wavelet transform (DWT) and the undecimated wavelet transform (UWT) in the time-scale plane.

and translates used. The most commonly used transforms are the *continuous*, *discrete* and *undecimated* (or stationary) wavelet transform. The continuous wavelet transform (CWT) is defined for all positive scales $s \in \mathbb{R}^+$ and all translation $\tau \in \mathbb{R}$. However, in practice, the CWT computes wavelet coefficients at each sampling interval and the scale is discretised logarithmically, with the upper bound of f_s limited by the Nyquist frequency [202]. The discrete wavelet transform (DWT) employs *dyadic*[1] scales, where the scale parameter is restricted to the range $s = 2^k,\ k \in \mathbb{Z}$. Similarly, for a given k, the translation parameter is restricted to $\tau = 2^k l,\ l \in \mathbb{Z}$. This ensures that wavelet atoms are mutually orthogonal [197]. The undecimated wavelet transform (UWT) restricts the scale parameter to the dyadic range $s = 2^k,\ k \in \mathbb{Z}$, but the translation parameter is allowed to take on any value, i.e. $\tau \in \mathbb{R}$.

Since the DWT and UWT utilise a subset of scales and translates, it is possible to view these transforms as a subsampled version of the CWT. Figure 5.4 shows the "sampling points" of the DWT and the UWT for a discrete signal at scales $2^k,\ k = 1, \ldots, 4$. At high scales (low frequencies), DWT wavelet coefficients are computed less frequently along the time axis, as the wavelet atoms have large support in the time domain and therefore are translated at longer intervals to avoid overlap. Conversely, at low scales (high frequencies), DWT wavelet coefficients are computed more frequently. UWT wavelet coefficients, on the other hand, are calculated for all dyadic scales at each sample point.

In practice, wavelet coefficients are only calculated for a subset of scales, where the maximum upper bound of the scaling parameter range ($s_{\max} = 2^{k_{\max}}$) is limited by the length of the signal. However, in order to ensure that the resulting set of analysis wavelets

[1]Based on the power of two

remains complete, it is necessary to define a *scaling* function $\phi(t)$ that will provide information corresponding to the set of wavelet coefficients at scales greater than $s_{\max}$ [198]. Therefore, the signal is decomposed using the wavelet function up to the maximum scale and the corresponding scaling function at this particular maximum scale, i.e.

$$W_s(\tau) = \frac{1}{\sqrt{2^k}} \int_{-\infty}^{+\infty} x(t)\psi^* \left(\frac{t-\tau}{2^k} \right) dt, \qquad k < k_{\max}, \tau \in \mathbb{R} \tag{5.8}$$

$$V_s(\tau) = \frac{1}{\sqrt{2^k}} \int_{-\infty}^{+\infty} x(t)\phi^* \left(\frac{t-\tau}{2^k} \right) dt, \qquad k = k_{\max}, \tau \in \mathbb{R} \tag{5.9}$$

The different WT methods have properties that suit some applications better than others, be it signal compression, noise filtering or time-frequency encoding. The major disadvantage of the CWT, in the context of ECG analysis, is that it is a highly redundant representation of the signal, as the analysing wavelets do not form an orthogonal basis. Therefore, not only is the CWT computationally expensive but the resulting wavelet coefficients are strongly correlated across neighbouring scales and translations. The DWT computes wavelet coefficients for mutually orthogonal wavelet atoms, i.e. there is no overlap between neighbouring wavelet atoms. However, this implies that wavelet coefficients are not calculated for the dyadic scales at each time sample, i.e. the vector of wavelet coefficients varies for each time sample. This is suitable for data compression purposes but unsuitable for a probabilistic ECG segmentation approach, where a constant-length feature vectors for each time sample is required [203]. In addition, DWT wavelet coefficients are not translation-invariant [204]. Translation-invariance refers to the property that when a signal is translated, "its numerical descriptors should be translated but not modified" [198]. In probabilistic approaches, translation-invariance improves the performance of model inference where a trained model is used for inference on an ECG signal that could be translated with respect to the training data set.

The UWT can be seen as a compromise between the continuous and discrete wavelet transforms, in that it also uses a dyadic scale range, which reduces spectral correlation between neighbouring time-frequency atoms, but calculates a wavelet coefficient for the dyadic scales at every time point required, thus ensuring a fixed-length vector of wavelet coefficients. Furthermore, the UWT is translation-invariant, such that a (circular) time-shift of the function will result in identical wavelet coefficients translated by the same amount [198]. Therefore, the UWT provides an adequate trade-off between temporal and spectral resolution for the purposes of ECG segmentation, de-nosing and R-peak

detection [205–207]. Lastly, the computational efficiency of the UWT filter bank algorithm (described in Appendix A.1) ensures that the computational costs are not excessive.

Practical considerations for wavelet analysis of ECG signals

In order to use wavelet analysis for ECG encoding and segmentation a number of practical considerations need to be addressed. The primary consideration is the choice of wavelet function. Additional concerns include boundary conditions and the choice of maximum scale $s_{\max}$. Finally, for waveform feature delineation, phase correction of wavelet coefficients needs to be considered. The choice of wavelet function depends on the particular application at hand, where a number of competing factors need to be balanced in order to maximise performance [208].

1. *Width*: the width of the wavelet is a trade-off between the resolution in the time domain and resolution in the frequency domain.

2. *Shape*: the wavelet function should reflect the types of features present in the signal.

3. *Complex or real*: a complex wavelet function will provide both amplitude and phase information and is better adapted for capturing oscillatory behaviour, whereas real wavelet functions return real coefficients, which is sufficient for peaks and discontinuity detection.

4. *Orthogonal or non-orthogonal*: orthogonal wavelets ensure that the analysis blocks are discrete and that there is no overlap between adjacent times, whereas non-orthogonal analysis is redundant and adjacent wavelet coefficients are correlated.

The circular filtering of the WT results in boundary effects on the wavelet coefficients. Typically, the signal is assumed periodic with a period equal to the length of the signal (N). However, this approach can be problematic if the absolute difference between the first and last samples is larger than the typical absolute difference between any two adjacent samples. Another approach is to use *reflective* boundary conditions, where the sample values are reflected about the boundary of the signal, i.e. $x(N+i) = x(N-i),\ i \in \mathbb{Z}$. This approach tends to produce smoother wavelet coefficients at the signal boundary [197]. Furthermore, the "width" of the boundary effects will increase with scale. Therefore, the maximum scale should take into account the length of the signal. One approach is to

select the maximum scale such that the length of the filters at this scale, $M_{s_{\max}}$, is less than or equal to the length of the signal, i.e. $M_{s_{\max}} \leq N \leq M_{s_{\max}+1}$ [197].

The discrete and undecimated WT can be computed in an efficient manner using a filter bank structure. A detailed description of the filter bank algorithm is provided in Appendix A.1. The algorithm is based on a class of filters known as *conjugate mirror filters* (CMFs[2]) that are specially designed pairs of high and low-pass finite impulse responses (FIR) filters. CMFs are lossless filters that can decompose a signal into a set of representative coefficients and perfectly reconstruct the signal from these coefficients, i.e. no part of the signal is lost in the process.

As a result of the filtering process, the resulting wavelet coefficients need to be corrected for the resulting phase shift in order to provide an accurate temporal representation [197]. The phase response is dependent on the scale because, as the length of the filters increases, the corresponding coefficients are time-shifted by a greater degree. Phase correction for a linear phase response is trivial. However, most wavelet functions and their associated filters have a non-linear phase response. In fact, the linearity of the phase response for a given wavelet function is another factor to consider in choosing between different wavelet functions. Walden and Contreras proposed a method of linearising the phase response via detailed analysis of the phase response of the effective band-pass filter at each scale [209]. Another, more practical approach proposed by Nason et al. empirically estimates the phase response of the effective band-pass at each level and applies phase correction based on this estimate [210].

5.1.2 ECG de-noising

The frequency content of a typical, resting ECG recording is within the range of 1.22 to 90 Hz (-40 db) [211]. However, the ECG is often corrupted by noise and physiological artefacts that overlap with the frequency range of the ECG. Figure 5.5 shows five examples of common noise sources and artefacts found in the surface ECG, namely:

- **Mains interference:** capacitance effects between main power supply (50 or 60 Hz) and the ECG recording equipment
- **Muscle artefact:** contraction of skeletal muscle under the ECG electrode

[2]CMFs are closely related to quadrature mirror filters (QMFs), however QMFs generally do not have a finite impulse response [198].

- **Movement artefact:** movement of the subject or electrode during ECG recording changing electrode contact impedance
- **Baseline wander:** change in electrode contact impedance due to increased perspiration and breathing-related body movements
- **Electrode noise:** a sharp change in electrode contact impedance, which results in a spike in the trace coming from that lead

Numerous digital filtering techniques have been developed to address the different types of characteristic noise typically seen in ECG recordings. For instance, notch filtering effectively removes mains interference, while low-pass filtering can often reduce muscle artefact. However, digital filtering techniques suffer from a number of drawbacks. Firstly, to design high-pass FIR filters with a cut-off frequency of 0.5 Hz that would not distort waveform features with similar frequency content, would require a filter with a large number of coefficients that would produce a long impulse response. Infinite impulse response (IIR) filters would be more computationally efficient, but have an even longer (infinite) impulse response and distort the waveform shape because of their non-linear phase response.

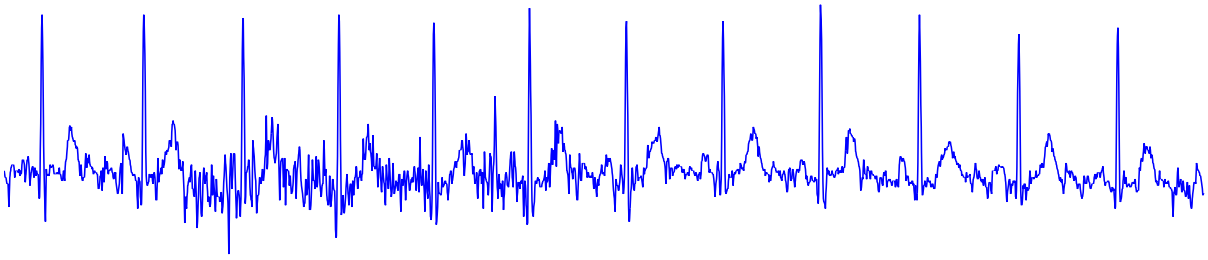
An additional problem is that the frequency components of the baseline wander, movement artefact and characteristic ECG features, such as the T-wave, can overlap, making the problem of removing noise interferences without distorting ECG feature morphology non-trivial [212]. As a result, linear time varying approaches have been proposed; such as cubic spline interpolation for baseline wander removal [213] and adaptive filtering methods, which estimate the cut-off frequencies based on heart rate and baseline level [214,215].

Wavelet de-noising

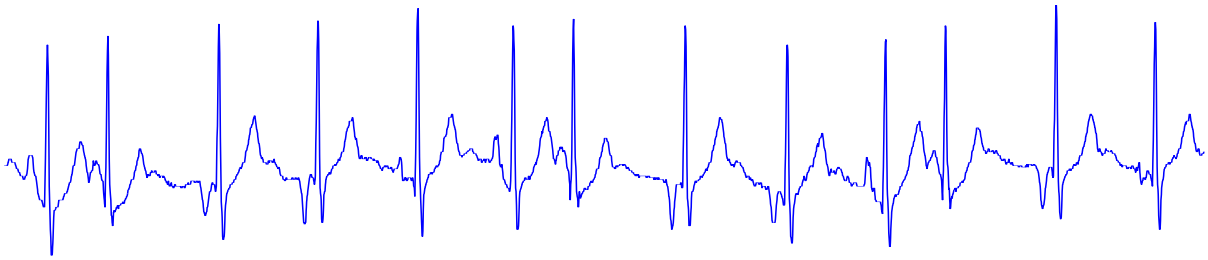
The wavelet de-noising paradigm describes how noisy data is transformed into the wavelet domain, how to apply thresholding to the wavelet coefficients at each scale to suppress those coefficients smaller than a certain amplitude, then how to transform back into the time domain. In this way it is possible to isolate and remove those wavelet coefficients judged to be noisy in different frequency bands (scales). Wavelet de-noising has been proposed using both DWT and UWT [204, 216]. However, in the presence of sharp signal discontinuities, the inverse DWT exhibits ripples in the reconstructed signal. The



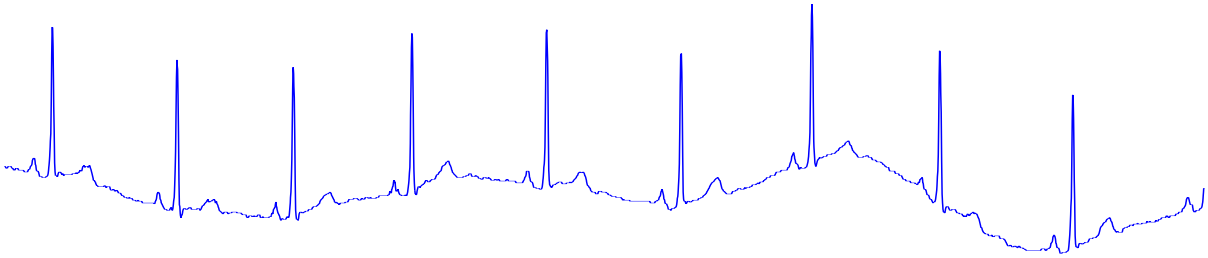
(a) Mains interference



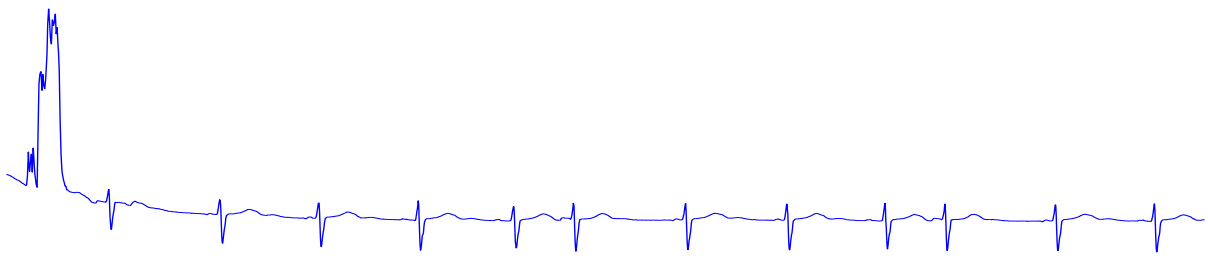
(b) Muscle artefact



(c) Movement artefact



(d) Baseline wander



(e) Electrode noise

Figure 5.5: Examples of different types of ECG noise

undecimated or stationary WT, on the other hand, effectively averages out the effect of discontinuities and therefore improves the performance of wavelet-based de-noising strategies [204].

Standard wavelet coefficient thresholding techniques come in two varieties, *hard* or *soft* thresholding. Soft thresholding subtracts the threshold from the wavelet coefficients, i.e.

$$W_s(t) = \begin{cases} sgn(W_s(t)) \cdot (|W_s(t)| - \gamma_s) & \text{if } |W_s(t)| > \gamma_s \\ 0 & \text{otherwise} \end{cases}, \tag{5.10}$$

where γ_s is the applied threshold for scale s [216]. Hard thresholding on the other hand, suppresses wavelet coefficients less than the applied threshold, i.e. $W_s(t) = 0$ if $|W_s(t)| \leq \gamma_s$. Obviously, a key factor in the performance of wavelet de-noising is the estimation of the applied threshold. Tikkanen et al. investigated the performance of four different threshold estimation procedures, namely *sure*, *heuristic sure*, *fixthres* and *minimax*, in de-noising ECG signals with various simulated noise sources [206]. These procedures were compared by applying the different threshold estimations in both hard and soft threshold de-noising methods and comparing optimised error measures and visual inspection of the de-noised ECG and the error signal [206]. Tikkanen et al. concluded that different threshold estimation procedures were optimal for different noise conditions. However, the *fixthres* estimation procedure with hard thresholding performed consistently well for the different types of noise.

In other work on wavelet de-noising of the ECG, Mozaffary and Tinati proposed a baseline wander removal algorithm based on wavelet binary tree decomposition [217]. The *energy* at each node in the wavelet decomposition tree is estimated and analysed to identify the frequency band of the baseline wander and reconstruct the original signal using the inverse WT, having removed the wavelet coefficients responsible for the baseline wander interference. Other work by Park et al. [218] and Zhang et al. [219] has used adaptive WT methods to minimise distortion of characteristic waveform features.

5.2 Interval Analysis

Automated interval analysis of the surface ECG waveform was first used in the early 1960s for arrhythmia analysis [220]. Since then numerous methods have been proposed for QRS detection and ECG waveform feature delineation. The algorithms that underlie these methods can be loosely defined as *rule-based* approaches, *model-based* approaches or

a combination thereof. Most rule-based ECG delineation algorithms have several stages. Firstly, the locations of the R-peaks are determined as the QRS complex is the most distinctive waveform feature of the ECG. The next stage is to search forwards and backwards from each R-peak to determine the waveform feature boundaries (i.e. Q_{on}, J and T_{off}). An alternative approach to rule-based methods is to construct a probabilistic model of the ECG and use the model to infer fiducial points in the ECG signal. Both threshold-based and probabilistic ECG segmentation methods are discussed in more detail below.

5.2.1 R-peak detection

Automated QRS detection has been an active research topic for over 30 years. Many methods have been proposed to identify the R-peak of the QRS complex. Köhler et al. present a comprehensive quantitative review of 27 published R-peak detection algorithms [221]. The methods can be loosely grouped in three main categories: approaches based on signal derivatives and digital filters, wavelet-based QRS detection and probabilistic methods. The methods vary in performance and complexity, although digital filtering and amplitude-based methods have become the most widely used due to their simplicity and low computational complexity. Wavelet-based methods were shown to perform well but were categorised as one of the more computationally intensive approaches.

In 1990, Friesen et al. compared the performance of nine algorithms based on signal derivatives and digital filters, using idealised test data corrupted by nine different noise conditions [212]. The results suggested that the algorithms based on amplitude and slope are most immune to muscle artefact. However, these algorithms are sensitive to baseline wander. Friesen et al. suggest that QRS detectors should combine amplitude and slope based peak detectors with some form of filtering to remove baseline fluctuations. Two methods that adopt this approach and are widely implemented are the adaptive QRS detector [222, 223] and the Li et al. multiscale wavelet analysis R-peak detector [224].

Adaptive QRS detector

In 1985, Sörnmo et al. and Pan and Tompkins independently developed a QRS detector that incorporated band-pass filtering with a peak energy-amplitude detection algorithm [222, 223]. Figure 5.6 shows a flowchart of the algorithm. It is divided into two stages, a preprocessing or feature extraction stage, followed by a decision stage. The preprocessing stage uses digital filtering techniques and non-linear operations to amplify the

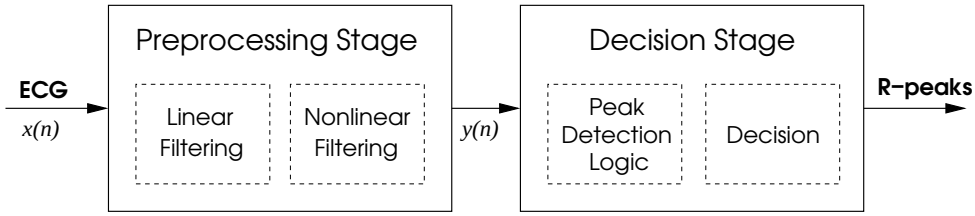


Figure 5.6: Flow chart of QRS detection algorithm structure [222, 223].

QRS complex in the ECG. The decision stage initialises thresholds using peak detection heuristics, which are then used to detect R-peaks in the feature signal.

The frequency components of a "typical" QRS complex lie within the range 10 to 25 Hz [221]. The aim of the preprocessing stage is to isolate those components and amplify the signal to enable robust amplitude-based peak detection. The signal is range normalised (± 1.0) before using a cascade of low- and high-pass filters to achieve a 3 dB pass-band from 8 to 16 Hz. This is to avoid significant overlap with other waveform features, such as the P or T-wave, and high-frequency noise interference. The filtered signal is then differentiated and squared before applying a sliding window integrator. The squaring processes amplifies the gradient information captured during the derivative stage. The width of the moving average window was chosen to be roughly the same width of a typical QRS complex.

The decision stage is divided into two phases, namely a learning phase, and a detection phase. The learning phase initialises detection thresholds and average RR-interval values. The second phase detects peaks in the preprocessed signal. The R-peak detection algorithm includes strategies, such as ignoring events during a refractory period (200 ms after the R-peak) and searching back using a lower threshold if no events are detected within 1.6 times the average RR-interval, to improve the performance of the algorithm. Pan and Tompkins [223] quote a sensitivity of 99.76% and a positive predictive value of 99.56% using the MIT/BIH arrhythmia database [225].

Digital filtering and amplitude-based QRS detectors, of which the Pan and Tompkins algorithm is arguably the most widely used, suffer from several limitations. Firstly, the algorithm fails to deal properly with particularly large T-wave or P-waves, which produce feature signal peaks that are mistaken for QRS complexes. Secondly, the algorithm only partially deals with baseline wander or baseline drift, which occur relatively frequently in Holter ECG recordings. A more robust approach to R-peak detection is based on the wavelet transform.

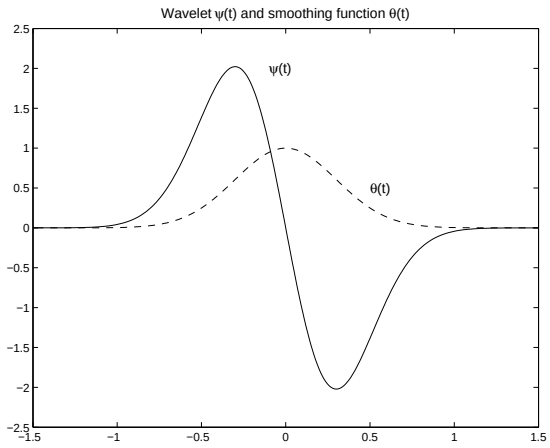


Figure 5.7: Wavelet function $\psi(t)$ defined as the first-order derivative a cubic spline fit of Gaussian function $\theta(t)$.

Wavelet-based R-peak detection

Several wavelet based QRS detectors have been proposed in recent years. The majority of the previous work is based on an edge-detection method proposed by Mallat and Zhong using multiscale analysis of wavelet coefficients [226]. The method relies on the use of a wavelet function derived from the first-order derivative of a smoothing function, i.e.:

$$\psi(t) = \frac{d\theta(t)}{dt}, \tag{5.11}$$

where $\psi(t)$ is the wavelet function and $\theta(t)$ is the smoothing function. The UWT of a signal can then be expressed as follows:

$$W_s(\tau) = x * \psi_{s,\tau} = x * \left(\frac{1}{s} \frac{d\theta_s}{dt} \right) = \frac{1}{s} \frac{d}{dt} \left(x * \theta_s \right). \tag{5.12}$$

As shown in Equation 5.12, the wavelet coefficients $W_s(\tau)$ are equivalent to the first derivative of the signal smoothed at scale s. In the special case of $\theta(t)$ being a Gaussian function, the extrema of W_s correspond to sharp variations in $x * \theta_s(t)$ and the detection of these extrema is identical to the method used in Canny edge detection [227]. Figure 5.7 shows the wavelet function $\psi(t)$ and the smoothing function $\theta(t)$ proposed by Mallat and Zhong [226]. The wavelet function is defined as the first-order derivative of a cubic spline[3] approximation of a Gaussian function with unit energy and zero mean.

Li et al. were the first to use the multiscale wavelet analysis method proposed by Mallat and Zhong [226] for identifying R-peaks [224]. Several other groups have extended the original work by Li et al. [224]. Sahambi et al. showed that the algorithm worked well in

[3]Piecewise polynomials used to approximate the best-fit curve to a set of data points.

the presence of baseline wander and high-frequency noise [228]. Martinez et al. generalised the algorithm proposed by Li et al. to identify the onset and offset points of the P-wave, QRS complex and T-wave [207]. Legarreta et al. extended the work by Li et al. by using the CWT instead of the DWT to increase the time-frequency resolution of the wavelet representation, allowing a more robust detection of the R-peak in the presence of noise [229].

The basic algorithm is based on the fact that sharp discontinuities, such as the R-peak, correspond to a zero-crossing in the wavelet coefficients. The algorithm defines *modulus maxima lines* as being lines connecting local extrema in wavelet coefficients across different scales. The majority of the QRS frequency content is captured in the scales 2^3 and 2^4. Therefore, the algorithm starts by identifying modulus maxima above an adaptive threshold in wavelet coefficients at scale 2^4. The modulus maxima lines are then determined by tracking these local extrema from 2^4 down to 2^1. This is achieved by searching for local extrema above adaptive thresholds "near" the location of the peak in the previous scale. The region in which local extrema are sought is defined as 10 ms on either side of the peak location at the larger scale.

Isolated and redundant modulus maxima lines are discarded from the set of modulus maxima lines. More specifically, any negative minimum peak identified at scale 2^1 that is 120 ms from the nearest positive maximum peak, is deemed to be an isolated peak and discarded. Similarly, if there are more than one negative minima within a 120 ms window, heuristics are employed to determine the most significant negative minimum and the rest are labelled redundant [207]. Finally, an R-peak is identified as the zero-crossing between a pair of negative and positive local extrema at scale 2^1. Once an R-peak is identified a refractory period is imposed so that no further R-peaks are detected within 200 ms of an R-peak. Similarly, if no R-peak is identified within 1.6 times the current RR-interval average, thresholds are adjusted and the same period is re-examined to identify the "missing" heart-beat.

5.2.2 Waveform feature delineation

Feature delineation is important for determining ECG intervals of clinical significance, such as the QT interval. In addition, ECG morphology analysis requires that specific segments in the ECG waveform, such as the JT segment, can be identified and extracted

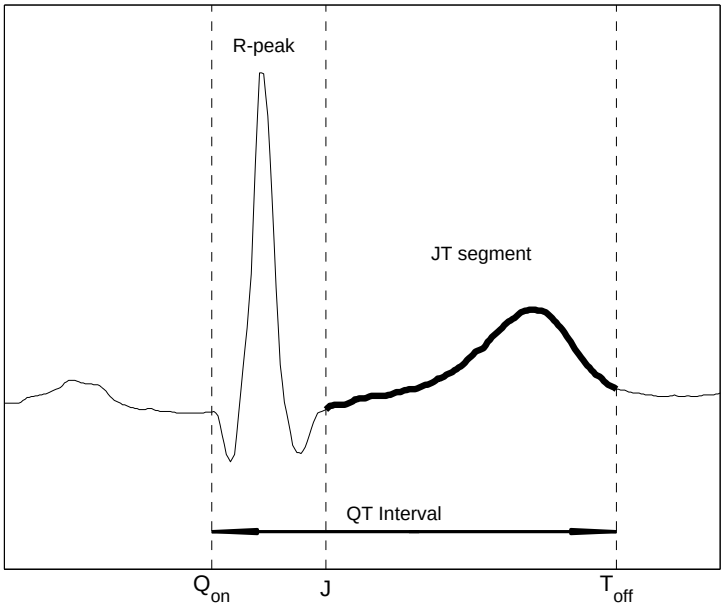


Figure 5.8: A typical ECG waveform with the critical waveform boundaries identified, namely Q_{on}, J and T_{off}. The JT segment, between J and T_{off}, is shown in bold. The QT interval is also identified by the double-arrow between Q_{on} and T_{off}.

from the signal. Figure 5.8 illustrates the fiducial points, intervals and signal segments that are important for characterising ventricular repolarisation using the surface ECG, including Q_{on}, J and T_{off}, QT interval and the JT segment, between J and T_{off}.

Early automated feature delineation algorithms were largely threshold-based, i.e. identifying the waveform feature boundary as the point where the signal or its derivative crosses a predetermined threshold [230]. A good example is the the *tangent* or *slope-intercept* method, first defined by Lepeschkin and Surawicz in 1952 [194]. It defines the offset of the T-wave as the intersection of the tangent line to the ECG after T-peak with the maximum downward gradient and the isoelectric line. In practice, the isoelectric line is defined using the portion of the signal after the T-wave and before the next P-wave [230]. However, the tangent method is sensitive to the amplitude of the T-wave because large T-waves result in a steeper tangent line that tends to intersect the isoelectric line before the true end of the T-wave. In the light of this, Xue and Reddy proposed a non-linear "correction" scheme based on the amplitude of the T-wave [230].

A number of threshold-based ECG delineation algorithms have been published. One popular algorithm is "ECGPUWAVE", which applies adaptive thresholds to the the low-pass derivative of a band-pass filtered ECG signal in order to determine the R-peaks and waveform feature boundaries in multi-lead ECG signals [231]. The waveform feature delineation relies on a differentiated threshold method whereby the threshold for deter-

mining T_{off} is defined as the peak amplitude of the differentiated ECG signal identifying the presence of a T-wave divided by a scaling factor, which was determined experimentally and is dependent on the peak value normalised by the maximum QRS slope.

The accuracy and performance of threshold-based segmentation algorithms has improved significantly as new methods of signal encoding, such as the wavelet transform, have increased the robustness of the segmentation algorithms to noise and other artefacts [207]. However, threshold-based algorithms are ultimately sensitive to the thresholds used in the detection stage. Template matching and dynamic time warping approaches to ECG segmentation suffer a similar fate, in that the performance of the algorithm is sensitive to the definition of one or more templates for the given waveform feature [232]. In order to overcome this problem, adaptive thresholds and templates were proposed, yet this raises the secondary problem of how adaptive the system should be. Probabilistic approaches, including neural networks and hidden Markov models, can overcome these difficulties to some degree [233]. The machine learning paradigm describes a process whereby a network or model is trained in some manner on a training data set and then used to infer fiducial points in new ECG signals. The advantage of this *data-driven* approach is that the performance of the system is no longer dependent on rule-based algorithms and thresholds, instead it is limited by the *quality* of the training data set.

HMM segmentation

Hidden Markov models (HMM) have been found to be well suited to segmenting the ECG signal as they offer an effective balance between descriptive modelling power, efficient inference and parameter learning [234]. In this instance, the ECG is viewed as the product of a *cyclostationary* stochastic process[4] where a *sequence* of characteristic waveform feature distributions are periodically called into action by the corresponding cardiac state. The sequence of waveform features observed in the ECG arguably obeys the Markov property in that the conditional probability distribution of future waveform features (or states) depends only upon the present state and not on any past states.

An HMM describes the statistical relationship between an observed sequence and a hidden state sequence, S. The HMM is governed by three parameters, namely an initial state distribution ($\boldsymbol{\pi}$), a state transition probability matrix ($\mathbf{A}$) and an observation density

[4]Cyclostationary implies that the stochastic dynamics of the system are made up of a combination of stationary probability distributions which are cycled through periodically.

model $\{\mathbf{B}_k|b_1, b_2, \ldots, b_K\}$ for each state K. In ECG segmentation applications using HMMs, the two most commonly used observation models are the Gaussian distribution and the Gaussian mixture model (GMM) [234, 235]. A GMM is a linear combination of M Gaussian functions such that the probability density can be described as follows:

$$p(x) = \sum_{j=1}^{M} P(j)p(x \mid j), \tag{5.13}$$

where $P(j)$ is the *mixing coefficient* and $p(x|j)$ is the normalised component density function. GMMs are particularly effective in modelling multi-modal data [236], as is the case for the ECG with significant waveform feature variation between patients. The complete set of HMM parameters is then given by $\lambda = \{\mathbf{A}, \boldsymbol{\pi}, \mathbf{B}\}$. Appendix B.1 describes the learning procedures and the well known Viterbi algorithm that is used to infer the optimal hidden state sequence for a given set of of observations.

HMMs have been applied to the ECG analysis in three main areas, namely beat detection, segmentation and classification. The first use of hidden Markov models for ECG analysis was a beat detection and classification system proposed by Coast et al. in 1990 [237]. Figure 5.9(a) illustrates the 7 state *left-right* HMM proposed by Coast et al. to identify *normal* beats. Two additional HMMs were developed to describe supraventricular and ventricular arrhythmias. Beats were then classified according to which of the three HMMs had the largest data likelihood, i.e. $\text{argmax}_m\, P(O \mid \lambda_m)$. The HMMs were trained using the Baum-Welch algorithm (see Appendix B.1.1) using band-pass filtered ECG signals. An approach to ECG beat classification was independently proposed by Koski [238]. The Baum-Welch algorithm was used to train the parameters of a 25-state HMM in an unsupervised manner. The approach used syntactic pattern recognition to encode the ECG by identifying the set of d primitive patterns. The observations were encoded using a d-dimensional Gaussian mixture model. Clavier and Boucher extended this work to include gradient information from the ECG waveform to improve the performance of Koski's model [239]. The approach used 12 ECG states that modelled the up and down slopes of the characteristic waveform features (P-wave, QRS complex and T-wave) as seen in Figure 5.9(b).

The application of HMMs to ECG segmentation enjoyed limited success due to the difficulties of encoding the signal and modelling the state density models on the observations. Graja and Boucher were the first to combine wavelet analysis with HMMs for

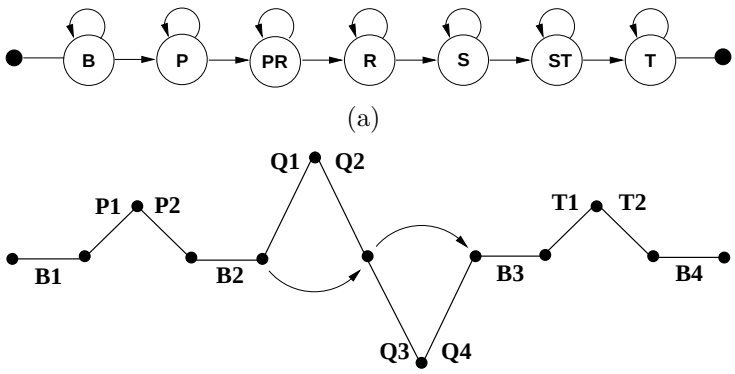


Figure 5.9: HMMs for ECG segmentation: (a) a 7 state left-right HMM of a normal beat [237], (b) a 12 state HMM of a normal beat [239]. The state transitions are *left-right* except for B2-Q3 and Q2-B3 (as indicated by the arrows) to model uniphase QRS complexes.

ECG segmentation [240]. The method used a hidden Markov tree model to identify the onset and offset points of the P-wave, QRS complex and T-wave. More recently, Andreão et al. proposed a HMM-based ECG segmentation and classification algorithm using the CWT [241]. Figure 5.10 illustrates the HMM structure used by the authors. The proposed method used multiple HMMs, with different HMMs employed to model different ECG morphologies. Each state was modelled by a left-to-right HMM chain with a different number of states (seen in Figure 5.10). The number of states per waveform feature was determined by trading off performance with time complexity resulting in 3 states each for baseline, P-wave and QRS complex models, 2 states each for PQ and ST segment models and 6 states for the T-wave state. A single, multi-variate Gaussian density model was chosen to model the observations associated with each state. The observation vector consisted of the wavelet coefficients at scales 2^2, 2^3 and 2^4. The HMMs were trained in an unsupervised manner using the Baum-Welch algorithm. HMM likelihood clustering, widely used in speech recognition, was implemented to identify the optimal number of different HMM models per state [242]. This enabled different waveform morphologies to be modelled by different HMMs. Four HMMs were found for the QRS complex, two HMMs for each of the other waveforms and one HMM for the baseline model. The HMM inference procedure used the one-pass algorithm [243] to reduce the time complexity of the ECG segmentation. The model was implemented in two dimensions: time and level, where the level is associated with the waveform model. In other words, level 1 consisted of the baseline HMM, level 2 consisted of the two P-wave HMMs and so forth. Therefore,

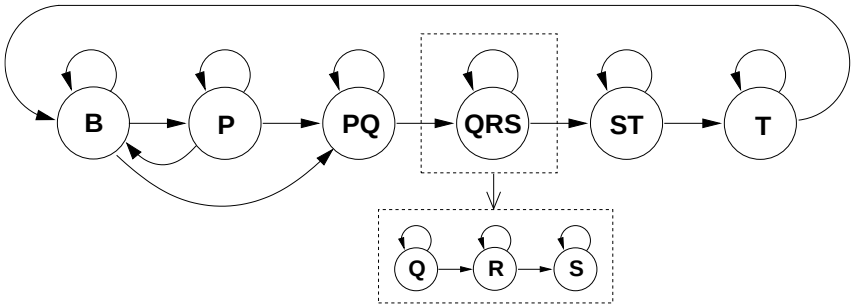


Figure 5.10: HMM structure used for ECG segmentation and beat classification proposed by Andreão et al. [244].

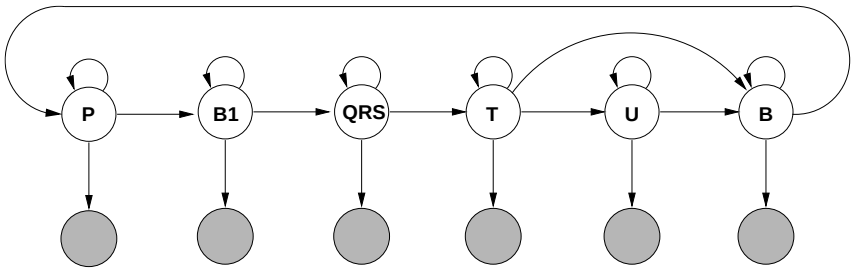


Figure 5.11: The 6-state HMM proposed by Hughes et al. for automated QT interval measurement [245]. The HMM states are states are indicated by the clear nodes, whereas the shaded node indicate the observation density models.

in order to transfer from one level l to the next level $l+1$, the model with the greatest data likelihood was chosen from level l to determine the appropriate state transition.

A limitation of the approaches proposed by Coast et al. a [237] and Andreão et al. [235] is the use of unsupervised learning to estimate the HMM parameters. Although unsupervised learning is the most common approach in speech recognition applications, the resulting model may not produce ECG segmentations that are consistent with those of expert analysts. In our research group, Hughes et al. developed an HMM segmentation algorithm that relied on expertly annotated ECG data to train the HMM in a supervised manner [205, 245]. Figure 5.11 illustrates the 6-state HMM used to segment the ECG. The ECG signal was encoded using the UWT. GMMs were used as the state observations density models, with the optimal number of components computed using a maximum length description criterion algorithm proposed by Figueiredo and Jain [246].

Hughes et al. extended their initial work by including state *duration constraints* to avoid double-beat segmentations [234]. In this scenario, the HMM inaccurately infers a complete beat, often only 50 ms in length, prior to the onset of the next beat. Hughes et al. proposed a duration constraint ($\tilde{d}_i$) that specified the minimum expected duration for each state in the model and was determined during the supervised learning procedure as

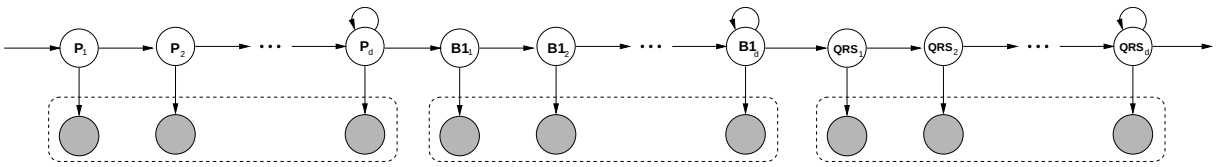


Figure 5.12: A HMM with duration constraints for ECG segmentation [247]. The observation models grouped together by the dotted line are "tied". In other words, the same observation model is used by all the tied states.

a percentage of the minimum state duration [243]. Figure 5.12 illustrates how a portion of the HMM in Figure 5.11 is augmented to satisfy its duration constraints. The HMM is augmented by inserting $\tilde{d}_i - 1$ additional *states* directly preceding each original state i. Each additional state has a self-transition probability of zero and a state transition probability of one. In addition, their observation densities are *tied* to the original state. Therefore, the $\tilde{d}_i - 1$ additional states form a simple left-to-right Markov chain, thus ensuring that each state has a minimum duration of $\tilde{d}_i$. Although duration constraints significantly increase the number of states in the HMM, the time complexity of the Viterbi algorithm is in fact given by $\mathcal{O}(TK\bar{K})$, where K is the number of states and $\bar{K}$ is the average state connectivity. Therefore, as the augmented states are left-to-right chains, the overall time complexity only increases approximately linearly with the number of additional states. To reduce the time complexity and performance of the HMM segmentation approach proposed by Hughes [247], Strachan and Hughes et al. proposed two separate HMMs, which only process sub-segments of the ECG waveform to detect $\mathrm{Q_{on}}$, J and $\mathrm{T_{off}}$ [248].

Confidence measures

A significant advantage of the probabilistic approach to ECG segmentation is that the *suitability of measurement* can be determined using the observation posterior probabilities. The suitability of measurement is important to consider as some ECG waveforms cannot reliably be used for manual or automated measurement, as a result of abnormal morphology, significant artefact or noise. As noted by Fenichel et al.,"Some ECGs are technically defective (with muscle artefact, misplaced leads, or other problems), and one should not attempt to derive useful data from them." [126]. Standard automated ECG segmentation algorithms are not able to distinguish between reliable measurements and those made on unsuitable ECG recordings.

Probabilistic methods can define the suitability of measurement by quantifying the

similarity of the ECG signal being analysed to the ECG recordings in the training data set. The ECG segmentations (for each heart beat) can then be accompanied with an appropriate *confidence measure*. This technique is of particular significance when the probabilistic model is trained using ECG recordings with expert measurements. Thus, the confidence measure captures the *suitability* of the ECG recording being analysed, as defined by a collection of expert analysts, by identifying ECG recordings with noise as well as unusual waveform morphologies. More informally, the confidence measure can be viewed as a measure of "normality" of the observed ECG sequence with respect to the ECG waveforms on which the HMM was trained. However, it must be noted in this respect that waveform morphologies that are not included in the training data set (eg. U-waves), would likely result in low confidence values.

In classification problems, the confidence measure is derived from the magnitude of the posterior probabilities of the relative classes. In the instance of a HMM with trained model parameters $\lambda = \{\mathbf{A}, \boldsymbol{\pi}, \mathbf{B}\}$, the posterior probability is defined as:

$$P(O_{1:T} \mid \lambda) = \sum_{S} P(O_{1:T}, S \mid \lambda) \tag{5.14}$$

$$= \sum_{S} P(S|\lambda) \cdot P(O_{1:T} \mid S, \lambda), \tag{5.15}$$

where S denotes all possible state sequences. Obviously, calculating Equation 5.15 for *all* possible state sequences is unfeasible for long signals and large number of HMM states. Therefore, it is common practice to estimate the posterior probability, relying on certain assumptions and using approximation methods [249].

One approach is to estimate the posterior probability as the joint probability of the observations *and* state sequence given the model, i.e. $p(O, S|\lambda)$. Therefore, for an observation sequence O and optimal state sequence S^* (as determined by the Viterbi algorithm), the joint likelihood can be computed as:

$$\begin{aligned} p(O_{1:T}S^*_{1:T} \mid \lambda) &= P(s^*_1) \prod_{t=1}^{T-1} P(s^*_{t+1} \mid s^*_t) \prod_{t=1}^{T} p(O_t \mid s^*_t) \\ &= \pi_{s^*_1} \prod_{t=1}^{T-1} a_{s^*_t s^*_{t+1}} \prod_{t=1}^{T} b_{s^*_t}(O_t) \end{aligned} \tag{5.16}$$

In practice, it is preferable to calculate the logarithm of the joint likelihood to avoid computational issues, i.e.:

$$\log p(O_{1:T}S^*_{1:T} \mid \lambda) = \log \pi_{s^*_1} + \sum_{t=1}^{T-1} \log a_{s^*_t s^*_{t+1}} + \sum_{t=1}^{T} \log b_{s^*_t}(O_t). \tag{5.17}$$

However, the contribution of the state transition probability, compared with the observation density, to the overall joint log likelihood in Equation 5.17 is negligible due to the fact that state transition probabilities are bounded to the range $[0, 1]$, whereas the observation *densities* span the range $[0, \infty)$. As a result, the joint log likelihood is dominated by the observation density, which can vary between state observation density models.

The joint log likelihood defined in Equation 5.17 can be calculated for any portion of the observation sequence $t_1 \rightarrow t_2$ provided $t_2 > t_1$. In this way it is possible to derive confidence measures for particular aspects of the ECG. For example, a heart beat confidence measure would be defined from $\mathrm{Q_{on}}$ to $\mathrm{T_{off}}$, whereas a T-wave confidence measure would be defined from the J-point to $\mathrm{T_{off}}$. To use the confidence measure as a standardised measure of confidence, it is necessary to normalise it with respect to segment duration. Hughes et al. used standard regression techniques to fit a linear regression model to the confidence measures in the training set [247]. The linear regression model was used to define the lower confidence bound of 99% level of confidence as the threshold for low confidence segmentations. In addition to the effects of duration on the decision boundary, a maximum and minimum duration weighting was applied to the decision boundary. The weighting function was set to 1.0 from the minimum to the maximum segment duration value and zero otherwise. In order to represent the joint log likelihood as a probability, Hughes proposed using a sigmoid function to normalise the joint log likelihood to the range [0,1] [234]. The sigmoid function was fitted to two points; the mean regression line was set to 0.85 and the lower 99% confidence boundary was set to 0.7.

Validity of HMM assumptions for ECG segmentation

In order to apply HMMs to the ECG for segmentation applications, it is necessary to discuss the various assumptions that are implicit in the application of HMMs and whether HMMs provide a faithful statistical description of the ECG. The Markov property that forms the basis of the HMM is that the probability of occupying a given state at the next time step is only dependent on the state occupied at the current time step, i.e.:

$$P(s_{t+1} \mid s_t, s_{t-1}, s_{t-2}, \ldots) \equiv P(s_{t+1}|s_t) \tag{5.18}$$

In the context of modelling the ECG, the Markov property is justifiably consistent with the cyclostationary nature of the ECG, since a typical sequence of ECG waveform features

takes the form simple left-to-right ordering:

$$\text{P-wave} \longrightarrow \text{QRS complex} \longrightarrow \text{T-wave} \longrightarrow \text{Baseline} \longrightarrow \text{P-wave} \longrightarrow \cdots$$

This simplified view of the ECG sequence does not take ectopic beats, or other cardiac pathologies resulting in unusual ECG features, into account. However, in the context of phase I clinical trials with healthy volunteers, the likelihood of these events is arguably negligible. Higher order HMMs with state transitions that take the n^{th} previous states into account, i.e.:

$$P(s_{t+1} \mid s_t, s_{t-1}, s_{t-2}, \ldots) \equiv P(s_{t+1}|s_t, s_{t-1}, \ldots, s_{t-n}) \tag{5.19}$$

could also be used to consider abnormal ECG waveform sequences.

HMMs assume that the state transition probabilities are time-invariant; thus for any two times t_1 and t_2 we assume that:

$$P(s_{t_1+1} = j \mid s_{t_1} = i) = P(s_{t_2+1} = j \mid s_{t_2} = i) \tag{5.20}$$

The assumption of stationary transition probabilities is justified as the statistics of the ECG state sequence are independent of the time at which the signal is sampled. However, the assumption that the signal samples "generated" by a given state are *independent* and *identically distributed* (i.i.d.) is arguably the most significant limitation in applying HMMs to ECG segmentation, since samples from a given waveform feature *are* dependent on the neighbouring samples. It is these statistical dependencies between successive samples that give rise to the characteristic waveform features.

The UWT of the ECG encodes temporal dependencies into the observation vector of wavelet coefficients. This approach has been found to work well in practice [234,235] and is often used in HMM-based speech recognition systems. In addition, temporal dependencies between observations vectors can be captured using derivative information or "delta-coefficients" [250]. The combination of UWT encoding and derivative features has been found to improve the performance of HMMs for ECG segmentation [234].

5.2.3 Heart-rate correction

As discussed in Section 1.2, the QT interval undergoes heart rate correction so that it can be compared with QT intervals measured at different heart rates. However, as highlighted earlier, population-based QT heart rate correction formulae introduce errors

into the interval analysis due to the high variability between individuals [19]. As a result, a number of individualised heart rate correction approaches have been developed, whereby a suitable regression model is fitted to a set of baseline (non-drug) interval measurements at various heart-rates for that individual. The fitted regression functions are then used to correct drug-related interval measurements.

Significant work has been undertaken to identify the *optimal* formulae for heart rate correction. Malik et al. investigated the performance of six generic QT/RR regression models, namely a linear model ($QT = \beta + \alpha \times RR$), a hyperbolic model ($QT = \beta + \alpha/RR$), a parabolic model ($QT = \beta \times RR^{\alpha}$), a logarithmic model ($QT = \beta + \alpha \times \ln(RR)$), a shifted logarithmic ($QT = \ln(\beta + \alpha \times RR)$), and an exponential model ($QT = \beta + \alpha e^{-RR}$), on interval data obtained (via automated interval measurement) from 50 healthy volunteers [195]. They found that the linear and shifted logarithmic regression models had the lowest residual error, averaging over all 50 patients. However, it was found that the shape of the QT/RR relationship differed among subjects. For example, the linear model was optimal for only 40% of the subjects, with the rest having non-linear optimal regression models.

An alternative approach that avoids the complexities of identifying the optimal HR correction formula, is to average all QT interval measurements, corresponding to a specific range of RR values. This approach is referred to as the *rate bin approach* [251]. This method has successfully been been applied to multiple measurements of ventricular repolarisation, including QT, T-peak to T_{off} interval, T-wave amplitude, ST-elevation and T-wave symmetry [252, 253]. The benefit of the rate bin approach is that the influence of HR on the drug's effect can be investigated. However, two limitations of this approach are that it loses information relating to the time course of the drug effect and requires overlapping RR intervals, which could prove problematic if a drug dramatically changes the heart rate. As is the case with sotalol, which significantly prolongs the RR interval as shown in Section 7.2.

Heart rate correction has also been applied to other ECG timing intervals and morphology-based biomarkers. Couderc et al. applied a linear regression model to T-wave area-based timing intervals and compared the heart rate corrected intervals with standard Bazett and Fridericia corrected intervals [7]. The population-based linear regression model provided the optimal heart rate correction. More recently, Couderc et al. applied a population-based

linear regression model to repolarisation parameters derived from the T-wave loop, which is constructed by projecting the 12-lead matrix onto the two principal projected eigenvectors obtained from singular value decomposition [254]. Morphology-based biomarkers, including those based on the T-wave loop, are discussed in more detail below.

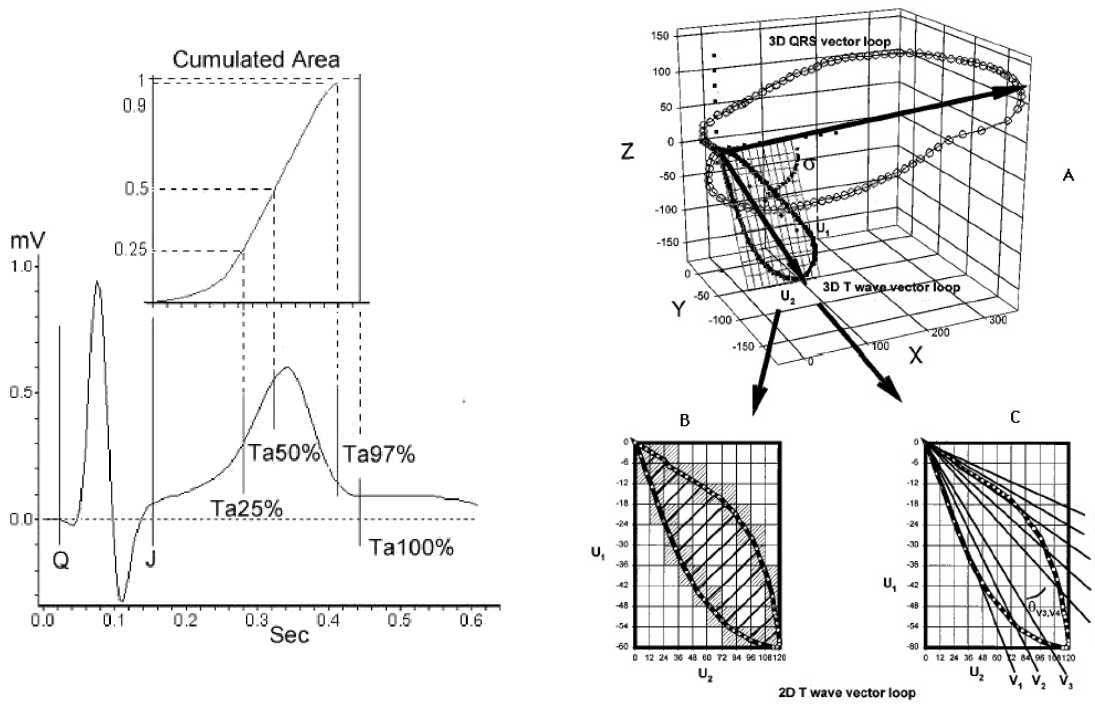
5.3 Morphology analysis

As discussed in Section 2.3.2, both increased duration and repolarisation heterogeneities are proarrythmic. Therefore, as the T-wave is known to capture all ventricular repolarisation activity information in the heart [39], T-wave morphology-based biomarkers have been proposed in an attempt to identify sensitive and specific biomarkers of drug-induced arrhythmia. The new biomarkers can be broadly classified into five groups: T-wave duration parameters, amplitude-based parameters, frequency-based parameters, parameters based on singular value decomposition of multi-lead ECG signals and parameters based on the T-wave loop. The following section will briefly review biomarkers in these five categories.

5.3.1 T-wave duration biomarkers

The focus for T-wave duration biomarkers has been on the terminal portion of the T-wave, i.e. from T-peak to T_{off} (T_{pe}). This interest is driven by *in vitro* studies that indicated that this period of repolarisation is linked with proarrhythmic activity [38]. Antzelevitch et al. have suggested that an increase in transmural heterogeneities of repolarisation is responsible for drug-induced arrhythmia and that T_{pe} is a measure of transmural heterogeneities of repolarisation [59]. Subsequent clinical investigations showed a significant correlation between life-threatening arrhythmia events and an increase in T_{pe} [255–258] .

Additional T-wave duration biomarkers are derived from the T-wave area and the T-wave loop (discussed in Section 5.3.5). Zareba, Moss and Konecki used biomarkers based on the cumulative T-wave area to distinguish between patients with repolarisation abnormalities [259]. The parameters included total repolarisation area, T-wave amplitude, time to 50% of total area (t_{A50}), the duration of the median 50% of the total area (t_{A25-75}), and the time to 97% of the total area (t_{A97}). A significant difference was found between LQTS patients and healthy normals for t_{A25-75} and t_{A50} parameters, whereas the other parameters showed poor separation between the two groups. More recently in 2003,



(a) (b)

Figure 5.13: T-wave morphology-based biomarkers: (a) T-wave duration biomarkers based on cumulative area of T-wave, reproduced from [7], (b) T-wave biomarkers based on T-wave loop, namely T-wave Cosine R-to-T (A), T-wave loop dispersion (B) and T-wave morphology dispersion (C). Reproduced from [260].

Couderc et al. proposed area-based timing intervals to identify changes in repolarisation due to sotalol [7]. They defined three timing intervals between Q_{on} and 25%, 50% and 97% of T-wave area (QTa25, QTa50 and QTa97), as shown in Figure 5.13(a). The QT interval in the ECG recordings was measured manually using the tangent method in lead V5 and the subsequent repolarisation parameters (QT, QT slope, QTa25, QTa50 and QT97) were measured and heart rate corrected using a population-based linear regression model. The area-based parameters were significantly increased by sotalol. The drug effect difference increased in magnitude towards T_{off}, with 29 ms increase in QTa25, 47 ms in QTa50 and 73 ms QTa97.

5.3.2 Amplitude-based T-wave biomarkers

Notched or biphasic T-waves have been linked with drug-induced arrhythmia [261]. Andersen et al. have proposed a number of parameters derived from changes in T-wave amplitude [42]. The proposed biomarkers are derived to characterise the *flatness*, *symme-*

try and *notched-ness* of the T-wave. The flatness parameters are based on the kurtosis[5] of the area-normalised JT segment. The notch score is based on the *radius of curvature* of the JT segment and describes the magnitude of curvature or fluctuations present in the JT segment. The symmetry parameter is determined using a ratio of the area under the ascending portion of the T-wave to the area under the descending portion of the T-wave. More recently, the effect of an I_{Kr} inhibiting anti-psychotic compound (Lu 35-138) on a weighted linear combination of these morphology biomarkers, termed a morphology combination score (MCS), was assessed [262]. The study found that the drug-effect on MCS was 1.8 times the effect on the Frediricia corrected QT interval (QTcF).

An alternative symmetry biomarker was proposed by Couderc et al. to investigate repolarisation morphology of LQTS patients with the KCNH2 mutation (LQT2) [41]. The proposed symmetry biomarker was defined as the ratio of the maximum ascending gradient (α_L) to the maximum descending gradient (α_R). Carriers of the LQT2 phenotype were found to have a significant decrease in maximum ascending slope (α_L). Symmetry parameters based on gradients of the T-wave are very sensitive to high frequency noise that can easily distort the ascending and descending slope values.

5.3.3 Frequency-based T-wave biomarkers

In addition to changes of T-wave morphology, the frequency of T-wave morphology changes has been shown to consistently correlate with ventricular arrhythmia [263]. T-wave alternans (TWA) was one of the first attempts to characterise these beat-to-beat changes in morphology [264]. Alternans are beat-to-beat changes in amplitude and morphology of ECG waveform features. The magnitude of the beat-to-beat variation is found to increase with heart rate and the onset of TWA generally occurs above a patient-specific heart rate threshold [265]. Initial studies showed that TWA had great potential in predicting ventricular arrhythmia [40].

Smith and Clancy et al. proposed a method for identifying microvolt TWA [266]. The power spectral density of the beat-to-beat T-wave amplitude differences was calculated using the fast Fourier transform. The T-wave was extracted from N consecutive beats using the tangent method. The beat-to-beat change in T-wave amplitude was then calculated and concatenated together to form a time series vector. A windowed fast Fourier

[5]A shape characteristic of a frequency distribution that reflects the sharpness of the peak.

transform was then applied to the vector and the resulting power spectrum calculated. A peak at 0.5 cycles/beat would indicate the presence of TWA.

Steinbigler et al. extended the concept of TWA to look at variations at all periodicities, and not only at every alternate beat [267]. They represented the time-aligned T-waves in two dimensions with the first dimension representing the T-wave segment and the second dimension representing the sequence of consecutive T-wave samples. They computed the two dimensional power spectral density and defined the T-wave spectral variance index (TWSV-I) as the inter-beat variation normalised by total T-wave variation, i.e.

$$\text{TWSV-I} = \frac{\sum_f |\mathcal{F}_1(f)| + \sum_f |\mathcal{F}_2(f)| > 0}{\sum_f |\mathcal{F}_1(f)|},$$

where $\mathcal{F}_1(f)$ and $\mathcal{F}_2(f)$ are different slices of the 2D frequency map. The TWSV-I method assumes that all T-wave frequency components are band limited to 0 - 50 Hz. TWSV-I successfully identified patients with ventricular arrhythmia from a group of 200 post myocardial infarction patients with 89% sensitivity and 78% specificity.

Couderc et al. proposed a TWA detection system independent of the accurate determination of the T_{off} [268]. The CWT was applied to a window of ECG signal from 100 ms after the R-peak and 220 ms before the next peak. Two parameters of temporal (beat-to-beat) variability in amplitude (TVA) and in time (TVT) were determined by analysing the magnitude variation and timing of peak values of the wavelet coefficients, respectively. They showed that LQTS patients with the SCN5A mutation (LQT1) have significantly increased TVA ($23\pm14\%$ *vs.* $8\pm4\%$, $p < 0.001$) and TVT ($14\pm17\%$ *vs.* $3\pm2\%$, $p < 0.004$) compared with healthy subjects.

5.3.4 Biomarkers based on singular value decomposition of the T-wave

Singular value decomposition (SVD) is a linear algebraic decomposition whereby a $m \times n$ matrix $\mathbf{A}$ with $p = \min(m, n)$ can be decomposed into $A = USV^T$, where U is an $m \times p$ column-orthogonal matrix, S is a diagonal matrix whose diagonal elements (s_i) are singular values of A with $s_1 \geq s_2 \geq \ldots \geq s_p$, and V is a $n \times p$ orthogonal matrix. The singular values of the matrix A are the square roots of the eigenvalues of the matrix $A^T A$, and the columns of the matrix V are the corresponding eigenvectors [269]. SVD has been applied to the ECG in a variety of applications, including noise filtering [270], ECG compression [271] and removing foetal ECG signals from maternal ECG signals [272].

The following parameters are derived from the SVD of T-wave segments.

T-wave Complexity Ratio

Prior at al. used SVD to quantity the complexity of repolarisation (CR) from the singular values of ST-T segments from 12 leads in healthy subjects and LQTS patients [273]. Three parameters were defined using the eight principal singular values $s_1 \geq s_2 \geq \ldots \geq s_8 \geq 0$ as follows:

$$CR_1 = \frac{s_2}{\langle s_i \rangle_{i=1}^{8}} \times 100$$
$$CR_2 = \frac{\langle s_i \rangle_{i=2}^{8}}{\langle s_i \rangle_{i=1}^{8}} \times 100$$
$$CR_3 = s_2/s_1 \times 100,$$

where $\langle \ldots \rangle$ is the root mean squared operator. The CR values were calculated for four consecutive beats then set to the average of these values. CR_{24h} was the average of these of these parameters of a 24 hour period and was found to be significantly higher in LQTS patients than in control subjects ($34 \pm 12\%$ *vs.* $13 \pm 3\%$, p< 0.0001). The predictive of CR_{24h} is 88%, comparable with QTc in classifying the healthy and LQTS subjects.

T-Wave Residua

The T-wave residuum (TWR) is similar to the CR parameter in that is uses the singular values to characterise heterogeneity in T-wave morphology [4] and is defined as:

$$TWR = \frac{\sum_{i=4}^{m} s_i^2}{\sum_{j=1}^{m} s_j^2}$$

5.3.5 T-wave loop morphology biomarkers

The T-wave loop can be constructed from the 12-lead system by projecting the project the multi-lead matrix A onto the principal orthogonal axes. A T-wave loop can then be defined in two or three dimensions as follows:

1. Let $\mathbf{A}$ be a $m \times n$ matrix with m samples from n leads
2. Perform SVD on $\mathbf{A}$ so that $\mathbf{A} = \mathbf{USV}^T$
3. Let $\mathbf{E}$ be the projection of $\mathbf{A}$ onto $\tilde{\mathbf{U}}$, i.e.

$$\mathbf{E} = \tilde{\mathbf{U}}^T \mathbf{A} = [e_1, e_2, ..., e_n],$$

where $\tilde{U}$ is the subset of $\mathbf{U}$ consisting of the first n columns corresponding with non-zero singular values.

4. The T-wave loop can then be constructed in two or three dimensions using $\tilde{E} = [e_1, e_2, e_3]$

Badilini et al. were the first to use the 3D vector loop reconstruction of the T-wave to assess ventricular repolarisation heterogeneity in healthy, post myocardial infarction and LQTS patients [274]. However, Acar et al. defined three new approaches to characterise ventricular repolarisation using the 3D reconstructed T-wave loop, namely the Total Cosine R-T, T-wave loop dispersion and T-wave Morphology Dispersion [275]. Zabel et al. used these T-wave loop morphology-based parameters to predict cardiovascular mortality in male US veterans [260]. Figure 5.13(b) illustrates the T-wave loop biomarkers that are defined below.

Total Cosine R-to-T

The Total Cosine R-to-T (TCRT) measures the angle between the QRS and T-wave vector loops. The orientation of the vector loops is determined by selecting the vector with the maximum energy for both the QRS and T-wave loops.

T-Wave Loop Dispersion

T-wave morphology dispersion (TLD) measures the variability of the 2D T-wave loop vector. It is calculated by encompassing the T-wave loop in a rectangle, which is then divided into 100 subdivisions. TLD is defined as the number of subdivisions through which the loop passes.

T-Wave Morphology Dispersion

The maximum T-wave vector is defined as the longest line from the start of the T-wave loop (J point) and the T-wave loop vector. T-wave morphology dispersion is defined as the mean of the angles between all the maximum T-wave vectors from all the lead vectors projected onto the two principal axes.

Early and Late Repolarisation Durations

Vaglio et al. proposed repolarisation duration parameters derived from the T-wave loop reconstructed from the projection of the T-wave onto the two principal eigenvectors [276].

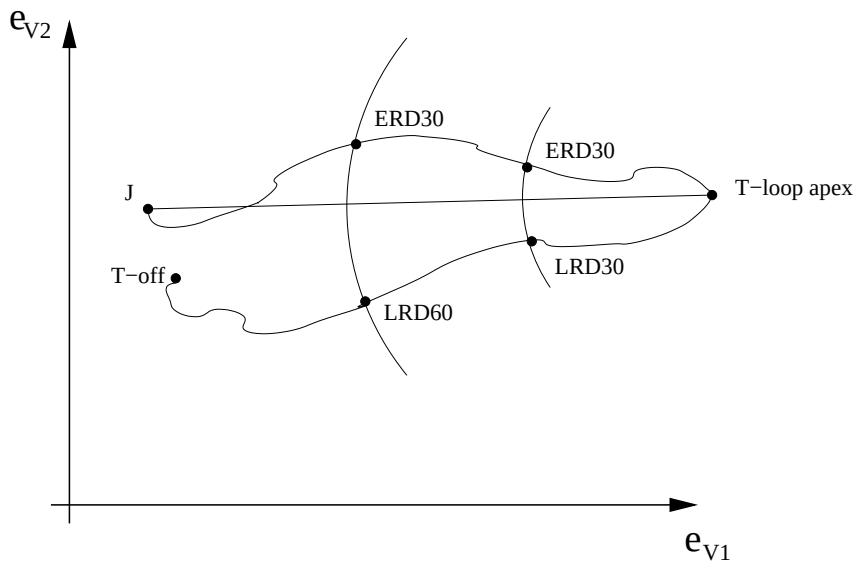


Figure 5.14: Schematic of the early and late repolarisation durations points, namely ERD_{30}, ERD_{60}, LRD_{30} and LRD_{60} [276]. The points are defined as the intersection of the arcs at 30% and 60% V_{max} with the T-wave loop.

Figure 5.14 schematically illustrates the early and late 30% and 60% repolarisation points on the T-wave loop. The points ERD_{30}, ERD_{60}, LRD_{30} and LRD_{60} were determined as follows:

1. Determine V_{max}, the vector with the maximum Euclidean distance from the J point
2. Calculate ERD_{30} and LRD_{30} as the intersection points of the arc at 30% V_{max} and T-wave loop
3. Similarly, calculate ERD_{60} and LRD_{60} as the intersection of the arc at 60% V_{max} and T-wave loop

5.4 Discussion

The demand for ever more sensitive and specific biomarkers for drug-induced arrhythmia has put pressure on ECG encoding, de-noising and waveform delineation methods. Considering the non-stationary nature of the surface ECG and the wide variety of noise, both physiological artefacts and other, it seems sensible to characterise and analyse the ECG in both the time and frequency domains. The UWT provides a redundant time-frequency signal representation that can be used for signal encoding, de-noising and QRS detection. With regards to waveform feature delineation, threshold-based methods are not able to provide any confidence measure associated with the automated measurements.

Therefore, a probabilistic machine learning approach to ECG segmentation is preferable. In particular, HMMs have been shown to successfully delineate the ECG waveform features [205, 235, 248]. However, it should be noted that if a confidence threshold is applied the number of beats analysed by the HMM approach might be different from the threshold based technique. Therefore, a comparison between the two methods should only compare those beats that are analysed by both methods.

Interval analysis of the ECG for characterisation of ventricular repolarisation should include the QT interval and the T-peak to T_{off} (T_{pe}) interval, as evidence suggests that pro-arrhythmic effects are captured in the latter phases of ventricular repolarisation [7, 276]. Furthermore, a subject-specific regression model should be fitted to baseline (non-drug) data and applied to subsequent measurements for heart-rate correction. As highlighted by Malik et al. [277], the optimal regression model might differ from subject to subject.

The wide variety of morphology-based biomarkers published in the literature necessitates the selection of a subset for further analysis. From the literature review is it clear that T-wave area and symmetry are both sensitive to drug effects. However, the physiological significance of parameters based on singular values, such as T-wave residua and T-wave complexity ratio is questionable. In particular, the physiological significance of the lower order singular values of the T-wave as a measure of repolarisation heterogeneities has been questioned [278]. Similarly, the electrophysiology underlying the morphology biomarkers derived from the T-wave loop, such as TLD and TCRT, remains uncertain. Therefore, this thesis will focus on the simplest characterisation of T-wave morphology, namely T-wave area, amplitude and symmetry, and investigate the effects of sotalol on these basic morphology-based biomarkers informed by the modelling results in Chapter 4. In addition, the application of individual heart rate correction techniques to these morphology-based biomarkers has not been investigated.

Chapter 6

Interval and Morphology Characterisation of Ventricular Repolarisation using the surface ECG

This chapter describes a novel algorithm for characterising ventricular repolarisation using the surface ECG. The algorithm extracts timing and morphology biomarkers from the ECG signal. The algorithm can be subdivided into three major phases, namely R-peak detection, probabilistic inference of waveform feature boundaries and characterisation of T-wave morphology. Each of these phases are described in detail. The segmentation algorithm, including R-peak detection and HMM inference, is evaluated by comparing it to expert measurements and a standard threshold-based segmentation algorithm on a clinical ECG data set of 10-second ECG recordings. The final section of this chapter describes the morphology analysis implemented in this thesis, in particular, the development of morphology-based biomarkers for characterising ventricular repolarisation.

6.1 Automated ECG segmentation algorithm

The objective of the segmentation algorithm is the accurate and robust identification of Q_{on}, R, J and T_{off}, so that interval and morphology-based biomarkers of ventricular repolarisation can be extracted from 24-hour Holter ECG recordings. As previously discussed, the automated analysis of the ECG is non-trivial due to the variability of the signal and the presence of noise and physiological artefacts. The combination of UWT and HMM segmentation is used to provide a robust way of identifying waveform boundaries. The automated annotations are also accompanied by a *confidence measure*, extracted from the probabilistic HMM segmentation, which allow low confidence beats to be excluded from further analysis (as discussed in Section 5.2.2).

A limitation of the HMM proposed by Hughes et al. [205] (as illustrated in Figure 5.11) is that it accommodates a transition from the baseline state of the previous beat to the PR state of the current beat. Therefore, the inference of the hidden states using the Viterbi algorithm is applied to the entire length of the signal. As discussed in Appendix B.2.1, the Viterbi algorithm is $\mathcal{O}(TK\bar{K})$, where K is the number of states, $\bar{K}$ is the average state connectivity and T is the length of the signal. Although, the approach proposed by Hughes et al. [205] is feasible for 10-second ECG recordings, it becomes computationally intensive for 24-hour Holter ECG recordings. In addition, the HMM architecture necessitates the inclusion of duration constraints to avoid double beat segmentation [205].

An alternative approach, as proposed by Strachan et al. [248], is to first identify a R-peaks using the robust Pan-Tompkins R-peak detection algorithm [223]), then to analyse a subset of the ECG signal using a trained HMM. The QRJT model proposed by Strachan et al. consists of two separate HMMs. The first HMM is used to detect the Q_{on} and J points, while the second HMM is used to detect T_{off}. The confidence measure of the QRJT model is calculated from the ECG segment processed by the HMM that locates T_{off}, i.e. the terminal portion of the T-wave. This does not take into account the morphology of the QRS complex or the rest of the T-wave and, therefore, is less likely to identify ECG beats contaminated with noise or with abnormal waveform morphology. In addition, the performance of the Pan-Tompkins algorithm has been shown to be sensitive to baseline wander and high-amplitude T-waves that could result in missed R-peaks [212].

The HMM segmentation algorithm implemented in this thesis combines the approaches proposed by Hughes et al. [245] and Strachan et al. [248]. Figure 6.1 illustrates the HMM

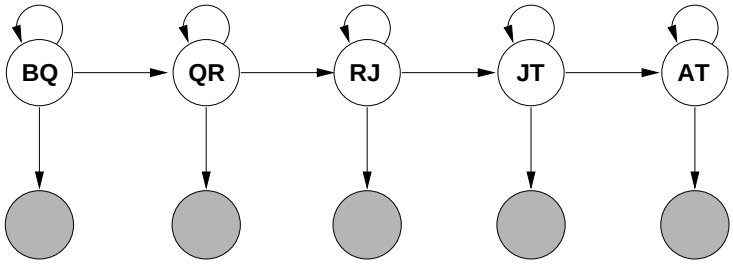


Figure 6.1: Hidden Markov model used to identify Q_{on}, R, J and T_{off}. The five-state HMM consists of a *before*-Q_{on} (BQ), QR, RJ, JT and an *after*-T_{off} (AT) state. The shaded nodes represent observation density models that are modelled using multi-variate Gaussian mixture models.

that identifies the Q_{on}, R, J and T_{off}. The model consists of five states, namely a left-to-right succession of *before*-Q_{on}, QR, RJ, JT and *after*-T_{off} states. The model does not include duration constraints. The segmentation algorithm is a combination of R-peak detection, using a multiscale wavelet analysis method proposed by Martinez et al. [207] (see below), and HMM segmentation for a subset of the ECG signal in a region near the R-peak. The sections below describe the R-peak detection algorithm, as well as the training of the HMM and subsequent inference using the trained model.

6.1.1 R-peak detection

As discussed in the previous chapter, R-peak detection applications using multiscale wavelet analysis are robust to baseline wander and high amplitude T-waves. Köhler et al. showed that R-peak detection methods using multiscale wavelet analysis were among the best performing R-peak detection algorithms ($> 99\%$ sensitivity and positive predictivity) in a review of 27 R-peak detection algorithms [221]. The computational load of wavelet-based R-peak detection algorithm is high in comparison to other R-peak detection algorithms. However, despite the relatively large computational load, the UWT wavelet coefficients can be used not only for the detection of R-peaks but also for HMM segmentation [205] and ECG de-noising procedures [206] (see Section 7.1.2 for a more detailed discussion).

The first step in applying the UWT to the ECG is to choose an appropriate wavelet function. As discussed in Section 5.1.1, the ideal wavelet function for R-peak detection, ECG segmentation and de-noising should satisfy the following criteria:

- Compact time localisation
- Appropriate degree of smoothness

- Realisation as a conjugate mirror filter (CMF) pair, which posses a near-linear phase response

The first wavelet of the *Coiflet* family, which has corresponding CMFs of length 6, satisfies all these requirements [197] and has been used successfully in HMM segmentation algorithms [234]. Previous R-peak detection and ECG segmentation approaches have primarily focused on wavelets that are either first or second derivatives of a Gaussian, or some approximation thereof. In particular, Li et al. [224], Sahambi et al. [228] and Martinez et al. [207] used a quadratic spline approximation of the first derivative of a Gaussian as an analysis wavelet for R-peak detection algorithms. Andreão et al. [235] used the second derivative of a Gaussian (commonly known as the *Mexican Hat* function) to encode the ECG for an HMM-based segmentation algorithm. More recently, Hughes and Tarassenko [205] showed that the biorthogonal spline wavelet, BIOR1.3, with low-pass and high-pass filters of length 6 and 2 respectively, out-performed the first Coiflet wavelet (COIF1) and the "least asymmetric" Daubechies wavelet (DB6). This result is probably due to the similarity of the BIOR1.3 wavelet to the first derivative of a Gaussian that has been shown to perform well in R-peak detection algorithms [207, 224, 228] and is commonly used for edge detection in image processing [227]. BIOR1.3 is roughly similar to the first derivative of a Gaussian function (as seen in Figure 5.3). Therefore, it offers a reasonable compromise between the various applications and signal characteristics.

The R-peak detection algorithm is based on the multiscale approach proposed by Martinez et al. [207]. As discussed in Section 5.2.1, this algorithm searches across scales 2^4 to 2^1 to identify *modulus maximum lines* (as discussed in Section 5.2.1) that are used to identify R-peaks as zero crossings between a pair of negative-positive maxima in the wavelet coefficients at scale 2^1. In this implementation the level-specific threshold is defined as

$$\epsilon_i = 0.3 * \sqrt{\frac{\sum_{n=1}^{N}(W_{2^i}n)^2}{N}}. \tag{6.1}$$

The local extrema larger than ϵ_i are selected in scales 2^i, $i = 1$ to 4. The modulus maxima lines are then identified by *tracking* the maxima from scale 2^4 to 2^1 and isolated and redundant peaks are removed, as described in [224]. In keeping with [207] and [224], a refractory period of 300 ms is enforced, to exclude candidate R-peaks following the identification of an R-peak, and the detection thresholds are lowered and the detection procedure repeated if no candidate R-peak is detected within 1.5 times the average RR

interval. However, in contrast to [207] the search for modulus maxima lines is restricted to the R-peak, as the trained HMM will be applied instead to identify the fiducial points, Q_{on}, R, J and T_{off}.

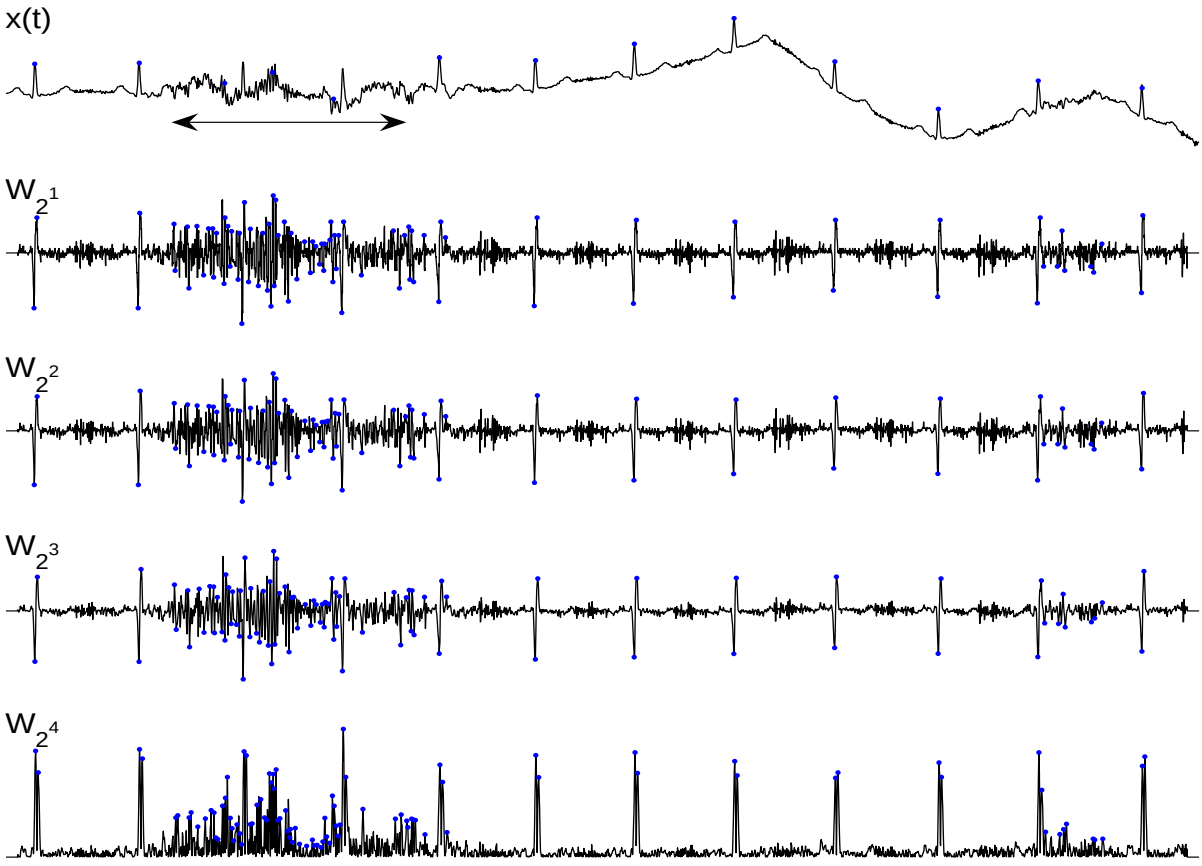
Figure 6.2(a) shows an example of the R-peak detection algorithm in the presence of baseline wander and muscle artefact. The original ECG signal is shown in the top panel, for which R-peaks are identified by blue dots. The wavelet coefficients for scales 2^1 through 2^3 are shown below along with the modulus of wavelet coefficients at scale 2^4. Local extrema exceeding the scale-specific threshold also identified by blue dots. The algorithm fails to detect the correct R-peak in the presence of high-frequency muscle artefact in the portion indicated by the double-arrow. However, it is able to detect R-peaks in the presence of baseline wander. Figure 6.2(b) illustrates the performance of the algorithm in the presence of large T-wave amplitudes, during which it correctly identifies the R-peak.

6.1.2 HMM feature delineation

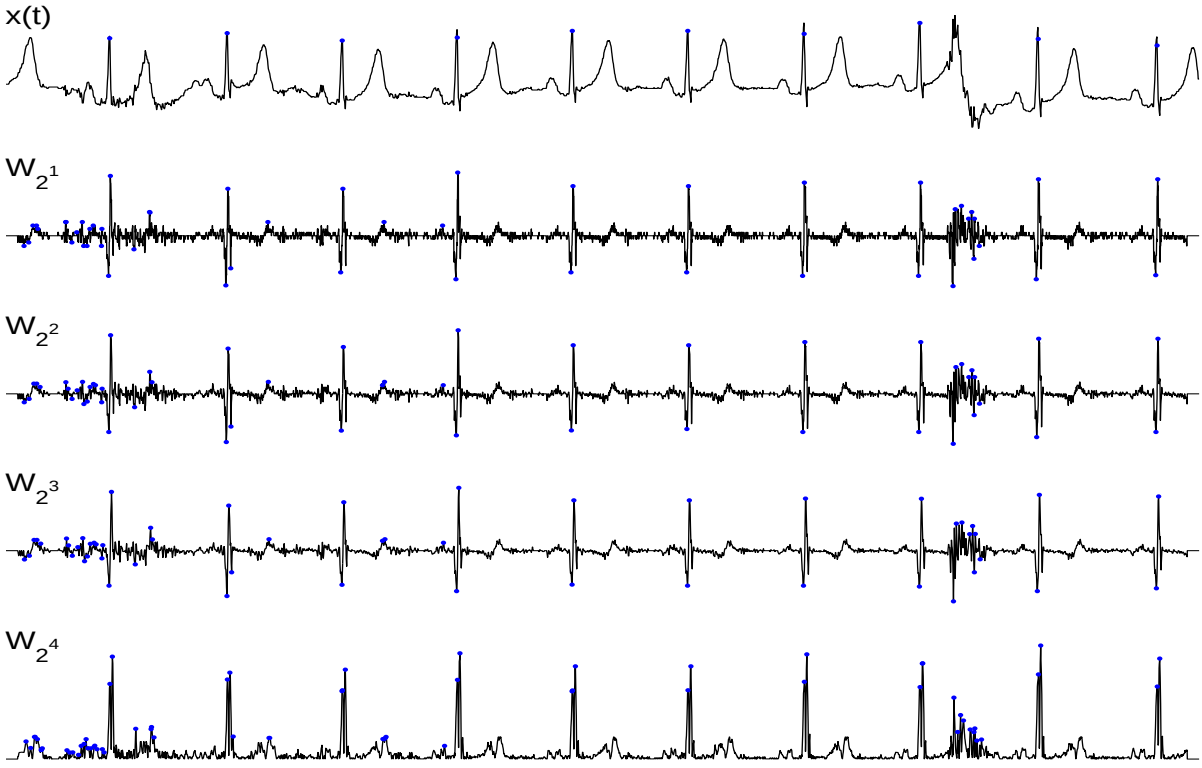
As discussed in Section 5.4 at the end of the previous chapter, a machine learning approach using a trained HMM approach to ECG feature delineation is preferred, as it allows a confidence measure to be derived from the posterior probabilities of the observation sequence. Confidence measures make it is possible to exclude beats that are deemed "unsuitable" for measurement from further analysis.

Training the HMM

The HMM was trained in a supervised manner on a clinical data set comprising of 10-second 12-lead ECG recordings sampled at 500 Hz and obtained in a Thorough QT Study for duloxetine [49]. The ECGs in this data set were recorded on the placebo day. The resulting data set consists of 18,731 10-second 12-lead ECGs recorded from 117 health normal volunteers. Twenty-one expert cardiac analysts manually analysed all the ECG recordings in the study. Each analyst was assigned a subset of volunteers and only measured the ECG recordings from these subjects. The lead that exhibited the *longest* QT interval in each 10-second 12-lead ECG recording, as determined by visual inspection, was chosen for manual analysis. The expert analysts identified three consecutive beats in each selected lead that were judged to be the easiest to measure and labelled P_{on}, Q_{on}, R, J and T_{off} in each of the three beats.



(a) Muscle artefact



(b) Large T-wave amplitudes

Figure 6.2: R-peak detection in the presence of (a) muscle artefact and baseline wander (b) large T-wave amplitudes. Blue dots identify the R-peaks in the ECG signal and local extrema in wavelet coefficients in scales 2^1 through 2^4.

ECG Lead	Selected (%)	ECG Lead	Selected (%)
I	0.6	V1	2.4
II	21.9	V2	22.1
III	1.0	V3	18.4
AVR	0.1	V4	5.0
AVL	0.4	V5	25.9
AVF	1.3	V6	0.9

Table 6.1: ECG lead measurement distribution

Table 6.1 shows the distribution of leads selected for manual analysis using the longest-lead approach. Leads II and V2 account for approximately 45% of the expert annotations. This is unsurprising as these two leads are also commonly selected in clinical studies as the lead for interval and morphology analysis across an entire ECG data set. Consistent with the work undertaken by Hughes et al. [205] and given the importance of leads II and V2, the remainder of the segmentation work in this chapter will focus on the development of probabilistic models and analysis methods for these two leads. However, the approach described in this thesis can be applied to *any* given lead of the surface ECG.

As described previously, the expert annotations identified only P_{on}, Q_{on}, R, J and T_{off}. Therefore, in order to train observation models for the BQ state, signal segments 60 ms before Q_{on} were extracted and used for training. Similarly, for the AT state, either the baseline segment until the next P_{on} was selected or if the beat was the final manually annotated beat, 120 ms of ECG signal after T_{off} was extracted and used for training the AT state. As implemented by Hughes et al. [205], the ECG was encoded using the wavelet coefficients from the UWT ($s_{\max} = 7$), i.e. the same UWT representation that was used for the R-peak detection (see previous section). Hughes et al. [205] showed how the inclusion of derivative information improved segmentation performance and so the 5-point first derivative of the wavelet coefficients for scales 2^4, 2^5 and 2^6 were calculated and included in the encoding vector. Thus, the resulting signal representation is a 10-dimensional observation vector. The signal was range normalised (± 1.0) prior to applying the UWT. The state observation probability densities were modelled using a multi-variate GMM with full covariance matrices. Again following Hughes et al. [205], the parameters for each GMM were estimated using a combined minimum-length-description model order selection and EM algorithm proposed by Figueiredo and Jain [246]. The remaining model parameters, namely the state transition matrix and initial state distribution, were determined in a supervised manner, as described in Appendix B.1. The final stage of the training proce-

HMM	Mean absolute errors (ms)			
	Q_{on}	R	J	T_{off}
Lead-II (n=8,602)	0.21 ± 4.44	0.20 ± 1.4	4.91 ± 7.19	-6.93 ± 9.03
Lead-V2 (n=8,968)	0.14 ± 3.07	0.75 ± 2.08	5.55 ± 6.96	-7.27 ± 8.54

Table 6.2: Mean absolute segmentation errors of HMM segmentation using 10-fold cross-validation for leads II and V2. The HMM were trained in a supervised manner using expert annotated ECG beats. The ECG encoding scheme is based on a combination of range normalisation, UWT encoding and derivative features.

dure consisted of learning the confidence models from the training ECG waveforms, as described in Section 5.2.2. The joint log likelihood for each QT segment in the training data set was computed. As proposed by Hughes et al. [247], a linear regression model was then fitted to the set of segment duration and joint log likelihood pairs. A sigmoid was then fitted to the mean regression line and the 99% lower confidence boundary so that the joint log likelihood of a QT segment from the test set could be normalised between 0 and 1.

HMM cross-validation

Ten-fold *cross validation* was used to determine the performance of the segmentation algorithm against the manual annotations in the training data set. In this method the data set is partitioned in ten equal subsets. Each iteration or fold selects a different combination of nine of the data subsets as the training data set and uses the remaining data subset as the test data set. For example, for the lead-II HMM, which has over 4,000 ECG records and 12,291 annotated beats, the training data set for each partition consists of approximately 3,200 records. The remaining 800 records make up the test data set. The partitioning process is repeated 10 times, with each subset used once as the test data set. The performance results from each *fold* are then averaged to obtain an overall estimate of segmentation performance.

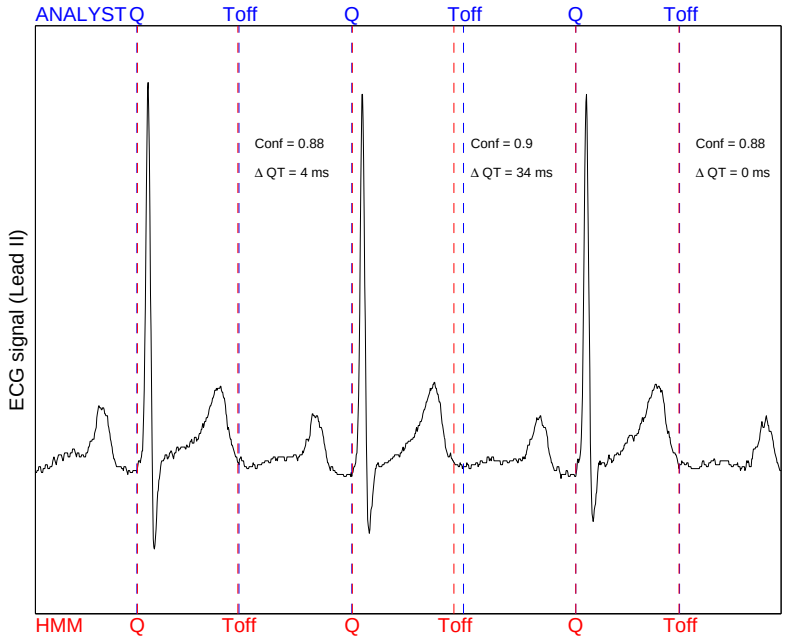
Table 6.2 shows the 10-fold cross-validation mean errors and the corresponding standard deviation, comparing the HMM segmentations with the expert analyst annotations on leads II and V2. The results show that the trained HMM model tends to produce earlier T_{off} segmentations than the manual annotations ($p < 0.0001$). Figure 6.3(a) illustrates several high confidence HMM segmentations from lead II in the test data set that place T_{off} earlier than the expert analyst. This is likely to be due to the significant overlap in the distributions of the encoded signal samples near the waveform feature boundaries.

This phenomenon is visible in Figure 6.3(b), which illustrates the log observation probabilities from all the Gaussian kernels in observation density models, for the central beat in Figure 6.3(a) with a QT error of 56 ms. The width of each state on the vertical axis corresponds to the number of kernels in the state GMM. For every sample, the Gaussian kernel with the largest responsibility[1] is highlighted. The time resolution of the figure gives the impression that there is overlap between the activation of the different kernels, but this only an artefact caused by the lack of resolution in the time axis as only the maximally activated kernel at every point in time is highlighted. As can be seen from the plot, the kernels in the AT state begin to be activated before the expert T_{off} annotation resulting in the early HMM T_{off} annotation. Solutions to this phenomenon are discussed in further work in Chapter 8.2.

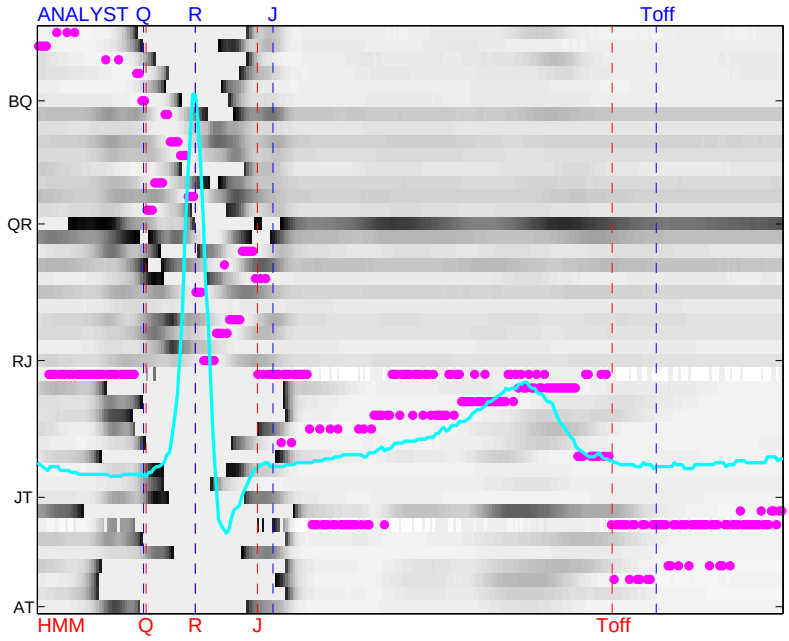
The performance of the automated HMM segmentation must be evaluated with the *inter-analyst variability* in mind. More specifically, this is the variability in measurements between expert analysts. Previous studies into this issue have shown that the inter-analyst variability (formally defined as the differences between QT interval measurements for two analysts measuring the same set of ECG recordings) has a mean absolute error of 7.8 ms and standard deviation of 9.6 ms (n=239) [279, 280]. Therefore, given that 21 expert analysts were used to annotate the training data set, we would expect a similar degree of variability in manual QT measurements between different analysts. To assess the accuracy of the HMM QT measurements, the difference between the HMM and expert analyst QT measurements for every manually annotated beat for leads II and V2 was determined. The mean error for lead II and V2 was found to be -6.72 ± 10.71 ms and -7.42 ± 9.16 ms, respectively. Furthermore, *intra-analyst* variability, i.e. the error observed between QT measurements by an expert analyst on the same ECG recordings in a double-blinded study, can also result in as much as 6.2 ms mean error and 5 ms standard deviation (n=81) [22]. Given that the HMM inference algorithm is deterministic, the HMM avoids intra-analyst variability errors in QT measurements.

Figure 6.4(a) shows the cumulative distribution of the confidence measures for all analysed beats in lead II in the test data sets (after 10-fold cross validation). In contrast, Figure 6.4(b) shows the cumulative distribution of confidence measures for beats in the

[1]The *responsibilities* quantify to what degree the Gaussian component is responsible for generating each data point, i.e. $P(z_n = j|\mathbf{x}_n)$, where $\mathbf{x}_n$ is the observation and and z_n is each Gaussian component in the mixture model.

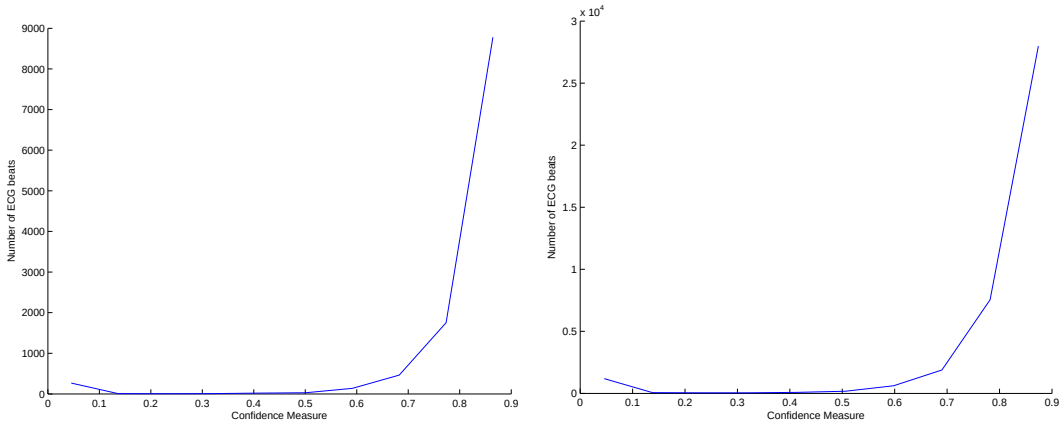


(a)



(b)

Figure 6.3: Automated versus manual annotations for a 10-second ECG recording from lead II in the test data set. The expert analyst's annotations are shown with blue dotted lines and the HMM annotations with red dotted lines. (a) Beats with large differences in QT values between manual and HMM annotations. (b) Log observation probabilities (or activations), i.e. $\log P(z_n = j|\mathbf{x}_n)$, for each Gaussian kernel in the GMMs for the central beat (shown in cyan). The individual kernel activations are shown on a grey-scale, where light values represent high activations and dark values represent low activations. The largest log observation probability for every sample is highlighted with a purple dot. The seeming overlap between highlighted kernels is an artefact due to the limited time resolution of the figure.



(a) Manual annotations (b) Automated annotations

Figure 6.4: Cumulative distribution of the HMM confidence measures for (a) the manually annotated beats and (b) all automated beats from lead V2 in the test data set.

test data set which were selected and annotated by the experts. Applying a confidence threshold of 0.7 to the later, results in 16.8% of the model segmentations in the lead II test set being labelled as low confidence, and 6.2% of the beats in the lead V2 test set. Applying a confidence threshold of 0.7 to all beats in the lead II and V2 test sets results in 18.9% and 7.5% of these beats being labelled as low confidence, respectively. As expert analysts select the beats from which they will most accurately be able to measure T_{off}, i.e. those beats with minimal noise or artefact, it is expected that the number of low-confidence beats amongst the expertly annotated beats should be lower than the number of low-confidence beats amongst the automated annotations.

Figure 6.5 shows a selection of low-confidence beats from the test data set. In each plot, the confidence value corresponds to the average of the confidence measures of the beats shown. For A, the R-peak detection algorithm fails to identify the R-peaks. This is due to large electrode spike artefact. In plot B, the muscle artefact at the start of the record results in poor T_{off} annotations. In plots C and D, the baseline wander results in low confidence values due to abnormal T-wave morphologies.

The performance of the HMM-based segmentation algorithm described in this section is compared with that of a standard threshold-based ECG segmentation algorithm, "ECGPUWAVE" (described in Section 5.2.2) [231]. In order to compare the two methods, Bland-Altman plots of the agreement between the QT intervals calculated by the segmentation algorithm and the corresponding QT interval as determined by an expert analyst are shown. The Bland-Altman plot is a way of comparing two methods of measurements by displaying the difference between the two sets of measurements against the average of

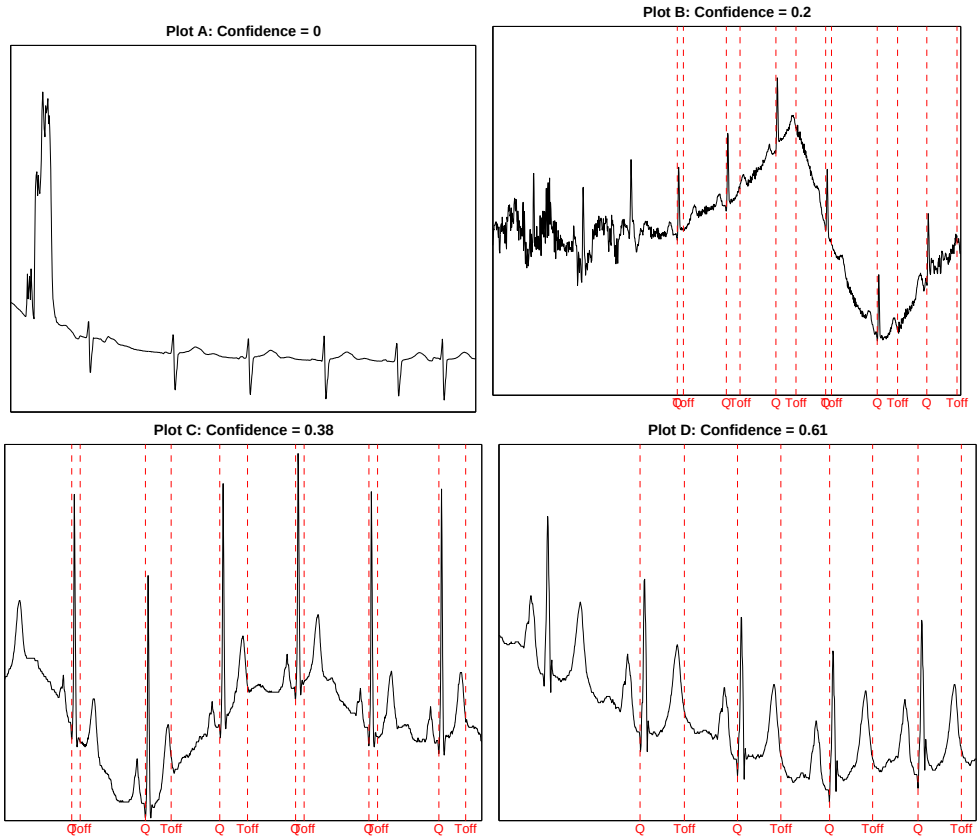
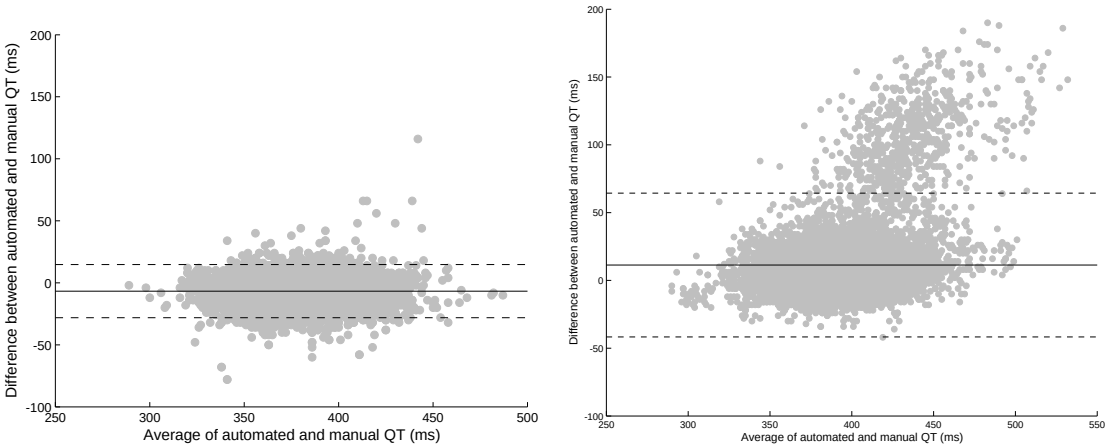


Figure 6.5: A selection of low confidence HMM segmentations with confidence measure less than 0.7 from lead II in the test set. The average confidence measure for all the beats displayed is shown.



(a) HMM (n=8,602) (b) ECGPUWAVE (n=12,010)

Figure 6.6: Bland-Altman plots of agreement between automated QT measurements from (a) HMM and (b) ECGPUWAVE segmentation algorithms and the corresponding manual QT measurements for lead II. The solid horizontal line indicates the mean QT difference and the dashed lines indicate the 2× standard deviation error bars.

the measurements [281]. This enables any systematic differences between the two measurements to be visualised, as well as any trend in the differences to be characterised.

Figure 6.6 shows the Bland-Altman plots for the high confidence QT intervals from the HMM and ECGPUWAVE segmentations evaluated on lead II. The plot for the ECGPUWAVE algorithm shows a significant number of positive outliers, indicated by the cloud of data points in the upper right portion of the plot. These points correspond to over-estimates of the QT interval by the ECGPUWAVE algorithm. In contrast, there is generally good *agreement* between the manual and HMM measurements, in that the data points in the HMM plot are well clustered around the mean difference. Although, the HMM algorithm tends to produce shorter QT intervals than the manual QT measurements, as previously discussed.

6.2 T-wave morphology characterisation

As discussed in Chapter 2.1, the morphology of the T-wave is primarily determined by the heterogeneities of repolarisation in the ventricles. The modelling results from Chapter 4 highlighted the sensitivity of morphology-based biomarkers to drug concentration and heart rate. In clinical studies, T-wave morphology-based biomarkers have been shown to be sensitive to noise and muscle artefact [252, 256]. Therefore, in characterising T-wave morphology it is necessary to define biomarkers that can be robustly determined in the presence of noise and adequately capture the shape of the T-wave. For T-wave morphology

characterisation, the segmentation procedure focus solely on the J - T_{off} segment. This segment is extracted from a filtered ECG signal, using the methods described below.

6.2.1 De-noising ECG

As discussed in Section 5.1.2, wavelet de-noising using the translation-invariant UWT is a suitable method for removing the noise and interference in the ECG. In particular, the application of a fixed threshold estimate was found to perform well in de-noising ECG signals with simulated noise [206]. Such an approach calculates the threshold with respect to the length and standard deviation of the signal as follows:

$$p = \sigma \cdot \sqrt{2 \ln N}, \tag{6.2}$$

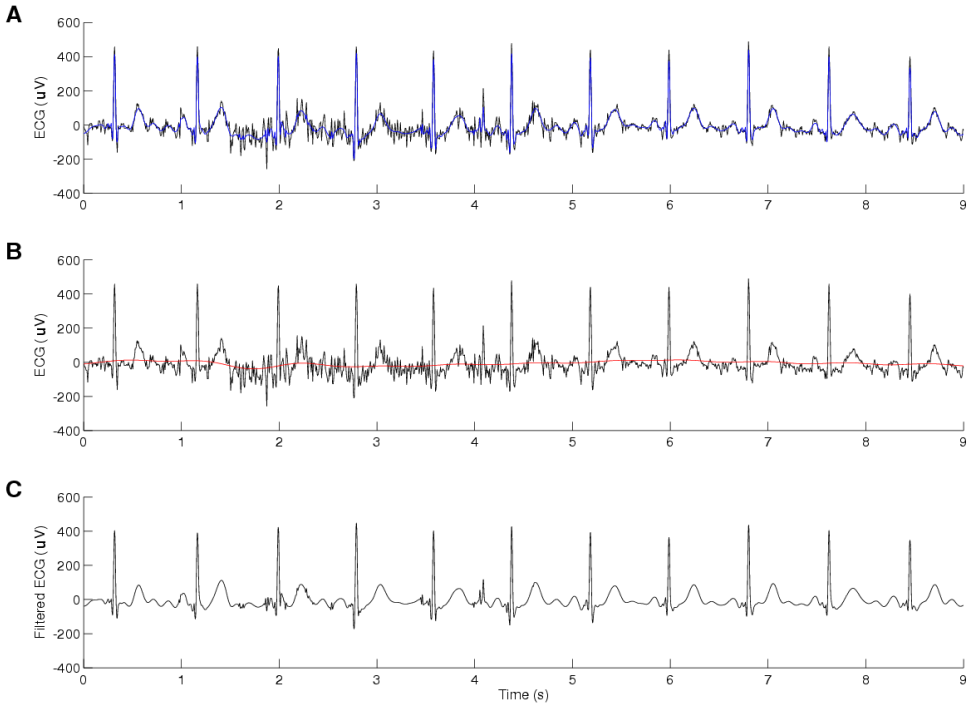
where N is the number of samples in the ECG signal [201]. Soft thresholding, as opposed to hard thresholding, does not introduce discontinuities in the wavelet coefficients, as it shrinks all coefficients that exceed the threshold to zero [216]. This tends to produce a smoother JT segment under visual inspection, after applying an inverse UWT.

The algorithm, therefore, applies the fixed threshold estimated using soft thresholding to the wavelet coefficients at each level. The inverse UWT is then used to reconstruct the de-noised ECG signal (see Appendix A.2 for details of the inverse UWT). Figure 6.7(a) shows an example of a 10-second ECG recording from lead-II that is corrupted by high-frequency noise. The wavelet de-noising procedure effectively removes the noise without adversely distorting the T-wave morphology.

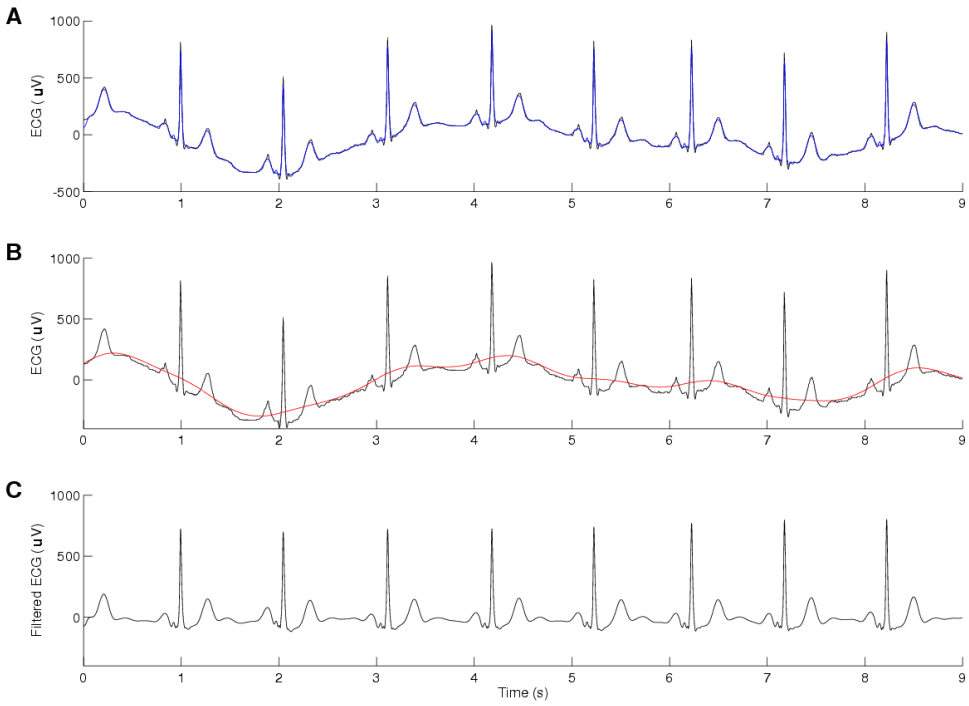
As highlighted in Section 5.1.2, the frequency components of baseline wander and the T-wave can often overlap. Baseline wander removal is achieved using a two-step de-noising process. Firstly, a *baseline* is constructed using the scale coefficients of the 7-level UWT decomposition. The reconstructed baseline signal is subsequently subtracted from the de-noised ECG signal, as previously described. Figure 6.7(b) illustrates the performance of the wavelet de-noising procedure removing baseline wander from a 10-second ECG recording from lead II.

6.2.2 Morphology biomarkers

A number of different T-wave morphology-based biomarkers have been proposed in the literature (see Section 5.3 for a full review). The modelling results presented in Chapter 4 show that an increase in sotalol concentration resulted in an increase in T-wave area,



(a) High frequency noise



(b) Baseline wander

Figure 6.7: De-noising and removing baseline wander from a 10-second ECG recording (lead II) using wavelet-based de-noising. In each case, Panel A shows the original ECG signal, Panel B shows the original signal with the wavelet-reconstructed baseline signal and Panel C shows the final smoothed ECG signal, constructed by subtracting the baseline from the de-noised signal.

amplitude and T-wave area-based symmetry. In addition, the modelling results showed that these effects were dose and heart rate dependent. The following T-wave morphology biomarkers will be investigated in the next chapter:

1. **Area:**
$$\sum_{n=1}^{T} f(n)\Delta x$$

2. **T-peak:** T-wave peak amplitude value.

3. **Gradient-based symmetry:** the ratio of the ascending gradient over the descending T-wave gradient. The ascending and descending gradients are defined as the gradient of the best-fit[2] straight line to T-peak $\pm 0.75 \times \mathrm{T}_{pe}$ for the portions of the waveform on either side of T-peak.

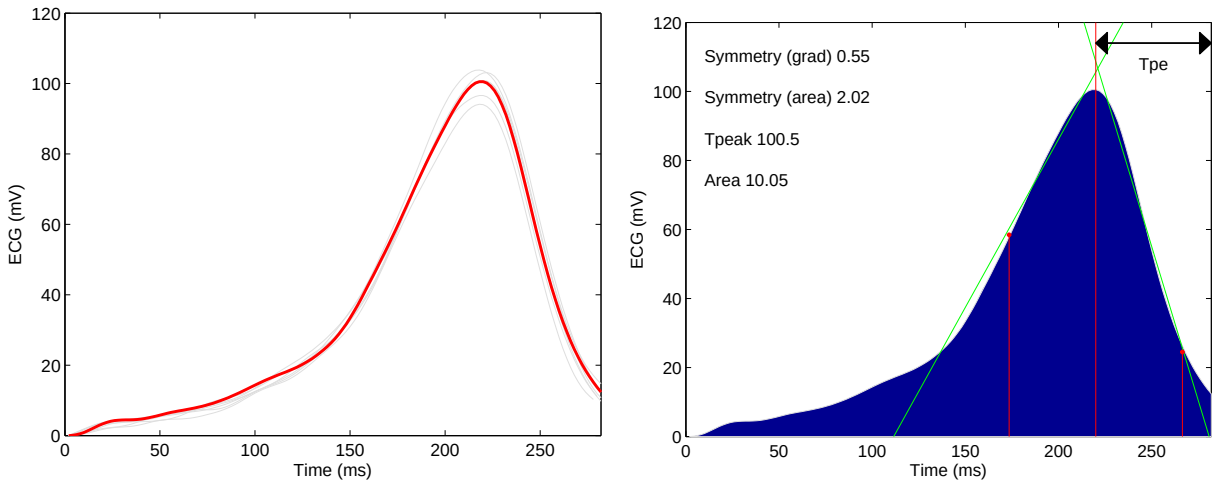
4. **Area-based symmetry:** the ratio of the area before T-peak occurs over the area under the descending slope of the T-wave. The area considered, similar to the gradient-based symmetry biomarker, is the area under $\pm 0.75 \times \mathrm{T}_{pe}$ either side of T-peak.

Prior to calculating the morphology biomarkers, the JT segment is "normalised" by subtracting the J-point value from the JT segment. Figure 6.8(b) shows morphology-based biomarkers derived from a typical JT segment. The area of the T-wave is highlighted in blue and the T_{pe} interval is shown. The portions of the T-wave that are used to determine the ascending and descending gradients are indicated with red lines , i.e. T-peak $\pm 0.75 \times \mathrm{T}_{pe}$. The associated biomarker values are also shown in the plot. Figure 6.8(a) shows the median JT segment (determined by length) from a 10-second recording from lead II.

6.3 Discussion

This chapter presented an algorithm for identifying Q_{on}, R, J and $\mathrm{T}_{\mathrm{off}}$ in ECG recordings. The algorithm combines wavelet analysis and probabilistic modelling. The ECG signal is encoded using the undecimated wavelet transform, which along with derivative coefficients, creates a 10-d observation vector. A hidden Markov model is trained in a supervised manner on a large data set (more than 18,000 beats) with expert annotations

[2]Implemented using MATLAB's *polyfit* function with a least-squares fitting technique.



(a) (b)

Figure 6.8: Morphology characterisation of ventricular repolarisation: (a) The median JT segment (determined by length) extracted from a 10-second recording from lead II. The segments are "normalised" by subtracting the J-point value from the segment (a) morphology-based biomarkers extracted from the smoothed, median JT segment, namely T-wave area, T-peak amplitude, gradient-based symmetry and area-based symmetry.

identifying P_{on}, Q_{on}, R, J and T_{off}. The segmentation algorithm tended to produce earlier T_{off} annotations than experts with the mean error of -6.72 ± 10.71 ms and -7.42 ± 9.16 ms for lead II and V2, respectively. The possible solutions for improving the segmentation algorithm are discussed in Section 8.2.

This chapter also presented an algorithm for the wavelet-based de-noising of the ECG recording using the UWT and soft-thresholding of wavelet coefficients using a fixed threshold estimate. The baseline wander was removed using a low-pass linear filtering with a 3db cut-off frequency of 1.6 Hz. The algorithm was successfully able to remove baseline wander and high frequency noise under visual inspection.

Chapter 7

The Effect of Sotalol on Ventricular Repolarisation

As discussed in Chapter 2, sotalol is a Class III anti-arrhythmic that is known to prolong ventricular repolarisation and induce torsades de pointes. The modelling results in Chapter 4 showed that an increase in sotalol concentration results in a prolongation of the duration of repolarisation and alters the morphology of the T-wave (as seen in the pseudo-ECG). These effects were seen to be dose and heart rate dependent (as discussed in Section 4.3). In this chapter, the automated ECG segmentation and morphology characterisation algorithms developed in the previous chapter are used to investigate the effect of sotalol of ventricular repolarisation in 24-hour Holter ECG recordings from an academic research study that investigated the effects of sotalol on the ECG recorded from health volunteers [49]. The objective of this chapter is to quantify the effects of sotalol on ventricular repolarisation, by extracting timing and morphology biomarkers from the Holter ECG recordings, and comparing the changes in the biomarkers with predictions made by the model in Chapter 4. This chapter will focus its analysis on lead II data although the methods can be applied to any of the surface ECG leads (given a trained HMM for each lead). The biomarkers of ventricular repolarisation used here include QT interval, T-peak to T_{off} interval, T-wave area, T-peak amplitude, T-wave area and gradient-based symmetry, as introduced in the previous chapter.

7.1 Analysis of 24-hour Holter ECG recordings

It was shown in the previous chapter that computation of interval and morphology biomarkers requires the implementation of both ECG segmentation and de-noising procedures. In this section, the previously developed segmentation and morphology characterisation algorithms are applied to 24-hour Holter ECG recordings. This section first describes the sotalol Holter ECG data set used in this investigation, followed by a brief overview of the segmentation and morphology characterisation algorithms as they are applied to 24-hour Holter ECG recordings. The effect of sotalol on the timing and morphology biomarkers is then discussed in detail.

7.1.1 Sotalol Holter ECG data set

The data set consists of 12-lead, 24-hour Holter ECG recordings from 26 healthy volunteers. The recordings were obtained during a controlled study of the effects of sotalol at Pharmacia's Clinical Research Unit (Kalamazoo MI, USA) [49]. The study was based on a three-day protocol; baseline day (D0), administration of 160 mg of sotalol (D1) and administration of 320 mg of sotalol (D2). The drug was administered orally at 08:00 on dosage days under fasting conditions and the subjects were given standard meals at noon and 18:00. Subjects were withdrawn from the study if pre-dose QTc was greater than 410 ms or any QTc within 6 hours after dosing was greater than 450 ms. As a result, data is available from only 11 subjects for D2. This could clearly bias the results to reduce the real change of sotalol induced effects.

The ECG signals were recorded using a H12 recorder (Mortara Instruments Inc., Milwaukee WI, USA) and were sampled at 180 Hz with 16-bit resolution. The recordings were time-stamped at the start of each ECG recording. The signals were recorded using dual-snap electrodes for precordial leads and single-snap electrodes for limb leads (Nikomed USA Inc., Doylestow PA, USA). The ECGs were exported from E-Scribe (Mortara Instruments Inc., Milwaukee WI, USA) into XML-HL7 format.

The 24-hour Holter recordings were extracted from the XML-HL7 format using a text parser that extracted the 12-lead ECG data and segmented it into 1440 time-stamped text files, each with one minute's worth of 12-lead ECG data. In order to use the HMM trained on the training data set described in Section 6.1.2, the one-minute segments of 12-lead ECG data from the sotalol study were resampled to 500 Hz, firstly by up-sampling by

a factor of 500 using bandlimited interpolation [282]. This relies on Shannon's sampling theorem that a continuously integrable signal with samples $x(nT_s)$, where $x \in \mathbb{N}$ and T_s is the sampling period, and bandlimited to $\pm 1/2T_s$, can be uniquely reconstructed as follows:

$$x(t) \equiv \hat{x}(t) = \sum_{n=-\infty}^{\infty} x(nT_s')h_s(t - nT_s') \tag{7.1}$$

where

$$h_s(t) = sinc(F_s't) = \frac{sin(\pi F_s't)}{\pi F_s't}$$

and $T_s' = nT_s$ ($n \in \mathbb{N}$) and $F_s' = 1/T_s'$. The signal is then downsampled by a factor of 180 resulting in a sampling frequency of 500 Hz.

7.1.2 Overview of algorithm

As discussed at the end of Chapter 6, the combination of wavelet R-peak detection and HMM segmentation is able to identify the fiducial points in the ECG waveform, allowing the QT interval to be measured and the morphology of the JT segment to be characterised. The entire process, from windowing to calculation of morphology biomarkers is shown in Figure 7.1. The algorithm has two parallel tracks; the first segments the ECG by identifying the R-peak, Q_{on}, J and T_{off}; the second track is a wavelet de-noising procedure that aims to remove baseline wander and high-frequency noise so that smooth JT segments can be extracted for morphological characterisation. The JT segments that are used for morphology characterisation are those extracted from high confidence beats, i.e. beats with a confidence measure greater than 0.7 (see Section 5.2.2). Each stage in the flowchart, shown in Figure 7.1, is described in further detail below.

0 Window Holter ECG

- Each 24-hour Holter ECG recording is split into separate files each comprising one minute of 12-lead ECG data

1 Undecimated wavelet transform

- Perform UWT using BIOR1.3 wavelet function; the UWT filter bank algorithm is described in detail in Appendix A.1

2a QRS detection

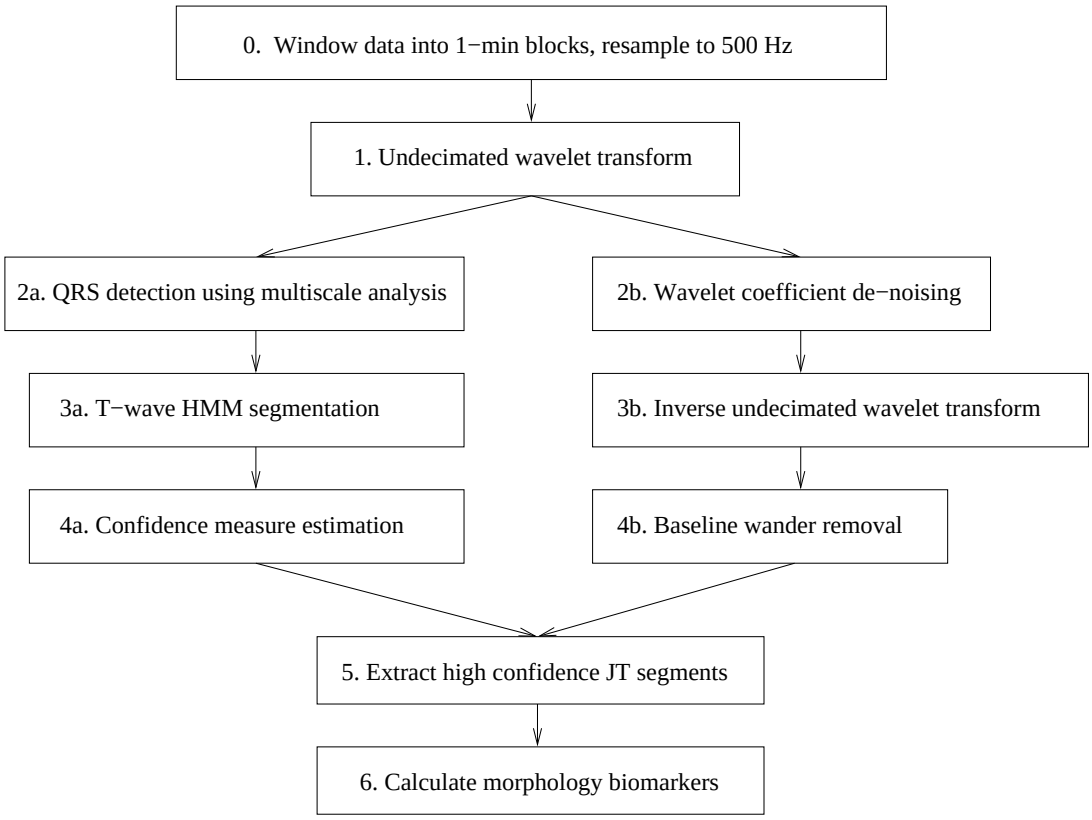


Figure 7.1: Flowchart of automated ECG analysis system for characterisation of ventricular repolarisation using 24-hour Holter ECG recordings.

- Identify R peaks using the multiscale wavelet analysis described in Section 6.1.1

2b UWT de-noising

- Apply fixed threshold de-noising approach using soft thresholding of the wavelet coefficients at all scales (see Section 6.2.1)

3a T-wave HMM segmentation

- Use the Viterbi algorithm with the trained HMM to identify Q_{on}, J and T_{off} in each one-minute ECG segment

3b Inverse undecimated wavelet transform

- Reconstruct the de-noised ECG signal from the UWT wavelet coefficients using the *average basis inverse* WT (see Appendix A.2)

4a Confidence measure estimation

- Calculate the confidence measure for each beat from the HMM posterior probability for each QT segment (see Section 5.2.2)

- Do not include beats with confidence measure less than 0.7 in further analysis

4b Baseline wander removal

- Use inverse UWT to reconstruct baseline using 7^{th}-level wavelet and scale coefficients, as discussed in Section 6.2.1
- Subtract resulting "baseline" from de-noised signal

5 Extraction of high-confidence JT segments

- Extract JT segments associated with high confidence measures from de-noised ECG signal

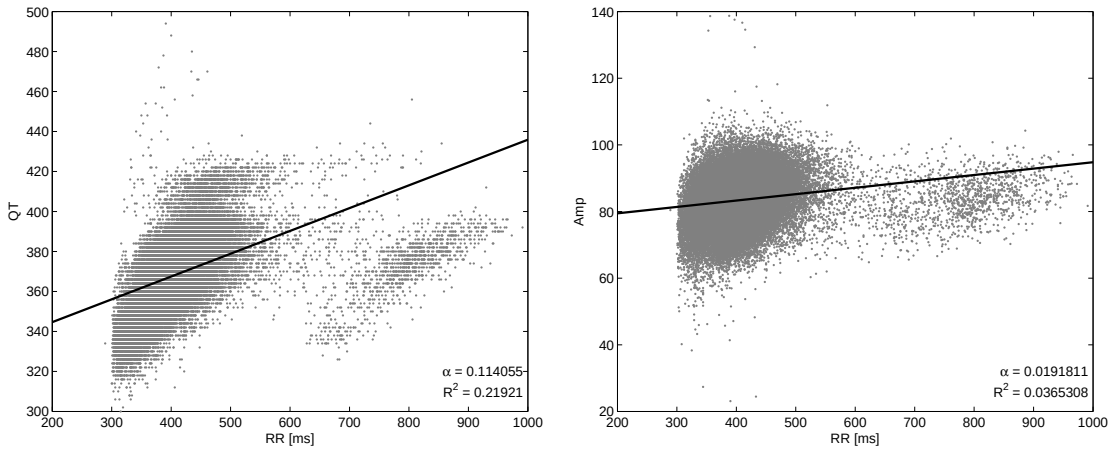
6 Morphology biomarkers

- Determine T-peak amplitude and T_{pe}
- Calculate T-wave area, gradient-based symmetry and area-based symmetry (see Section 5.3)

7.1.3 Heart-rate correction of biomarkers

As discussed in Section 5.2.3, heart rate correction techniques are typically applied to ECG timing intervals. This effectively enables interval measurements at different heart rates to be compared, which is necessary for isolating the drug effect on the timing interval in question. There is some evidence that T-wave morphology-based biomarkers are also dependent on heart rate [253, 256]. For instance, a study of amiodarone showed T_{pe} to be dependent of heart rate [283]. Similarly, a recent study from 62 healthy subjects found T-wave amplitude to be dependent on heart rate, with slower heart rates exhibiting larger T-wave peak values [253]. However, a study of the effects of sotalol on T_{pe} found T_{pe} to independent of heart rate [7].

To investigate whether the morphology biomarkers studied in this thesis are dependent on heart rate a linear regression model of the form $B = \beta + \alpha \mathrm{RR}$, where B is the interval or morphology biomarker and RR is the RR-interval of the preceding heart beat, was fitted to data extracted from the baseline day (D0). Linear regression modelling has been used for HR correction of the QT interval with some success [195], although it must be noted that the underlying relationship might be non-linear. Previous work has shown that



(a) (b)

Figure 7.2: Scatter plot of (a) QT and (b) T-wave peak amplitude (T_{amp}) versus RR interval for 24 hours of ECG recording for one subject on baseline day (D0). The robust linear regression line is shown with the associated correction factor (α) and R^2 values.

there is significant variation in the QT-RR relationship between individuals, with only 40% of individuals having a QT-RR relationship that could be described as linear [195].

Figure 7.2 shows two examples of biomarker dependence on heart rate from one subject. Over 56,000 high confidence measurement beats were identified from the baseline day (D0). Timing and morphology biomarkers were then extracted from each high confidence beat. Figure 7.2(a) shows the scatter plot of QT versus RR interval for the full 24-hour period from D0. Similarly, Figure 7.2(b) shows the scatter plot of T-wave amplitude versus RR interval. A linear regression model was fitted to the data resulting in correction factors (α) of 0.1141 and 0.0192 for QT interval and T-wave amplitude, respectively. The goodness-of-fit (or variability) of the regression model can be obtained by calculating

$$R^2 = 1 - \sqrt{\frac{\sum_{i=1}^{N}(y_i - y_i')^2}{\sum_{i=1}^{N}(y_i - \bar{y})^2}}, \tag{7.2}$$

where y_i is the observed value, y_i' is the predicted value and $\bar{y}$ is the mean value for a set of N values. The R^2 values for QT-RR and T_{amp}-RR pairs in Figure 7.2 are 0.2192 and 0.03653, respectively. Although, the heart rate dependence of the QT interval has been well documented and discussed [19], limited work has been done to investigate the heart rate of dependence of T-wave morphology.

Table 7.1 shows the average α and R^2 values (with standard deviations) for each of the biomarkers across all 26 subjects in the data set for lead II. The results show that the QT interval exhibits the greatest heart rate dependency of the biomarkers used in this thesis. The α values for morphology biomarkers, with the exception of T-peak amplitude,

Biomarker	**Linear correlation coefficient** (α)	**Goodness-of-fit** (R^2)
QT	0.0987 ± 0.0310	0.3436 ± 0.1343
T_{pe}	0.0004 ± 0.0117	0.0149 ± 0.0165
T_{area}	0.0032 ± 0.0033	0.1459 ± 0.1556
T_{amp}	0.0290 ± 0.0314	0.1497 ± 0.1647
T_{symG}	0.0002 ± 0.0004	0.0182 ± 0.0214
T_{symA}	0.0001 ± 0.0002	0.0157 ± 0.0152

Table 7.1: Heart rate correction factors (α) and goodness-of-fit values (R^2) for timing and morphology biomarkers across all subjects for lead II.

are very low ($\alpha < 0.01$). The symmetry biomarkers (T_{SymG} and T_{SymA}) show the least heart rate dependence of all the biomarkers. The average QT correction factor of 0.0987 is within the typical range [284]. As expected there is relatively large variance in the correction factor across all the subjects. The large variance and low R^2 values could be due to hysteresis effects [27]. To overcome hysteresis effects an improved approach would to only consider those measurements at the end of a segment of stationary RR intervals to be sure that the measurements reflect steady state and are free of hysteresis effects.

As discussed in Section 5.2.3, individualised heart rate correction offers an improvement over population-based correction methods. This is confirmed by the large variance in α values in Table 7.1. As a result, the assessment of the effect of sotalol on interval and morphology biomarkers users individualised heart rate correction based on:

$$B_c = B + \alpha(1 - \mathrm{RR}), \tag{7.3}$$

where B is the selected biomarker and α is the individualised correction factor from the linear regression model fitted to the baseline biomarker measurements (with RR interval) for that patient.

7.2 Effect of sotalol on biomarkers of ventricular repolarisation

To assess the effect of sotalol on the interval and morphology biomarkers, a median filter was applied to each of the heart rate corrected biomarkers extracted from the high-confidence beats in each one-minute analysis window (as discussed in Section 7.1.2). This gives one representative biomarker per minute. Figure 7.3 shows the one-minute median, interval and morphology biomarkers from one subject for 24-hour Holter recordings from each of the D0, D1 and D2 days. A 15-minute moving average filter is applied to the

one-minute representative biomarkers and used in subsequent analysis. It is unclear from Figure 7.3 that sotalol has a significant effect on RR, QT, T_{pe}, T_{area}, T_{amp}, T_{SymG} and T_{SymA}.

Figure 7.4 illustrates the same biomarkers (as shown in the previous figure) from the same patient, except that individualised heart rate correction is applied to each biomarker. The application of heart rate correction does not seem to alter the effects of sotalol on any of the biomarker for this patient. However, in order to assess the effect of heart rate correction on the interval and morphology biomarkers, the mean drug effect across all subjects, with and without heart correction is compared.

Figure 7.5 illustrates the average effect of 160 and 320 mg sotalol on the interval biomarkers (QT and T_{pe}) across all subjects in the study. The mean effect across all subjects (26 for D1 and 11 for D2) for QT and T_{pe} is shown as a percentage change with respect to baseline. The percentage change between drug and non-drug is calculated for every minute averaged over a 30-minute period. Error bars associated with each point represent one standard deviation on either side of the mean. As a result of the use of the moving average filter, the first and last 30 minutes are not shown. The figure shows the drug effect for both the raw interval measurements as well as the heart rate corrected intervals.

Sotalol results in a significant increase of RR, QT and T_{pe} with $p < 0.0001$ using the Wilcoxon rank-sum test with 95% significance level. The effects of sotalol on the RR, QT and T_{pe} are also dose-dependent ($p < 0.0001$). The timing of the maximum effect of sotalol on RR, QT and T_{pe} occurs between 2 to 4 hours after dosing, which is consistent with the pharmacokinetics of sotalol that reaches its peak plasma concentration ($C_{\max}$) 2-4 hours after an oral dose [285].

In addition, sotalol results in a decrease in.

The timing of the maximum effect on T_{area}, T_{amp} and T_{SymA} occurs approximately 7 hours after dosing.

Figure 7.6 illustrates the average effect of 160 and 320 mg sotalol on the morphology biomarkers, namely T_{area}, T_{amp}, T_{SymA} and T_{SymG}, across all subjects in the study. As with the previous figure, the mean effect is shown as a percentage change with respect to baseline for both the raw and heart rate corrected biomarker measurements. Sotalol results in a dose-dependent increase in T_{amp} and T_{SymG} ($p < 0.0001$). In contrast, sotalol

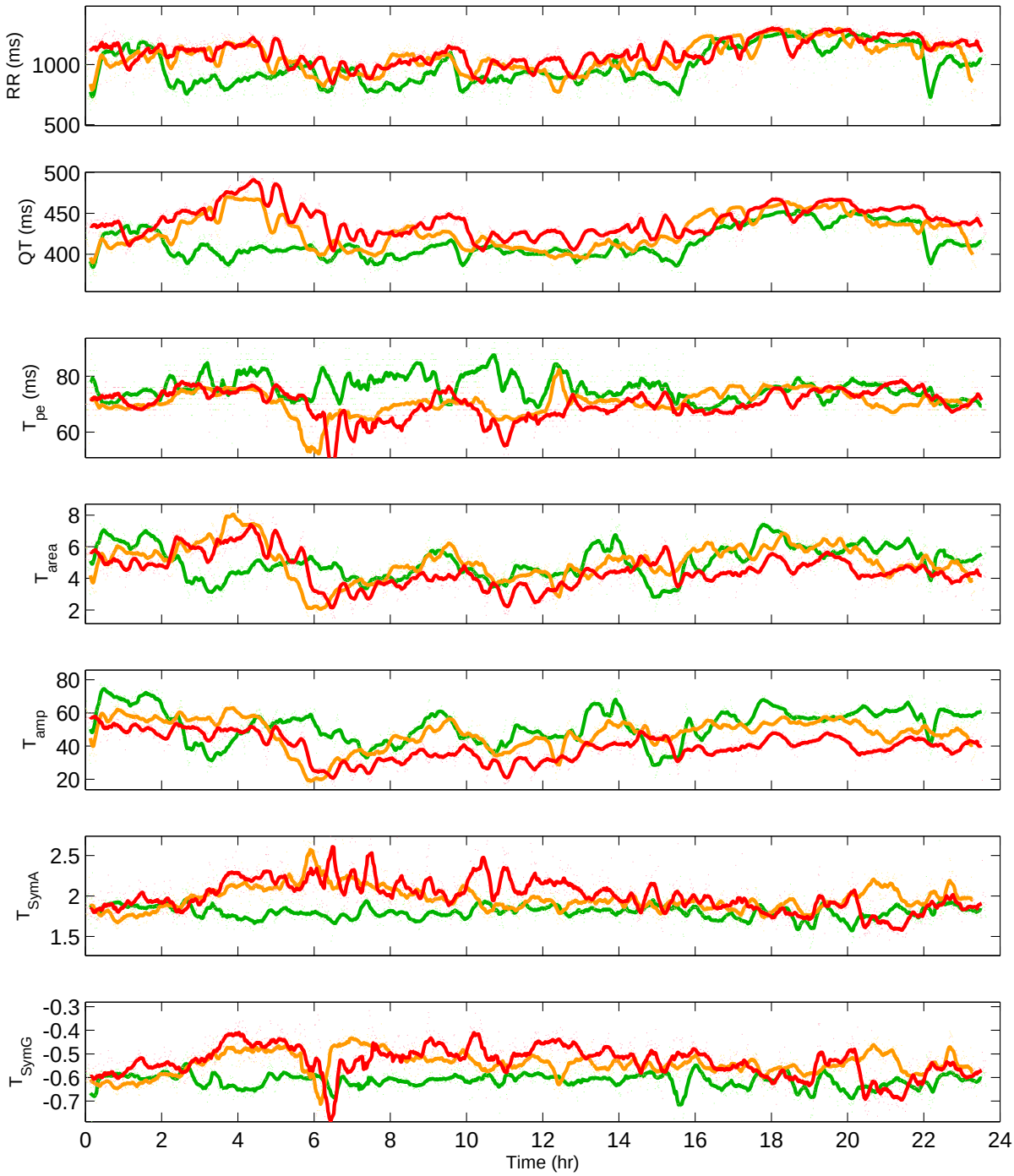


Figure 7.3: Individual interval and morphology biomarkers for a 24-hour Holter ECG recording from lead II for one subject from baseline day (green), D1 (amber) and D2 (red). A median filter is first applied to each one-minute analysis window to generate a representative biomarker per minute. A 15-minute moving average is then applied to the full 24-hour time series and is shown in the plot as a solid line

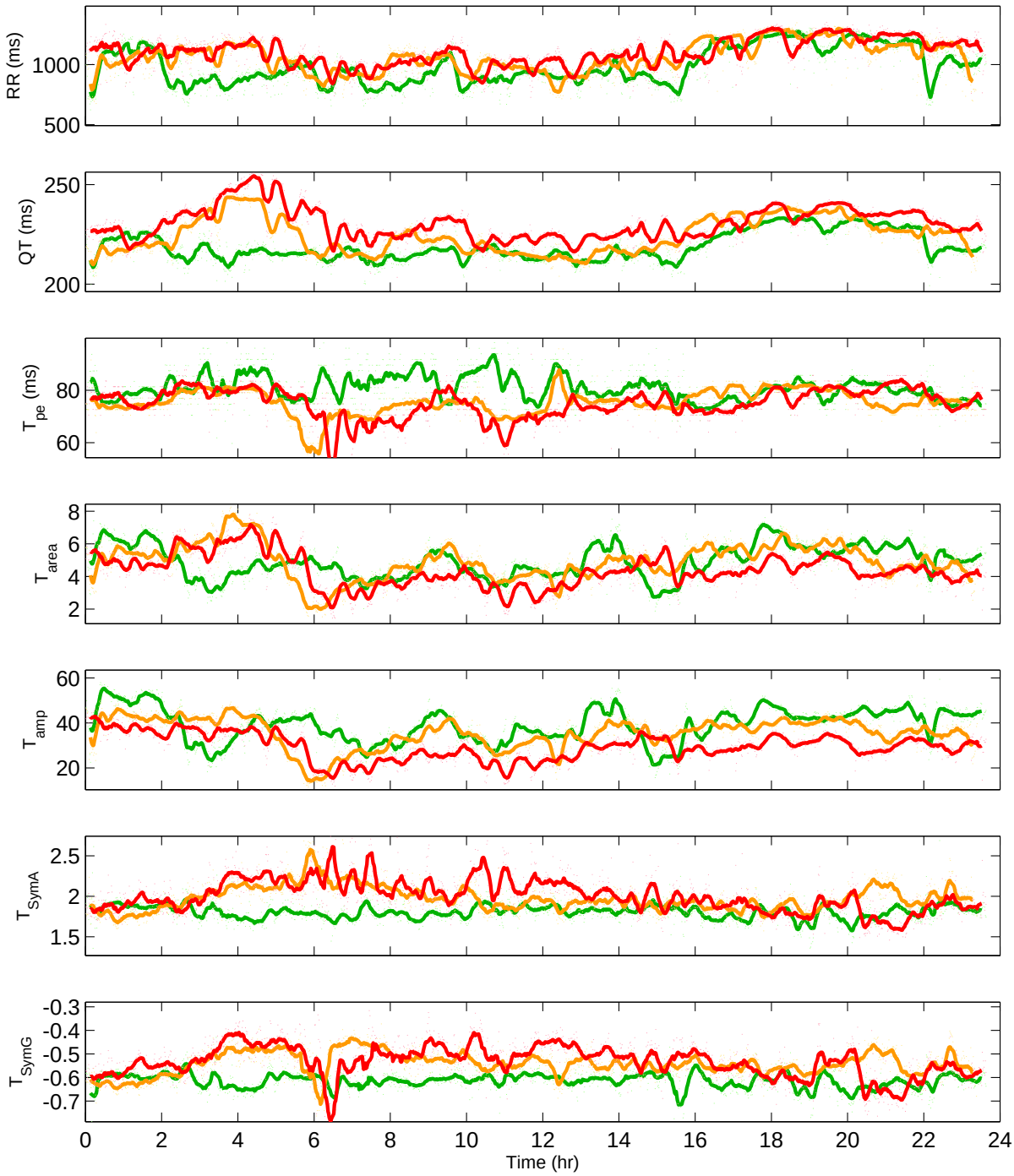


Figure 7.4: Individual heart rate corrected interval and morphology biomarkers for a 24-hour Holter ECG recording from lead II for one subject from baseline day (green), D1 (amber) and D2 (red). A median filter is first applied to each one-minute analysis window to generate a representative biomarker per minute. A 15-minute moving average is then applied to the full 24-hour time series and is shown in the plot as a solid line.

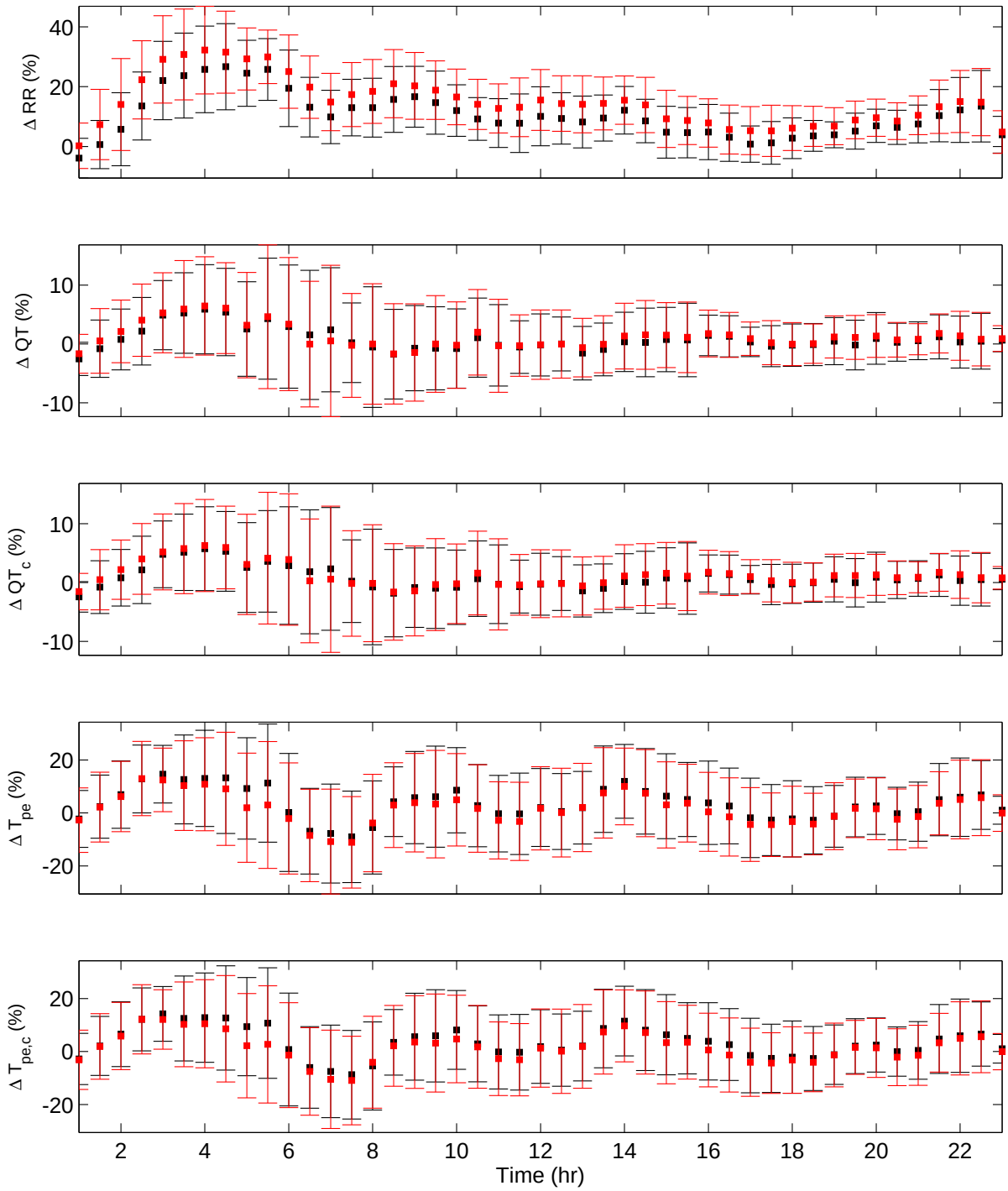


Figure 7.5: Mean effect of 160 ms (black) and 320 mg (red) of sotalol on RR, QT and T_{pe} across all subjects in the study. The drug effect on the heart rate corrected QT and T_{pe} interval is shown beneath the respective interval plots on the same vertical axis scale. The mean change in heart rate corrected biomarker, with respect to baseline, for each 30-minute period is shown, with error bars associated with each point representing one standard deviation on either side of the mean. Note the different scales on the vertical axes of different biomarkers.

results in a dose-dependent decrease of T_{area} and T_{SymA} ($p < 0.0001$). The mean T_{area} effect shows an initial increase up to 3 hours after dosing before decreasing, reaching a maximum absolute effect of 22.39% at 420 min after dosing for 160 mg sotalol. In contrast, the mean effect of 160 mg sotalol on T_{amp} increases reaching a maximum of 16.69% at 450 min after dosing. The effect of sotalol on T-wave symmetry biomarkers is also varied. The mean T_{SymA} effect shows a decrease with the effect of sotalol, with a maximum effect of -25.75% for 160 mg sotalol, 300 min after dosing. The mean T_{SymG} effect, on the other hand, shows a dramatic increase with the effect of sotalol, reaching a maximum effect of 39.57% at 240 min after dosing. The effect of heart rate correction on the biomarkers across all subjects for 160 mg sotalol is varied. Individual heart rate correction had a significant effect on QT, T_{area} and T_{amp} ($p < 0.0001$). The effect of heart rate correction on T_{pe} was less pronounced ($p = 0.021$).

The varied effect of sotalol on interval and morphology biomarkers has been observed in similar studies of sotalol. Couderc et al. [7] investigated the effects of sotalol on T-wave area-based repolarisation duration parameters from 38 healthy volunteers and found that the increase of repolarisation duration due to sotalol was smallest at 25% total cumulative area (29 ms), larger at the 50% mark (47 ms) and greatest at 97% total cumulative area (73 ms). In other words, the effect of sotalol on the duration of repolarisation is more exaggerated towards the end of the repolarisation process. This might explain the varied effects observed morphology biomarkers.

The magnitude and timing of the mean maximum effect is important in understanding the effects of sotalol on ventricular repolarisation. Table 7.3 lists the mean maximum effect, the timing of the maximum effect and a dimensionless measure of biomarker sensitivity for both heart rate corrected and raw biomarker measurements. The sensitivity of each biomarker (S) is calculated as the absolute maximum mean effect normalised by the sum of the biomarker variance across all subjects, i.e.

$$S = \frac{\max |\bar{E}_t|}{\sqrt{\sum_{i=1}^{N} \sum_{n=1}^{T} \sigma_{i,n}^2}}, \tag{7.4}$$

where $\bar{E}_t$ is the average biomarker effect at time t, and $\sigma_{i,n}^2$ is the variance for the nth 30-minute window for patient i.

The results in Table 7.3 show raw and heart rate corrected biomarkers. The morphology-based biomarkers are more sensitive to the drug effect, with T_{SymA} showing the greatest

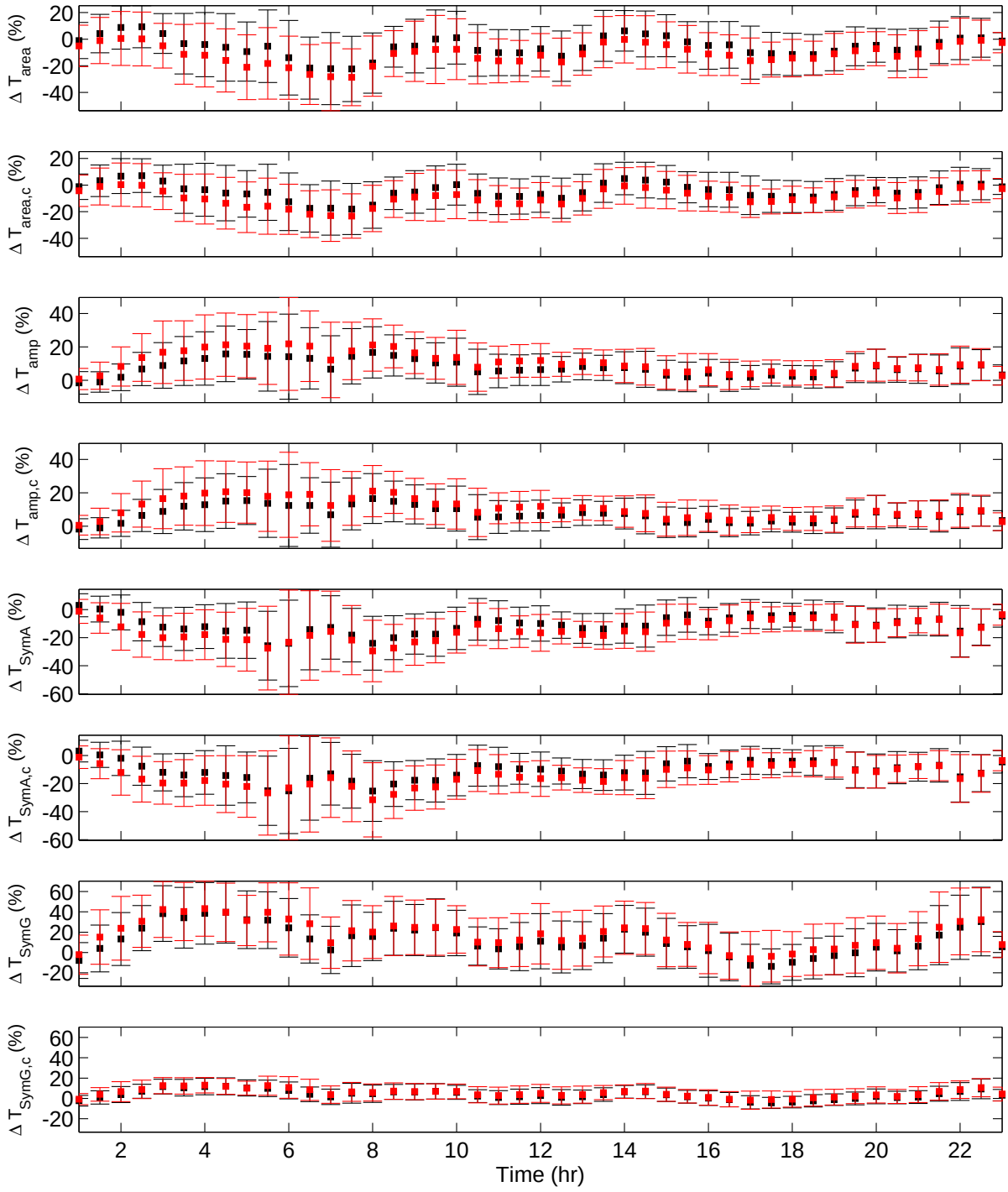


Figure 7.6: Mean effect of 160 ms (black) and 320 mg (red) of sotalol on morphology biomarkers, namely T_{area}, T_{amp}, T_{SymA} and T_{SymG}, across all subjects in the study. The drug effect on the heart rate corrected morphology biomarkers is shown beneath the respective interval plots on the same vertical axis scale. The mean change in heart rate corrected biomarker, with respect to baseline, for each 30-minute period is shown, with error bars associated with each point representing one standard deviation on either side of the mean. Note the different scales on the vertical axes of different biomarkers.

(a) Interval and morphology biomarkers

Biomarker	**Max effect (%)**		**Time (min)**		**Sensitivity**	
	D1	D2	D1	D2	D1	D2
QT	5.90	6.46	210	210	0.1437	0.1441
T_{pe}	14.63	12.99	150	120	0.1440	0.1232
T_{area}	-22.39	-28.66	420	420	0.1786	0.2266
T_{amp}	16.69	21.75	450	330	0.2085	0.2453
T_{SymA}	-25.75	-29.49	300	450	0.2553	0.2674
T_{SymG}	39.57	43.19	240	210	0.2394	0.2387

(b) Heart rate corrected biomarkers

Biomarker	**Max effect (%)**		**Time (min)**		**Sensitivity**	
	D1	D2	D1	D2	D1	D2
QT	5.76	6.30	210	210	0.1473	0.1466
T_{pe}	14.22	12.16	150	120	0.1484	0.1223
T_{area}	-17.99	-23.29	420	420	0.1844	0.2266
T_{amp}	16.52	20.98	450	450	0.2131	0.2463
T_{SymA}	-25.34	-31.57	450	450	0.2517	0.2837
T_{SymG}	11.96	13.00	240	210	0.2467	0.2397

Table 7.2: Summary of the drug effects of 160 mg (D1) and 320 mg sotalol on interval and morphology: (a) shows the results for the raw interval and morphology biomarkers, whereas (b) shows the results from heart rate corrected biomarkers. The maximum mean effect and the timing of that effect is shown for D1 (n=26) and D2 (n=11). The biomarker sensitivity, i.e. maximum absolute effect over the total variance of the biomarker, is shown for each drug day.

sensitivity to sotalol concentration. The sensitivity of QT and T_{pe} is comparable. In all instances, save one, heart rate correction tends to reduce the mean maximum effect. In terms of the magnitude of the mean maximum effect, T_{SymA} shows the largest effect after heart rate correction, whereas without heart rate correction T_{symG} shows a 39.6 and 43.2% increase with for 160 mg and 320 mg of sotalol, respectively.

The effect of sotalol tends to exhibit an earlier mean maximum effect on QT and T_{pe} intervals, with the maximum effect for the QT interval occurring around 210 min after dosing on both dosage days. The maximum effect on the morphology biomarkers, with the exception of T_{symG}, tends to occur later, around 420 to 450 min, after dosing. The maximum effect of T_{symG} occurs at 240 min for 160 mg and 210 min for 320 mg.

7.3 Discussion

The results reported above can now be discussed in the light of the insights gained from the modelling simulations in Chapter 4. But first, it is important to acknowledge that the pharmacological effect of sotalol is two-fold: firstly, that it slows the heart rate and, secondly, that it blocks I_{Kr}. The impact of these two sotalol effects on ventricular repolarisation, as characterised by the interval and morphology biomarkers, will sometimes act together and sometimes against each other.

The Holter results in this chapter have shown that sotalol has a significant effect on the heart rate, as well as the timing and morphology biomarkers ($p < 0.0001$). With the exception of T_{area} and T_{SymA}, the effect of sotalol tends to increase the biomarkers (including the RR interval). T_{area} seems to initially increase before decreasing, reaching a maximum drug effect of -22.39% at 420 min for 160 mg sotalol. T_{SymA}, on the other hand, decreases steadily between 2 to 10 hours after dosing. The decrease of T_{SymA} might be due to the decrease in heart rate.

As presented in Table, the sensitivity of the morphology biomarkers is greater than the QT or T_{pe} intervals. In addition, the maximum effect tends to take place after the maximum effect on the RR interval. A possible explanation is that the effect of sotalol on TDR is delayed or that the effect on heart rate effects the morphology biomarkers. This could be investigated further by controlling subject heart rate during the first six hours of the study.

The modelling results in Section 4.3 showed that T_{pe} and T_{amp} increased the most with

increasing sotalol concentration (see Figure 4.17). However, in the Holter ECG results the T-wave symmetry biomarkers, T_{SymA} and T_{symG}, showed the largest absolute effect with sotalol. Due to the fact that sotalol effects the latter phases of repolarisation, this phenomenon is not altogether unsurprising. However, the decrease in T_{area} observed in the Holter results is not predicted in the model and implies that there is a decrease in the magnitude and duration of the repolarisation gradients. This might be caused by a increase in opposing repolarisation transmural and apex-basal gradients between the epicardial and mid-myocardium, and the mid-myocardium and endocardium in the intact heart which is not sufficiently captured by the model.

Chapter 8

Discussion

This final chapter summarises the main contributions of this thesis, discusses the limitations of the modelling work and the techniques developed within it, and finally presents a number of future research directions and challenges.

8.1 Summary

The objective of this thesis was to identify alternative biomarkers for assessing the proarrhythmic potential of new pharmaceutical compounds. The combined approach of using both forward cardiac modelling and automated ECG analysis, allowed the effects and underlying mechanisms of sotalol to be investigated on interval and morphology biomarkers. The major results of this investigation can be summarised as follows:

- T-wave morphology biomarkers are more sensitive than the QT and T_{pe} intervals to the effects of sotalol on ventricular repolarisation

This thesis also contributed to both the cardiac modelling and automated ECG analysis fields. The contributions to these two fields are discussed in more detail below.

Cardiac modelling

The early chapters of this thesis presented a novel computational model of the interaction between the drug compound sotalol and I_{Kr}. The I_{Kr}-sotalol model was incorporated within a human ventricular AP model arranged in a multi-cellular 1-D fibre so that the mechanisms underlying sotalol's effects on repolarisation dynamics, as characterised by biomarkers derived from a simulated pseudo-ECG signal, could be investigated. The benefits of this approach over traditional inverse analysis for repolarisation dynamics can be summarised as follows:

- The ability to *simulate* a wide range of conditions
- The ability to *derive* biomarkers on sub-cellular, cellular and multi-cellular scales.

Previous attempts to model the effects of drugs on cardiac activity have been limited to the cellular level, with a few notable exceptions [164,165], and these have not investigated the effects on human tissue. As previously discussed in Chapter 4, the models implemented in this thesis have consistently been based on human tissue.

The effects of sotalol on the ventricular repolarisation dynamics based on the analysis of simulation results at the sub-cellular, cellular and multi-cellular levels can be summarised as follows:

- Reduction in I_{Kr}
- Spatially-heterogeneous prolongation of APD that is most pronounced in the mid-myocardial cells
- Prolongation of the duration of repolarisation (QT and T_{pe} intervals)
- Increase in transmural dispersion of repolarisation.

The effects of sotalol were observed to be dose and heart rate dependent. Morphology biomarkers tended to be more sensitive to the presence of sotalol than the QT interval.

Automated ECG analysis

This thesis has also presented a new approach for automated ECG interval and morphology analysis based on the use of wavelet encoding and probabilistic models. The benefits of this approach can be summarised as follows:

- The ability to *learn* from ECG data set annotated by human experts
- The ability to produce *confidence measures* for automated ECG annotations
- The ability to *characterise* T-wave morphology in 24-hour Holter ECG recordings in a robust and efficient manner.

Given the wide range of ECG morphologies and noise present in 24-hour Holter ECG recordings, the wavelet transform is particularly well suited for the analysis of the ECG

because it is able to capture and isolate the varying spectral characteristics of the waveform. The same UWT coefficients can be used for R-peak detection, signal encoding and ECG de-noising. In addition, the probabilistic approach allows a statistical *confidence measure* to be determined for the annotations generated by the HMM so that those waveforms with *low confidence* can be identified and excluded from subsequent morphology analysis.

Although the use of hidden Markov models for ECG interval analysis has been explored previously [205, 237, 238, 241, 248] the combination of wavelet-based R-peak detection and beat-specific HMM feature delineation has not previously been investigated. Chapter 6 of this thesis showed how this approach can be efficiently implemented to ensure the robust segmentation and characterisation of T-wave morphology. This was then applied to 24-hour Holter ECG recordings to investigate the effects of sotalol on ventricular repolarisation. These can be summarised as follows:

- Prolongation of the RR, QT and T_{pe} intervals
- Increase in T-peak amplitude and gradient-based T-wave symmetry
- Decrease in T-wave area and area-based T-wave symmetry
- The maximum effect of sotalol on morphology biomarkers occurs after the maximum effect on QT and T_{pe} intervals.

The effects of sotalol on T-wave morphology biomarkers, which are dose-dependent, are obscured by the dependency of these biomarkers on heart rate.

8.2 Limitations and future work

There are a number of limitations in work reported in this thesis, which may be overcome by opening up new avenues for further research. This section will discuss the limitations of both the modelling work and the automated ECG analysis methods, and briefly discuss further work relating to these limitations.

Multi-cellular modelling

The parameters used in the 1-D model were determined from human tissue. However, a 1-D fibre is a vast simplification of the intact human ventricular myocardium. A sensitivity

analysis should be conducted to adequately assess the effects of sotalol concentration on the interval and morphology biomarkers, as characterised from the pseudo-ECG. An appropriate sensitivity analysis would measure the change in model output (pseudo-ECG) having varied a single model parameter in a predefined region of the parameter space [286].

However, to limit such an analysis to an 1-D fibre geometry would be futile because of the inherent limitations of the geometry. For example, the inter-cellular coupling is limited to the longitudinal axis of the fibre, which is not the case in myocardial tissue. Therefore, it would be better to construct a multi-cellular geometry that would allow for a realistic representation of intact human myocardium so that an in-depth sensitivity analysis of the model could be conducted. A 2-D or 3-D wedge model might be sufficient to investigate to what extent the model parameters affect the impact of sotalol's inhibition of I_{Kr} on ventricular repolarisation dynamics.

Dual effect of sotalol

As discussed in Section 1.5, sotalol is a racemic compound that has both Class II (β-blocking properties) and Class III (prolonged action potential) anti-arrhythmic effects on the heart. The model presented in this thesis only characterises the effect of sotalol on I_{Kr}, i.e. Class III effects. However, as discussed in Section 7.3, T-wave morphology biomarkers are found to be more sensitive to both heart rate and drug effects. To understand to what extent heart rate and I_{Kr} inhibition affect T-wave morphology, it would be necessary to expand the model to include the sotalol's Class II effect. Alternatively, it might be worthwhile conducting an exercise stress ECG study[1] with healthy volunteers to control the heart rate so that the effects of sotalol and heart rate on morphology biomarkers can be thoroughly investigated using surface ECG recordings.

Composite HMMs

The greatest limitation of the HMM segmentation algorithm is the assumption of statistical independence between successive observations, as discussed in Section 5.2.2. The use of wavelet encoding and derivative features in the HMM observation vector is an attempt to incorporate temporal and spectral "context" from neighbouring ECG signal samples into each HMM observation vector. Although this approach works reasonably

[1] An exercise stress ECG test requires the subject to walk or pedal on an exercise machine to test the effect of exercise on the heart.

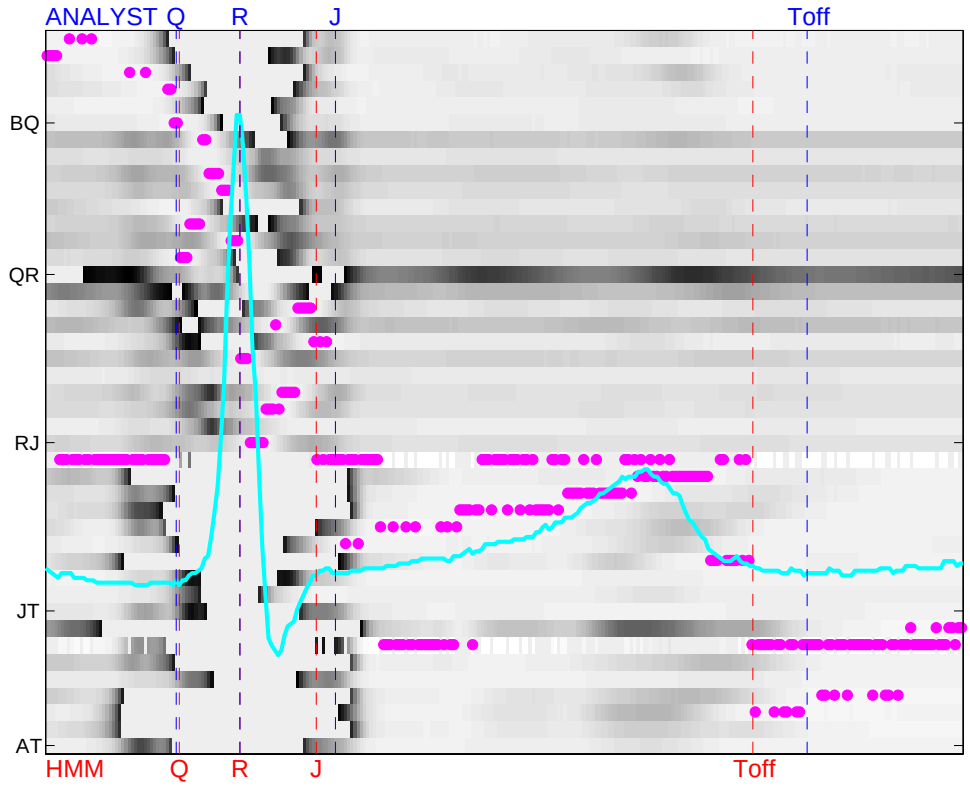


Figure 8.1: Log observation probabilities, i.e. $\log P(z_n = j|\mathbf{x}_n)$, for each Gaussian kernel in the GMMs for one ECG waveform (shown in cyan). The individual kernel activations are shown on a grey-scale, where light values represent high activations and dark values low activations. The largest log observation probability for every sample is highlighted with a purple dot.

well in practice, it does not adequately capture the temporal dependencies in a typical ECG waveform.

Figure 8.1 illustrates the log observation probabilities (or activations) for each Gaussian kernel in the state GMM observation models. The kernel activations in given a GMM state observation model are independent form each other. In practice, however, there will typically be a sequence ordering in the activation of the kernels over the course of a normal ECG waveform, as seen in Figure 8.1. This ordering, or sequencing, information is lost in the HMM structure and therefore it is possible for the model to produce erroneous segmentations (with high confidence) for some ECG waveforms. Such is the case for segmentation shown in the figure, where $\mathrm{T_{off}}$ is 34 ms before the expert annotation.

To overcome this problem it would be necessary to incorporate the dynamics or sequencing information for the kernel activation within each state into the HMM architecture. One possible approach would be reduce each state with a GMM observation model into a left-to-right HMM, whereby each kernel in the GMM becomes a single Gaussian

observation model for each state in the left-to-right model. In this approach, the sequencing information of kernel activation would be incorporated into the transition matrix of the new HMM architecture. The self-transition and exit probabilities in the transition matrix could be estimated from the GMM mixing coefficients. However, the sequencing information of the kernels would still need to be determined.

A possible approach for overcoming this problem would be to use a two-step learning strategy. The first learning phase would be implemented as described in Section 6.1.2. The second phase would take the training segments for each particular state and partition the training segment into N equal sections, where N is the number of kernels in the GMM state observation model. The kernel *most* responsible for each section could then be determined by sorting some representative statistic (e.g. median) of the distribution of kernel responsibilities for each portion. This sequence information, along with the estimates of exit- and self-transition probabilities, would enable the transition probability matrix of the new HMM to be defined.

Cumulative distribution function with Viterbi

As discussed in Section 6.1, GMMs are effective in modelling multi-modal data and are often used as observation models in speech recognition systems [243]. However, if the data density between two states is significantly different then the density values for similar or overlapping regions of the data space will be significantly different. This is one of the reasons for the early T_{off} annotation error. The GMM for the JT state has to cover a much broader area of the data space than the baseline state. As a result, the density values for the overlapping regions around T_{off} will be much larger for the baseline-state GMM than for the JT-state GMM. The Viterbi algorithm (discussed in Appendix B.2.1) does not normalise or scale the density values for the "peakiness" of the density function and so the inference process tends to set the state transition from JT to baseline state earlier than the true T_{off}.

This problem could be partially overcome by the method proposed above for reducing the composite HMM structure to a left-to-right combination of HMM states, with a single Gaussian as the observation density model. A better approach would be to use the cumulative distribution function and probabilistic values (between 0 and 1) in the Viterbi algorithm, instead of density values. This would significantly increase the computational

burden of the Viterbi algorithm, particularly if a GMM were used as the observation density model because the probability value would have to be computed by integrating under the probability contour for any given observation [287]. However, this approach could also be implemented for the reduced HMM architecture with single Gaussian density models, which might provide improved performance and computational efficiency.

8.3 Conclusion

In this thesis a combined approach of forward cardiac modelling and inverse ECG analysis has been adopted to investigate the effects of sotalol, a compound known to have pro-arrhythmic effects, on ventricular repolarisation. A computational model of sotalol and I_{Kr}, an ion channel that plays a critical role in ventricular repolarisation, was developed. This model was incorporated into a model of the human ventricular myocyte, and subsequently arranged in a 1-D fibre model of 200 cells. In parallel, an automated ECG analysis method based on machine learning, signal processing and time-frequency analysis was developed to identify fiducial points in ECG waveforms for interval and morphology analysis.

The thesis has investigated the mechanisms underlying the effects of drug inhibition of I_{Kr} on ventricular repolarisation as captured by the simulated ECG signal. Secondly, it has shown how the combination of UWT encoding and HMM inference can be effectively used to segment 24-hour Holter ECG recordings. Finally, the thesis has provided insight into the drug effects of sotalol on ventricular repolarisation as captured by biomarkers extracted from the surface ECG.

Appendix A

Wavelet Analysis

A.1 Undecimated wavelet transform

The undecimated wavelet transform (UWT) has been described in literature under a number of different names including *stationary* WT [**?**], the *maximal overlap* DWT [197] and the *translation-invariant* WT [204]. The UWT extends the DWT by allowing the time-shift parameter to take on any value [**?**]. The set of UWT time-frequency atoms can be described as follows:

$$\psi_{2^k,\tau}(t) = \frac{1}{\sqrt{2^k}}\psi\left(\frac{t-\tau}{2^k}\right), \qquad k \in \mathbb{Z}, \tau \in \mathbb{R}. \tag{A.1}$$

The wavelet atoms do not form an orthogonal basis, and the resulting wavelet coefficients are redundant and strongly correlated with neighbouring coefficients along the time axis. However, a significant advantage of the UWT is that it is translation invariant, i.e. a shift in the time domain results in an equal shift in the wavelet domain. More formally, the undecimated wavelet transform of a function $x \in \mathbb{L}^2(R)$ is given by:

$$W_s(\tau) = \frac{1}{\sqrt{2^k}}\int_{-\infty}^{+\infty} x(t)\psi^*\left(\frac{t-\tau}{2^k}\right)dt, \qquad k \in \mathbb{Z}, \tau \in \mathbb{R} \tag{A.2}$$

where $W_s(\tau)$ are the translation-invariant UWT coefficients at scale $s = 2^k$ and time-shift τ, and $\psi^*(t)$ is the complex conjugate of the mother wavelet.

The UWT can be computed in an efficient manner using a filter bank structure, in much the same way that the discrete WT is implemented. For a detailed description of the DWT please refer to [197]. The algorithm is based on a class of filters known as *conjugate mirror filters* (CMFs). These filters are specially designed pairs of high-pass and low-pass filters with finite impulse responses (FIR), which enable a signal to be decomposed into a set of representative coefficients and then perfectly reconstructed from these coefficients. The high-pass filter is referred to as the *wavelet* filter and generally assigned the letter g.

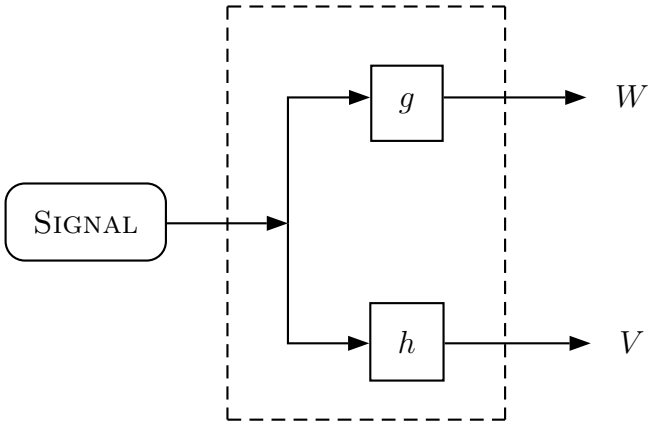


Figure A.1: The basic building block of the undecimated wavelet transform (UWT), a pair of conjugate mirror filters (CMFs). This filter bank structure is equivalent to a single level UWT.

The low-pass filter is known as the *scaling* filter and denoted using the letter h. Figure A.1 shows a basic pair of CMFs that form the basis of the filter bank algorithm.

The wavelet filter, g, satisfies the following conditions:

$$\sum_{m=1}^{M} g_m = 0 \tag{A.3}$$

$$\sum_{m=1}^{M} g_m^2 = 1 \tag{A.4}$$

$$\sum_{m=-\infty}^{\infty} g_m \cdot g_{m+2i} = 0,\ i \in \mathbb{Z},\ i \neq 0. \tag{A.5}$$

where M is the number of filter coefficients [197]. Equations A.3 and A.4 ensure that the impulse response of the filter has zero mean and unit energy, respectively. Equation A.5 ensures that the impulse response is orthogonal to its even shifts in the dyadic scale range. As a result of this orthogonality constraint the length of the filter (M) must be even.

The scaling filter h is identical to the high-pass filter except that

$$\sum_{m=1}^{M} h_m = \sqrt{2}. \tag{A.6}$$

This ensures that the impulse response of the low-pass filter has non-zero mean, i.e. if $H(\omega)$ is the Fourier transform function of h then in the frequency domain Equation A.6 is equivalent to $H(0) = \sqrt{2}$ [282]. The final condition classifying g and h as conjugate mirror filters is that the two filters are mutually orthogonal:

$$\sum_{m=-\infty}^{\infty} g_m \cdot h_{m+2i} = 0,\ i \in \mathbb{Z}. \tag{A.7}$$

Equation A.7 can be satisfied if the filters are defined in the following manner:

$$g_m = (-1)^{m+1} \cdot h_{M-1-m}, \tag{A.8}$$

$$h_m = (-1)^m \cdot g_{M-1-m}. \tag{A.9}$$

Finally, To ensure translation-invariance and wavelet analysis on dyadic scales only, the coefficients of the UWT wavelet and scaling filters are normalised for each level k as follows:

$$h^k = \frac{h}{2^{k/2}}, \tag{A.10}$$

$$g^k = \frac{g}{2^{k/2}}. \tag{A.11}$$

Figure A.2 shows the filter bank structure for the UWT. Given a signal $x(t)$ of length N, the wavelet and scaling coefficients at $k = 1$ can then calculated as

$$W_2(\tau) = \sum_{m=1}^{M} h_m^1 x(\tau - m \mod N), \tag{A.12}$$

$$V_2(\tau) = \sum_{m=1}^{M} g_m^1 x(\tau - m \mod N), \tag{A.13}$$

where $\tau = 0, \ldots, N-1$. For $k > 1$, the wavelet and scaling coefficients are obtained as follows

$$W_{2^k}(\tau) = \sum_{m=1}^{M} h_m^k V_{2^{k-1}}(\tau - 2^{j-1}m \mod N), \tag{A.14}$$

$$V_{2^k}(\tau) = \sum_{m=1}^{M} g_m^k V_{2^{k-1}}(\tau - 2^{j-1}m \mod N). \tag{A.15}$$

Therefore the wavelet and scaling coefficients, W_{2^k} and V_{2^k}, at each level are obtained by circular filtering with respect to the wavelet and scaling filters, h^k and g^k. The samples from the wavelet filter g^k becomes the wavelet UWT coefficients at scale $s = 2^k$, whereas the output from the scaling filter h^k branch becomes the input for the CMFs at the next level $k+1$. This recursive procedure allows the UWT coefficients to be computed for each scale $s = 2^k,\ k = 1, \ldots, k_{\max}$, from a cascade of CMFs. Finally, the scaling coefficients are equivalent to the low-pass filter output at the maximum scale $s_{\max}$ [197].

To ensure dyadic scaling the CMFs at successive levels, $2^{k-1} - 1$ zeros are inserted between the original filter coefficients. For example, the first three levels of the wavelet

Level	Scale	3db Pass-band (Hz)
1	2	> 159.2
2	4	$46.4 \sim 104.4$
3	8	$21.6 \sim 48.8$
4	16	$10.8 \sim 24.20$
5	32	$5.6 \sim 12$
6	64	$2.8 \sim 6$
7	128	$1.60 \sim 3$

Table A.1: Amplitude responses and 3db pass-bands of the filters in a UWT filter bank using a cubic spline approximation of the first derivative of a Gaussian as the wavelet function

filter coefficients of the UWT are given by:

$$h^1 = \{h_0^1, h_1^1, \ldots, h_{M-1}^1\} \tag{A.16}$$

$$h^2 = \{h_0^2, 0, h_1^2, 0, \ldots, 0, h_{M-1}^2\} \tag{A.17}$$

$$h^3 = \{h_0^3, 0, 0, 0, h_1^3, 0, 0, 0, \ldots, 0, 0, 0, h_{M-1}^3\} \tag{A.18}$$

This procedure is known as *algorithme á trous* and ensures that the UWT can be computed in time $\mathcal{O}(N \log N)$, for a signal of length N [197].

Each CMF pair at each level of the filter bank can be considered as a specially designed *band-pass* filter that satisfies a constant relative bandwidth property, referred to as "constant-Q" [**?**]. This property refers to the *quality* Q of the filter and is defined as:

$$Q = \frac{f_0}{\Delta f}, \tag{A.19}$$

where f_0 is the centre frequency of the filter, and Δf is the bandwidth of the filter at an amplitude response of $|G(f_0)|/\sqrt{2}$. Therefore, for constant-Q filters the bandwidth of the filter is directly proportional to the centre frequency of the filter. Thus, the UWT filter bank algorithm can be considered as a cascade of band-pass filters that sub-divide the frequency axis in a *logarithmic* fashion, i.e. as the scale doubles, the bandwidth of the corresponding filter halves. Table A.1 shows the effective 3 db pass-bands for a 7-level UWT using a cubic spline approximation of the first derivative of a Gaussian as the wavelet function.

The UWT can also be viewed as a matrix-vector product between a suitably defined UWT projection matrix $\mathcal{W}$ and the vector of signal samples $\mathbf{X}$ of length N, i.e. $\mathbf{W} = \mathcal{W}\mathbf{X}$. The matrix of wavelet and scale coefficients, denoted $\mathbf{W}$ has $k_{\max} + 1$ rows, where $k_{\max}$ is the maximum level of the UWT decomposition. More specifically, the first level UWT

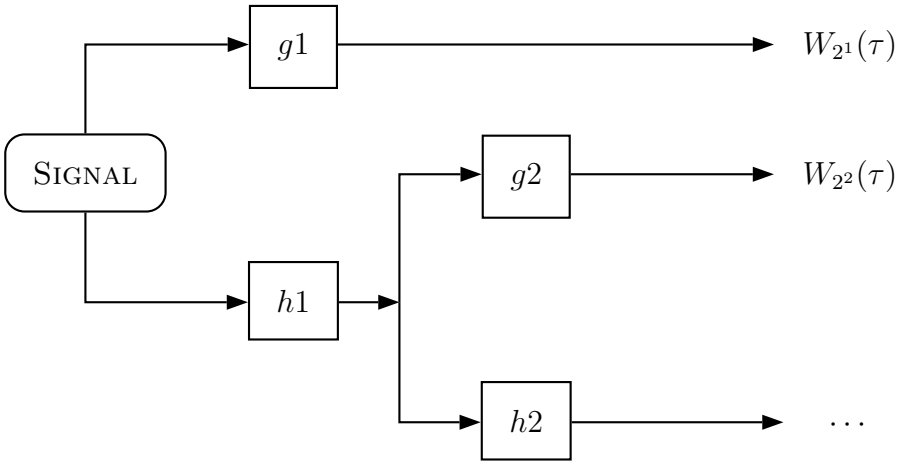


Figure A.2: Filter bank structure of conjugate mirror filters (CMFs) for the undecimated wavelet transform.

can be given by:

$$\begin{bmatrix} \mathbf{W_1} \\ \mathbf{V_1} \end{bmatrix} = \begin{bmatrix} \mathcal{A}_1 \\ \mathcal{B}_1 \end{bmatrix} \mathbf{X} \tag{A.20}$$

where $\mathcal{A}_1$ and $\mathcal{B}_1$ are $N \times N$ matrices of wavelet and scale filter coefficients, respectively. The rows in $\mathcal{A}_1$ and $\mathcal{B}_1$ are composed of time-reversed filter coefficients followed by a series of zeros, with each successive row circularly shifted (to the right) by one, i.e.:

$$\mathcal{A}_1 = \begin{bmatrix} g1_{M-1} & g1_{M-2} & \cdots & g1_1 & g1_0 & 0 & \cdots & 0 \\ 0 & g1_{M-1} & \cdots & g1_2 & g1_1 & g1_0 & \cdots & 0 \\ \vdots & \vdots & \ddots & \vdots & \vdots & \ddots & vdots & \\ g1_{M-2} & g1_{M-3} & \cdots & 0 & 0 & 0 & \cdots & g1_1 \end{bmatrix}.$$

The matrices $\mathcal{A}_1$ and $\mathcal{B}_1$ effectively implement the circular convolutions performed by the CMFs.

More generally, the UWT up to level $k_{\max}$ is given by:

$$\begin{bmatrix} \mathbf{W_1} \\ \mathbf{W_2} \\ \vdots \\ \mathbf{W}_{k_{\max}} \\ \mathbf{V}_{k_{\max}} \end{bmatrix} = \begin{bmatrix} \mathcal{A}_1 \\ \mathcal{A}_2\mathcal{B}_1 \\ \vdots \\ \mathcal{A}_{k_{\max}}\mathcal{B}_{k_{\max}-1}\cdots\mathcal{B}_1 \\ \mathcal{B}_{k_{\max}}\mathcal{B}_{k_{\max}-1}\cdots\mathcal{B}_1 \end{bmatrix} \mathbf{X}, \tag{A.21}$$

where $\mathcal{A}_k$ and $\mathcal{B}_k$ are $N \times N$ matrices, with each row composed of time-reversed filter coefficients corresponding to the k^{th} level wavelet and scale filter, respectively, with successive rows circularly shifted (to the right) by one[1] [197].

[1]This definition of $\mathcal{A}_1$ and $\mathcal{B}_1$ assumes that the length of the CMFs at the maximum scale is less than or equal to the length of the signal, i.e. $(2^{k_{\max}} - 1)(M - 1) + 1 \leq N$. If this is not the case, the matrices must be defined in terms of the *periodised* versions of the filters h and g (see page 32. of [197]).

A.2 Inverse Undecimated Wavelet Transform

An important property of CMFs is that they allow a signal to be perfectly reconstructed from the decomposed set of representative coefficients. In order to reconstruct the original signal, a set of reconstruction (or synthesis) filters corresponding to the decomposition (or analysis) filters, h and g, is required. The reconstruction filters, denoted by $\bar{h}$ and $\bar{g}$, are simply time-reversed versions of the original CMFs:

$$\bar{h} = h_{M-m-1}, \tag{A.22}$$

$$\bar{g} = g_{M-m-1}. \tag{A.23}$$

As a result, in the Fourier domain, the reconstruction filters have an identical amplitude response but an opposite phase response, i.e. they are 180° out of phase when compared with the decomposition filters. The reconstruction filters therefore act as *anti-aliasing* filters, and perfectly cancel out the aliasing introduced by the decomposition filters at each level of the filter bank [198].

The inverse DWT applies a filter bank algorithm to the dyadic wavelet coefficients to reconstruct the original signal. The inverse DWT is both *complete* and *unique*. However, as previously mentioned, the UWT is a redundant representation of the original signal [197]. Therefore, the inverse operator is not unique. Several approaches have been proposed to reconstruct the original signal from the UWT coefficients. The first approach is known as the *ϵ-basis inverse* of the UWT and selects some sequence ϵ of 0's and 1's to select from the UWT coefficients those corresponding to the ϵ-decimated DWT and then applies the inverse DWT to the selected coefficients to reconstruct the original signal. The second approach, known as the *average basis inverse*, corresponds to finding the inverse of every possible sequence of ϵ and averaging the results. More specifically, given the first level wavelet and scale coefficients, $\mathbf{W_1}$ and $\mathbf{V_1}$, the original signal, $\mathbf{X}$, can be determined as follows:

$$\mathbf{X} = \frac{1}{2}\left(\mathbf{B}_1^T\mathbf{W}_1 + \mathbf{A}_1^T\mathbf{V}_1 + \mathbf{B}_{\tau,1}^T\mathbf{W}_{\tau,1} + \mathbf{A}_{\tau,1}^T\mathbf{V}_{\tau,1}\right) \tag{A.24}$$

Thus, more generally, for a signal of length 2^K, the original signal can be obtained recursively by evaluating the scale coefficients at each level, which requires $\mathcal{O}(K2^K)$ for K levels. Figure A.3 illustrates the recursive procedure used to reconstruct the original signal from K level UWT wavelet and scale coefficients.

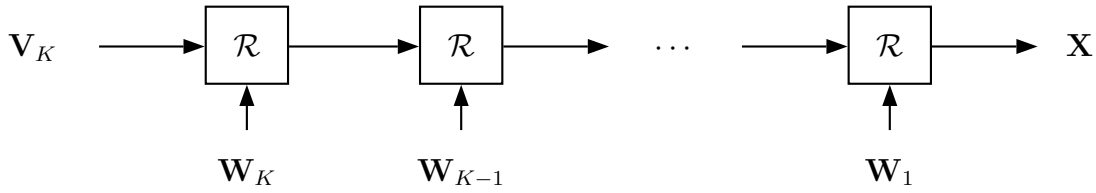


Figure A.3: Recursive process for reconstruction of the original signal, $\mathbf{X}$, from a J level UWT wavelet and scale coefficients.

Appendix B

Algorithms for HMM Implementation

B.1 Learning HMM parameters

As previously described in Section 5.2.2, a hidden Markov model (HMM) consists of three parameters, namely an initial state distribution ($\boldsymbol{\pi}$), a state transition probability matrix ($\mathbf{A}$) and an observation density model $\{\mathbf{B}_k|b_1, b_2, \ldots, b_K\}$ for each state K. The Expectation-Maximisation (EM) algorithm describes a general procedure for estimating the maximum likelihood parameters in statistical models given an *incomplete* data set. The "missing" data refers to a set of hidden or latent variables that, if known, would significantly simplify the estimation problem. In the case of training a HMM on ECG data, the missing data would be the waveform state labels associated with each data sample. The EM algorithm, referred to as the Baum-Welch algorithm when applied to HMMs, is used to train a HMM in an *unsupervised* learning mode. In *supervised* learning the initial state distribution $\boldsymbol{\pi}$ and state transition matrix $\mathbf{A}$ can be estimated using a *frequentist* approach, whereby the relative frequency of expert measurements identifying the K hidden states is used to determine $\boldsymbol{\pi}$ and $\mathbf{A}$. The initial state distribution π_i is calculated as the number of state observations n_i over the total number of observations, i.e.:

$$\pi_i = \frac{n_i}{\sum_{k=1}^{K} n_k}, \ i = 1, \ldots, K \tag{B.1}$$

The state transition probability matrix $\mathbf{A}$ can be estimated as the number of transitions between state i and j over the total number of transitions from state i, i.e. :

$$a_{ij} = \frac{n_{ij}}{\sum_{k=1}^{K} n_{ik}}, \tag{B.2}$$

where each element a_{ij} is an estimate of the probability of moving from state i to state j.

B.1.1 Baum-Welch algorithm

In unsupervised learning the objective is to determine the "optimal" model parameters from a given set of observations in a training data set without state labels. The Baum-Welch (BW) algorithm uses an initial guess of the model parameters to *estimate* the missing component labels, this is the E-step (or *expectation*). The maximisation step (or M-step) then uses these new values to update the model parameters by *maximising* them using the estimated *missing* data. These two steps are repeated until a suitable convergence criterion is satisfied. Thus, the general structure of the BW algorithm can be summarised as follows:

1. **Initialise:** Estimate the model parameters θ^1

2. **E-step:** Compute the function $\mathcal{Q}(\theta, \theta^l)$ as follows:

$$\mathcal{Q}(\theta, \theta^l) = \sum_{\mathbf{Z}} p(\mathbf{Z}|\mathbf{X}, \theta^l) \log p(\mathbf{Z}|\mathbf{X}, \theta^l). \tag{B.3}$$

3. **M-step:** Compute the new model parameters θ^{l+1} that maximises $\mathcal{Q}(\theta^{l+1}, \theta^l)$, as follows:

$$\theta^{l+1} = \underset{\theta}{\operatorname{argmax}}\, \mathcal{Q}(\theta, \theta^l) \tag{B.4}$$

4. **Loop:** Return to step 2 unless convergence criterion has been met

A fundamental property of the BW algorithm is that it will converge on a local maximum of the data log likelihood function, regardless of the choice of initial model parameters.

More formally, the BW algorithm maximises the data log likelihood $P(O \mid \lambda)$ of a given training data set for any initial estimate of the HMM model parameters $\lambda = (\mathbf{A}, \boldsymbol{\pi}, \mathbf{B})$. The missing data, $\mathbf{Z}$, is the *true* underlying state sequence that generated the given observation sequence. Therefore, it is necessary to consider the pairwise state probabilities $\xi_t(i, j)$ given the Markov dependency between the model states. The posterior probability of being in state s_i at time t and state s_j at $t+1$ given the model and observation sequence can be defined as:

$$\xi_t(i, j) = P(q_t = s_i, q_{t+1} = s_j|O, \lambda). \tag{B.5}$$

The E-step consists of calculating the expected values of these pairwise state probabilities using the forward and backward variables described in Section B.2.2 in the form

$$\begin{aligned}\xi_t^{l+1}(i,j) &= \frac{P(q_t = s_i, q_{t+1} = s_j, O|\lambda^l)}{P(O \mid \lambda^l)},\ t = 1, \ldots T-1 \\ &= \frac{\alpha_t(i) a_{ij} b_j(O_{t+1}) \beta_{t+1}(j)}{\sum_{i=1}^{K} \sum_{j=1}^{K} \alpha_t(i) a_{ij} b_j(O_{t+1}) \beta_{t+1}(j)}. \end{aligned} \tag{B.6}$$

It is possible to compute the state posterior probabilities $P(q_t = s_i \mid O, \lambda^l)$ by summing $\xi_t^{l+1}(i,j)$ over j or using the forward and backward variables as follows:

$$\begin{aligned}\gamma_t^{l+1}(i) &= \sum_{j=1}^{K} \xi_t^l(i,j)\ t = 1, \ldots T-1 \\ &= \frac{\alpha_t(i)\beta_t(i)}{p(O_{1:T}|\lambda^l)}. \end{aligned} \tag{B.7}$$

The M-step consists of updating the model parameters based on the values calculated in Equations B.6 and B.7. The summation of $\gamma_t^{l+1}(i)$ over time index t can be interpreted as the expected number of transitions made from state s_i. Similarly, summation of $\xi_t^l(i,j)$ over t can be interpreted as the expected number of transitions from state s_i to state s_j. The summation is from *t=1* to *t=T-1* because of the pairwise property of $\xi_t^l(i,j)$, therefore excluding the last time sample as the pairwise probability is undefined for time point T. The re-estimation formulae for model parameters $\boldsymbol{\pi}$ and $\mathbf{A}$ are:

$$\pi_t^{l+1}(i) = \gamma_1^l(i) \tag{B.8}$$

$$a_{ij}^{l+1} = \frac{\sum_{t=1}^{T-1} \xi_t^l(i,j)}{\sum_{t=1}^{T-1} \gamma_t^l(i)}. \tag{B.9}$$

The update formulae for the observation model depend on the type of model chosen to represent the HMM. In the case of GMM observation models, the posterior state probabilities are incorporated into the GMM update formulae defined in Equations B.14, B.15 and B.16 as follows:

$$P^{l+1}(j) = \frac{1}{N} \frac{\sum_{t=1}^{T} \gamma(k) R_n^l(j)}{\sum_{t=1}^{T} \gamma(k)}, \tag{B.10}$$

$$\boldsymbol{\mu}_j^{l+1} = \frac{\sum_{t=1}^{T} \gamma(k) R_n^l(j) \mathbf{x_n}}{\sum_{t=1}^{T} \gamma(k) R_n^l(j)}, \tag{B.11}$$

$$\boldsymbol{\Sigma}_j^{l+1} = \frac{\sum_{t=1}^{T} \gamma(k) R_n^l(j) (\mathbf{x}_n - \boldsymbol{\mu}^{l+1}(j))(\mathbf{x}_n - \boldsymbol{\mu}^{l+1}(j))^T}{\sum_{n=1}^{N} \gamma(k) R_n^l(j)}. \tag{B.12}$$

An important issue concerning the implementation of the BW algorithm is the initialisation of the model parameters, which requires an estimatation of the model parameters. This can implemented randomly or using *a priori* knowledge of the system.

B.1.2 EM for Gaussian mixture models

In order to learn the parameters of the observation density model, all of the observations corresponding to the expert state label i are extracted and used as the training data set for the observation model. The methods of learning the model parameters given the observation data, depend on the type of model. In the case of a GMM, the process of calculating the number of components, the mixing coefficients and the Gaussian parameters (μ_j and Σ_j) has two stages. Firstly, the optimal number of components needs to be identified. Secondly, the mixing coefficients and Gaussian parameters need to be optimised for the given set of observations. This is normally done using the Expectation-Maximisation (EM) algorithm.

The first challenge in learning the model parameters given a training data set is defining the complexity of the model. This corresponds to the number of components in the mixture model. Determining the number of components is a trade off between data generalisation and over-fitting the data, both of which are undesirable. Clustering is one of the classic problems in machine learning and many different methods have been proposed in literature to tackle this problem. Euclidean distance based clustering algorithms are perhaps the most common, of which the k-means clustering algorithm is the arguably the most popular due its speed and simplicity. Alternative methods such as principal component analysis (PCA) and minimum length description (MLD) criterion algorithms offer improved performance at the cost of increased time complexity. The second problem is learning the model parameters for the given model structure.

Given the number of components, the EM procedure for learning the parameters of a GMM involves using a random initial guess of the model parameters to estimate the component labels (E-step). The M-step then uses the new component labels to update the model parameters. More formally, if the set of component labels $\{Z|z_1 z_2 \cdots z_n\}$ that identifies the component that generated each data point x_n then the E-step calculates the *expected* values of the labels given the current model parameters, i.e.:

$$\begin{aligned} R_n^l(j) &= P(z_n = j|\mathbf{x}_n, \theta^l) \\ &= \frac{p(\mathbf{x}_n|z_n = i, \theta_j^l)P^l(j)}{\sum_{m=1}^{M} p(\mathbf{x}_n|z_n = m, \theta_m^l)P^l(m)} \end{aligned} \tag{B.13}$$

The responsibilities, $R_n^l(j)$, quantify to what degree each component is *responsible* for generating each data point x_n. The M-step uses these responsibilities to update the

parameters of the GMM as follows:

$$P^{l+1}(j) = \frac{1}{N}\sum_{n=1}^{N} R_n^l(j) \tag{B.14}$$

$$\boldsymbol{\mu}_j^{l+1} = \frac{\sum_{m=1}^{N} R_n^l(j)\mathbf{x}_n}{\sum_{m=1}^{N} R_n^l(j)} \tag{B.15}$$

$$\boldsymbol{\Sigma}_j^{l+1} = \frac{\sum_{m=1}^{N} R_n^l(j)(\mathbf{x}_n - \boldsymbol{\mu}_j^{l+1})(\mathbf{x}_n - \boldsymbol{\mu}_j^{l+1})^T}{\sum_{m=1}^{N} R_n^l(j)} \tag{B.16}$$

B.2 HMM inference

HMM inference is essentially the problem of determining the "optimal" state sequence for given observation sequence. There are many ways of defining what is *optimal*. One possible approach is to define the optimal state sequence as that sequence that maximises the expected number of correctly classified individual states, i.e.:

$$s_t^* = \underset{i}{\text{argmax}}\{P(s_t = i \mid O_{1:T}, \lambda)\}, \tag{B.17}$$

where s_t^* is the *optimal* state at time t and can be computed efficiently using the *forward-backward* recursive procedure [243]. However, Equation B.17 finds the optimal state at each time point without taking into account the transitions of resulting state sequence. For instance, a particular observation at time t might identify the P-wave as the optimal state, even though the state at $t-1$ was the QRS-complex. Therefore, given the observation data, the most probable state sequence can be re-defined using Bayes' rule as:

$$\begin{aligned} S^* &= \underset{S}{\text{argmax}} \left\{ \frac{p(S, O_{1:T} \mid \lambda)}{p(O_{1:T} \mid \lambda)} \right\} \\ &= \underset{S}{\text{argmax}}\{p(S, O_{1:T} \mid \lambda)\}. \end{aligned} \tag{B.18}$$

B.2.1 Viterbi Algorithm

The *Viterbi algorithm* is used to find the state sequence S^* that maximises the joint distribution $p(S, \mathbf{O}_{1:T} \mid \lambda)$, given the observation sequence $(\mathbf{O}_{1:T})$ and the trained model [**?**]. Viterbi defines $\delta_t(i)$ as the highest probability along a single path, which accounts for the first t observations and ends in state i, i.e.

$$\delta_t(i) = \max_{s_1 s_2 \cdots s_{t-1}} p(s_1 s_2 \cdots s_t = i, O_1 O_2 \cdots O_t \mid \lambda). \tag{B.19}$$

In order to calculate the value of δ for time $t+1$, we need to take into consideration the possible state transitions and the associated observation probability density, i.e.:

$$\begin{aligned}\delta_{t+1}(i) &= \max_{s_1 s_2 \cdots s_t} p(s_1 s_2 \cdots s_{t+1} = i, O_1 O_2 \cdots O_{t+1} \mid \lambda) \\ &= \max_j \{\delta_t(j) a_{ji}\} \cdot b_i(O_{t+1}). \end{aligned} \tag{B.20}$$

In order to determine the optimal state sequence, it is necessary to store that maximised Equation B.20 for each time point t and state i as $\psi_t(i)$, i.e.:

$$\psi_{t+1}(i) = \operatorname*{argmax}_j \{\delta_t(j) a_{ji}\}. \tag{B.21}$$

The Viterbi algorithm is a *dynamic programming* procedure, which takes advantage of the fact that the problem can be sub-divided into a number of interdependent sub-problems [**?**]. The Viterbi algorithm is divided into four stages: initialisation, forward pass, termination and backward pass. The complete procedure can be described as follows:

1. **Initialisation:**

$$\delta_1(i) = \pi_i b_i(O_1),\ i = 1, \ldots, K \tag{B.22}$$

$$\Psi_1(i) = 0,\ i = 1, \ldots, K \tag{B.23}$$

2. **Forward pass:**

$$\delta_t(i) = \max_j \{\delta_{t-1}(j) a_{ji}\} \cdot b_i(O_{t+1}),\ i, j = 1, \ldots, K \tag{B.24}$$

$$\psi_t(i) = \operatorname*{argmax}_j \{\delta_{t-1}(j) a_{ji}\},\ i, j = 1, \ldots, K \tag{B.25}$$

3. **Termination:**

$$s_T^* = \operatorname*{argmax}_j \{\delta_T(j)\},\ j = 1, \ldots, K \tag{B.26}$$

4. **Backwards pass:**

$$s_t^* = \psi_{t+1}(s_{t+1}^*), \quad t = T-1, T-2, \cdots, 1 \tag{B.27}$$

Figure B.1 is a schematic diagram of the Viterbi algorithm with the HMM states represented in a lattice structure. The figure shows the forwards and backwards passes of the algorithm. On the forward pass the arrays $\psi(i)$ and $\delta(i)$ are populated for all times t and hidden states i. On the return pass the state with the highest δ_T value is

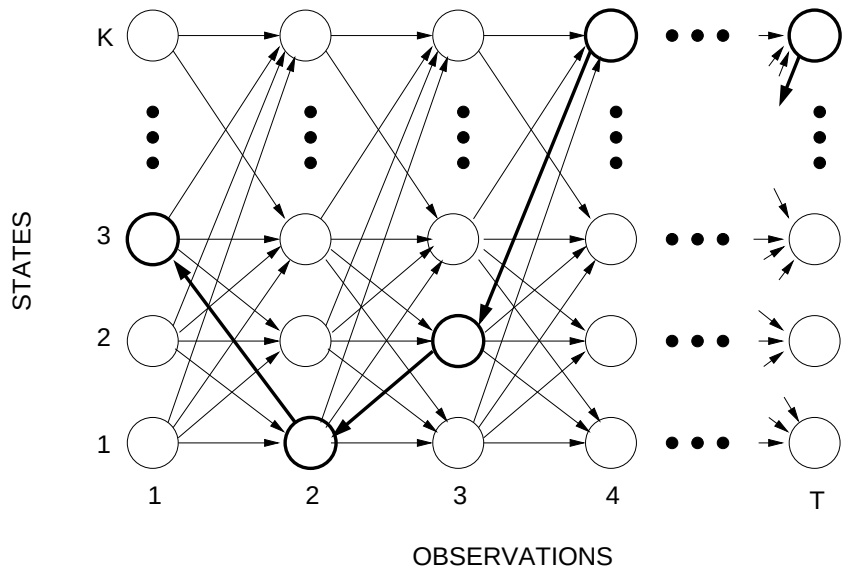


Figure B.1: Schematic diagram of the Viterbi algorithm using a lattice representation of HMM states. The forward pass nodes are clear, whereas the backwards pass identifies the state with the highest δ_t value (dark outlined nodes) and traces back through the matrix $\mathbf{\Psi}$ highlighting the path with maximum likelihood.

identified and the algorithm traces back through the matrix $\mathbf{\Psi}$, identifying the path with the maximum likelihood.

In practice, the Viterbi algorithm requires a scaling procedure to ensure that the $\delta_t(i)$ values do not underflow the machine precision of the computer. This procedure is described in full detail in Appendix B.2.3. The Viterbi algorithm is made relatively computationally efficient by avoiding the necessity of calculating the probability of every possible state sequence, which would be impractical for large values of K and T. The time complexity of the Viterbi algorithm for a fully-connected HMM, known as an *ergodic* HMM, with K states is $\mathcal{O}(TK^2)$. For HMMs that are not ergodic, then the time complexity is reduced even further, as Equation B.20 need only maximise those actually connected to state i. Therefore, the time complexity is given by $\mathcal{O}(TK\bar{K})$, where $\bar{K}$ is the average state connectivity.

B.2.2 Forward-backward procedure

In addition to determining the optimal state sequence from a given sequence of observations, it is often desirable to determine the probability of an observed sequence given a HMM, i.e. $P(O_{1:T} \mid \lambda)$. In a generative sense, this can be described as the likelihood of the data having been generated by the HMM. The data likelihood is determined using the *forward-backward* procedure, which uses two variables to define the partial sequence

probability. The forward and backward variables are subsequently used to calculate the overall observed sequence probability. The forward variable $\alpha_t(i)$ is the probability of the partial observation sequence up until time t, i.e. $P(O_{1:t}, s_t = i \mid \lambda),\ i = 1, \ldots, K$. The forward variable can be determined as follows:

$$\alpha_1(i) = \pi_i b_i(O_1), \tag{B.28}$$

$$\alpha_{t+1}(i) = \left(\sum_{j=1}^{K} \alpha_t(j) a_{ji} \right) b_i(O_{t+1}),\ t = 1, \ldots, T-1. \tag{B.29}$$

The backwards variable $\beta_t(i)$ is the probability of the partial observation sequence from *t+1* to the final observation T, i.e. $P(O_{t+1}O_{t+2} \cdots O_T \mid s_t = i, \lambda),\ i = 1, \ldots, K$. It can be solved as follows:

$$\beta_T(i) = 1, \tag{B.30}$$

$$\beta_t(i) = \sum_{j=1}^{K} a_{ij} b_j(O_{t+1}) \beta_{t+1}(j),\ t = T-1, T-2, \cdots, 1. \tag{B.31}$$

The observed probability or data likelihood given the model, $P(O_{1:T}|\lambda)$, is obtained by then be defined as

$$P(O_{1:T}|\lambda) = \sum_{i=1}^{K} \alpha_t(i) \beta_t(i),\ t = 1, \ldots, T. \tag{B.32}$$

B.2.3 Scaling for HMMs

The forward and backwards variables, $\alpha_t(i)$ and $\beta_t(i)$, require scaling to avoid underflow when using the precision range of most computers. In order to understand the necessity for scaling, consider the definition of $\alpha_t(i)$ in Equation B.29, i.e.:

$$\alpha_t(i) = \prod_{t'=1}^{t-1} a_{q_{t'} q_{t'+1}} \prod_{t'=1}^{t} b_{q_{t'}}(O_{t'}).$$

Since each a and b term is generally significantly less than 1, as t increases $\alpha_t(i)$ tends exponentially to zero. Therefore, the aim of scaling $\alpha_t(i)$ and $\beta_t(i)$ is to ensure that the variables remain within the precision range of the computer for length of the signal observations [243].

Recall that the *forward* variable $\alpha_t(i) = P(O_{1:t}, s_t = i \mid \lambda)$, the *backward* variable $\beta_t(i) = P(O_{t+1}O_{t+2} \cdots O_T, s_t = i \mid \lambda)$ and that the joint posterior probability of going from state i to state j at time t can be computed in terms of the forward and backward

variables

$$\begin{aligned}\xi_t(i,j) &= P(s_t = i, s_{t+1} = j \mid O, \lambda) \\ &= \frac{\alpha(i)a_{ij}b_j(O_{t+1})\beta_{t+1}(j)}{P(O|\lambda)}.\end{aligned} \tag{B.33}$$

Furthermore, recall that the probability of being in state i at time t is related to $\xi_t(i,j)$ and can be described as:

$$\begin{aligned}\gamma_t(i) &= \sum_{j=1}^{K} \xi_t(i,j) \\ &= \frac{\alpha_t(i)\beta_t(i)}{P(O|\lambda)}.\end{aligned} \tag{B.34}$$

Rahimi corrects methods presented by Rabiner to compute γ_t and $\xi_t(i,j)$ using scaled variables $\hat{\alpha}$ and $\hat{\beta}$ [**?**].

The recursive equations for calculating the scaled forward variable $\hat{\alpha}_t(i)$ such that

$$\hat{\alpha}_t(i) = \frac{\alpha_t(i)}{\sum_{j=1}^{K} \alpha_t(j)} = C_t\alpha_t(i) \tag{B.35}$$

are defined as follows:

$$\begin{aligned}\bar{\alpha}_1(i) &= \alpha_1(i), \\ \bar{\alpha}_{t+1}(i) &= \sum_{j=1}^{K} \hat{\alpha}_t(j)a_{ji}b_i(O_{t+1}), \\ c_{t+1} &= \frac{1}{\sum_i \bar{\alpha}_{t+1}(i)}, \\ \hat{\alpha}_{t+1}(i) &= c_{t+1}\bar{\alpha}_{t+1}(i).\end{aligned}$$

A definition of the scaled variable C_t in Equation B.35 can be expressed in terms of c_t as follows:

$$\begin{aligned}C_t &= \frac{C_{t+1}}{c_{t+1}} = \frac{1}{c_{t+1}\sum_{j=1}^{K} \alpha_{t+1}(j)}, \\ C_{t+1} &= C_t c_{t+1} = \prod_{\tau=1}^{t+1} c_\tau.\end{aligned} \tag{B.36}$$

The scaling variable D_t for the *backward* variable β can be determined from C_t as follows:

$$D_t = \prod_{\tau=t}^{T} c_\tau, \tag{B.37}$$

$$D_{t+1} = \frac{1}{C_t}\prod_{\tau=1}^{T} c_\tau = C_T. \tag{B.38}$$

The recursive equations for the determining the backward scaled variable, $\hat{\beta}_t(i) = D_t\beta(i)$, can then be defined as follows:

$$\begin{aligned}\bar{\beta}_T(i) &= \beta_T(i),\\ \bar{\beta}_t(i) &= \sum_{i=1}^{K} a_{ij} b_j(O_{t+1})\hat{\beta}_{t+1}(i),\\ \hat{\beta}_t(i) &= c_t\bar{\beta}_t(i).\end{aligned}$$

The posterior probabilities $\xi_t(i,j)$ can be calculated using the scaled variables $\hat{\alpha}_t$ and $\hat{\beta}_t$ as follows:

$$\begin{aligned}\xi_t(i,j) &= \frac{1}{P(O|\lambda)}\alpha_t(i)a_{ij}b_j(O_{t+1})\beta_{t+1}(j)\\ &= \hat{\alpha}_t(i)a_{ij}b_j(O_{t+1})\hat{\beta}_{t+1}(j).\end{aligned} \tag{B.39}$$

The probability of being in state i at time t can then be computed from ξ using Equation B.34 as follows:

$$\begin{aligned}\gamma_t(i) &= \sum_{j=1}^{K}\xi_t(i,j) = \frac{1}{P(O|\lambda)}\alpha_t(i)\beta_t(i)\\ &= \hat{\alpha}_t(i)\hat{\beta}_t(i)\frac{1}{c_t}.\end{aligned} \tag{B.40}$$

An alternative method of scaling the critical variables $\alpha_t(i)$ and $\beta_t(i)$ is to calculate them in the logarithmic domain, thus Equations B.28 and B.29 can be written as:

$$\log\alpha_1(i) = \log\pi_i + \log b_i(O_1), \tag{B.41}$$

$$\log\alpha_{t+1}(i) = \log\sum_{j=1}^{K} e^{\log\alpha_t(j)+\log a_{ji}} + \log b_i(O_{t+1}). \tag{B.42}$$

Similarly, the backward scaled variable can be solved as follows:

$$\log\beta_T(i) = 0, \tag{B.43}$$

$$\log\beta_t(i) = \log\sum_{j=1}^{K} e^{\log a_{ji}+\log b_i(O_{t+1})+\log\beta_{t+1}(j)}. \tag{B.44}$$

However, it should be noted that the term $\exp\{\cdots\}$ is still prone to underflow. To solve this problem, consider the computation of

$$\begin{aligned}\log\sum_{i=1}^{N} e^{x_i} &= \log\{e^{x_{max}}\sum_{i=1}^{N} e^{x_i - x_{max}}\}\\ &= x_{max} + \log\sum_{i=1}^{N} e^{x_i - x_{max}},\end{aligned}$$

where $x_{max} = \max_i\{x_i\}$. Since $x_i - x_{max} \leq 0$ for all i, then $\sum_{i=1}^{N} e^{x_i - x_{max}}$ is limited by N and the final result will fall within the dynamic range of the computer. In the context of the EM algorithm for HMMs, the log likelihood of the data can then be defined as:

$$\log p(O_{1:T} \mid \lambda) = \log \sum_{i=1}^{K} \exp\{\log \alpha_T(i)\}. \tag{B.45}$$

The posterior probabilities or responsibilities are then defined as:

$$\xi_t^{l+1}(i,j) = \exp\{\log \alpha_t(i) + \log a_{ij} + \log b_{t+1}(j) + \log \beta_{t+1}(j) - \log p(O_{1:T}|\lambda^l)\}, \tag{B.46}$$

$$\gamma_t^{l+1}(i) = \exp\{\log \alpha_t(i) + \log \beta_t(i) - \log p(O_{1:T}|\lambda^l)\}. \tag{B.47}$$

Bibliography

[1] J. Lazarou, B. H. Pomeranz, and P. N. Corey. Incidence of adverse drug reactions in hospitalised patients: a meta-analysis of prospective studies. *J Am Med Assoc*, 279:1200–1205, 1998.

[2] M. M. Straus, C. J. M. Miriam, et al. Non-cardiac QTc-prolonging drugs and the risk of sudden cardiac death. *Eur Heart J*, May 11 2005. Available at eurheartj.oupjournals.org.

[3] International Conference on Harmonisation of Technical Requirements for Registration of Pharmaceuticals for Human Use (ICH). The clinical evaluation of QT/QTc interval prolongation and proarrhythmic porential for non-antiarrahythmoic drug. [Internet] http://www.ich.org/cache/compo/276-254-1.html, May 2005.

[4] M. Zabel, M. Malik, et al. Analysis of T-wave morphology from the 12-lead electrocardiogram for prediction of long-term prognosis in male US veteran. *Circulation*, 1005:1066–1070, 2002.

[5] D. Roden. Drug-induced prolongation of the QT interval. *N Engl J Med*, 350:1013–1022, 2004.

[6] J. Morganroth. A definitive or Thorough Phase 1 QT ECG Trial as a requirement for drug safety assessment. *J Electrocardiol*, 37(1):25–29, 2004.

[7] J. P. Couderc, W. Zareba, et al. Identification of Sotalol-induced changes in repolarization with T-wave area-based repolarization duration paramemeters. *J Electrocardiol*, 36(Suppl):115–120, 2003.

[8] A. J. Moss, W. Zareba, et al. ECG T-wave patterns in genetically distinct forms of the hereditary Long QT Syndrome. *Circulation*, 92:2929–2934, 1995.

[9] S. Brode, B.N. Singh, and K.P Anderson. Sotalol. *Cardiac Electrophysiol. Rev.*, 2:221–214, 1998.

[10] J. Cooper. Electrocardiography 100 years ago. origins, pioneers, and contributors. *N Engl J Med*, 315(7):461–464, 1986.

[11] A. R. Houghton and D. Gray. *Making sense of the ECG*. Arnold, London, UK, 1997.

[12] J. Wu, J. Wu, and D. Zipes. Early afterdepolarizations, U waves and Torsades de Pointes. *Circulation*, 105(6):675 – 676, 2002.

[13] S. T. Andersen, R. L. Burr, et al. *Advanced electrocardiography*. SpaceLabs Medical, Inc., Redmond, WA, USA, 1995.

[14] F. N. Wilson, F. D. Johnston, et al. The precordial electrocardiogram. *Am Heart J*, 27:19–85, 1944.

[15] E. L. Heilbron. Advances in modern electrocardiographic equipment for long-term ambulatory monitoring. *Cardiac Elec Rev*, 6(3):185–189, 2002.

[16] W. Zareba, A. Moss, and F. Badilini. *Noninvasive electrocardiography: clinical aspects of Holter monitoring*, chapter 23, pages 405–419. WB Saunders, London, UK, 1996.

[17] G. X. Yan and C. Antzelevitch. Cellular basis for the Brugada syndrome and other mechanisms of arrhythmogenesis associated with ST-segment elevation. *Circulation*, 100:1660–1666, 1999.

[18] J. J. Struijk, J. K. Kanters, et al. Classification of long-QT sydrome based on discriminant analysis of T-wave morphology. *Med Bio Eng Comput*, 44:543–549, 2006.

[19] M. Mailk. Problems of heart rate correction in assessment of drug-induced QT interval prolongation. *J Cardiovasc Electrophysiol*, 12:411–420, 2001.

[20] H. C. Bazett. An analysis of the time-relations of electrocardiograms. *Heart*, 7:353–370, 1920.

[21] T. G. Hammond, L. Carlsson, A. S. Davis, et al. Methods of collecting and evaluating non-clinical cardiac electrophysiology data in the pharmaceutical industry: results of an international survey. *Cardivasc Res*, 49:741–750, 2001.

[22] M. Malik. Errors and misconceptions in ECG measurement used for the detection of drug induced QT interval prolongation. *J Electrocardio*, 37:25–33, 2004.

[23] J. H. Burke, F. A. Ehlert, et al. Gender-specific differences in the QT interval and the effect of autonomic tone and menstrual cycle in healthy adults. *Am J Cardiol*, 79(2):178–81, 1997.

[24] R. M. Rangayyan. *Biomedical Signal Analysis*. Wiley-IEEE Press, New York, USA, 2002.

[25] A. Murray, N. B. McLaughlin, et al. Errors in manual measurement of QT intervals. *Br Heart J*, 71:386–390, 1994.

[26] J. R. Milne, D. E. Ward, R. A. Spurrell, and A. J. Camm. The ventricular paced QT interval: the effects of rate and exercise. *PACE*, 5:352–358, 1982.

[27] C. P. Lau, A. R. Freedman, et al. Hysteresis of the ventricular paced QT interval in response to abrupt changes in pacing rate. *Cardiovasc Res*, 22:67–72, 1988.

[28] C. P. Day, J. M. McComb, et al. QT dispersion: an indication of arrhythmia risk in patients with long QT intervals. *Br Heart J*, 63:342–344, 1990.

[29] J. A. Kors, G. Van Herpen, et al. Qt dispersion as an attribute of T-loop morphologhy. *Circulation*, 99:1458–1463, 1998.

[30] M. Malik, B. Acar, et al. QT dispersion does not represent electrocardiographic interlead heterogeneity of ventricular repolarization. *J Cardiovasc Electrophysiol*, 11:835–43, 2000.

[31] J. C. Cowan, K. Yusoff, et al. Importance of lead selection in QT interval measurement. *Am J Cardiol*, 61(1):83–87, 1988.

[32] M. Malik and V. N. Batchvarov. Measurement, interpretation and clinical potential of QT dispersion. *J Am Coll Cardiol*, 36:1749–1766, 2000.

[33] P. Kligfield, B. Tyl, M. Maarek, and P. Maison-Blanche. Interval differences between superimposed global and individual lead ECG complexes. *Ann Noninvasive Electrocardiol*, 12(2):145–152, 2007.

[34] L. Hondeghem. Thorough QT/QTc not so thorough: Removes torsadogenic predictors from the T-wave, incriminates safe drugs, and misses profibrillatory drugs. *J Cardiovasc Electrophysiol*, 17(3):337–340, 2006.

[35] S. H. Hohnloser and B. N. Singh. Proarrhythmia with class III anti-arrhythmic drugs: definition, electrophysiologic mechanisms, incidence, predisposing factors, and clinical implications. *J Cardiovasc Electrophysiol*, 6(10):920–936, 1995.

[36] L. Hondeghem, L. Carlsson, and G. Duker. Instability and triangulation of the action potential predict serious arrhythmia, but APD prolongation is antiarrhythmic. *Circulation*, 103:2004–2013, 2004.

[37] C. Clancy and Y. Rudy. Cellular consequences of HERG mutations in long QT syndrome precursors to sudden cardiac death. *Cardiovasc Res*, 50:301–313, 2001.

[38] C. Antzelevitch. Tpeak-Tend interval as an index of transmural dispersion of repolarization. *Eur J Clin Inv*, 21(7):555–557, 2001.

[39] J. M. Kootsey and E. A. Johnson. The origin of the T-wave. *Crit. Rev. Bioeng.*, 4(3):223–270, 1980.

[40] S. H. Hohnloser, T. Klingenheben, et al. T wave alternans as a predictor of recurrent ventricular tachyarrhythmias in ICD recipients: prospective comparison with conventional risk markers. *J Cardiovasc Electrophysiol*, 9:1258–1268, 1998.

[41] J. P. Couderc, S. McNitt, et al. Repolarization morphology in adult LQT2 carriers with borderline prolonged QTc interval. *J Heart Rhythm*, 3(12):1460–1466, 2006.

[42] M. P. Andersen, J. Q. Xue, et al. Quantification of T-wave mophorlogy improves identification of IKr inhibition in congenital and drug induced long QT syndrome. In *Comput Cardiol*, volume 34, page [In print]. IEEE, 2007.

[43] K. H. W. Ten Tusscher, D. Noble, et al. A model for human ventricular tissue. *Am J Physiol Heart Circ Physiol*, 286:H1573–H1589, 2004.

[44] K.H. Ten Tusccher and A.V. Panfilov. Alternans and spiral breakup in human ventricular tissue model. *Am. J. Physiol. Heart Circ. Physiol.*, 291:H1088–H1100, 2006.

[45] A. Bueno-Orovio, E. M. Cherry, and F. H. Fenton. Minimal model for human ventricular action potentials in tissue. *J Ther Biol*, 253(3):544–560, 2008.

[46] D. Noble and Y. Rudy. Models of cardiac ventricular action potentials: iterative interaction between experiment and simulation. *Phil Trans R Soc: Math Phys Eng Sci*, 359(1783):1127–1142, 2001.

[47] M. Potse, R. Coronel, T. Opthof, and A. Vinet. Simulating t-wave parameters of local extracellular electrograms with a whole-heart bidomain reaction-diffusion model: Size matters. In *Proc EMBS*, pages 6644–6647, Lyon, France, 2007. IEEE.

[48] B. Rodríguez and N. Trayanova. Upper limit of vulnerability in defibrillation model of the rabbit ventricles. *J Electrocardiol*, 36(Suppl):51–56, 2003.

[49] N. Sarapa, J. Morganroth, et al. Electrocardiographic identification of drug-induced QT prolongation: assessment by different recording and measuring methods. *Ann of Noninv Electrocardio*, 9(1):48–57, 2004.

[50] Wapcaplet. Diagram of the human heart. [Internet].

[51] D. D. Streeter, W. E. Powers, et al. *Cardiovascular System Dynamics*, chapter Three-dimensional fiber orientation in the mammlian left ventricular wall, pages 73–84. MIT Press, Cambridge MA, 1989.

[52] R. Plonsey and R. C. Barr. *Bioelectricity: a quantitative approach*. Kluwer Academic/Plenum Publishers, New York, USA, 2nd edition, 2000.

[53] A. Guyton and J. Hall. *Textbook of Medical Physiology*. Prism Books Lt. Bangalore, India, 9 edition, 1996.

[54] D. Roden, J. R. Balser, et al. Cardiac ion channels. *Ann Rev Physiol*, 64:431–475, 2002.

[55] E. Marban. Cardiac channelopathies. *Nature*, 415:213–218, Jan 2002.

[56] H. Abriel, J. Schläpfer, et al. Molecular and clinical determinants of drug-induced long QT syndrome: an iartogenic channelopathy. *Swiss Med Wkly*, 134:685–694, 2004.

[57] W. Howard and P. Martin. Gap junctions: structure and function. *Mol Membr Bio*, 19(2):121–136, 2002.

[58] E. Drouin, F. Charpentier, et al. Electrophysiologic characteristics of cells spanning the left ventricular wall of human heart: evidence for presence of M cells. *J Am Coll Cardiol*, 26(1):185–192, 1995.

[59] C. Anzelevitch, G. X. Yan, et al. Transmural dispersion of repolarization and arrhythmogenicity. *J Electrocardiol*, 32:158–165, 1999.

[60] W. Shimizu and C. Antzelevitch. Cellular and ionic basis for T-wave alternans under long QT conditions. *Circulation*, 99:1499–1507, 1999.

[61] G. Seemann, F. B. Sachse, et al. Quantitative reconstruction of cardiac electromechanics in human myocardium: regional heterogeneity. *J Cardiovasc Electrophysiol*, 14(Suppl):S219–S228, 2003.

[62] Inc. Pearson Education. Cardiac electrical conduction. [Internet].

[63] R. A. Greenbaum, S. Y. Ho, et al. Left ventricular fibre architecture in man. *Heart*, 45:248–263, 1981.

[64] J. S. Mitcheson, J. Chen, et al. A structural basis for drug-induced long QT syndrome. *PNAS*, 97(22):12329–12333, 2000.

[65] D. J. MacNeil. The side effect profile of class III antiarrhythmic drugs: focus on d,l-Sotalol. *Am J Cardiol*, 80(8A):90G–98G, 1997.

[66] D. A. Doyle, J. M. Cabral, et al. The structure of the potassium channel: molecular basis of K^+ conduction and selectivity. *Science*, 280(5360):69–77, 1989.

[67] Y. Jiang, A. Lee, et al. X-ray structure of a voltage-dependent k^+ channel. *Nature*, 423:33–41, 2003.

[68] S. B. Long, E. B. Campbell, and R. MacKinnon. Crystal structure of a mammalian voltage-dependent Shaker family K^+ channel. *Science*, 309:897–903, 2005.

[69] Y. Zhou, J. H. Morais-Cabral, A. Kaufman, and R. MacKinnon. Chemistry of ion coordination and hydration revealed by a k^+ channel-fab complex at 2.0åresolution. *Nature*, 414:43–48, 2001.

[70] Y. Jiang, V. Ruta, J. Chen, A. Lee, and R. MacKinnon. The principle of gating charge movement in voltage-dependent k^+ channel. *Nature*, 423:42–48, 2003.

[71] M. C. Sanguinetti and M. Tristani-Firouzi. hERG potassium channels and cardiac arrhythmia. *Nature*, 440:463–469, 2006.

[72] M. Tristani-Firouzi, J. Chen, et al. Molecular biology of K^+ channels and their role in cardiac arrhythmias. *Am J Med*, 110:50–59, 2001.

[73] Y. Lu, M. P. Mahaut-Smith, et al. Effects of premature stimulation on HERG K(+) channels. *J Physiol*, 537(3):843–51, 2001.

[74] G. Berecki, J. G. Zegers, et al. Herg channel (dys)function revealed by dynamic action potential clamp technique. *Biophys. J.*, 88:566–578, 2005.

[75] S. Wang, S. Liu, et al. A quantitative analysis of the activation and inactivation kinetics of HERG expressed in xenopus oocytes. *J Physiol*, 502:45–60, 1997.

[76] M. C. Sanguinetti, C. Jiang, et al. A mechanistic link between an inherited and an acquired cardiac arrhythmia: HERG encodes the I_{kr} potassium channel. *Cell*, 81:299–307, 1995.

[77] J. S. Mitcheson, J. Chen, and M. C. Sanguinetti. Trapping of a methanesulfonanilide by closure of the HERG potassium channel activation gate. *J Gen Physiol*, 115(3):229–240, 2000.

[78] J. P. Lees-Miller, Y. Duan, et al. Molecular determinant of high-affinity dofetilide binding to HERG1 expressed in xenopus oocytes: Involvement of s6 sites. *Mol Pharmacol*, 57:367–374, 2000.

[79] J. Kamiya, R. Niwa, et al. Molecular determinants of hERG channel block. *Mol Pharm*, 69:1709–1716, 2006.

[80] G. E. Kirsch, E. S. Trepakova, et al. Variability in the measurement of hERG potassium channel inhibition: effects of temperature and stimulus pattern. *J Pharm Tox Meth*, 50:93–101, 2004.

[81] B. Darpö. Spectrum of drugs prolonging QT interval and the incidence of torsades de pointes. *Eur Heart J*, 3 Suppl. K:70–80, 2001.

[82] J. Jalife. Ventricular fibrillation: mechanisms of initiation and maintenance. *Ann Rev Physiol*, 62:25–50, 2000.

[83] F. Dessertenne. La tachycardie ventriculaire a deux foyers opposes variables. *Arch Mal Couer*, 59:263–272, 1966.

[84] S. Poelzing and D. S. Rosenbaum. *The hERG cardiac potassium channel: function and drug-induced long QT syndrome*, chapter Cellular mechanisms of Torsades de Pointes. John Wiley & Sons Ltd, Chichester, UK, 2005.

[85] A. J. Camm, M. Malik, et al. *Acquired Long QT Syndrome*. Blackwell Publishing, Oxford, UK, 2004.

[86] L. M. Hondeghem. Relative contributions of TRIaD and QT to proarrhythmia. *J Cardivasc Electrophysiol*, 18(6):655–657, 2007.

[87] M. A. Vos, J. M. Van Opstal, et al. Electrophysiologic parameters and predisposing factors in the generation of drug-induced Torsades de Pointes arrhythmias. *Pharm & Thera*, 92:109–122, 2001.

[88] T. Yang and D. Roden. Extracellular potassium modulation of drug block: Implications for Torsades de Pointes and reverse use-dependance. *Circulation*, 93:407–411, 1996.

[89] C. E. Conrath, A. A. Wilde, et al. Gender differences in long QT syndrome: effects of beta=adrenoceptor blockade. *Cardiovasc Res*, 15(3):770–776, 2002.

[90] J. Silva and Y. Rudy. Subunit interation determines iks participation in cardiac repolarization and repolarization reserve. *Circulation*, 112:1384–1391, 2005.

[91] A. J. Camm, M. J. Janse, et al. Congenital and long QT syndrome. *Eur Heart J*, 21(15):1232–1237, 2000.

[92] B. N. Singh. Controlling cardiac arrhythmias: an overview with a historical perspective. *Am J Cardiol*, 80(8A):4G–15G, 1997.

[93] C. Antzelevitch and W. Shimizu. Cellular mechanisms underlying the long QT syndrome. *Cur Opin Cardiol*, 17(1):43–51, 2002.

[94] Y. Rudy and J. R. Silva. Computational biology in the study of cardiac ion channels and cell electrophysiology. *Q Rev Biophys*, 39(1):57–116, 2006.

[95] D. Noble. Computational models of the heart and their use in assessing the actions of drugs. *J Pharmacol Sci*, 107:107–117, 2008.

[96] C.H. Luo and Y Rudy. A dynamic model of cardiac ventricular action potential. I. Simulations of ionic currents and concentration changes. *Circ.Res.*, 74:1071–1096, 1994.

[97] W. Thomson. chapter On the theory of the electrical telegraph, pages 61–75. The University Press, Cambridge, UK, 1855.

[98] A. L. Hodgkin and W. A. H. Rushton. The electrical constants of a crustacean nerve fibre. *Proc Roy Soc Lon B*, 133:444–479, 1946.

[99] J. L. Greenstein, R. W. Wu, et al. Role of the calcium-independent transient outward current I_{to1} in shaping action potential morphology and duration. *Cell Biology*, 87:1026–1033, 2000.

[100] S. Weidmann. Electrical constants of trabecular muscle from mammalian heart. *J Physiol*, 210:1041–1054, 1970.

[101] L. Clerc. Directional difference of impulse spread in trabecular muscle of mammalian heart. *J Physiol*, 255:355–346, 1976.

[102] L. Tung. *A bi-domain model for describing ischemic myocardial d-c potentials*. PhD thesis, MIT, Cambridge, MA, USA, 1978.

[103] W. T. Miller and D. B. Geselowitz. Simulation studies of the electrocardiogram: I. The normal heart. *Circ Res*, 43(2):301–315, 1978.

[104] C. S. Henriquez and R. Plonsey. Simulation of propagation along a cylindrical bundle of cardiac tissues. I. Mathematical formulation. *IEEE Trans Biomed Eng*, 37(9):850–860, 1990.

[105] C. S. Henriquez and R. Plonsey. Simulation of propagation along a cylindrical bundle of cardiac tissues. II. Results of simulation. *IEEE Trans Biomed Eng*, 37(9):861–875, 1990.

[106] C. S. Henriquez. Simulating the electrical behavior of cardiac tissue using the bidomain model. *Crit Rev Biomed Eng*, 21(1):1–77, 1993.

[107] N. Trayanova, J. Eason, and F. Aguel. Computer simulations of cardiac defibrillation: a look inside the heart. *Comput Visual Sci*, 4:259–270, 2002.

[108] M. Potse, B. Dube, et al. A comparison of monodomain and bidomain reaction-diffusion models for action potential propagation. *IEEE Trans Biomed Eng*, 53:2425–2435, 2006.

[109] R. FitzHugh. Thesholds and plateaus in the hodgkin-huxley nerve equations. *J. Gen. Physiol.*, 43:867–896, 1960.

[110] J. Nagumo, S. Animoto, and S. Yoshizawa. An active pulse transmission line simulating nerve axon. *Proc. Inst. Radio Engineers*, 50:2061–2070, 1962.

[111] AL. Hodgkin and AF. Huxley. A quantitative description of membrane current and its application to conduction and excitation in nerve. *J. Physiol.*, 117:500–544, 1952.

[112] K. S. Cole and H. J. Curtis. Electrical impedance of the squid giant axon during activity. *J Gen Physiol*, 22:649–670, 1939.

[113] D. Noble. Cardiac action and pacemaker potential based on Hodgkin-Huxley equations. *Nature*, 188(495-497), 1962.

[114] F. G. Ball and M. S. P. Sansom. Ion-channel gating: model identification and parameter estimation from single channel recordings. *Proc R Soc Lond B*, 236:385–416, 1989.

[115] J. Lee, B. Smaill, and N. Smith. Hodgkin-Huxley type ion channel characterization: an improved method of voltage clamp experiment parameter estimation. *J Theor Biol*, 242:123–134, 2004.

[116] G.W. Beeler and H. Reuter. Reconstuction of action potential in ventricular myocardial fibres. *J. Physiol.*, 268:177–210, 1977.

[117] C. H. Luo and Y. Rudy. A model of ventricular cardiac action potential: depolarization, repolarization, and their interaction. *Circ Res*, 68:1501–1526, 1991.

[118] C.H. Luo and Y Rudy. A dynamic model of cardiac ventricular action potential. II. Afterdepolarizations, triggered activity, and potentiation. *Circ.Res.*, 74:1097–1113, 1994.

[119] L. Priebe and D. J. Beuckelmann. Simulation study of cellular electric properties in heart failure. *Circ Res*, 82(11):1206–1223, 1998.

[120] E. Carmeliet. Electrophysiologic and voltage clamp analysis of the effects of sotalol on isolated cardiac muscle and Purkinje fibers. *J Pharmacol Exp Ther*, 232(3):817–825, 1985.

[121] C. M. Armstrong and F. Benzanilla. Inactivation of the sodium channel II: gating channel experiments. *J Gen Physiol*, 70:567–590, 1977.

[122] F. Benzanilla and C. M. Armstrong. Inactivation of the sodium channel I: gating channel experiments. *J Gen Physiol*, 70:549–566, 1977.

[123] E. Neher and B. Sakmann. Single-channel currents recorded from membrane of denervated frog muscle fibres. *Nature*, 260:799–802, 1976.

[124] D. Colquhoun and A. G. Hawkes. On the stochastic processes of single ion channels. *Proc R Soc London*, 211:205–235, 1981.

[125] B. Hille. *Ion Channels of Excitable Membranes*. Sinauer Associates, Inc, Sunderland MA, USA, 3rd edition, 2001.

[126] R. R. Fenichel, M. Malik, et al. Drug-induced Torsades de Pointes and implications for drug development. *J Cardiovas Electrophsiol*, 15:475–495, 2004.

[127] O. F. Hutter and D. Noble. Rectifying properties of heart muscle. *Nature*, 188:495, 1960.

[128] D. Noble and R. W. Tsien. Outward membrane currents activated in the plateau range of potentials in cardiac purkinje fibres. *J Physiol*, 200(1):205–231, 1969.

[129] M. C. Sanguinetti and N. K. Jurkiewicz. Two components of cardiac delayed rectifier K+ current. Differential sensitivity to block by class III antiarrhythmic agents. *J Gen Physiol*, 96(1):195–215, 1990.

[130] J. Zeng and Y. Rudy. Early afterdepolarizations in cardiac myocytes: mechanism and rate dependence. *Biophys J*, 68(3):949–964, 1995.

[131] W. R. Silverman, B. Roux, and D. M. Papazian. Structural basis of two-stage voltage-dependent activation in K^+ channels. *Proc Nat Acad Sci USA*, pages 2935–2940, 2003.

[132] C. S. Oehmen, W. R. Giles, and S. S. Demir. Mathematical model of the rapidly activating delayed rectifier potassium current I(Kr) in rabbit sinoatrial node. *J Cardiovasc Electrophysiol*, 13(11):1132–1140, 2002.

[133] M. Fink, D. Noble, et al. Contributions of HERG K^+ current to repolarization of the human ventricular action potential. *Prog Biophys Mol Biol*, 96:357–376, 2008.

[134] A. O. Verker, R. Wilders, et al. Role of sequence variations in the human ether-a-go-go related gene (HERG, KCNH2) in the Brugada syndrome. *Cardiovasc Res*, 68(3):441–53, 2005.

[135] R. Mazhari, J. L. Greenstein, et al. Molecular interactions between two long-QT syndrome gene products, HERG and KCNE2, rationalized by in vitro and in silico analysis. *Circ Res*, 89(1):33–38, 2001.

[136] J. Kiehn, A. E. Lacrenda, and A. M. Brown. Pathways of HERG inactivation. *Am. J. Physiol. Heart Circ. Physiol.*, 277(1):H199–H210, 1999.

[137] M Weerapura, S. Nattel, et al. J physiol. *State-dependent barium block of wild-type and inactivation-deficient HERG channels in Xenopus oocytes*, 526(2):265–278, 2000.

[138] J. Kiehn, A. E. Lacerda, et al. Molecular physiology and pharmacology of HERG: single channel currents and block by dofetilide. *Circulation*, 94(10):2572–2579, 1996.

[139] T. Kenakin. Principles: receptor theory in pharmacology. *Trends Pharm Sci*, 25(4):186–192, 2004.

[140] A. J. Clark. *The mode of action of drugs on cells*. Arnold, London, UK, 1933.

[141] A. J. Clark. *Handbook of Experimental Pharmacology*. Verlig Von Julius Springer, Berlin, Germany, 1937.

[142] B. Hille. Local anesthetics: hydrophilic and hydrophobic pathways for the drug-receptor reaction. *J Gen Physiol*, 69:497–515, 1977.

[143] A. Hill. The possible effects of the aggregation of the molecules of hemoglobin on its dissociation curves. *J Physiol*, 40:4–7, 1910.

[144] O. Yifrach. Hill coefficient for estimating the magnitude of cooperativity in gating transitions of voltage-dependent ion channels. *Biophys J*, 87:822–830, 2004.

[145] L. M. Hondeghem and B. G. Katzung. Time and voltage dependent interactions of anti-arrhythmic drugs with cardiac sodium channels. *Biochim Biophys Acta*, 472:373, 1977.

[146] C. M. Armstrong. Time course of TEA^+-induced anomalous rectification in squid giant axons. *J Gen Physiol*, 50:491–503, 1966.

[147] C. F. Starmer, A. O. Grant, and H. C. Strauss. Mechanisms of use-dependent block of sodium channels in excitable membranes by local anesthetics. *Biophys J*, 46:15–27, 1984.

[148] J. R. Balser, B. Nuss, et al. Local anesthetics as effectors of allosteric gating: lidocaine effects on inactivation-deficient rat skeletal muscle Na channels. *J Clin Invest*, 98(12):2874–2886, 1996.

[149] A. Zhou, Q. Gong, et al. Properties of HERG channels stably expressed in HEK293 cells studied at physiological temperature. *Biophys J*, 74:230–241, 1998.

[150] J. A. Yao, X. Du, et al. Estimation of potency of HERG channel blockers: impact of voltage protocol and temperature. *J Pharmacol Toxicol Methods*, 51(1):146–153, 2005.

[151] A. O. Grant, L. J. Strauss, et al. The influence of pH on the electrophysiologic effects of lidocaine in guinea pig ventricular myocardium. *Circ Res*, 47:542–550, 1980.

[152] C. W. Clarkson and L. M. Hondeghem. Evidence for a specific receptor site for lidocaine, quinidine and bupivacine associated with cardiac sodium channels in guinea pig ventricular myocardium. *Circ Res*, 56:496–506, 1985.

[153] Starmer CF and Courtney KR. Modeling ion channel blockade at guarded binding sites: application to tertiary drugs. *Am J Physiol. Heart Circ Physiol*, 251(4):H848–H856, 1986.

[154] N. Kambouris, B. Nuss, et al. A revised view of cardiac sodium channel "blockade" in the long-QT syndrome. *J Clin Inves*, 105:1133–1140, 2000.

[155] C. E. Clancy, Z. I. Zhu, and Y. Rudy. Pharmacogenetics and anti-arrythmic drug therapy: a theoretical investigation. *Am. J. Physiol. Heart. Circ. Physiol.*, 292:H66–H75, 2007.

[156] D. J. Snyders and A. Chaudhary. High affinity open channel block by dofetilide of HERG expressed in a human cell line. *Mol Pharma*, 49(9):949–955, 1996.

[157] C. Chloe, E. Schulze-Bahr, et al. C-terminal HERG (LQTS) mutations disrupt i_{Kr} channel regulation through 14-3-3ϵ. *Human Mol Gen*, 15(19):2888–2902, 2006.

[158] S. Liu and R. Rassmusson. Hodgkin-Huxley and partially couples inactivation models yield different voltage dependence of block. *Am J Physiol (Heart Circ Physiol)*, 272:H2013–H2022, 1997.

[159] K. Tsujimae, S. Suzuki, S. Murakami, and Y. Kurachi. Frequency-dependent effects of various I_{Kr} blockers on cardiac action potential duration in a human atrial model. *Am J Physiol Heart Circ Physiol*, 293:H660–H669, 2007.

[160] M. Perry, F. B. Sachse, and M. C. Sanguinetti. Structural basis of action for a human ether-a-go-go related gene 1 potassium activator. *Proc Natl Acad Sci USA*, 104(34):13827–13832, 2005.

[161] D. H. Yan and K. Ishihara. Two Kir2.1 channel populations with different sensitivities to Mg^+ and polyamine block: a model for the cardiac strong inwards rectifier K^+ channel. *J Physiol*, 563(3):725–744, 2005.

[162] B. Trénor, J. M. Ferrero, et al. Effects of pinacidil on reentrant arrhythmias generated during acute regional ischemia: a simulation study. *Ann Biomed Eng*, 33(7):897–906, 2005.

[163] M. Courtemanche, R. J. Ramirez, and S. Nattel. Ionic mechanisms underlying human atrial action potential properties: insights from a mathematical model. *Am J Physiol Circ Physiol*, 275:H301–H321, 1998.

[164] G. A. Gintant, J. T. Limberis, et al. The canine Purkinje fiber: an in vitro model system for acquired long QT syndrome and drug-induced arrhythmogenesis. *J Cardiovasc*, 2001(5):607–618.

[165] D. Bottino, R. C. Penland, et al. Preclinical cardiac safety assessment of pharmaceutical compounds using an integrated systems-based computer model of the heart. *Biophys Mol Biol*, 90:414–443, 2006.

[166] S. H. Hohnloser and R. L. Woosley. Sotalol. *Drug Therapy*, 331(1):31–38, 1994.

[167] M. C. Sanguinetti and J. S. Mitcheson. Predicting drug-hERG channel interactions that cause long QT syndrome. *Trends Pharm Sci*, 26(3):119–124, 2005.

[168] H. Numaguchi, F. M. Mullins, et al. Probing the interaction between inactivation gating and D-Sotalol block of HERG. *Circ Res*, 87:1012–1018, 2000.

[169] K. Shankland and D. S. Sivia. Unit cell determination of sotalol hydrochloride by powder X-ray diffraction. *Int J Pharmaceutics*, 139:9–14, 1996.

[170] P. S. Spector, M. E. Curran, et al. Class III antiarrhythmic drug block HERG, a human cardiac delayed rectifier K^+ channel. *Circ Res*, 78:499–503, 1996.

[171] C. Fiset, Z.P. Feng, et al. [^{3}H]Dofetilide binding: biological models that manifest solely the high or the low affinity binding site. *J Moll Cell Cardiol*, 28:1085–1096, 1996.

[172] M. Nabauer, D. J. Beuckelmann, et al. Regional differences in current density and rate-dependent properties of the transient outward current in subepicardial and subendocardial myocytes of human left ventricle. *Circulation*, 93:169–177, 1996.

[173] E. Drouin, G. Lande, and F. Charpentier. Amiodarone reduces transmural heterogeneity of repolarization in the human heart. *J Am Coll Cardiol*, 32:1063–1067, 1998.

[174] G. R. Li, J. Feng, L. Yue, and M. Carrier. Transmural heterogeneity of action potentials and i_{to1} in myocytes isolated from the human right ventricle. *Am J Physiol*, 275:H369–H377, 1998.

[175] J. M. Morgan, D. Cunningham, and E. Rowland. Dispersion of monophasic action potential duration: demonstrable in humans after premature ventricular extrastimulation but not in steady state. *J Am Coll Cardiol*, 19:1244–1253, 1992.

[176] M. P. Nash, C. P. Bradley, et al. Human hearts posses large regions of steep and flat APD resitution. *Europace*, 6(Suppl 1):187, 2004.

[177] Z. Qu, J. N. Weiss, and A. Garfinkel. Cardiac electrical resitution properties and stability of reentrant spiral waves: a simulation study. *Am J Physiol*, 276:H269–H283, 1999.

[178] M. P. Nash, C.P Bradley, et al. Whole heart APD restitution properties in cardiac patients: a combined clinical and modelling study. *Exp. Physiol.*, g1:33g–35g, 2006.

[179] H. V. Huikuri and Yli-Mäyry. Frequency dependent effects of d-sotalol and amiodarone on the action potential duration of the human right ventricle. *Pacing Clin. Electrophysiol.*, 15:2103–2107, 1992.

[180] J. Melichercik, J. Brachmann, et al. Rate and time dependent effects of d-sotalol on the monophasic action potential after sudden increase of the heart rate. *Pac Clin Elelctrophsiol*, 22(1):65–72, 1999.

[181] G. Schram, L. Zhang, et al. Ranolazine: ion-channel-blocking actions and *in vivo* electrophysiological effects. *Brit J Pharmacol*, 142:1300–1308, 2004.

[182] R. H. Clayton. Computational models of normal and abnormal action potential propagation in cardiac tissue: linking experimental and clinical cardiology. *Physiol Meas*, 22:R15–R34, 2001.

[183] K. Gima and Y. Rudy. Ionic current basis of electrocardiographic waveforms: a model study. *Circ Res*, 90:889–896, 2002.

[184] G. Li, B. Yang, et al. Transmembrane I_{Ca} contributes to rate-dependent changes of action potentials in human ventricular myocytes. *Am J Physiol Heart Circ Physiol*, 276(1):H98–106, 1999.

[185] M. Lieberman, T. Sawanobori, J. M. Kootsey, and E.A. Johnson. A synthetic strand of cardiac muscle: its passive electrical properties. *J. Gen. Physiol.*, 65:527–550, 1975.

[186] J. Crank and P. Nicolson. A practical method for numerical evaluation of solutions of partial differential equations of the heat-conduction type. *Adv Comput Math*, 6(1):207–226, 1996.

[187] R.M. Shaw and Y Rudy. Ionic mechanisms of propagation in cardiac tissue: Roles of the sodium and l-type calcium currents during reduced excitability and decreased gap junction coupling. *Circ. Res.*, 81:727–741, 1997.

[188] G. X. Yan, W. Shimizu, and C. Antzelevitch. Characteristics and distribution of M cells in arterially perfused canine left ventricular wedge preparations. *Circulation*, 98:1921–1927, 1998.

[189] S. Rush and H. Larsen. A practical algorithm for solving dynamic memrbane equations. *IEEE Trans Biomed Eng*, 25(4):389–392, 1978.

[190] H. Z. Wang, P. R. Brink, and G. J. Christ. Gap junction channel activity in short-term cultured human detrusor myocyte cell pairs: gating and unitary conductances. *Am J Physiol Cell Physiol*, 291:C1366–C1376, 2006.

[191] R. M. Shaw and Y. Rudy. Electrophysiological effects of acute myocardial ischemia: a mechanistic invetigation of action potential conduction and conduction failure. *Circ. Res.*, 80:124–138, 1997.

[192] P.M. Taggart, T. Sutton, et al. Inhomogeneous transmural conduction during early ischemia in patients with coronary artery disease. *J. Mol. Cell. Cardiol.*, 32:621–639, 2000.

[193] G. X. Yan and C. Antzelevitch. Cellular basis for normal T wave and the electrocardiographic manifestations of the long QT syndrome. *Circulation*, 98:1928–1936, 1998.

[194] E. Lepeschkin and B. Surawicz. The measurement of the QT interval of the electrocardiogram. *Circulation*, 6:378–388, 1952.

[195] M. Malik, P. Färbom, et al. Relation between QT and RR intervals is highly individual among healthy subjects: implications for heart rate correction of the QT interval. *Heart*, 87:220–228, 2002.

[196] P. Smetana, V. Batchvarov, et al. Sex differences in the rate dependence of the T wave descending limb. *Cardiovasc Res*, 58:549–554, 2003.

[197] D. B. Percival and A. T. Walden. *Wavelets methods for time series analysis*. Cambridge University Press, Cambridge, UK, 2000.

[198] S. Mallat. *A wavelet tour of signal processing*. Academic Press, 2 edition, 1999.

[199] A. Graps. An introduction to wavelets. In *IEEE Comput Sci Eng*, volume 2, pages 50–61, June 1995.

[200] I. Daubechies. Ten lectures on wavelets. In *Society for Industrial and Applied Mathematics*, Pennsylvania, USA, 1992.

[201] M. Mistii, Y. Misiti, G. Oppenheim, and J. M Poggi. *Wavelet toolbox user's guide*. The MathWorks Inc., 2 edition, 2000.

[202] P. S. Addison. Wavelet transforms and the ECG: a review. *Physiol Meas*, 26:155–199, 2005.

[203] A. Djohan, T. Q. Nguyen, and W. J. Tompkins. ECG compression using discrete symmetric wavelet transform. In *Eng Med Biol Soc*, pages 167–168, Montreal, Canada, 1999. IEEE.

[204] R. R. Coifman and D. L. Donoho. *Wavelets in Statistics*, chapter Translation-invariant de-noising, pages 125–150. Springer, New York, USA, 1995.

[205] N. P. Hughes and L. Tarassenko. Probabilistic models for automated ECG interval analysis in Phase 1 studies. Technical Report BSP 08-01, University of Oxford, 2008.

[206] P. E. Tikkanen. Nonlinear wavelet and wavelet packet denoising of the elctrocardiogram signal. *Biol. Cybern.*, 80:259–267, 1999.

[207] J. P. Martinez, R. Almeida, et al. A wavelet-based ECG delineator: evaluation on standard databases. In *IEEE Trans Biomed Eng*, volume 51, pages 570–581, 2004.

[208] C. Terrence and G. P. Compo. A practical guide to wavelet analysis. *Bull Am Meteor Soc*, 79(1):61–78, 1998.

[209] A. T. Walden and C. A. Contreras. The phase-corrected undecimated discrete wavelet packet transform and its application to the timing of events. *Proc Roy Soc A*, 454:2243–2266, 1998.

[210] G. P. Nason and T. Sapatinas. Wavelet packet transfer function modelling of non-stationary time series. *Stat Comput*, 12:45–56, 2002.

[211] D. P. Golden, J. R. Roger, A. Wolthuis, and G. W. Hoffler. A spectral analysis of the normal resting electrocardiogram. In *IEEE Trans. BME*, volume 20, pages 366–372, 1973.

[212] Friesen GM, Jannett TC, et al. A comparison of the noise sensitivity of nine QRS detection algorithms. *IEEE Trans Biomed Eng*, 37(1):85–98, 1990.

[213] C. R. Meyer and Kelser H. N. Electrocardiogram baseline noise estimation and removal using cubic splines and state-space computation technique. *Comput Biomed Res*, 10:459–470, 1977.

[214] P. S. Hamilton. A comparison of adaptive and non-adaptive filters for reduction of power line interference in the ECG. *IEEE Trans. Biomed. Eng.*, 43:105–109, 1996.

[215] L. Sörnmo. Time varying digital filtering of ECG baseline wander. *Med Biol Eng Comput*, 31(5):503–508, 1993.

[216] D. L. Donoho. De-noising by soft-thresholding. *IEEE Trans. Info. Theory*, 41(3):613–627, 1995.

[217] B. Mozaffary and M. A. Tenati. ECG baseline wander elimination using wavelet packets. *Trans Eng Comp Tech*, 3:22–24, 2004.

[218] K. L. Park, K. L. Lee, and H. R. Yoon. Application of a wavelet adaptive filter to minimise distortion of the ST-segment. *Med. Biol. Eng. Comput.*, 36:581–586, 1998.

[219] W. Zhang, X. Wang, et al. Noise reduction in ECG signal based on adaptive wavelet transform. In *Proc. IEEE Eng. Med. Biol.*, Shanghai, China, Sept 2005.

[220] C. L. Feldman. Computer detection of cardiac arrhythmia: historical review. *Amer Rev Diag*, 2(5):138–145, 1983.

[221] B.-U. Köhler, C. Hennig, and R. Orglmeister. The priniciples of software QRS detection. *IEEE Eng Med Biol*, 21(1):42–57, 2002.

[222] L. Sörnmo, O. Pahlm, and M. E. Nyg'ard. Adaptive QRS detection: a study of performance. *IEEE Trans. Biomed. Eng.*, 32:392–401, 1985.

[223] J. Pan and W. J. Tompkins. A real-time QRS detection algorithm. In *IEEE Trans Biomed Eng*, volume 32, pages 230–236, 1985.

[224] C. Li, C. Zheng, and C. Tai. Detection of ECG characteristic points using wavelet transform. In *IEEE Trans Biomed Eng*, volume 42, pages 21–28, 1995.

[225] MIT Bioengineering Division. MIT/BIH aarrhythmia database - tape directory and format specification. Technical Report BMEC TR00, Beth Israel Hospital, Boston, MA, USA, 1980.

[226] S. Mallat and S. Zhong. Characterization of signals from multiscale edges. *IEEE Trans Pattern Anal Mach Intell*, 14(7):710–732, 1992.

[227] J. Canny. A computational approach to edge detection. *IEEE Trans Patt Anal Machine Intell*, 8:679–698, 1986.

[228] J. S. Sahambi, S. M. Yandon, and R. K. P. Bhatt. Using wavelet transforms for ECG characterization: an on-line digital signal processing system. In *IEEE Eng Med Biol*, volume 16, pages 77–83, 1997.

[229] I. Romero Lagarreta, P. S. Addison, M. J. Reed, et al. Continuous wavelet transform modulus maxima analysis of the electrocardiogram: beat-to-beat characterisation and beat-to-beat measurement. *Int J Wavelets Multiresol Inf Proc*, 3:19–42, 2005.

[230] Q. Xue and S. Reddy. Algorithms for computerized QT analysis. *J Electrocadiol*, 30(Suppl):181–186, 1998.

[231] P. Laguna, R. Jane, and P. Caminal. Automatic detection of wave boundaries in multilead ECG signals: validation with the CSE database. *Comput Biomed Res*, 27:45–60, 1994.

[232] H. Vullings, M. Verhaegen, and H. B. Verbruggen. Automated ecg segmentation with dynamic time warping. In *Proc Eng Med Biol Soc*, volume 1, pages 163–166, Hong Kong, China, 1998. IEEE.

[233] N. Maglaveras, T. Stamkopoulos, et al. ECG pattern recognition and classification using non-linear transformations and neural networks: a review. *Int J Med Inform*, 52(1):191–208, 1998.

[234] N. P. Hughes. *Probabilistic models for automated ECG interval analysis*. PhD thesis, University of Oxford, Oxford, UK, 2006.

[235] R.V. Andreão, B. Dorizzi, and J. Boudy. Ecg signal analysis through hidden markov models. *IEEE Trans Biomed Eng Soc*, 53(8):1541–1549, 2006.

[236] G. J. McLachlan and D. Peel. *Finite mixture models*. John Wiley & Sons, Inc., 2000.

[237] D. A. Coast, R. M. Stern, et al. An approach to cardiac arrhythmia analysis using hidden Markov models. In *IEEE Trans Biomed Eng*, volume 37, pages 826–836, 1990.

[238] A. Koski. Modelling ECG signals with hidden Markov models. *Artif Intellig Med*, 8:453–471, 1996.

[239] L. Clavier and J. M. Boucher. Segmentation of electrocardiograms using hidden Markov model. In *IEEE Eng Med Biol Soc*, pages 1408–1409, Amsterdam, 1996.

[240] S. Graja and J. M. Boucher. Multiscale hidden Markov model applied to ECG segmentation. In *WISP 2003: IEEE International Symposium on Intelligent Signal Processing*, pages 105–109, 2003.

[241] Andre ao R. V. and J. Boudy. A comparison of wavelet transforms through an HMM based ECG segmentation and classification system. In *Proc Int Conf Biomed Eng*, pages 264–269. IASTED, 2006.

[242] L.R. Rabiner, C.H. Lee, B.H. Juang, and J.G. Wilpon. Hmm clustering for connected word recognition. In *Proc Acoust Speech Sig Proc*, volume 2, pages 405–408. IEEE, 1989.

[243] L. R. Rabiner. A tutorial on hidden Markov models and selected applications in speech recognition. *Proceedings of the IEEE*, 77(2):257–286, 1989.

[244] R. V. Andreão and J. Boudy. Combining wavelet transform and hidden Markov models for ECG segmentation. *J App Sig Proc*, 2007(1):85–95, 2007.

[245] Hughes NP, Tarassenko L, and Roberts SJ. Markov models for automated ECG interval analysis. *In Advances of Neural Information Processing Systems*, 16, 2004.

[246] M. A. T. Figueiredo and A. T. Jain. Unsupervised learning of finite mixture models. *IEEE Trans Pattern Analysis and Machine Intelligence*, 24(3):381–396, 2002.

[247] N. P. Hughes and L. Tarassenko. Automated QT interval analysis with confidence measures. In *Comput Cardiol*, volume 31, Chicago, USA, 2004. IEEE.

[248] I. G. Strachan, P. H. Hughes, et al. Automated QT analysis that learns from cardiologist annotations. *Ann Noninvasive Electrocardiol*, 14(Suppl. 1):S9–S21, 2009.

[249] H. Jiang. Confidence measures for speech recognition: a survey. *Speech comm*, 45:455–470, 2005.

[250] S. Furui. Speaker-independent isolated word recognition using dynamic features of the speech spectrum. In *IEEE Transactions on Acoustics, Speech and Signal Processing*, volume 34, pages 52–59, 1986.

[251] F. Badilini, P. Maison-Blanche, et al. QT interval analysis on ambulatory electrocardiogram recordings: a selective beat averaging approach. *Med Biol Eng Comput*, 37:71–79, 1999.

[252] F. Extramiana, P. Maison-Blanche, M. J. Cabanis, et al. Clinical assessment of drug-induced QT prolongation when associated with heart rate changes. *Clin Pharmacol Ther*, 77:247–258, 2005.

[253] F. Extramiana, A. Leenhardt, and P. Maison-BLanche. ECG evaluation of ventricular properties: the importance of cardiac cycle length. *Ann Noninvasive Electrocardiol*, 14(Suppl. 1):S54–S59, 2009.

[254] J. P. Couderc, M. Zhou, N. Sarapa, and W. Zareba. Investigating the effect of sotalol on repolarisation intervals in health young individuals. *J. Electrocardiol.*, 41:595–602, 2008.

[255] J. S. Hevia, C. Antzelevitch, et al. Tpeak-Tend and Tpeak-Tend dispersion as risk factors for ventricular tachycardia/ventricular fibrillation in patients with the Brugada syndrome. *J Am Coll Cardiol*, 47(9), 1828-1834 2006.

[256] J. P. Couderc, W. Zareba, et al. T-wave morphology and arrhythmic events in patients with dilated cardiomyopathy. In *Comput Cardiol*, volume 30, pages 149–152. IEEE, 2003.

[257] A. Lubinski and E. Lewicka-Nowak. New insight into repolarization abnormalities in patients with congenital long QT syndrome: the increased transmural dispersion of repolarisation. *Pacing and Clin Electrophysiol*, 21:172–175, 1998.

[258] M. Viitasalo, L. Oikarinen, et al. Amulatory electrocardiographic evidence of transmural dispersion of repolarization in patients with long QT syndrome type 1 and 2. *Circulation*, 106:2473–2478, 2002.

[259] W. Zareba, A. J. Moss, and J. A. Konecki. TU wave area-derived measures of repolarization dispersion in the long QT syndrome. *J Electrocardiol*, 30 (Suppl):191–195, 1997.

[260] M. Zabel, B. Acar, et al. Analysis of 12-lead T-wave morphology for risk stratification after myocardial infarction. *Circulation*, 102:1252–1257, 2000.

[261] C. Antzelevitch. Ionic, molecular, and cellular bases of QT-interval prolongation and torsade de pointes. *Europace*, 9(Suppl. 4):4–15, 2007.

[262] C. Graff, J. Matz, et al. Sensitivity of t-wave morphology and the QT interval to small drug-induced electrocardiograph changes. In *Comput Cardiol*, volume 35, pages 319–323. IEEE, 2008.

[263] J. M. Pastore, S. D. Girouard, et al. Mechanism linking T-wave alternans to the genesis of cardiac fibrillation. *Circulation*, 99:1385–1394, 1999.

[264] S. B. Platt, J. M. Vijgen, et al. Occult T wave alternans in long QT syndrome. *J Cardiovasc Electrophysio*, 7:114–148, 1996.

[265] D. Rosenbaum, L. Jackson, et al. Electrical alternans and vulnerability to ventricular arrhythmias. *New Eng J Med*, 330:235–241, 1994.

[266] J. M. Smith and E. A. Clancy. Electrical alternans and cardiac electrical instability. *Circulation*, 77:110–121, 1988.

[267] P. Steinbigler, R. Haberl, et al. T-wave spectral variance - a new method to determine inhomogeneous repolarization by T-wave beat-to-beat variability in patients prone to ventricular arrhythmias. *J Electrocardiol*, 30(Suppl):137–144, 1997.

[268] J. P. Couderc, W. Zareba, L. Burattini, and A. J. Moss. Beat-to-beat repolarization variability in LQTS patients with the SCN5A sodium channel gene mutation. *Pacing Clin Electrophysiol*, 22(11):1581–1592, 1999.

[269] D. A. Forsyth and J. Ponce. *Computer vision: a modern approach.* Pearson Education, Inc., Upper Saddle River, NJ, USA, 2003.

[270] J. S. Paul, M. R. Reddy, and V. J. Kumar. A transform domain SVD filter for suppression of muscle noise artefacts in exercise ECGs. In *Trans Biomed End*, volume 47, pages 654–663. IEEE, 2000.

[271] J. J. Wei, C. J. Chang, N. K. Chou, and J. J. Gwo. ECG data compression using truncated singular value decomposition. In *Trans Biomed Eng*, volume 5, pages 290–299. IEEE, 2001.

[272] A. Al-Zaben and A. Al-Smadi. Extraction of foetal ECG by combination of singular value decomposition and neuro-fuzzy inference system. *Phys Med Biol*, 51:137–143, 2006.

[273] Prior SG, Mortara DW, et al. Evaluation of the spatial aspects of T-wave complexity in the long QT syndrome. *Circulation*, 96:3006–3012, 1997.

[274] F. Badilini, J. Fayn, et al. Relationship between three-dimensional T wave loop morphology and scalar QT dispersion. *Anns Noninvas Electrocardiol*, 2:146–157, 1997.

[275] B. Acar, G. Yi, et al. Spatial, temporal and wavefront direction characteristics of 12-lead T-wave morphology. *Med Biol Eng Comput*, 37:574–584, 1999.

[276] M. Vaglio, J. P. Couderc, X. Xia, and W. Zareba. Fractionated repolarization induced by sotalol in healthy subjects. *Computers in Cardiology*, 32:523–526, 2005.

[277] M. Malik, K. Hnatkova, and V. Batchvarov. Differences between study-specific and subject-specific heart rate corrections of the QT interval in investigations of drug induced QTc prolongation. *Pacing and Clin Electrophysiol*, 27:791–800, 2004.

[278] A. Moss. What resides in the T wave residuum? *J Cardiovasc Electrophysiol*, 16(9):952, 2005.

[279] J. Morganroth and H. M. Pyper. The use of electrocardiogram in clinical drug development: part 1. *Clinical Research Focus*, 12(6):17–23, 2001.

[280] G. Savelieva, X. Yi, K. Guo, K. Hnatkova, and M. Malik. Agreement and reproducibility of automatic versus manual measurement of qt interval and qt dispersion. *Am J Cardiol*, 81:471–477, 1998.

[281] J. M. Bland and D. G. Altman. Comparing methods of measurement: why plotting difference against standard method is misleading. *Lancet*, 346(8982):1085–1087, 1995.

[282] L. R. Rabiner and B. Gold. *Theory and Application of Digital Signal Processing*. Prentice-Hall, Inc., Engelwood, NJ, USA, 1975.

[283] P. Smetana, E. Pueyo, and K. Hnatkova. Effect of amiodarone on the descending limb of the T-wave. *Am J Cardiol*, 92:742–746, 2003.

[284] K. Knatkova and M. Malik. "optimum" formulae for heart rate correction of the qt interval. *Pac Clin Electrophsiol*, 22(11):1683–1687, 1999.

[285] Kowey PR, Marinchak RA, et al. Pharmacologic and pharmacokinetic profile of class III antiarrhythmic drugs. *Am J Cardiol*, 80(8A):16G–23G, 1997.

[286] J. Reid. Structural identifiability in linear time-invariant systems. *IEEE Trans Automat Control*, 22(2):242–246, 1977.

[287] P. Paalanen, J. Kamarainen, J. Llonen, and H. Kälviäinen. Feature representation and discrimination based on Gaussian mixture model probability densities - practices and algorithms. *Pattern Recognition*, 39(7):1346–1358, 2006.

[288] G. P. Nason and B. W. Silverman. *Wavelets and Statistics*, chapter The stationary wavelet transform and some statistical applications, pages 281–300. Springer-Verlag, 1995.

[289] M. J. Shensa. The discrete wavelet transform: wedding the a trous and Mallat algorithms. In *IEEE Trans Sig Proc*, volume 40, pages 2464–2482, 1992.

[290] M. Vitterli and J. Kovačevič. *Wavelets and subband coding*. Prentice-Hall, Englewood Cliffs, NJ, 1995.

[291] A. J. Viterbi. Error bounds for convolution codes and asymptotically optimal decoding algorithm. *IEEE Trans Inf Theory*, 13:260–269, 1967.

[292] T. H. Cormen, C. E. Leiserson, and R. L. Rivest. *Introduction to algorithms*. MIT Press/McGraw Hill, Cambridge, MA, 1990.

[293] A. Rahimi. An erratum for "a tutorial on hidden markov models and selected applications in speech recognition". [Internet] http://xenia.media.mit.edu/∼rahimi/rabiner/rabiner-errata/rabiner-errata.html, Dec 2000.